IN VITRO SIMULATION OF THE HUMAN PROXIMAL COLON TO ADVANCE BIOPHARMACEUTICS MODELLING

By

CONNOR O'FARRELL

A thesis submitted to
the University of Birmingham
for the degree of
DOCTOR OF PHILOSOPHY

School of Chemical Engineering
College of Engineering and Physical Sciences
University of Birmingham
February 2023

ABSTRACT

The Dynamic Colon Model (DCM) is an advanced in vitro model of the human proximal colon. This thesis takes an existing DCM through design, development and validation work to full application as an advanced biopharmaceutical dissolution apparatus. The model was improved in terms of robustness, longevity and industry-integratability. The number of motility patterns until failure was increased from < 80 ($n = 3$) to $> 14,400$.

Magnetic resonance imaging (MRI) showed that the DCM mimicked wall motion, luminal flow patterns and velocities of the contents of the human proximal colon. The segmented architecture and peristaltic activity of the DCM generated flow profiles that were distinct from compendial dissolution apparatuses. Different motility patterns and media viscosities were shown to be classifiable by the degree of mixing-related motion using a new MR tagging method. Furthermore, flow studies were used to inform the design of a digital twin that robustly replicated flow patterns in the DCM under different physiological conditions (media viscosity, volume, and peristaltic wave speed).

Five biorelevant motility patterns extracted from in vivo data were applied to the DCM which significantly affected theophylline release from a controlled release tablet. The concentration profiles of theophylline were markedly localized when measured at different segments of the DCM tube, highlighting the importance of a segmented lumen in intestine models and in generating spatial information to support simple temporal dissolution profiles.

It is recommended that viscosity and shear rates are considered when designing future dissolution test methodologies for hydrophilic matrix-based controlled-release for-

mulations. Mean wall shear rates were strongly time and viscosity dependent although peaks were comparable to previously published estimates of the USPII operated at 25 and 50 rpm. The shear stresses invoked by the unstimulated, healthy adult human colon may be lower than those in the USP II at 25 rpm and thus insufficient to achieve total release of a therapeutic compound from a dosage form. When operated under stimulated conditions, measured drug release in the DCM was between that measured at 25 and 50 rpm in the USP II.

Ultimately, an in silico physiologically-based biopharmaceutic (PBB) model was developed for theophylline in Gastroplus®. To predict theophylline pharmacokinetics from a controlled release tablet formulation, Uniphyllin Continus®, dissolution profiles from the DCM were integrated as global mean data and regional release profiles. The latter used spatiotemporal data collected in the DCM to model drug dissolution and distribution throughout the continuous caecum-ascending colon lumen. Predicted absorption rate was inherently sensitive to hydrodynamics (using the USP II apparatus as a control). Motility patterns which caused drug to accumulate in the caecum resulted in a lower predicted absorption rate than those which performed better at homogenising the lumen, which may have consequences for formulation performance in subjects with impaired motility. Recommendations are made to further compartmentalise the colon in PBB modelling platforms to improve prediction performance for controlled release formulations.

ACKNOWLEDGMENTS

A huge thank you to the dream team of supervisors: Prof Mark Simmons, Prof Hannah Batchelor, and Dr Konstantinos Stamatopoulos. You always went the extra mile to help out and made the PhD experience a truly positive one overall. Thanks also to Dr Richard Greenwood for his support that came mostly in the form of curry.

Acknowledgements go to Steve Brookes, Andrew Tanner and Chyntol Kanhimbe for the technical support received throughout, and to the EPSRC and AstraZeneca for funding this research. Special thanks to Dr. Eva Karlsson and the Biopharmaceutics team at AstraZeneca AB R&D Gothenburg for hosting me in Sweden and for their warm welcome and guidance during my time there.

I want to express my gratitude for the many life-long friends made during my time in Birmingham and of course for Jaz. Honorable mentions go to the Old Mo, Diwan's and my academic protégé, Patrick. Lastly, to my mum for her unwavering support and for enduring my endless monologues about 'the colon' during my cycle rides home from the lab at any hour of the day.

Contents

List of Figures

List of Tables

Chapter One

Introduction

1.1 Overview

The effective treatment of colonic disease has become a significant global public healthcare issue. Inflammatory bowel disease (IBD), encompassing Crohn's disease and ulcerative colitis, affects an estimated 2.5 - 3 million people across Europe [1]. The disease course is chronic and fluctuates in and out of episodes of relapse and remittance, inflicting significant health risk and socioeconomic burden on the patient and approximately five billion Euros per year to healthcare systems [1].

Incidence is increasing at an alarming rate, notably in regions where IBD was previously uncommon, such as South-East Asia [2]. This trend has paralleled the adoption of a 'westernised' diet in these areas; a quantum leap in dietary composition from agricultural produce to ultra-processed foods which have recently been positively associated with risk of developing IBD in a prospective cohort study [3]. Key identifiers of the 'western diet' are refined sugars and a reduction of fibre (among other factors), which have long been attributed to elevated risk of developing IBD according to a systematic review by Hou *et al.* [4].

In response, substantial research efforts have been directed towards the develop-

ment of colon-targeted drug delivery systems. The increased specificity of such systems has established therapeutic advantages, innately for clinical treatment of local disease sites such as colorectal cancers and chronic disorders such as IBD, but also for the systemic delivery of therapeutic protein and peptide molecules. However, annual costs per patient have been increasing, with significant costs attributable to the use of biologics [1, 5]. Therefore a strong case can be made to focus on the reformulation of existing drug products to increase efficacy.

Understanding of the interaction of drug formulations with the colonic environment is currently hampered by a lack of in vitro tools which mimic the complex hydrodynamics and mixing in the colonic environment. For example, the most commonly used dissolution testing apparatus is the United States Pharmacopeia (USP) paddle dissolution apparatus II (USPII); a glass beaker with a hemispherical base and a metal bi-winged paddle which is not representative of mixing conditions within the colon. Predictive dissolution test methods are essential to streamline pharmaceutical research and development. A suite of advanced, physiologically relevant models should permit a significant portion of formulation optimisation in the in vitro space and reduce the need for in vivo studies that carry heavy associated monetary, time and resource costs. However, performance of a dosage form is highly variable according to a multitude of factors such as GI fluid composition, motility and disease state. Of course the ultimate in vitro model would accurately reproduce the anatomy, physical pressures, motility, luminal composition, absorption and secretion processes, microbiome and more, but unfortunately such a model doesn't yet exist. Therefore, it is important to identify which models are most suitable for testing and development of a specific formulation. For example, many controlled release formulations are hydrophilic matrix tablets that release drug material via erosion, which is caused by mixing processes inside the lumen of the intestine. To develop such a product, a model that is able to reproduce colonic fermentation processes may be of little use, however a model that could reproduce fluid dynamics inside the colon could offer extremely helpful insights.

Little is known about intestinal fluid dynamics; the velocities, shear rates and mixing profiles induced by colonic motor patterns. In vivo, vast inter- and intrapatient variability has been widely observed in motility studies [6, 7]; a principle advantage of using an in vitro model is the ability to predetermine biorelevant parameters such as motility pattern, media properties and characteristics of tracking particles. This permits assessment of the interplay between these parameters, unlike inside the dynamic in vivo colonic environment. Furthermore, in vivo experiments are often invasive and capacity for repeats per subject and the number of subjects is limited, highlighting the importance of in vitro testing.

The dynamic colon model (DCM) was invented by Stamatopoulos [8] to replicate the anatomy, mixing patterns and physical pressures of the human proximal colon [9, 10]. This region of the colon in particular is favourable for drug delivery, as it has the highest free water content and lowest luminal viscosity in the region, which promotes mixing and drug dissolution. Additionally, the sudden increase in microbial activity and proximity to the ileocecal junction where pH reaches its peak in the GI tract, are highly exploitable for drug delivery systems that use a trigger mechanism to achieve targeted release. The DCM is currently the only in vitro model with a design rooted in clinical measurements and observations. A standout feature is the segmented lumen, which is essential to reproduce physiologically-relevant peristaltic patterns.

The colon receives undigested food material (chyme) from the ileum through the ileocaecal junction. This is represented by the ileum terminal on the DCM, the injection point for dosage forms, dyes etc. The ileocaecal valve joins the colon at the top of the caecum – the pouch-like base of the ascending colon. The ascending colon extends from the caecum to a sharp bend known as the hepatic flexure. The ascending colon has a segmented appearance comprising saccules called haustra. Contraction of smooth circular muscle causes a haustrum to distend whilst the next downstream haustrum is relaxed, driving the luminal contents forward at a rate controlled by a complexity of factors that

maximise water absorption whilst avoiding over-solidification [11]. This spatiotemporally coordinated pattern of muscle activity is referred to as colonic motility. The DCM uses a computer controlled hydraulic system to mimic colonic motility by inflating and deflating the silicone membrane of each haustrum, thus replicating fluid mixing patterns of the human ascending colon observed in vivo.

Relatively little is known about the colon in comparison to other organs of the body. This is a rapidly developing field, with huge research efforts working to reveal the mysteries of the microbiome and the gut-brain axis. In the field of neurogastroenterology, significant progress is being made with the application of magnetic resonance imaging (MRI) to image the colon, which is otherwise difficult to access. Somewhat in parallel to in vivo research, this project uses MRI techniques to synchronise visualisation and quantification of mimic intestinal wall motion and the flow of the fluid contents inside the DCM.

MR tagging is a technique that has been used to visualise flows inside the human proximal colon. This thesis takes this approach a step further using computer vision programs (written by the author) to quantify the displacement of tagged fluid in previously published in vivo image sequences of the human proximal colon. This gave rise to direct measurements of intestinal flows without the use of a tracer that may produce results skewed by its relaxation time. Following this, the DCM was positioned inside the MRI doughnut and the mimic intestinal wall motion was captured concomitantly to the motion experienced by the tagged contents. Comparison between in vivo and in vitro phantom datasets facilitated a verification of the physiological relevance of the DCM.

In line with Industry 4.0, this project also demonstrates the early stages of a coupled in-vitro-in-silico approach to simulation of the proximal colon. It is highlighted how a validated in vitro model can be used to generate the range of data required to inform the design of a digital twin of the system. This stems from the ability to isolate and control a range of parameters in vitro to explain the physics that underpin GI motility.

The in vitro dissolution profile is a key input to simple compartmental and more complex physiologically based pharmacokinetic (PBPK) models to predict in vivo pharmacokinetic parameters and bioequivalence.

1.2 Thesis aims and objectives

This thesis ultimately aims to use the DCM to develop understanding of intestinal hydrodynamics and how these conditions may impact drug release from a solid oral dosage form.

To begin, existing models of the colon are reviewed and areas are highlighted in which the DCM offers unique value as a research tool for the testing and development of colon-targeted drug formulations. Building on this, research priorities are then directed towards development of the DCM towards becoming an industry-ready option for dissolution testing, through means of:

- improving the robustness and reproducibility of the design and streamlining the maunfacturing process for the DCM.
- providing further insight into flow fields and the dependence of space and time on paramters such as velocities and shear rates that drive dissolution inside the DCM.
- using in vivo data to verify physiological relevance of the wall motion and hydrodynamics inside the DCM.
- applying new knowledge of luminal fluid dynamics to inform the design of, and validate a digital twin of the system.
- exploring the capacity of the DCM to reproduce a range of biorelevant motility patterns and investigating the extent and variability of drug release from extended release formulations under such conditions.

1.3 Thesis structure

The structure of the thesis is outlined below.

Chapter 2 is a critical literature review including excerpts that have been previously published in Advanced Drug Delivery Reviews (ADDR) **'In vitro models to evalate ingestible devices: present status and current trends'** [12] and **'In vivo models to evalate ingestible devices: present status and current trends'** [13]. An overview of colonic function and anatomy is provided before introducing the concept of drug delivery and the available means of colonic drug delivery in particular. Subsequently, the range of in vitro models available for testing controlled release dosage forms is explored. From this section, the advantages of the DCM as an in vitro dissolution apparatus become clear, prior to summarising previous studies and applications of the DCM and the knowledge gaps that remain.

Chapter 3 outlines the design challenges presented by the DCM and the solutions reached that enabled the model to be used as a high-throughput research tool ready for to deliver the work for this thesis and to ease integration into an industry workflow.

Chapter 4 leverages MRI approaches that have recently found application to the human colon to quantify flows inside the DCM under a simple propagating contraction, derived from in vivo data. This chapter takes in vivo MR tagging a step further than has previously been conducted, to quantify flows inside the human proximal colon following intestinal wall contractions. The same technique was applied to the DCM as a means of verifying the flows that the flows inside the DCM are physiologically representative. This provides a new insight into how motion of the colonic walls may control the luminal hydrodynamics that influence drug release from a dosage form inside the proximal colon. This chapter

was published in Pharmaceutics **'Luminal fluid motion inside an in vitro model of the human ascending colon assessed using magnetic resonance imaging'** [14].

Chapter 5 uses MRI techniques to evaluate flow profiles and shear rates in the DCM under the influence of media viscosity, fluid volume and propagation speed of a wall contraction. This information is used to inform the design and validation of a digital twin of the model. This chapter was published in Pharmaceutics **'Simulating the Hydrodynamic Conditions of the Human Ascending Colon: A Digital Twin of the Dynamic Colon Model'**. Pharmaceutics 14(1). [15, 16]

Chapter 6 presents a thorough dissolution study using the DCM. This chapter uses in vivo data to integrate biorelevant motility patterns into the DCM and assess the impact on drug release from an extended release tablet as published in Pharmaceutics **'The Effect of Biorelevant Hydrodynamic Conditions on Drug Dissolution from Extended-Release Tablets in the Dynamic Colon Model'** [17].

Chapter 7 details the construction of a PBPK model for theophylline. The effect of integrating dissolution data from the DCM and USP II on predictivity of theophylline PK characteristics from a controlled release formulation was explored.

Chapter 8 summarises the conclusions of this thesis, from which suggestions are made as to the direction of future work.

1.4 Publications arising from this thesis

- Stamatopoulos *et al.* [10]. **Dynamic Colon Model (DCM): A Cine-MRI Informed Biorelevant In Vitro Model of the Human Proximal Large Intestine Character-**

ized by Positron Imaging Techniques. Pharmaceutics 12(7):659.

Contributions: Writing - Review & Editing.

- Stamatopoulos *et al.* [13]. **In vivo models to evaluate ingestible devices: Present status and current trends**. Advanced Drug Delivery Reviews (177).

  Contributions: Conceptualization, Methodology, Formal analysis, Investigation, Resources, Data Curation, Writing - Original Draft, Writing - Review & Editing, Visualization.

- O'Farrell *et al.* [12]. **In vitro models to evaluate ingestible devices: Present status and current trends**. Advanced Drug Delivery Reviews (ADDR) 178.

  Contributions: Conceptualization, Methodology, Software, Validation, Formal analysis, Investigation, Resources, Data Curation, Writing - Original Draft, Writing - Review & Editing, Visualization.

- O'Farrell *et al.* [14]. **Luminal Fluid Motion Inside an In Vitro Dissolution Model of the Human Ascending Colon Assessed Using Magnetic Resonance Imaging**. Pharmaceutics 13(10), 1545.

  Contributions: Conceptualization, Methodology, Software, Validation, Formal analysis, Investigation, Resources, Data Curation, Writing - Original Draft, Writing - Review & Editing, Visualization.

- O'Farrell *et al.* [18]. **Formulation of an antibacterial topical cream containing bioengineered honey that generates reactive oxygen species**. Biomaterials Advances 133.

  Contributions: Conceptualization, Methodology, Software, Validation, Formal analysis, Investigation, Resources, Data Curation, Writing - Original Draft, Writing - Review & Editing, Visualization.

- Schütt *et al.* [16] and Schütt *et al.* [19]. **Simulating the Hydrodynamic Conditions of the Human Ascending Colon: A Digital Twin of the Dynamic Colon Model**.

Pharmaceutics 14(1).

Contributions: Conceptualization, Methodology, Software, Validation, Formal analysis, Investigation, Resources, Data Curation, Writing - Original Draft, Writing - Review & Editing, Visualization.

- O'Farrell *et al.* [17]. **The Effect of Biorelevant Hydrodynamic Conditions on Drug Dissolution from Extended-Release Tablets in the Dynamic Colon Model**. Pharmaceutics 4(10), 2193.

  Contributions: Conceptualization, Methodology, Software, Validation, Formal analysis, Investigation, Resources, Data Curation, Writing - Original Draft, Writing - Review & Editing, Visualization.

- Stamatopoulos *et al.* [20] **Integrating in vitro dissolution profiles from the in vitro Dynamic Colon Model (DCM) to physiologically based biopharmaceutic modelling (PBBM) to predict the in vivo performance of a modified-release formulation of theophylline**. Pharmaceutics 15(3), 882.

  Contributions: Methodology, Software, Validation, Formal analysis, Investigation, Resources, Data Curation, Writing - Review & Editing.

1.5 Conference presentations arising from this thesis

- AIChE Annual Meeting. 2019, Orlando.
- CDT in Formulation Engineering Annual Conference. Birmingham, 2019
- CDT in Formulation Engineering Annual Conference. Birmingham, 2020.
- CDT in Formulation Engineering Annual Conference. Birmingham, 2021.
- CDT in Formulation Engineering Annual Conference. Birmingham, 2022.
- APS PharmSchi. Belfast, 2022.

- ColoTan 3rd Symposium. Parma, 2023.
- Mixing 17. Porto, 2023 (Presentation accepted).

1.6 Business case

Understanding the behaviour of dosage forms in the colon is a topic of growing medical and societal concern. This is essential to developing formulations that are successful in achieving sufficiently high drug concentrations in the colon to treat local disease effectively. Oral administration of drugs remains the most common route that is considered least invasive and most convenient, however PK and bioavailability issues are prevalent. The European Medicines Agency (EMA) and the US Food and Drug Administration (FDA) have made a call for research into new predictive tools and novel drug delivery systems. This has led to the formation of research groups spanning industry and academia such as ORbiTo (Oral biopharmaceutical Tools) and COLOTAN (colon targeting network).

As such, advanced in vitro dissolution systems form a cornerstone of modern approaches to research by global pharmaceutical firms in the transition to a model-first approach wherein digitisation of experiments is key. An array of evaluative tools is currently available and widespread throughout industry, however the focus is heavily skewed towards the upper GI tract. There is a distinct lack of validated models of the colon with high physiological relevance and predictive capability.

The Dynamic Colon Model (DCM) is poised to help understanding of how biorelevant motility can affect dosage form behaviour and drug dissolution in the colon. This thesis develops the tool itself toward being adaptable into a typical laboratory workflow in the pharmaceutical industry. Vital knowledge is gained on how the model can recapitulate biorelevant wall motion and fluid dynamics and how these conditions may affect the performance of a CR dosage form. The thesis culminates in the application of dissolution

data from the DCM to inform a PBPK model of a theophylline CR formulation, to improve predictions of in vivo pharmacokinetic (PK) characteristics, which is ultimately the end-use of the model.

Chapter Two

Literature review

This chapter contains excerpts published in Advanced Drug Delivery Reviews (ADDR) 178: 'In vitro models to evaluate ingestible devices: Present status and current trends' [12] and Advanced Drug Delivery Reviews (ADDR) 177: 'In vivo models to evaluate ingestible devices: Present status and current trends' [13] for which C O'Farrell was 1st and 2nd author respectively.

2.1 Overview of colonic function and anatomy

The colon is the final region of the GI tract, shown in Figure 2.1. The macro function of the GI tract is as a mixing system to transit nutrients to the appropriate site for absorption. On a micro scale the epithelium works as an absorptive system.

The colon is anatomically divided into four sections: ascending (AC) (or proximal), transverse (TC), descending (DC) (or distal), and sigmoid, with a total length of up to 1.5 m in adult humans. The colon has three longitudinal bands of muscle on the outer surface and a segmented structure; the segments are referred to as haustra [22]. At the junction of the ileum and colon is the caecum; a downward pouch that is about 5 - 7 cm long. The AC extends vertically from the caecum and is 15 cm long; at the top there is a sharp bend

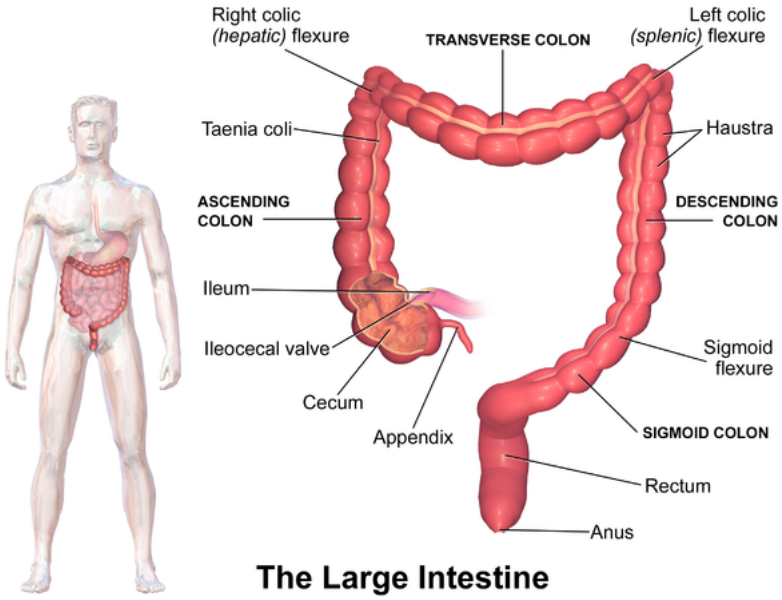

Figure 2.1: Diagram of the human colon [21].

where it becomes the TC [22]. The TC is typically 45 cm long and is considered to be the most mobile portion of the large intestine [22]. Another sharp turn defines the start of the DC which is about 25 cm long and joins to the sigmoid colon [22]. The sigmoid colon is 35 - 40 cm long and joins to the rectum which is 12 - 15 cm in length [22, 23]. The diameter of the colon varies from the widest part being the caecum with a diameter of 7.5 cm and the sigmoid colon being the narrowest at 2.5 cm [23]. The major function of the colon is maintaining water balance, supporting the microbiome, and the production of faeces. Although the surface of the colon is smoother than that in the small intestine, microvilli are present on transverse furrows of the colon to improve the surface area and aid in the maintenance of osmolarity. Much of the surface of the colon is columnar epithelial cells which explains the smooth surface appearance [22].

2.1.1 Colonic volumes

Table 2.1 presents colonic volumes determined using magnetic resonance imaging (MRI). Volumes represent anatomical volume rather than fluid volume, unless stated. Develop-

ment of appropriate models of the colon rely on replication of the capacity of this organ and as such the information in Table 2.1 can inform the biorelevance of the range of in vitro apparatus available. The data shows that the volume of the colon can change depending upon the conditions and that the fluid within the colon does not fill this organ. Furthermore, the fluid that is present is not present as a continuous body, rather in pockets each of a small volume, primarily located in the AC [24].

Table 2.1: Details on the colonic fluid volume (all reported in mL) present in adults reported in the literature. Note that some studies report colonic volume and not the volume of fluid present within the colon. AC, TC, DC and RSC are ascending, transverse, descending and rectosigmoid colon respectively; IBS-D is irritable bowel syndrome type-D; LOP = loperamide; SIM = simethicone; CRF = corticotropin releasing factor; Oxc = oxycodone; Mcg = macrogol; PRN = PR naloxone; FC = Functional constipation.

Ref	N	Measurement	Prandial state	AC	TC	DC	Notes / Key Findings
[25]	12, healthy	Free water volume	Fasted, fed	Colonic water volumes (13 ± 12), intersubject variability 1 – 44 (fasting), 2 – 97(fed).	Water pockets: 2 mL(median).		Water pockets found close to caecum, AC & DC. No food effect on water volume but increased no. pockets from 4-6.
[26]	18, healthy	Water in AC	Drink containing 5 % mannitol in 350 mLwater.	6.9 ± 1.2, LOP: 6.8 ± 1.5 and LOP + SIM: 4.5 ± 0.9	-	-	LOP, LOP + SIM delayed arrival of fluid to the AC.
[27]	25 IBS-D	Colonic volumes	Fasted	205 ± 69	232 ± 100	151 ± 71	10 % expansion of AC volume when fed (rice pudding meal).
	75 healthy			203 ± 75	198 ± 79	160 ± 86	
[28]	25 healthy	Segmental and whole intestinal chyme content (water volume)	Fasted	177 (147-208)	192 (159-226)	133 (110-157)	No intrapatient variability between days. Total volume 1. 760 (662 - 858) mL, 2. 757 (649-865) mL). Defaecation only affected RSC reducing volume from 329 (248-409) to 183 (130-236) mL).
	7 healthy			186 (159-212)	197 (155 - 240)	193 (111-168)	
[29]	4 healthy	Regional water	No restrictions	200 (170-260)	201 (114-243)	148 (122-179)	Total colonic volume 819 (687-899)
[30]	12 healthy	Colonic volume and gas effects of gluten	Fasted -> GF bread	250 ± 119	289 ± 95	209 ± 73	-
			Fasted -> bread	256 ± 149	212 ± 73	187 ± 92	-
			Fasted -> bread + gluten	224 ± 128	178 ± 86	172 ± 77	-
[31]	24 w/ FC	Effect of PEG stimulus on gut volumes	a) Fasted b) 120 min after PEG ingestion	a) 314 ± 101 b) 597 ± 170	-	-	Total colon volume a) 847 ± 280 b) 1505 ± 387
	24 w/ IBS-C		a) Fasted b) 120 min after PEG ingestion	a) 226 ± 71 b) 389 ± 169	-	-	Total colon volume a) 662 ± 240 b) 1039 ± 418

Table 2.1: Details on the colonic fluid volume (all reported in mL) present in adults reported in the literature. Note that some studies report colonic volume and not the volume of fluid present within the colon. AC, TC, DC and RSC are ascending, transverse, descending and rectosigmoid colon respectively; IBS-D is irritable bowel syndrome type-D; LOP = loperamide; SIM = simethicone; CRF = corticotropin releasing factor; Oxc = oxycodone; Mcg = macrogol; PRN = PR naloxone; FC = Functional constipation.

Ref	N	Measurement	Prandial state	AC	TC	DC	Notes / Key Findings
[32]	11 healthy male, 10 healthy female	Effect of IV CRF on fructose malabsorption	a) Baseline fasted b) 45 min post-fructose ingestion	a) 210 ± 77 b) 270 ± 109	-	-	-
			a) Baseline fasted b) 45 min post-fructose ingestion	a) 226 ± 74 b) 252 ± 83	-	-	-
[33]	25 healthy male	Effect of opioid-induced bowel dysfunction on colon volumes	Oxycodone Day 1	177 (147-208)	192 (159-226)	133 (110-157)	Increase in AC, TC and DC volumes
			Oxycodone Day 5	249 (202-291)	230 (190-270)	153 (132-175)	Increase in AC, TC and DC volumes
			Placebo Day 1	186 (159-212)	197 (155-240)	139 (111-168)	Increase in AC, TC and DC volumes
			Placebo Day 5	211 (184-238)	183 (152-213)	121 (101-142)	Increase in AC and RSC volumes, decrease in TC and DC volumes
[34]	10 healthy	Effect of feeding and defaecation on colonic volumes	Low residue diet day 4	*Total colon volume: 479 ± 36 (non-gaseous content)*			Daily faecal volume 145 ± 15 mL10.6 ± 1.6 gas evacuations (daytime)
			High residue diet day 4	*Total colon volume: 616 ± 55 (non-gaseous content)*			Daily faecal volume 223 ± 19 mL. 16.5 ± 2.9 gas evacuations (daytime).
[24]	12 healthy	Total and segmental free water	Fasted	*11 ± 5 pockets of 2 ± 1* mL*resting liquid mostly in AC*			High inter-subject variability with number of pockets ranging from 0 – 89 and amount of water ranging from 0 – 49 mL.
			30 mins post-ingestion of 240 mLwater	*17 ± 7 pockets of 7 ± 4* mL*resting liquid mostly in AC*			
[35]	11 healthy	Free water	Fasted	*2 (0-7)*			-
			Fed Macrogol t=60 min	*140 (104-347)*			-
			Fed Macrogol t=120 min	*146 (32-227)*			-
	11 constipated		Fasted	*11 (1-29)*			-
			Fed Macrogol t=60 min	*228 (91-259)*			-
			Fed Macrogol t=120 min	*84 (3-195)*			-

Table 2.1: Details on the colonic fluid volume (all reported in mL) present in adults reported in the literature. Note that some studies report colonic volume and not the volume of fluid present within the colon. AC, TC, DC and RSC are ascending, transverse, descending and rectosigmoid colon respectively; IBS-D is irritable bowel syndrome type-D; LOP = loperamide; SIM = simethicone; CRF = corticotropin releasing factor; Oxc = oxycodone; Mcg = macrogol; PRN = PR naloxone; FC = Functional constipation.

Ref	N	Measurement	Prandial state	AC	TC	DC	Notes / Key Findings
[35]	9 healthy	Effect of psyllium on volumes	Fasted placebo (Mdx)	138 (114-208)	132 (99-188)	111 (60-185)	-
			Fasted psyllium 10.5 g/d	213 (152-285)	215 (119-332)	142 (117-213)	-
			Fasted psyllium 21.5 g/d	251 (191-301)	228 (163-362)	132 (87-225)	-
	20 constipated		Fasted placebo (Mdx)	270 (174-361)	362 (221-438)	221 (130-278)	-
			Fasted psyllium	390 (320-412)	366 (267-547)	246 (221-336)	-
[36]	20 healthy	Effect of Oxc + Mcg and PRN + Oxc on segmental water	Oxc + PRN day 1	220 ± 25	258 ± 42	187 ± 32	Total colonic volume 941 ± 108
			Oxc + PRN day 5	257 ± 41	295 ± 47	210 ± 51	Total colonic volume 1036 ± 176
			Oxc + Mcg day 1	216 ± 39	270 ± 59	184 ± 55	Total colonic volume 812 ± 158
			Oxc + Mcg day 1	277 ± 53	323 ± 51	231 ± 44	Total colonic volume 1123 ± 145

2.1.2 Colonic transit time

It is known that there is wide variability in the transit time within the colon of adults with range of 12 - 72 hours reported in a normal population [37]. The technique used to measure the transit can affect measurements reported and this is discussed in further detail in the second part of this review paper [13]. There is a meta-analysis on colonic transit times of ingested solid oral dosage forms that may also be useful for the reader [38]; particularly as this highlighted that larger units can move more quickly through the colon compared to multi-units.

2.1.3 Colonic motility

The haustra of the colon relax and contract, expanding and reducing the volume of the lumen respectively. Colonic motility describes these patterns of contractile activity that cause mixing and transit of the contents. The stimuli that initiate this motion remain ambiguous, but triggers are generally thought to include local biochemical changes in the lumen or distension of the lumen caused by intraluminal accumulation of colonic content. Typically, motility follows a circadian rhythm where motility is typically inhibited at night time [23]. Ingestion of fatty meals have been shown to have a stronger influence on motility compared to carbohydrate based meals [39]. This is a developing field of knowledge, with the first translational consensus on terminology and definitions published by Corsetti *et al.* [40] in 2019. The majority of current knowledge on colonic motility in humans has been acquired following bowel preparation and local sedation, which are necessary to place manometric catheters. Although subject to this hindrance, a number of different motility patterns have been identified using high resolution manometry [41]. However, MRI studies of the undisturbed colon have also revealed a range of different motility patterns with minimal intervention [10, 27, 35].

2.1.4 Colon media composition

Diakidou *et al.* [42] found that the level of triglycerides, diglycerides and cholesterol esters was undetectable in the supernatant of healthy human AC contents after ultracentrifugation. However, palmitic acid, linoleic acid, oleic acid, phosphatidylcholine, and cholesterol were measured at levels (mean (±standard deviation)) of 49.6 (± 43.7), 37.4 (± 29.6), 32.8 (± 36.7), 362 (± 210), and 1703 (± 1764) μM respectively in the fasted state, and 103.8 (± 112.1), 47.8 (± 30.0), 73.4 (± 81.7), 539 (± 393), and 1882 (± 1325) μM in the fed state [42]. Fed state colonic contents tend to have decreased protein concentration compared to fasted state [42]. Surface tension is generally higher in the colonic contents (42.7 mN m^{-1} in the fasted state and 39.2 mN m^{-1} in the fed state) than in the small intestine [43]. Osmolarity is typically lower (81 mOsm kg^{-1} in the fasted state and 227 mOsm kg^{-1} in the fed state) than in the small intestine [43]. This may be because the majority of protein digestion occurs upstream of the colon, resulting in dilution of protein contents when contents arrive from the terminal ileum into the AC. In animals it has been shown that fasting reduces concentration of small chain fatty acids (SCFAs) [44]. No published data is available on the viscosity of human AC contents. Composition of the colonic microbiota is beyond the scope of this review.

2.1.5 Colon media pH

Colonic pH is highly variable between pH 5.0 and 8.0 as shown by Figure 2.2. This figure also includes data from pigs and dogs which are commonly used as animal models.

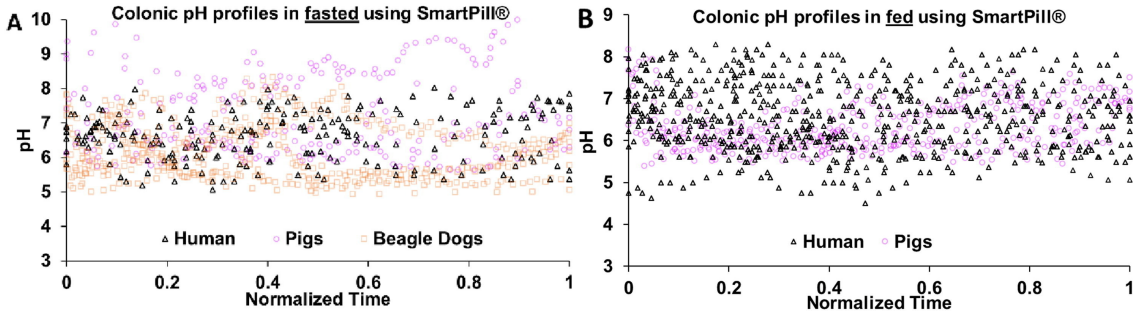

Figure 2.2: pH profiles of the whole colon in humans (n = 10) using the Intellicap® [45] and in pigs (n = 4) [46] and dogs (n = 6) [47] using the SmartPill® under fasted (A) and fed (B) conditions. Appears as presented in Figure 5 of Stamatopoulos *et al.* [13] wherein data was collated and presented by K. Stamatopoulos. Time was normalised according to the duration of the GI transit times.

2.2 Colonic disease, drug delivery and controlled release formulations

2.2.1 Treatment of colonic disease

The effective treatment of colonic diseases has become a significant global public health-care issue. Colorectalcancer (CRC) is the third most deadly and fourth most commonly diagnosed cancer worldwide, with its incidence rising in developing nations [48]. The incidence of inflammatory bowel disease (IBD) is increasing at a highly concerning rate in previously low-incidence regions such as Asia [2]. Across Europe, an estimated 2.5-3 million people are affected by inflammatory bowel disease (IBD), with an associated cost estimation for healthcare systems of 4.6 – 5.6 billion Euros / year [1].

Drug delivery is a wide concept that leverages formulation engineering and molecular design techniques to create an effective means of deliver the drug molecule or active pharmaceutical ingredient (API) to the intended part of the body. A dosage form can be thought of as the package that is carefully designed such that an effective dose of API can

be delivered easily and safely with minimum side effects and drug degradation/waste. A dosage form is required for many reasons: Many APIs can be highly potent and it would be difficult and dangerous for a patient to handle and prepare an accurate dose that can be in the microgram size range [49]. Many drugs have unpleasant organoleptic qualities (taste and smell) that deter patient adherence [50]. Many molecules are sensitive to the environment; and may degrade when being stored and handled (temperature, moisture, light) or administered (pH – sensitive molecules in the acidic environment of the stomach), leading to an ineffective dose. A high concentration of the drug at the point of administration could cause irritation (e.g., skin lesions, ulceration of the oesophagus). Therefore, API molecules are typically mixed with other ingredients to make a dosage form that is easy to handle such as a solution or suspensions (both are common as vaccines), a cream (such as topical antimicrobials), aerosol (inhalers) or familiar tablets and capsules.

2.2.2 Drug delivery

As in nature, form follows function, and the dosage form is designed based on the drug delivery route. Common drug delivery routes include oral, ocular, nasal, pulmonary, transdermal, parenteral, topical, intracecal, vaginal and rectal [50]. Table 2.2 summarises common drug delivery routes (although many more exist) and the dosage forms typically associated. Approximately 90 % of conventional drugs are delivered orally, which is an excellent route in terms of patient compliance.

2.3 Colonic drug delivery

Colonic drug delivery is achieved through oral administration of a controlled release dosage form that releases a significant portion of drug inside the colon, available for absorption or local therapeutic effect. Therefore, the vehicle resists release of the API in the upper GI

Table 2.2: Common drug delivery routes and associated dosage forms

Drug delivery route	**Typical dosage form**	**Process**
Ocular/opthalmic	Solution, gel, cream	Dropped or sprayed onto the surface of the eye
Otic	Solution	Dropped into the ear
Nasal	Solution or suspension	Sprayed into the nostrils
Pulmonary	Aerosol	Inhaled (inhaler or tube/mask)
Buccal	Lozenge	Placed inside the cheek
Sub-lingual	Lozenge or tablet	Placed below the tongue
Oral	Tablet, capsule, solution	Swallowed
Transdermal	Patch, microjet, microneedle	Applied to skin for delivery through the dermis layer
Parenteral	Solution, suspension, emulsion, or reconstituted lyophilized powder	Injected through the skin into the: epidermis (intradermal), bloodstream (intravenous), subcutaneous tissue (subcutaneous) or muscle tissue (intramuscular)
Topical	Cream	Applied directly to the target site (e.g., a burn)
Intrathecal	Solution	Injected into spinal fluid
Vaginal	Cream, suppository	Inserted into the vagina
Rectal	Cream, suppository	Inserted into the rectum

tract and then exploits some factor or combination of factors unique to the GI environment of the ileocecal junction (ICJ) and / or colon in order to release the payload.

Advances in colon targeted delivery have resulted in novel or improved approaches to targeted local treatments for inflammatory bowel disease (Crohn's disease and ulcerative colitis) [51–53] and colorectal cancer [54]. Table 2.3 provides a summary of common colonic disease states, the corresponding therapeutics and method of delivery. A drug delivery vehicle to treat local colonic diseases should facilitate delivery and deposition of the API to the colonic region, diseased tissue targeting and intracellular access. The latter can be problematic for poorly water-soluble drugs. Patients with colonic diseases may produce high levels reactive oxygen species (ROS) and inflammatory cytokines, have an imbalance of important antioxidants, may suffer from mucosal injury [55]. It is therefore also paramount to consider the effects of pathophysiological changes in the microenvironment surrounding disease sites. Additionally, there is great interest in using the colonic microenvironment as a site of entry of drugs into systemic circulation for treatment of diseases such as diabetes [56]. For example simvastatin, a type of statin, has been shown to have three-times greater bioavailability when delivered to using a delayed-release formulation compared to an immediate release formulation, potentially attributable to the comparably low levels of luminal and mucosal metabolic enzymes [57]. There is also lower proteolytic activity in the colon which may also be beneficial for the delivery of biologics such as proteins, peptides and monoclonal antibodies [58–61].

The microbiome exhibits large inter- and intrapersonal diversity and imbalances can influence the onset of both local and systemic diseases [62–64]. The microbiome itself is often thought of as the last organ', capable of affecting pharmacokinetic (PK) characteristics to enhance clinical efficacy for the treatment of systemic diseases such as human immunodeficiency virus (HIV), Parkinson's disease, coeliac disease and diabetes [65–70]. For colon-targeted drug delivery systems, the ascending colon in particular is usually the favourable site as it has the highest free water content and lowest luminal viscosity in the

Table 2.3: Colon-targeted drug deliery - disease, active molecules and delivery methods.

Treatment method	**Diseases**	**Common APIs**
Local	Inflammatory bowel diseases (Crohn's and ulcerative colitis), chronic pancreatitis, irritable bowel syndrome, colorectal cancer, pancreatactomy, cystic fibrosis	Hydrocortisone, budenoside, prednisolone, sulfaselazine, olsalazine, mesalizine, balsalazide, gigestive enzyme supplements, 5-fluorouracil
Systemic	Gastric irritation, gastroesophageal reflux disease (GERD), Salmonella typhi (Typhoid)	Non-steroidal antiflammatory drugs (NSAIDs), steroids, insulin, oral live attenuated typhoid vaccine, probiotics

region, which promotes mixing and drug dissolution. Additionally, the sudden increase in microbial activity and proximity to the ileocecal junction where pH is widely known to peak in the GI tract, are favourable for drug delivery systems that utilise these factors.

2.4 Orally-administered controlled release dosage forms

Controlled release formulations are manipulated to delay, sustain drug or target drug release. Controlled release formulations carry many benefits such as reducing the dosing frequency and consequently improving patient compliance; reducing potential for toxicity; less drug waste; minimal fluctuation in blood plasma concentration; reduced risk of side effects and augmented treatment efficacy [71]. This is because the delivery system maintains a constant level of drug in systemic circulation and diseased tissue for an extended period of time.

The non-API constituents of a dosage form are known as excipients. Considering orally administered dosage forms, these typically include fillers, binders, disintegrants, functional polymers, glidants, lubricants, dyes, flavouring agents. Dyes and flavourings

can make an oral dosage form more palatable, masking unpleasant flavours and / or imparting enjoyable qualities, as a sweetener may do. These ingredients increase organoleptics with the aim to increase patient adherence to medication. Binders lend structural integrity and help to hold the tablet together post-compression. Disintegrants are usually hydrophilic compounds that swell rapidly and significantly on contact with water. When this happens to components of a tablet post-ingestion, the structure ruptures into smaller fragments, increasing surface area and rate of dissolution. Fillers are inert compounds that increase the size of the tablet to improve ease of handling; API content can be as small as low milligram to micrograms. Glidants and lubricants and improve the flowability of a powder mixture during manufacture and prevent material from adhering to machinery. This also improves the surface finish of tablets by reducing friction between the powder and die during tabletting.

2.4.1 Time-dependent hydrophilic matrix tablets

Colonic drug delivery can be achieved using non-targeted, controlled release formulations that simply take an extended amount of time to release the API. This results in minimal drug release in the uppeer GI tract and a significant portion of drug being released in the ileum and colon. Polymers are often used in controlled release formulations to achieve the desired release profile. For example, reservoir systems wherein drugs are encapsulated within inert water-insoluble polymeric membranes [72, 73]. One of the most common and successful orally administered controlled release dosage forms is the hydrophilic matrix tablet [74]. These formulations are an affordable technology with well-documented success and widely accepted confidence in their performance. This system comprises a solid dispersion API throughout a matrix of biodegradable, hydrophilic polymer. Cellulose derivatives, such as hydroxymethyl/ethyl cellulose, are a popular choice for the polymer in these formulations due to advantageous swelling properties, biocompatibility (non-toxic), ease of handling and wide availability. These formulations are not typically

'targeted', the time-dependence may result in the release of a significant portion of the drug-load inside the colon. However, some choice polymers may exhibit a pH-sensitive solubility that can hinder release in the upper GI tract and increase targeting capabilities.

Figure 2.3 depicts the evolution of the macro-scale processes that a typical hydrophilic matrix system exhibits, which are important to understand from the perspective of both the polymer and the API.

Fist, consider the polymer. When the dry tablet (a) becomes surrounded by aqueous fluid (upon ingestion) (b) the tablet surface becomes wet and the polymers begin to hydrate, forming a viscous gel layer [75]. Hydration causes the polymers to expand and the tablet body to increase in diameter, as shown by the growing tablet size from (a) to (d). Simultaneously, the hydrated gel layer advances towards the core of the tablet with time as water gradually ingresses. After sufficient hydration, the gel-like like matrix becomes susceptible to dissolution and erosion, the latter of which is driven by the hydrodynamics of the system – primarily the mixing conditions but also the viscosity, volume and composition of the surrounding media. Hydrodynamic forces begin to erode polymer material at the surface (c) and eventually penetrate the tablet body (d) until the unit fragments (e).

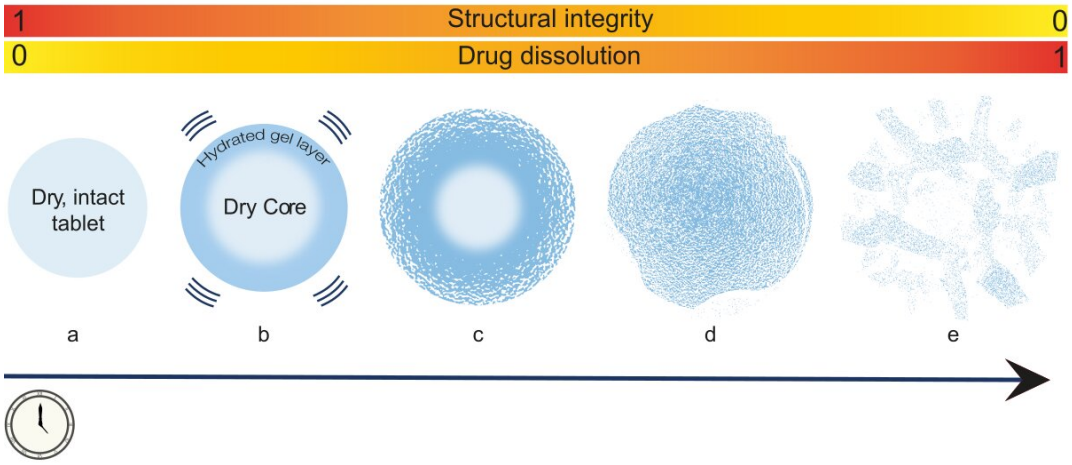

Figure 2.3: Interaction of a hydrophilic matrix tablet with water. a) Dry intact hydrophilic matrix tablet. b) On contact with water, surface polymers gelate and the dosage form swells c) Water ingresses and the gel layer approaches forming a viscous gel layer.

From the perspective of the API, on exposure to aqueous fluids (b) drug molecules at the surface dissolve into the surrounding fluid, causing a small burst release effect. As the polymers hydrate to form a gel – an environment suitable for drug molecules to dissolve. Dissolved API diffuses through the gel, following Fickian diffusion principles (Equations 2.1 and 2.2), towards the bulk fluid. As drug molecules diffuse out of the matrix, the porosity of the system increases and the structural integrity diminishes.

Fick's first law (Equation 2.1) states that the diffusive molar flux (J) is proportional to the concentration gradient (dc/dx)

$$J = D\frac{dc}{dx} \tag{2.1}$$

Fick's second law (Equation 2.2) incorporates distance, stating that the rate of change of concentration at a specific location in space (dc/dt) is proportional to the second derivative of concentration with respect to distance (d^2c/dx^2).

$$\frac{dc}{dt} = D\frac{d^2c}{dx^2} \tag{2.2}$$

Drug release is proportional to the diffusion coefficient D, which describes the ability of the dissolved drug molecule to diffuse through the gel. This is affected by physicochemical characteristics of the drug (particle size, solubility), the polymer, (chain length, gel viscosity) and the matrix (porosity, tortuosity) [75–77].

Additionally, excipient polymers with a higher molecular weight may require a longer time to hydrate and form a gel layer, resulting in a pronounced lag time in drug release. Therefore, physiological phenomena such as gastric emptying time, small intestine transit time and composition of GI fluids are significant in determining drug release. Furthermore, as the polymers swell and the diameter of the tablet increases, the length of the diffusion path (dx) from the tablet core to the bulk fluids is also extended. This is inversely proportional to release rate (Equation 2.2). to control the rate of swelling and in turn, dosage, using a sustained release, this is particularly important for ulcerative colitis drugs which are administered at high strength [78]. Other factors are also at play such as drug/polymer ratio and manufacturing parameters such as compression force and tablet shape.

Post-hydration, the hydrodynamics of the environment that govern the shear and normal forces on the tablet surface drive erosion of the matrix and release of the drug. Erosion results in the formation of smaller fragments wherein the surface area of tablet material exposed to fluids is augmented, driving drug dissolution rate. Mixing performance of the surroundings are also instrumental in maintaining a concentration gradient (dc) between the tablet body and the surrounding fluids.

Hydrophilic matrix systems alone typically achieve a sustained release and may reside in the colon for extended periods of time while drug is being released due to the time required for polymer hydration, drug diffusion and matrix degradation. However,

to improve colon-targeting, polymers may be chosen that have a pH-sensitive swelling profile. The range of colon-targeted formulation designs is extensive, from the reservoir and matrix systems mentioned in this section, to those that leverage nanotechnology such as liposomes, dendrimers, exosomes, carbon nanotubes and nanoemulsions. Adepu and Ramakrishna [79] recently reviewed the broad range of controlled release dosage form designs available. The following section highlights some of the key approaches used for colon targeted release in particular.

2.4.2 Approaches to colon targeting

The colonic environment has many features that make it a targetable site for drug delivery. This section describes those that are most applicable to colon-targeted drug release, which has been reviewed in greater detail by Amidon *et al.* [80].

pH dependent systems

Conventional, clinically embraced approaches to colon targeted drug delivery utilise enteric-coated systems, which pursue colonic delivery through exploiting the distinct increase in pH upon reaching the ileocecal junction to ensure the target site is reached before effecting a controlled API release. Accordingly, polymers suitable for employment as an enteric coating must have a pH-sensitive dissolution threshold of > pH 6.0. This commonly includes methacrylic acid copolymers, such as Eudragit® (Eu)S, EuL and EuFS [81], which are most commonplace in currently marketed formulations that deliver anti-inflammatory drugs for IBD therapy. These compounds have ionisable carboxyl groups which are responsible for the pH-sensitive dissolution threshold. Crowe *et al.* [82] developed Eu L100-coated tablets for colonic delivery of V565, an anti-tumour antibody. This tablet exhibited the sustained drug release at pH $\geq$ 6.0 but no drug release during 2 hour incubation in acidic conditions. In vivo studies in monkeys also supported the sustained

release of V565 in the intestine for the topical treatment of IBD [82].

Despite the wide-ranging commercial use of enteric formulations, it has been long-established that inconsistencies are often observed in the site of release in vivo due to the vast inter- and intrasubject variability in GI pH, resulting in the target release site being missed [83, 84]. GI pH is a dynamic range that is influenced by diet, disease state, fluid volumes, motility and water intake [85, 86]. Those with ulcerative colitis exhibit a more acidic colonic environment compared to healthy subjects, leading to incomplete drug release from enteric coated systems at the target site [86]. Even in healthy humans the abrupt decrease in pH from the terminal ileum to the caecum can mean that enteric polymers are not subjected to solubilising pH conditions for a sufficient duration to release the drug. This is particularly problematic in formulations that use increased coating thicknesses to ensure prevention of premature release in the upper GI tract [86]. Furthermore, considering the widely used Eudragit®(Eu)-S coating, studies have shown that EuS films, irrespective of application as an organic solution or an aqueous polymeric dispersion, are inept at selectively delivering drug substance to the colon [87]. Since, the inability of organic EuS-coated tablets to achieve timely disintegration has been confirmed under fasted, fed and pre-feed statuses [88], whilst various marketed tablets coated with EuS suffer from incomplete release in some cases [89]. Ibekwe *et al.* [88] suggested that disintegration of these tablets is affected by the interplay of multiple physiological factors including GI pH, feed status and intestinal transit time.

For these reasons, enteric coatings are often combined with other types of delivery system, as explained in the following sections.

Microbiome-triggered systems

The microbiome approach to colon-targeted drug delivery exploits the immense metabolic activity of the microbiota. Specifically, that associated with enzymes encoded by the mi-

crobiome of the colon, which can metabolise polysaccharides that resist degradation in the upper GI tract and exhibit properties favourable for use as coatings or matrices for a colon-specific drug-delivery vehicle [90, 91]. Particularly, naturally-occurring polysaccharides such as pectin, chitosan, amylose and guar gum are preferable for use in industry due to their availability at large scale, relatively low cost and safety profile approval for use as pharmaceutical excipients [81]. Many polysaccharides display high mucoadhesiveness, prolonging the contact time and area between the delivery system and the mucosa of the target site, collectively increasing the capacity for mass transport phenomena involved in delivering the drug.

Some polysaccharides have structural characteristics that make them favourable for drug-loading: high adsorption capacity, specific surface area and is biodegradability, which lends to its wide-ranging use for encapsulation of delicate compounds (sensitive to oxidation, low hydrophilicity, low pH resistance etc.) across food [92], pharmaceutical [93] and many other industries [94]. However, polysaccharide-based delivery systems also have some potential drawbacks, such as a broad range of molecular weights and variable chemistry, but principally their high hydrophilicity and aqueous solubility. This may result in the early and undesirable drug release in the upper GI tract if this approach is used as a single colon-targeting mechanism. Accordingly, polysaccharides are often treated with varying degrees of cross-linking agents [95] or combined with pH-dependent coatings overcome this issue; notably the use of disulphide cross-linked polysaccharides [96].

Combined pH dependent systems

As mentioned above, there has been a recent push to improve the targeting of pH-dependent colon-targeted formulations through combining this approach with other techniques. Several dual approaches of release in both a pH- and time-dependent manner have been shown to be more effective in overcoming pathophysiological variability to reduce premature drug release in the upper GI tract and increase the consistency of colonic release com-

pared to a pH-dependent system alone. For example, dual-coated systems of EuS variants [97, 98], combinations of EuS and ethyl cellulose [92], Eu FS/NM and Metolose [93], Eudracol® (coatings of Eu RL/RS and Eu FS 30D) [94] and microspheres combining time-and-pH-dependent systems [93]. Park *et al.* [95] prepared a bisacodyl-loaded tablet by coating with different combinations of pH-sensitive (EuS, EuL) and time dependent polymers (Eu RS). Drug release from the tablet was minimal in the simulated gastric and intestinal fluids while extensive drug release was observed in the colon. Foppoli *et al.* [96] also reported the effective colonic delivery of 5-aminosalicylic acid in both fed and fasted states based on the combination of time-dependent and pH-dependent approaches using low viscosity HPMC and EuL.

ColoPulse technology is an innovative pH responsive coating technology, which incorporates super-disintegrants in the coating matrix to accelerate the disintegration at the target site [99], [100–102]. The incorporation of a super-disintegrant in a non-percolating mode leads to a more reliable and pulsatile drug release. Previous studies demonstrated that ColoPulse tablets enabled the site-specific delivery of the active substance to the ileo-colonic region of Crohn's patients as well as healthy subjects [99, 100]. Furthermore, food and time of food intake did not affect the targeting effectiveness of ColoPulse delivery systems [100].

Resistant starch is a polysaccharide that can resist digestion by mammalian pancreatic amylase, but is readily digested by amylases produced by over 50 % of bacteria in the human colon [103]. Phloral technology integrates the bacteria-sensitive resistant starch and pH-sensitive EuS (insoluble at pH < 7.0) to form a single dual-mechanism matrix film coating. In vivo Gamma scintigraphy studies by [104] demonstrated consistent disintegration of the dosage form at the ileocaecal junction / large intestine in fasted, fed and an intermediate pre-feed state in 8 healthy human volunteers with notably high variability in gastric emptying times. A similar investigation by Ibekwe *et al.* [88] using tablets coated with just Eu S followed identical protocol with the same healthy volunteers to find that

29.17 % of tablets failed to disintegrate at all. The marked improvement observed through incorporating resistant starch is described as a fail-safe system to enhance site-specificity through utilising the ubiquitous microbiota should the pH threshold for EuS not be reached in subjects or low fluid volumes inhibit disintegration [104].

In addition, nano-/micro-particles also hold great potential for specifically targeting inflamed colonic tissues and enhance drug uptake. Accordingly, various formulations that have combined pH-dependent nanoparticle systems have been developed for colon-targeted drug delivery [105–115].

2.5 In vitro models

Recreating human physiology is complex. The colon is no exception, due to its dynamic nature and different component parts, specifically the composition of intestinal fluids, fluctuations in volume and an irregular, discontinuous motility system and how these change by time and location, particularly after ingestion of food.

An ideal model should incorporate macro and micro parameters whilst also mimicking the transit and regional differences. The regional differences can be significant; these can be considered with respect to the architecture of the organ of interest; the cellular epithelial layer, composition of the luminal fluid within that organ as well as the flow and motility. In addition, these aspects can differ in response to ingestion of food or in response to disease which further complicates the model systems. The ideal system would incorporate key features of both the macro and microenvironment; these features are detailed in Table 2.4.

Table 2.4: A summary of macro- and microenvironmental conditions of the GI tract that may be replicated by a biorelevant model.

Macroenvironment	Biorelevant luminal media: composition; volumes and distribution Representative motility patterns (hydrodynamic conditions) Representative transit times between GI regions Representative pressures from within the GI tract Dynamic response in luminal media to the ingestion of food/digestion products and intestinal secretions Feedback mechanisms (e.g., caloric content in small intestine controlling gastric emptying)
Microenvironment	Human derived cells that represent all layers of the mucosa and is stable for sufficiently for experimental work An epithelial substratum with a 3D structure that replicates the in vivo environment A fluidic system that provides adequate oxygenation and nutrients to the cell medium, as well as relevant physiological shear stress A flexible substrate to provide cycle deformation to the epithelium in a physiologically relevant manner Biochemical environment that replicates the crosstalk between epithelium/immune system and microbiota to maintain homeostasis Differentiation of lymphatic uptake from overall absorption

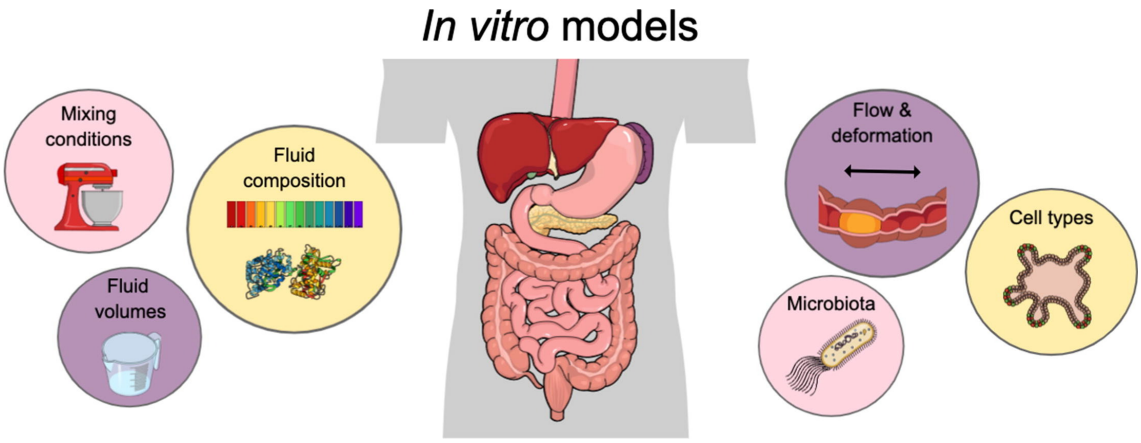

Figure 2.4: In vitro models of the GI tract as shown in Figure 1 of O'Farrell *et al.* [12].

2.5.1 In vitro macro-models

This part of the literature review describes the landscape of the existing range of macro-scale in vitro tools that are available to characterize orally administered drug delivery vehicles that reach the colon. Models are presented with details on their benefits and limitations with regards to the evaluation of such dosage forms and examples of their use in the evaluation of such devices is presented where available. The multitude of models available provides a suite of tools that should be selected on the functionality of the dosage form and the mechanism of its function.

Macro-scale models of the GI tract may be useful for simulating the conditions that an orally-administered solid oral dosage form may have to endure to protect a therapeutic payload. These may be the physicochemical characteristics of GI media in physiologically relevant geometries and volumes or GI motility to produce relevant intraluminal flows and shear forces. Recapitulation of geometry, motility and flow may be most useful for dosage forms that rely on hydrodynamics to achieve complete release of the payload, such as hydrophilic matrix tablets [75]. Further, macroscale models may be useful for the development of dosage forms that exploit intraluminal physicochemical properties and the products of complex physiological processes such as digestion and fermentation [116]. This review details the macro-scale models available for simulation of such processes in

the colon, from basic compendial apparatus used in the pharmaceutical industry, to more advanced in vitro models for pharmaceutical and food-based research. Dynamic models are defined as those where there can be a change in any relevant component that reflects the GI luminal environment; this may include a change in volume or composition of the media or a change in the motility pattern applied. Multicomponent models are those that include more than one region of the GI tract, for example both the stomach and small intestine.

Simulated colonic media

All macro-scale models of the colon must include a model fluid, based on the contents of the lumen. The fluid within the colon changes from the watery fluid that exits the small intestine to the drier faeces that exits the colon. Simulated fluid thus may be dependent upon the region of the colon as well as the purpose for which they are used. Colonic drug delivery systems can be designed to release their drug load based on changes in media pH, the presence of microbiome or time. Thus, the media used in any in vitro test needs to be relevant for the conditions to be simulated. There are fewer standardized simulated colonic fluids in comparison the FaSSIF and FeSSIF recipes that are widely used as simulated small intestinal fluids. In addition, research into foods and digestion has also generated a wide number of simulated colonic fluids. Basic simulated fluids use buffers at the most suitable pH of the colon whereas other methods incorporate the use of enzymes. There are several recipes for simulated colonic fluid (SCoF) that replicate the pH, osmolality, buffer capacity and ionic strength of colonic fluid characterized from humans [117]. There are also recognized recipes that replicate fasted state and fed state simulated colonic fluid (FaSSCoF and FeSSCoF). It should be noted that the composition of the media can affect the release profile for oral drugs, particularly the use of the more physiologically relevant bicarbonate buffer in place of phosphate buffers [118].

Due to the large variety in media that can be used the reader is referred to existing

literature on this topic: dissolution media for dosage forms triggered by colonic microflora [119, 120]; simulated fluids of the AC [43]; simulated fluid to evaluate probiotics [121]; the reproducibility of using faecal slurries in bioreactors [122].

USP apparatus

There are four USP apparatus that are used to simulate the gastro-intestinal environment in drug product development: (i) USP I apparatus (basket); (ii) USP II apparatus (paddle); (iii) USP III apparatus (reciprocating cylinder) and (iv) USP IV apparatus (flow through cell). These are summarised in Table 2.5. Overall, the key benefits of pharmacopoeial models are that they are widely available and reproducible, validated pieces of equipment that are simple, easy to install, use and maintain. USP models may be suitable for the development of dosage forms wherein media composition is essential to achieve the desired release; however, the lack of physiologically representative geometry and hydrodynamics make them an unsuitable choice for the development of dosage forms that interact with mechanical performance such as motility and pressure, for example, luminal flow rates, Reynolds numbers [123], GI lumen volumes and relevant shear forces. In the lower intestine, 200 mL and below is generally considered an appropriate volume of fluid [25, 42].

Modified USP apparatus

Modified pharmacopoeial apparatus to mimic the colon

Pharmacopoeial apparatus has been used previously to mimic colonic conditions. The range of methods used is presented in Table 2.6 which also shows the simulated fluids used within these studies. Modified dissolution apparatus is widely used due to the accessibility and reproducibility of this apparatus globally.

Transfer models

To better simulate passage of a dosage form through the GI tract, a dissolution transfer model may be used to subject a dosage form to progressive region-specific environmental changes. A dissolution transfer model using USP apparatus was first described in 1999 [124]. In brief, a peristaltic pump was used to transfer dissolved drug within simulated gastric fluids into a USP dissolution vessel containing fasted state simulated intestinal fluid (FaSSIF) or fed state simulated intestinal fluid (FeSSIF) as the acceptor phase. The apparatus allowed both the transfer rates (0.5-9 mL/min) and the agitation rate (50, 75 and 150 rpm) within the intestinal vessel to be adjusted [124]. A multicompartment dissolution system has been developed by modifying a conventional six-vessel USP dissolution system to include a "gastric" compartment, an "intestinal" compartment, and an "absorption" compartment [125]. The gastric compartment contained 250 mL dissolution medium (0.1 N HCl, pH 1.2) that is transferred to the intestinal vessel at a rate of 4.5 mL/min; this rate was reduced to reflect slower gastric emptying in elderly patients with a rate of 3.1 mL/min. In addition to fluid flow from the stomach to the intestine undissolved solids were also moved by washing with simulated intestinal media. The gastric vessel was stirred at 100 rpm with a paddle. The “intestinal” compartment is linked to an absorption vessel to simulate the absorption by removing the dissolved drug where the flow rate between these

Table 2.5: Assessment of compendial USP in vitro dissolution apparatus (Y= yes; N = no).

Feature	**USPI / USPII**	**USPIII**	**USPIV**
Geometry	Cylindrical vessel, hemispherical base	Cylindrical vessels, flat meshed base	Cylindrical cell with coned bottom
Volume	0.1, 1, 2, 4 L	300 mL	Standard cell diameters of 12 and 22.6mmfor volume of 8 or 19 mL.
Mixing system	Rotating basket containing dosage form (USP I) / Impeller (USP II)	Reciprocating cylindrical vessels	Peristaltic pump delivering sinusoidal flow of 240 - 960 $mL\,h^{-1}$ at 120 $\pm$ 10 pulses min^{-1}.
Dynamic pH	Requires media dilution or vessel change	Requires multiple media in different vessels	Requires operator to change pump source
Transparent	Y	Y	Y
Temperature control	Y	Y	Y
Absorption	N	N	N
Microbiota	N	N	N
Peristalsis	N	N	N
Relevant pressures	N	N	N
Human-derived cells	N	N	N

vessels is adjusted based on the permeability of the compound under test. The volume in the intestinal compartment is maintained at 510 mL by use of a reservoir; the media is FaSSIF at pH 6.5 and the system is stirred at 100 rpm by a paddle apparatus [125]. The Biorelevant Gastrointestinal Transfer (BioGIT) model is a transfer model based on USP dissolution apparatus where fluid from the gastric compartment is transferred to the duodenal compartment. It has been shown to be useful for evaluating formulation performance particularly, after administration of conventional or enabling products of highly permeable drugs. The gastric compartment consists of 250 mL FaSSGF (within a mini vessel of 500 mL) with stirring at 75 rpm [126].

Supplementary buffer systems

The use of bicarbonate buffer was introduced in 2003 by McNamara *et al.* [127] and improvements on how to use this with standard dissolution apparatus were presented by Fadda *et al.* [128] and further improved upon by Merchant *et al.* [129]. The USPI and USPII were most commonly used for dissolution of orally ingestible dosage forms, however it was not possible to use the physiologically relevant buffer system. Therefore, Garbacz *et al.* [130] investigated the pH shift caused by CO_2 loss in different bicarbonate buffer systems and reported that evaporated CO_2 can be partly substituted by sparging with gas mixtures, such as 5 (v/v) CO_2 and N_2 [130]. Subsequently, the Physio-Stat was introduced, an automated device for monitoring and regulating the pH of bicarbonate buffers, developed using the USP II dissolution apparatus system. The Physio-Stat is composed of a pH electrode, a gas diffuser, a digital microcontroller and a proportional valve system, driven by a bespoke software based on an AVR-GCC open-source platform. Later, Garbacz *et al.* [131] developed the Physio-Grad device, a robust system which enables a biorelevant simulation of intestinal pH gradients without changing the ionic strength of the solution. The Physio-grad system has been used by Zakowiecki *et al.* [132]. Both the Physio-Stat and Physio-Grad can be used in non-pharmacopeial systems and may be applicable to various

models of the small intestine and colon.

Table 2.6: Summary of studies that used pharmacopeial apparatus to mimic the colonic environment. Y = Yes, N = No, GIS = Gatrointestinal simulator, FaSSIF = Fasted state simulated intestinal fluid, FaSSCoF = Fasted stated simulated colonic fluid, FeSSCoF = Fed state simulated colonic fluid

Ref	Dissolution apparatus	Media volume	Media comp.	Bile salt [Y/N]	Viscosity [Y/N]	Microbiota [Y/N]	Mixing	Prior upper GI fluids [Y/N]	Duration [min]	In vivo link [Y/N]
[133]	USPII	500 mL	sodium phosphate buffer	N	N	N	75 rpm	N	240	N
[134]	USPII	500 mL	FaSSCoF	N	N	N	50 rpm	N	1440	N
[135]	USPIII	250 mL	SCoF	Y	N	N	10 dpm	Y	960	N
[136]	USPII stress test device	1160 mL	Hanks hydrogen carbonate buffer (pH 6.8) with 0.1 % Tween 80	N	N	N	200 rpm + stress cycle	Y	1560	N
	USPII	1000 mL	Hanks buffer, Krebs buffer, NaHCO3 solution	N	N	N	50 and 100 rpm	Y (dynamic pH)	720	N
[130]	USPII stress test device	1150 mL	USP pH6.8 buffer with 1 % SDS	N	N	N	50 and 100 rpm	N	360	N
[137]	GISS (based on USPII)	1000 mL	Simulated colonic fluid	N	N	N	50 rpm	Y	400	N
[138]	USPII and USPIII	200 mL	SCoF	N	N	N	10 dpm, 420 um mesh. USPII undefined	Y	240	Y
[139]	Paddle apparatus (unspecified)	6 mL	FaSSIF	N	N	N	100 rpm	N (HCl for pH)	120	Y
[140]	mini USPII (paddle adapted for viscosity)	200 mL	FaSSCof, FeSSCoF v2	Y	Y (fed state)	N	40 or 100 rpm	Y	160	Y
[141]	USPI	1000 mL	FTM	Y	N	Y	100 rpm	N (HCl for pH)	1440	Y
[142]	USPIII, USPIV	235 mL	FaSSCof, FeSSCoF	N	N	N	6 dpm, 4 mLmin-1	N	360	Y
[143]	USPIII, USPIV	235 mL	FaSSCof, FeSSCoF	N	N	N	6 dpm, 4 mLmin-1	Y	360 faS, 540 feS	Y
[144]	USPIII, USPIV	235 mL	FaSSCof, FeSSCoF	Y	N	N	6 dpm, 4 mLmin-1	Y	120	Y
[145]	USPI	1000 mL	FTM supplemented with probiotics (BIOMIX-1)	N	N	Y	100 rpm	Y	1080	Y
[98]	USPII	500 mLgastric, 900 mLintestinal	HCl, pH6 phosphate buffer	N	N	N	100 rpm gastric, 50 rpm intestinal	Y (HCl)	210	Y

Fermentation models of the colon

Multi-compartmental fermentation models of the colon typically feature three fermentation reactors, as initially proposed in 1988 by Gibson *et al.* [146]. Fermentation is not possible to study in vivo, therefore in vitro simulated fermentation models are highly valuable. These models make possible the study of metabolite production by complex microbial ecosystems. Sampling from faecal matter does not reflect the in situ production of metabolites, and the ecological composition of colonic content varies drastically with progress along the GI tract, therefore faecal sampling is most valid for evaluation of the rectal environment. However, most in vitro models however lack absorption capacity to model uptake of metabolites by the epithelium and therefore reflect true intraluminal concentrations. Most in vitro fermentation models are fed through fecal inoculum whereas the PolyFermS uses a microencapsulation technique. Many in vitro fermentation models are static, however Venema & van den Abbeele [147] highlighted a non-physiologically slow rate of conversion in "static cultures" (as opposed to continuous "dynamic" cultures). Furthermore, most models only include microbial populations common to the colonic lumen, neglecting those of the mucosa. Overall, fermentation models of the colon may be suitable for dosage forms that utilise particular microbiological populations or their metabolites for release.

Overview of non-pharmacopeial macro-models of the colon

In this section, a brief outline of non-pharmacopeial in vitro models that incorporate a colon environment is presented in the order in which they were published, the relative attributes are also compared in Table 2.6.

The evaluation of the in vitro models was based on criteria associated with features of the macroenvironment that were presented in Table 2.4. The evaluation of the biorelevance of the luminal media was based upon factors associated with the luminal

composition used within the system. These were scored using the levels of simulation of luminal composition that have previously been reported [148, 149]. These levels are: level 0 is pH only; level 1 is pH plus buffer capacity; level 2 includes bile components, dietary lipids, lipid digestion products and osmolality (this includes FaSSCoF and FeSSCoF) and level 3 also includes dietary proteins, enzymes (not digestion products) and viscosity effects. For the colon additional details on the pH control in each section of the colon is provided as well as whether the microbiota is present; these were scored as 1 where the pH was controlled to a value matching those found in vivo and also 1 where the microbiota was present. The volume used within the system was reported and this was considered to be biorelevant where the volume was similar to the capacity of the human adult colon; biorelevant conditions scored 1 where as non-biorelevant scored 0. The column on the biorelevant luminal media is the sum of the biorelevance scores for the previous four columns.

The representative anatomy provides details of the shape and dimensions of the compartment used to mimic the colon; where these were broadly similar to the dimensions of the colon they scored 1 and where they accurately mimicked the dimensions, they scored 2.

The level of biorelevant motility score comprised the components of the agitation mechanism and pattern of agitation. Where the mixing mechanism applied was consistent with mixing in the colon, via compression of the walls of the mixing vessel a score of 1 was applied. The pattern of agitation scored 1 for discontinuous mixing and 2 where the profile of discontinuous mixing matched that reported in vivo. Where the pressures matched those in vivo, a score of 1 was provided to the model. The overall scores for the biorelevance of motility was the sum of the scores for mixing mechanism, pattern of agitation and pressures. Where the transit time was reported this was scored 1 where it was in line with in vivo data and zero where it was not.

Several models of the colon also include a gastric and/or small intestine compart-

ment. However, it is the colonic conditions that are detailed in this section. The data presented in Table 2.7 highlights the array of in vitro models of the colon that are reported in the literature. The majority focused on reproducing the luminal environment in terms of media composition, mainly as they have been used to probe digestion. However, there are some models displayed efforts to replicate the colonic motility.

Table 2.7: Summary of in vitro models of the colon. FS = Faecal slurry, PC = Proximal colon, cap = capacity, BRS = Biorelevance score.

Model name, ref	AC/TC/DC Volume (mL)	Media (Level, type)	pH Control	Microbiota present	Luminal media BRS	Architecture / geometry	Anatomical BRS	Mixing mechanism	Agitation pattern	Pressure	Motility BRS	Intestinal transit	Transit time BRS	Absorptive function
3-Stage Continuous Culture System [146]	AC: 300 TC: 500 DC: 800	3, FS	AC: 6.0 TC: 6.5 DC: 7.0	Y	6	Cylindrical beaker	0	Stirring	Continuous	Not reported	0	Mapped to in vivo data	1	N
3-Stage Continuous Culture System [150]	AC: 80 TC: 100 DC: 120	3, FS	AC: 5.5 TC: 6.2 DC: 6.8	Y	6	Cylindrical vessel	0	Magnetic stirrer	Continuous	Not reported	0	27.1 h or 1 66.7 h	1	N
SHIME [151]	AC: 500 TC: 800 DC: 600	3, FS	AC: 5.6-5.9 TC: 6.1-6.4 DC: 6.6-6.9	Y	5	Cylindrical vessel	0	Magnetic stirrer	Continuous	Not reported	0	72-76 h	0	Y
BCFFM [152]	100	3, FS	7.2	Y	6	Cylindrical vessel	0	Stirring	Continuous	Not reported	0	24 h	1	N
EBFM [152]	100 (one stage)	2, fluid	7.2	Y	5	Cylindrical vessel	0	Stirring	Continuous	Not reported	0	24 h	1	N
3-Stage Tubular [153]	Flow through system	3, FS	Y, 5.8	Y	5	Cylindrical vessel	0	Not reported	Not reported	Not reported	0	40 h	1	Y - water, metabolites
Enteromix [154]	AC: 3 TC: 5 DC: 7	3, FS	AC: 5.5 TC: 6.0 DC: 6.5–7.0	Y	5	Cylindrical vessel	0	Magnetic stirrer	Continuous	Not reported	0	48 h	1	N
VTT 1-Compartment Fermentation Model [155]	10	3, FS	Controlled, no reported value	Y	5	Cylindrical vessel	0	Orbital mixing	Continuous	Not reported	0	24 h	1	N
ARCOl [156–158]	Cap. 2000, working 450	3, FS	6	Y	6	Cylindrical vessel	0	Stirring	Continuous (400 rpm)	Not reported	0	72 h	1	Y - passive
Polyferm-S [159]	300	3, FS	5.7	Y	6	Cylindrical vessel	0	Overhead mixing	Continuous	Not reported	0	7.5 h	0	N
TNO TIM-2 [160]	200mLcap., 120mLworking	3, FS	6	Y	6	Flexible cylindrical tube	0	Tubular contractions	Discontinuous	Not reported	2	Mapped to in vivo data	1	Y-passive

Table 2.7: Summary of in vitro models of the colon. FS = Faecal slurry, PC = Proximal colon, cap = capacity, BRS = Biorelevance score.

Model name & ref	AC/TC/DC Volume (mL)	Media (Level, type)	pH Control	Microbiota present	BRS of luminal media	Architecture / geometry	Anatomical BRS	Mixing mechanism	Agitation pattern	Pressure	Motility BRS	Intestinal transit	BRS of transit time	Absorptive function
SIMGI [161, 162]	AC: 250 TC: 400 DC: 300	3, FS	AC: 5.6 ± 0.2, TC: 6.3 ± 0.2, DC: 56.8 ± 0.2	Y	6	Cylindrical vessel	0	Stirring	Continuous	Not reported	0	76 h	0	N
M-SHIME [163]	AC: 500, TC: 800, DC: 600	3, FS	AC: 5.6–5.9 TC: 6.1–6.4 DC: 6.6–6.9	Y Mucosal and luminal	5	Cylindrical vessel	0	Magnetic stirrer	Continuous	Not reported	0	72–76 h	0	Y
SBFS [121]	100	3, FS	6.5	Y	6	Cylindrical vessel	1	Stirring	Continuous	Not reported	1	24 h	1	N
CoMiniGut 5 [164]	3	, FS	AC: 5.7–6.0 TC: 6.0–6.5 DC: 6.5–6.9	Y	5	Cylindrical vessel	0	Magnetic stirrer	Continuous	Not reported	0	AC: 0–8 h TC: 8–16 h DC: 16–24 h	1	Y
MicroMatrix [122]	6	3, FS	6.8	Y	6	Cylindrical vessel	0	Orbital mixing	Continuous, 250 rpm	Not reported	0	24 h	1	N
Toddler SHIME [165]	AC: 100 TC: 160 DC: 120	3, FS	AC: 5.4–5.6 TC: 6.0–6.3 DC: 6.3–6.5	Y	6	Cylindrical vessel	0	Magnetic stirrer	Continuous	Not reported	0	24 h	1	N
Dynamic Colon Model (DCM) [9, 10]	290 mL(cap.); 100 mLworking volume	1, fluid	Not reported	N	6	Anatomically accurate model of human AC	2	Segmental contractions	Mapped from in vivo data	Mapped from in vivo data	4	Mapped from in vivo data	1	N

The simulator of the Human Intestinal Microbial Ecosystem (SHIME) The SHIME (ProDigest, Ghent) is composed of five reactors connected in series to reproduce the entire GIT with a focus on fermentation, representing the stomach and small intestine, followed by the ascending, transverse and descending colon respectively. The system was validated in 1993 based on evaluation of fermentation fluxes and products such as indicator bacterial groups, volatile fatty acids, enzymatic activity and headspace gases, however simulation is limited to luminal microbes only. Reactors are double jacketed glass vessels interconnected through peristaltic pumps; the transit time from beginning to end being 72–76 h [151]. The entire system is anaerobic, and each reactor is a double jacketed glass vessel. The colon simulators are continuously stirred reactors with constant volume, residence and pH control; ascending colon: 500 mL, 20 h, pH 5.6 – 5.9; transverse: 800 mL, 32 h, 6.1–6.4; descending: 600 mL, 24 h, pH 6.6 – 6.9. These reactors are filled with nutritional medium and inoculum prepared from human faecal matter and the ascending colon mimic reactor receives media from the small intestine reactor containing a mixture of artificial stomach and pancreatic juices and the initial feed which includes resistant starches. The SHIME model is an evolution of the Reading Model, introduced by Macfarlane *et al.* [166], in that the SHIME includes simulation of upper GI conditions. An updated version of this apparatus is presented in Section 4.6.12. The SHIME model offers the opportunity to evaluate the stability of APIs under colonic conditions, including the complete gut microbiota, however it was not possible to find data with in vivo correlations from this apparatus.

Toddler-SHIME Bondue *et al.* [165] adapted the SHIME to reflect the colonic microbiota of healthy donors aged 1 – 2 years old, highlighting that the 'first 1000 days of life' determine the gut microbiota composition and can have long term influences on health. In addition to inoculation with faeces from healthy children, modifications were made to adapt the system in terms of volumes and pH with the ascending: 100 mL, pH 5.4 – 5.6; transverse: 160 mL, pH 6.0 – 6.3; descending colon: 120 mL, pH 6.3 – 6.5 in addition to

age-appropriate changes to the nutritional medium.

TNO TIM-2 The TNO TIM-2 is a dynamic in vitro model of the colon [160]. The model consists of four interconnected glass compartments containing a flexible membrane representing the lumen. The space between the glass and the flexible membrane is filled with water, the temperature of which can be controlled to maintain the desired temperature of the apparatus. Additionally, pressure can be applied to the water following a controlled sequence to cause the flexible membrane to contract, mimicking colonic peristalsis. A level sensor in the system maintains the volume at 120 mL through control of a pump to expel contents. This model boasts one of the most complex fermentation models of the colon simultaneous to applying physiologically relevant mixing conditions compared to many fermentation models which are simply stirred. The model is fed with inoculum of human faecal suspension. Accumulation of microbial metabolites is prevented by a bespoke dialysate system which enables TIM-2 to maintain an active microbiota for up to 3 weeks. Gases produced by the microbiota can be sampled, in addition to material content sampled from the lumen or sample port. The system is maintained at pH 5.8 by secretion of NaOH, representing that of the human proximal colon. The effect of several food components that have been well-established in vivo have been confirmed in TIM-2; including the bifidogenic nature of inulin [167].

Dynamic colon model (DCM) The Dynamic Colon Model (DCM) is an anatomically representative in vitro model of the human ascending colon, designed based upon cine-MRI images that showed the anatomical architecture and wall motility patterns of the undisturbed colon [10]. The DCM is comprised of 10 haustral segmental with a total length of 200mm(209 $\pm$ 47mmis the length of the caecum-ascending colonic region in humans [168]) and volume of 290 mL(within the physical range of 76 – 390 mL. Each haustral segment is connected to a syringe controlled by a stepper motor which pushes and pulls the plunger of the syringe to pre-programmed displacement values, inflating and

deflating the DCM wall to manipulate the degree of luminal occlusion. The pattern of contractile activity is synchronised between segments to reproduce the widely accepted law of the intestine [169]. Manometric studies showed that the DCM can reproduce the physical amplitudes within the human colon [9]. The current design of the DCM operates: (i) in a horizontal orientation in accordance with the normal supine position adopted by patients during scintigraphy and MRI procedures; (ii) in the fed state in which more frequent propagating sequences of pressure waves occur in the proximal colon [170]. The DCM is the only in vitro model to data (known by the authors) to replicate peristaltic motility in a lumen with the segmented architecture of the human colon. The DCM may be suitable for the development of erodible dosage forms wherein intraluminal hydrodynamics and colonic motility are significant in achieving the desired release, rather than the complex physicochemical characteristics of GI fluids. Although a vast range media can be used inside the DCM across different levels of complexity, the system is not anaerobic and therefore cannot support relevant microbial activity and fermentation.

2.5.2 In vitro micro-models

Many dosage forms must overcome difficulties faced at the microenvironmental level, such as low drug permeability and retention at the epithelial surface, enzymatic degradation and shear forces due to peristalsis [171]. As such, in vitro epithelial models of the GI tract could be useful to test for device binding, mucoadhesion/penetration, and delivery of small molecules and cytotoxicity studies. These models may reproduce the colonic epithelium, which is similar to that of the small intestine in that it is specialized for absorption and lined with crypts, however there is a distinct absence of villi [172]. Another distinguishing feature between the small and large intestinal epithelia is the elevated abundance of mucous-secreting goblet cells in the colonic epithelium. Although the work in this thesis does not include modelling of the microenvironment, it is an important area to consider in terms of future work direction.

Although not the typical dosage form, a range of orally ingestible micro- or nanodevices containing drug reservoirs have been developed which require interaction with the microenvironment for functionalization, often the release of a therapeutic, and could therefore benefit from the implementation of physiologically accurate in vitro models of the GI microenvironment. These atypical dosage forms aim to enhance drug stability through protection against harsh upper GI conditions to improve targeting and uptake [171, 173–182]. An interesting example is ingestible micro- or nanodevices that undergo chemical actuation under specific GI conditions, such as pH, to trigger selfpropulsion [183–189], followed by mucoadhesion and delivery of a therapeutic payload to the epithelial microenvironment [183, 184, 186–188]. Due to the lack of appropriate in vitro models, self-propulsion devices have been tested mostly in murine models to date [183–185, 189].

Most conventional in vitro models of the GI microenvironment involve Caco-2 monolayer models in static Transwell plates have been used for the development of passive drug delivery devices in the past [171, 173, 174, 176, 177, 180–182]. Caco-2 are an immortal human cell line of the colorectal adenocarcinoma; however, these cells are known to differentiate to resemble enterocytes when cultured as a monolayer. These static models are used primarily to study small intestinal barrier function or to model drug permeation and are highly standardised. However, although these cells have the capacity to perform the basic functions of native intestinal epithelial cells, they do not represent the cellular diversity of the intestinal epithelium and present a two-dimensional (2D) culture 9 format, failing to recapitulate the three-dimensional (3D) villus-crypt microarchitecture of the GI epithelium. Furthermore, other intestinal differentiated functions are absent such as cytochrome P450-based drug metabolism and the ability to produce a significant mucous layer asthese cells secrete the gastric mucin (MUC)5AC, but not MUC2 which is typical of the intestinal tract [190]. Additionally, these models cannot support the coculture of commensal microbiome with the epithelial cells as the bacteria rapidly overpopulate the system and contaminate the human cell cultures within one day. Therefore, static models do not accurately reflect human intestinal physiology. Static 2D models have been widely

documented and are not included in this review.

Organoid models of the colon

GI epithelial organoids provide a more sophisticated in vitro model of the GI epithelium. Organoids are recently developed self-organising three-dimensional (3D) cellular cultivations embedded in a laminin-rich extracellular matrix and a medium containing specific supplementary growth factors to mimic the native extracellular environment. Compared with other primary cell cultures, organoids are advantageous in that they possess indefinite proliferative capacity in culture without incurring genetic aberrations or alterations and retaining characteristics representative of the original tissue. Organoids can also be stored cryogenically and subsequently thawed like traditional cultures. These models boast a wealth of drug metabolising enzymes, making them attractive for pharmacologic investigations and drug development with high potential for use in the development of ingestible devices. Organoids constitute a valued system to study epithelial mucosal biology and both normal and abnormal GI physiology.

An example image of an organoid is shown in Figure 2.5, in part B a comparison to traditional monolayers is shown. Colonoids grown as 2D epithelial monolayers on permeable Transwell inserts are rapidly becoming the new gold standard. These models comprise goblet cells and an apical mucous layer, permitting studies of pathogen-mucus interaction [191].

Organoids develop according to the genome of the donor, which permits them to model genetic diseases such as cystic fibrosis [193, 194] and colorectal cancer [195, 196], in addition to bacterial/viral infection such as by C. difficile [197], human rotavirus [198–200], E. Coli [191, 201, 202] and SARS-CoV-2 [203].

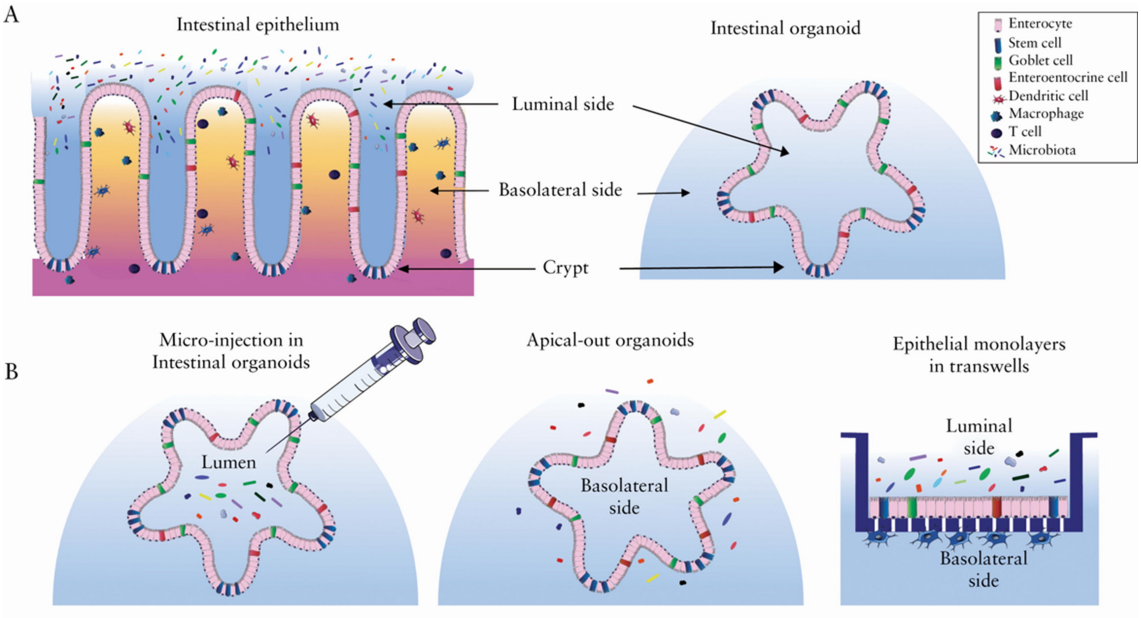

Figure 2.5: Intestinal epithlium and organoid development. A) The intestinal epithelium and organoid development. B) 3D organoids and organoid-derived models. This image is taken from [192] and was originally published in an Open Access article distributed under the terms of the Creative Commons Attribution License (http://creativecommons.org/licenses/by/4.0/), which permits unrestricted reuse, distribution, and reproduction in any medium.

Organ-on-a-chip models of the colon

Organ-on-a-Chip systems are recently developed microphysiological systems that leverage the manufacturing technology behind computer microchips to create a microfluidic device in which GI-derived epithelial cell culture can take place. Recent reviews of GI organ-on-a-chip models are available that cover all areas of the GI tract [204, 205].

Generally, these models have two microchannels; one (apical) lined with epithelial cells, representing the intestinal lumen and the other (basal) representing a blood vessel. The mimic lumina are typically separated by a flexible, semi-permeable membrane that permits the exchange of soluble molecules between channels. Media is pumped through each channel to replicate the dynamic in vivo environment. Some microfluidic chip models include neighboring channels lined by a confluent layer of microvascular endothelial cells, commensal microbes, immune cells and pathogenic bacteria [204, 205]. Some models also permit the application of cyclic mechanical forces to exert deformation patterns matching in vivo contractile activity. The chip housing permits the integration of elements such as sensors, electrodes or valves. Furthermore, the housing is typically optically transparent to facilitate analysis through light, fluorescence and confocal microscopy. Media samples can be withdrawn to allow assay for drug concentration, dissolved O_2, metabolites, pH and signaling molecules. A diagram of the duodenum-intestine-chip in Figure 2.6 illustrates the typical setup of such devices.

In a landmark study of 2020, the first of its kind Colon Chip was produced by Sontheimer-Phelps *et al.* [207] using primary patient-derived fragmented colonoids that produced a mucous bilayer with similar thickness to the living human colon, which permitted non-invasive visual analysis of mucosal physiology in real time [190]. Table 2.8 presents microfluidic models of the colon including the Colon Chip.

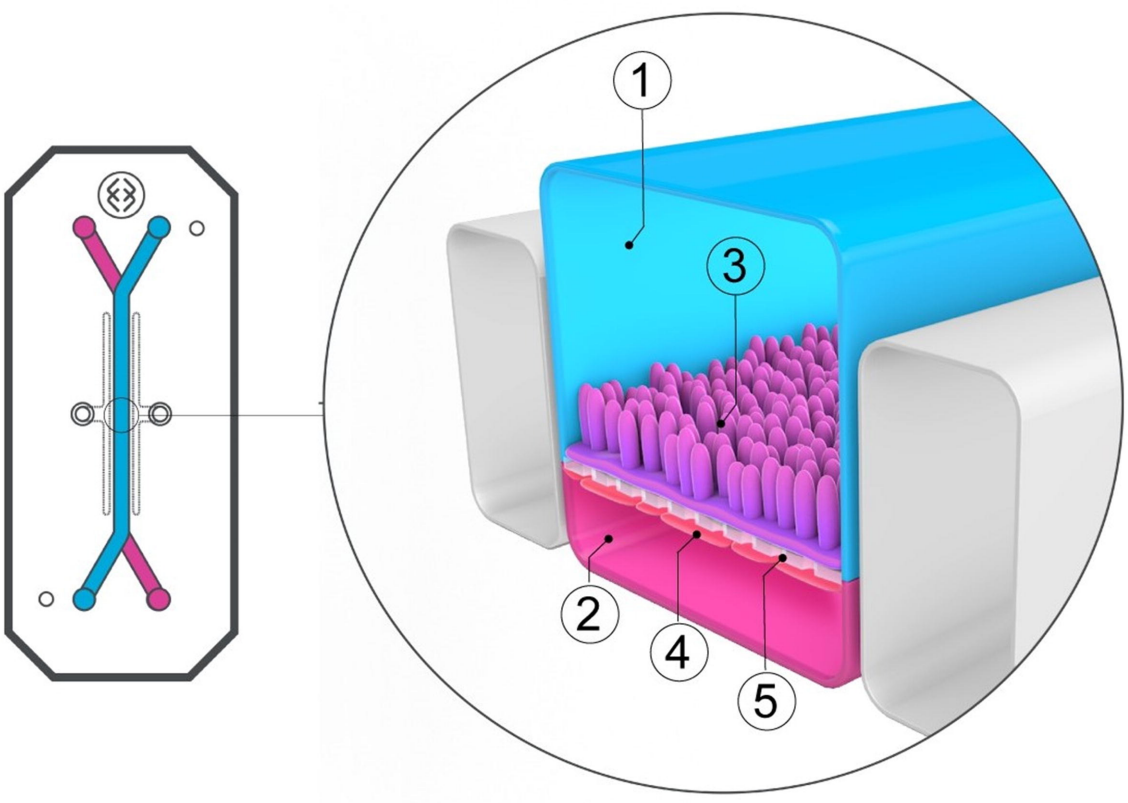

Figure 2.6: Schematic representation of a Duodenum Intestine-Chip, including its physical macro appearance from the top (left) and vertical section (right) showing: the epithelial (1; blue) and vascular (2; pink) cell culture microchannels populated by intestinal epithelial cells (3) and endothelial cells (4), respectively, and separated by a flexible, porous, ECM-coated PDMS membrane (5). This image was taken from [206] and was originally published in an Open Access article distributed under the terms of the Creative Commons Attribution License (http://creativecommons.org/licenses/by/4.0/), which permits unrestricted reuse, distribution, and reproduction in any medium.

Table 2.8: Microfluidic models of the colon. VSL3 is a therapeutic probiotic formulation containing Lactobacillus acidophilus, Lactobacillus plantarum, Lactobacillus paracasei, Bifidobacterium breve, Bifidobacterium longum, and Bifidobacterium infantis; Hmm = human microbiome metabolites; Mmm = mouse microbiome metabolites; WSS = Wall shear stress; Interferon = IFN.

Ref	Cell type	Lumen dimensions	luminal flow	Molecular transport	WSS	Mucous layer thickness	Peristalsis	Commensal microbiota	Disease or pathogen	Co-culture with other cells
[208]	Human Caco-2 & AC colonoid	W: 1mmL: 10mmH: 0.15mmMT: 20 μm	30, 100 & 200 mL h^{-1}	N	0.02 dyne cm^{-2} at 30 μL h^{-1}	N	10% strain at 0.15 Hz	N	N	N
[209]	Colonoids	H: 1000 μm W: 1000 μm MT: 50 μm	60 mL h^{-1}	N	N	n/a	N	Hmm or Mmm	EHEC	N
[210]	Colonoids	H: 1000 μm W: 1000 μm V = 28.041 μL Cell surface 28 mm^2	60 mL h^{-1}	N	n/a	n/a	10% strain at 0.15 Hz	N	IFN-γ in inflammation and leaky-gut	N
[211]	Colonoid	H: 500 μm W: 1000 μm L: 10 mm MT: 50 μm	30 + mL h^{-1}	N	N	N	N	N	N	N
[207]	AC and sigmoid colonoids	H: 1000 μm W: 1000 μm MT: 50 μm	1.6, 6 & 10 mL h^{-1}	N	n/a	570 μm	N	N	PGE2 (UC model)	N
[212]	Colonoids	W: 400 μm OrganoPlate	n/a	N	n/a	n/a	N	N	IBD	Monocyte-derived macrophages
[213]	Murine colonoid	H: 1000 μm W: 1000 μm MT: 50 μm	n/a	N	n/a	n/a	N	Human and mouse microbiota	S. Typhimurium	N

2.5.3 In silico models

Adjacent to or instead of dissolution testing, (commercially available) in silico models can be used to predict drug behaviour in vivo.

Physiologically-based pharmacokinetic (PBPK) modelling

PBPK models are compartmental models wherein each compartment represents a physiologically discrete entity, such as a different organ or tissue (brain, kidey, lungs, muscle etc.) and blood flow transports material between them. PBPK models are used to mechanistically interpret and predict absorption, distribution, metabolism and excretion (ADME) properties of drugs in the human body [214]. These models are built on a combination of molecular biopharmaceutical properties and physiological attributes of the target or representative population. Data derived from in vitro experimental work, in silico predictions and preclinical and clinical trials are used to predict the magnitude and variability of key PK parameters that build the knowledge base of how drugs are processed by human physiology.

The dissolution, absorption, distribution, clearance and excretion processes can be modelled by a system of interconnected ordinary differential equations (ODEs). In-house PBPK models exist in the literature [215–219], however commercially available software packages are available, including Gastroplus™ (Simulations Plus Inc, Los Angeles, CA, USA), Simcyp™ (Certara UK Holdings Ltd., Sheffield, UK) and PK-Sim ® (Bayer Technology Services Gmbh, Leverkusen, Germany).

Gastroplus® is rooted in the advanced compartmental absorption and transport (ACAT) model. The ACAT model simulates the GI tract as nine compartments in series: the stomach, duodenum, jejunum 1 & 2, ileum 1-3, caecum and colon. Each compartment is described by a set of parameters including pH, transit time, volume, surface enhance-

ment factors, bile salt concentration, and characteristics of the surface area available for absorption.

Simcyp® is built on the Advanced Dissolution Absorption and Metabolism (ADAM) model which is described extensively by Jamei *et al.* [220]. This is a development of the ACAT model, key differences being an extra ileum compartment 'ileum IV' and no 'caecum' compartment, compared to ACAT in Gastroplus. Additionally, ADAM accounts for dynamically changing fluid volumes available for dissolution in each compartment, due to ingestion of fluids and the secretion and absorption of GI fluids.

PK-Sim ® (Bayer Technology Services) describes the GI tract using a dispersion model. This is essentially a continuous tube with physicochemical properties that vary as a function of space, rather than a series of individual compartments.

These software packages enable simulations in a single individual or an entire population that is customisable to fit the target or representative population. However, in all of these packages the GI tract is assumed to be homogenously mixed and there are no hydrodynamic input variables such as agitation speeds, shear rates or mixing performance. These may be important for accurately predicting regional absorption and dissolution from CR formulations.

Recently, the term physiologically based biopharmaceutics modelling (PBBM) has been introduced to describe the modeling approach primarily orientated toward establishing a link between biopredictive in vitro dissolution testing and mechanistic drug absorption modeling [221]. PBBM models represent a more holistic approach to modelling the journey of an API from oral the point of oral administration. Mechanistic considerations are given to the interactions of the API and dosage form excipients with the surrounding GI environment. This can involve disintegration, polymer swelling, hydration and erosion to liberate and dissolve an API from its dosage form. API may also be subjected to precipitation and redissolution phenomena due to dynamically changing pH and local

fluid volumes. PBBM is therefore a useful tool for developing an in vitro in vivo correlation (IVIVC) between the in vitro release or dissolution profile of a dosage form and an in vivo response, such as in vivo dissoluition or absorption profiles obtained through deconvolution of human plasma concentration (C_p)-time data. This can be used to reduce the regulatory burden (IVIVC in lieu of costly trials and bioequivalence (BE) studies) and more recently for formulation quality by design.

Mostly, this has involved the incorporation of dissolution profiles using compendial apparatuses such as the USPII [222]. However, there exists an important opportunity to advance this field using dissolution data from more advanced biorelevant dissolution equipment, particularly for CR formulations that transit through multiple regions of the GI tract before completing drug release.

Predictions of in vivo PK characteristics of immediate release (IR) dosage forms are widely reported with high confidence. This is due to the relative simplicity of the drug release and dissolution processes, which occur almost immediately in the gastric compartment by design. However, the lack of well-established mechanistic models for the interaction of excipients with the GI environment limits the application of bottom-up PBBM modelling to CR formulations. As opposed to instant dissolution, there is a process that consists of many difficult to predict elements acting in series and/or parallel to one another such as polymer-media interactions (swelling, hydration, erosion), drug-polymer interactions, food effects (e.g., viscosity, fat, proteins and fibres), fluctuating hydrodynamics and more. To tackle this complexity, in vitro dissolution profiles under conditions that mimic key control variables are typically integrated into PBBM models in one of three ways:

- To directly import an in vitro dissolution profile into a PBPK model [223, 224].
- To treat in vitro dissolution profiles as release profiles (of undissolved or dissolved drug) and use these as an input to mechanistic models (e.g., ADAM in Simcyp® or ACAT in Gastroplus®) to model the ADME processes of the API.

- Use a Weibull function to optimise the PBB model such that the prediction matches a dissolution profile measured in vitro [225, 226].

This highlights the value of in vitro dissolution profiles in predicting the in vivo performance of CR formulations. The benefits of integrating more advanced in vitro dissolution tools, such as TIM-1, into PBBM models have been demonstrated to support formulation selection and predict food effect observed in clinical studies [227]. However, the number of studies that have actually integrated advanced in vitro tools into PBBM models is limited. Hence, PBBM models still typically rely on compendial in vitro dissolution methods to derive empirical parameters that inform simulations for MR formulations.

The choice of in vitro model and in silico platform pairing for development of a PBBM model is likely to differ depending on the intended (or observed, yet unintended) fate of the dosage form in question. Obviously, an in vitro model that replicates the colonic environment is likely to be most useful for generating a release profile compared to an in vitro model of the stomach. Perhaps less obvious is that Gastroplus™may be more applicable for PBBM modelling of this type of dosage form since it includes a compartment for the caecum in addition to the ascending colon, compared to just a single 'colon' compartment in Simcyp.

Hydrodynamic in silico models

An alternative in silico approach is to simulate the hydrodynamics of the luminal environment. This has strong application in modelling how gastrointestinal motility can influence drug release from a dosage form and subsequent dissolution. Disruption of a dosage form and the subsequent dissolution and distribution of the API is largely driven by hydrodynamics, especially for extended dosage forms with an erodible hydrophilic matrix (see Section 2.4.1).

Intestinal flow can be modelled as the flow of multiphase (solid, liquid and gas) contents through a collapsible tube. This type of flow is common across all vessels carrying fluids within the body. A thorough review was carried out on the early works of biofluid mechanics in the flexible tubes by Grotberg & Jensen [228]. Additionally, Misra & Pandey [229] reviewed the use of computational flow dynamics (CFD) to study transport phenomena in the GI tract, however many of which employed rigid walls of the lumen. Some CFD models were based on anatomical measurements taken from in vivo MRI studies and considered the effect of peristaltic contractions in the small intestine [230] and stomach [231, 232]. However, these models did not attempt a two-way coupling of the motor activity in the walls and the luminal fluid contents.

In the majority of works, the walls were considered rigid, however Sinnott *et al.* [233] implemented a mass and spring representation for the membrane and smoothed particle hydrodynamics (SPH) to model the fluid. This enabled contractile motion of the walls to mimic peristalsis and study the motion incurred by the contents. Particle methods such as SPH operate through discrete simulated particles interacting with each other through the exchange of some quantity such as heat or attractive/repulsive force, and in response, subsequently update their physical properties such as temperature or position [234]. Sinnott *et al.* [235] developed another SPH model that coupled the flow of luminal content and flexure of the wall to investigate the complex relationships between gut contractility and flow of the digesta. It was found that high lumen occlusion is required for effective propulsion of contents with a high viscosity. In these models, the authors considered the filled intestine, however it is common that the intestine is only partially filled [25].

Alexiadis *et al.* [236] built on this initiative and built a similar mathematical model to simulate the motion of viscous fluids in the partially filled colon. SPH was once again used for modelling the fluid, whilst coarse grained molecular dynamics (CGMD) was used to simulate the wall. This model revealed two fundamental mechanisms of mass transport: 'surfing' motion of fluid at the surface and 'pouring' which causes deeper mixing based

on the change in cross section area of adjacent regions of the lumen. Alexiadis *et al.* [234] went on to develop a multiphysical model that integrated deep learning mechanisms into particles; meaning that particular particles (such as those representing the intestinal wall) can learn from information about other particles (such as those representing the luminal fluid) and adjust their behaviour accordingly. The artificial neural network comprising the particles that represented the intestinal wall were given the 'goal' of transporting the contents of the lumen in a predefined direction. The artificial neural network could learn autonomously how to coordinate its contractions and 'learn' peristalsis, but could not adapt its peristalsis to best suit the contents of the lumen based on their physical properties.

Schütt *et al.* [237] used a similar approach to Alexiadis *et al.* [236] to compare flows in the completely filled colon, partially filled colon and a colon filled with multiphase contents (gas and liquid) when subjected to identical peristaltic waves. For this approach, a lattice spring model (LSM) was used to model the solid, flexible colonic wall. Highest velocities and lowest transit times were observed in the colon model completely filled with liquid, which also displayed the greatest degree of mixing of the luminal contents. No significant differences were observed between the partially filled model and that with biphasic contents except a slight increase in regional velocities of the liquid in the gas-liquid model. Ultimately, the filling level affected the shear forces within the lumen.

Following this, Schütt *et al.* [238] went on to simulate a range of stimulated (triggered by oral administration of polyethylene glycol (PEG) and maltose) motility and unstimulated 'baseline' motility patterns observed in clinical MRI studies of the healthy adult human colon. It was found that motility pattern and viscosity had significant effects on the dissolution profile of a simulated solid dosage form. It was found that isolated peaks in shear stress n the tablet surface arose due to the discontinuous nature of the motility patterns, with the stimulated patterns provoking the highest frequency of shear stress activity, thus achieving highest release.

2.6 Dynamic Colon Model

The DCM was built to address the lack of physiologically-relevant means of agitation in the existing suite of in vitro tools. Regarding drug delivery, motility patterns a) determine the normal and shear forces responsible for driving erosion and break up of a dosage form, b) mix the contents of the lumen to maintain a concentration gradient between the dosage form and the surrounding fluid and c) drive convective transport of the dosage form.

Previous work has been carried out to characterise the hydrodynamics inside the DCM under a cyclic antegrade propagating wall contraction that was based on in vivo observations. Firstly, the pressure profiles generated by contractions of the flexible wall of DCM tube were recorded using a manometer in fluids of increasing viscosity, presented in Figure 2.7. The key finding was that the measured pressure signal increased with viscosity. The measured pressures generated by the wall motion of the DCM tube fell within the range of in vivo amplitudes recorded with the use of high resolution catheters, however the viscosity of the colonic fluid and the occlusion degree of the colon wall were unknown [170].

Previous studies used positron emission particle tracking (PEPT) and positron emission tomography (PET) to visualise the translational response of tracer particles to an antegrade CPPW inside the DCM; from dye molecules [9] to millimeter scale spheres [10].

PEPT is a non-invasive visualisation technique, developed at the University of Birmingham [239, 240], that can be used to track the motion of a radionuclide particle in three-dimensional space with high spatial and temporal resolution. However, the accuracy of PEPT is inversely related to the thickness of any physical barriers between the detectors and the tracer, i.e. walls of a mixing system. PEPT was used as a means of non-invasively tracking the motion of particles with different densitites [10] in differently

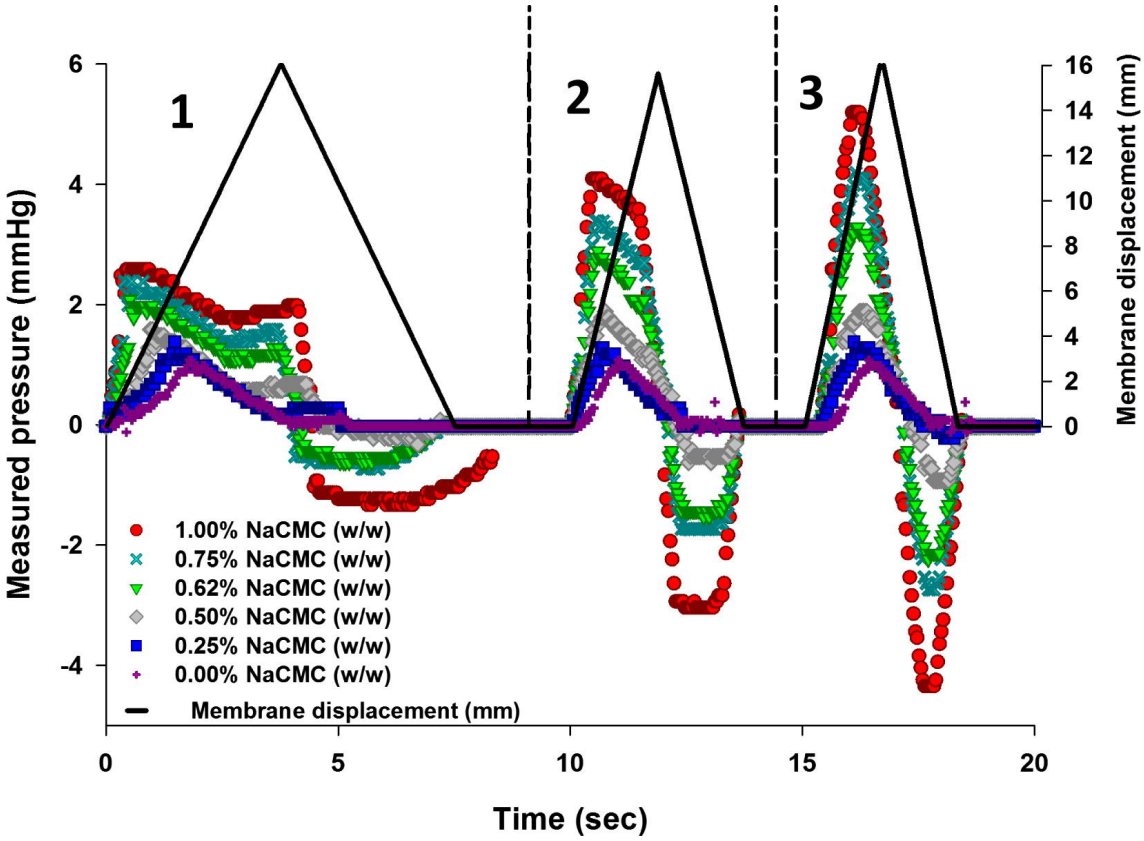

Figure 2.7: Measured changes in pressure on the lumen for different NaCMC (700,000) concentrations (•1.00%, ×0.75%, ▼0.62%, ⋄0.50%, □0.25%, +0.00%, (w/w)) and membrane occlusion rates: (1) 4.3 mm s^{-1}; (2) 8.5 mm s^{-1}; (3) 16.6 mm s^{-1}. Images adapted from Figure 4 of [9] with permission.

viscous media, as shown in Figure 2.8. Particle motion was described using an occupancy map in the Cartesian coordinate system normalised about the centre of the DCM cross section. At the time of the experiments, PEPT was limited to a single tracer particle, therefore investigations of neutrally buoyant and floating particles were conducted separately.

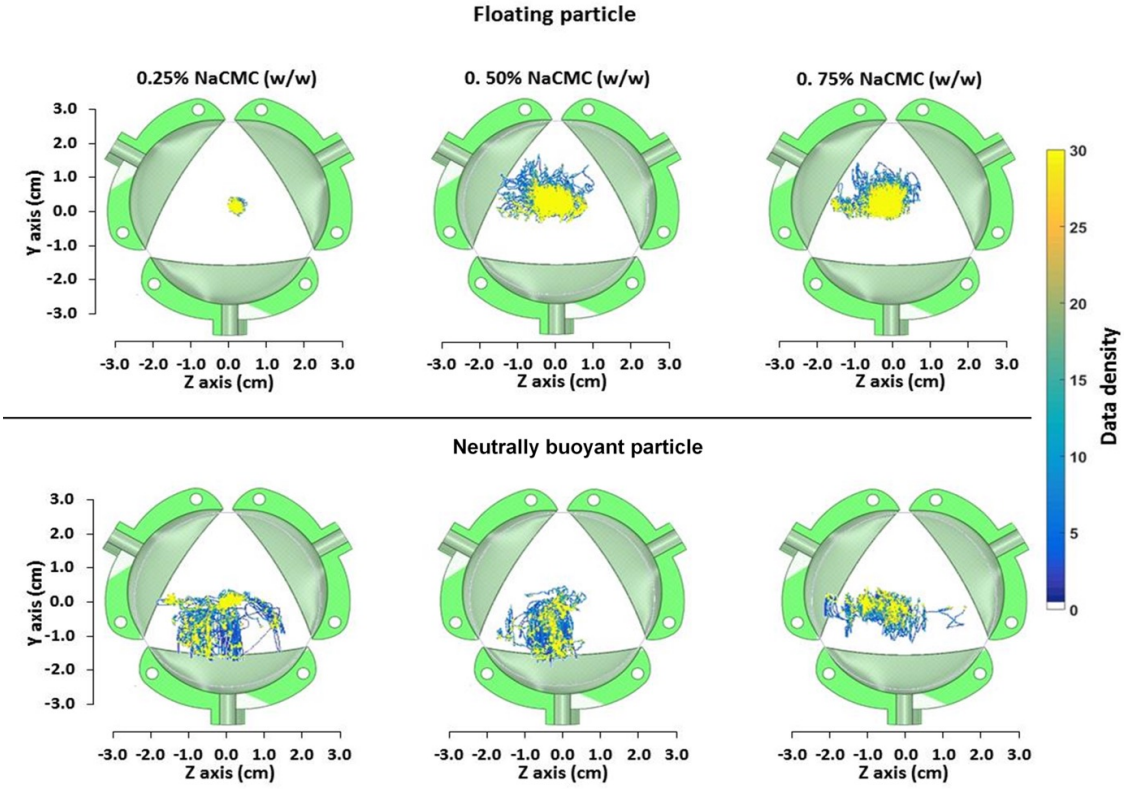

Figure 2.8: Positron emission particle tracking data density plots illustrating the radial displacement of a floating and neutrally buoyant particle in the DCM in media of different viscosity, as presented in Figure 8 of Stamatopoulos *et al.* [10], from which permission to use this figure has been obtained.

Stamatopoulos *et al.* [10] found that the radial location of the floating particles remained largely unchanged throughout the experiment in the least viscous media, whereas the neutrally buoyant particle in the same media covered a far more extensive area, suggesting a significant increase in the intensity of radial mixing in the bulk fluid compared to at the surface. Increasing media viscosity increased the radial coverage of the floating

particle, indicating that radial surface mixing is less extensive in media of lower viscosity. Increasing media viscosity restricted the *y* displacement of the neutrally buoyant particle.

From this data, Stamatopoulos *et al.* [10] suggested that low viscosity fluids could be more prone to a sloshing motion inside the DCM, whereas an increase in viscosity damps this motion and promotes plug flow (albeit pulsatile). It was also found that the response of a tracer particle to an antegrade CPPW inside the DCM was highly dependent on initial radial location of the particle. The principles observed can be extrapolated to apply to non-uniform agglomerates of a dosage form, or different types of particles / vehicles that are used as tracers in vivo. Considering the latter, different tracer densities are likely to be partly responsible for the high variability in transit times observed in vivo, such as manometry measurements. The variability in these findings may help to explain the high variability observed when colonic movements are correlated solely with pressure waves, since Stamatopoulos *et al.* [10] demonstrated that the DCM reproduced consistent pressure force profiles associated with CPPWs with fixed media viscosity.

As a measuring technique for the DCM, PEPT is a Lagrangian approach best applied as an understanding of how surface-based and bulk-based particles react to flow fields inside the DCM. Since a dosage form may disintegrate into agglomerates of varying physical characteristics, this PEPT data shows how changes in buoyancy affect particle distribution. However, in order to fully map flow fields inside the DCM, an infeasible quantity of PEPT experiments using particles with different characteristics in different starting positions would be required.

PET is a measurement technique used clinically for quantification and subsequent assessment of physiological function, for example blood flow, consumption of oxygen and metabolic activity inside the body. PET maps local spatial concentrations of a tracer

(analogous to a drug) during the different stages of a motility cycle. Stamatopoulos *et al.* [9] observed the accumulation of tracer molecules around the caecum and ileum terminal likely due to lack of propulsion forces at the early stages in development of an antegrade propagating wave.

Media viscosity was shown to influence the convective mass transport of tracer as can be seen in Figure 2.9 [9]. Increasing viscosity from 0.25 to 0.50 % (w/w) NaCMC (Figure 2.9 Parts 1 and 2 respectively) decreases the uniformity of tracer distribution along the lumen. This was shown by lower intensity of the radioactive signal as x-axis position increases from $0-20$ cm. Furthermore, the amount of tracer remaining around the caecum increased with viscosity, whilst a transition to plug flow was also observed in the distribution of the remaining tracer along the lumen following $5-10$ antegrade propagating sequences (Figure 2.9. Parts 2c and 2d). As the wave reaches the end of the lumen, media flows up the wall of the rigid siphon without passing over the flexure, before gravity forces induce backflow. The higher viscosity media used imparted more resistance to backflow, thus a more significant accumulation of tracer is observed around $x = 13 \pm 1.5$ cm. These phenomena have also been observed during in vivo scintigraphy studies [241–243].

While detailed and insightful, questions remain unanswered as to the the synchronisation of wall motion and fluid flow and flow measurements without the downfalls of a tracer particle, such as inherent relaxation time. Further, the luminal hydrodynamics are yet to be verified against in vivo data. The latter being essential to validation of the DCM as a biorelevant in vitro dissolution model.

Manometry techniques are used to measure intraluminal pressure activity during contractions of the colonic wall, with significant advances being made using high resolution manometry in recent years [41, 244–246]. However, little information is available

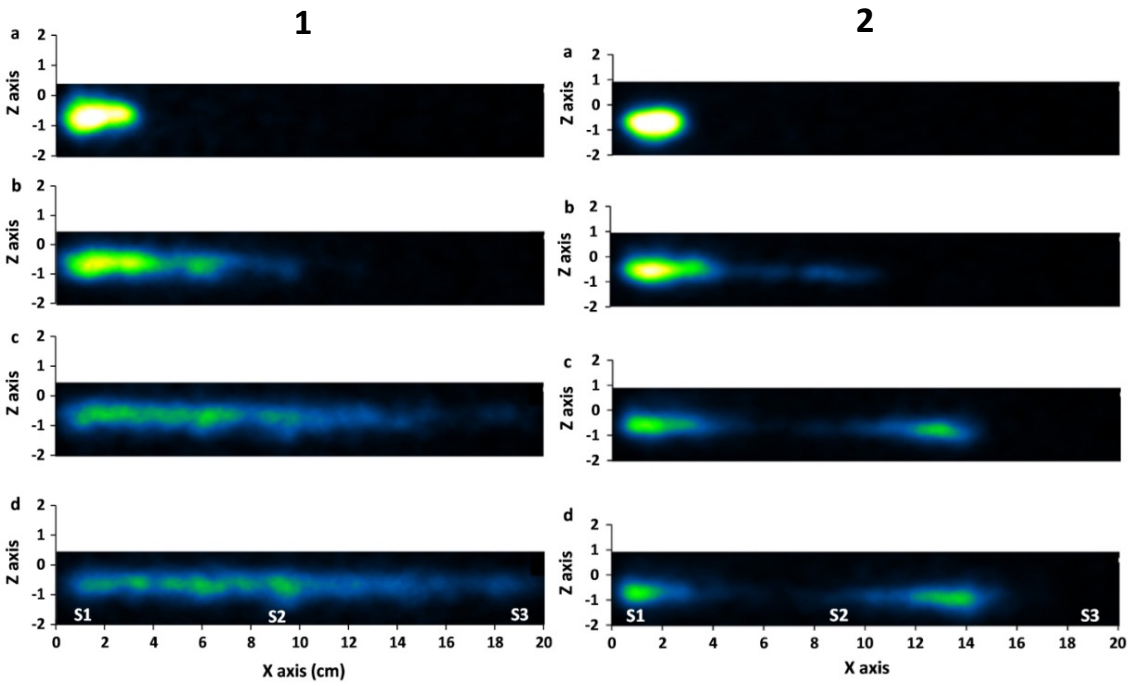

Figure 2.9: PET images showing the dispersion of a solution of 18F along the x and z axes of the DCM lumen (where the caecum is located at $x = 0$ and the hepatic flexure at $x = 20$) following (a) injection into the ileum terminal, (b) first antegrade wave, (c) fifth antegrade wave and (d) tenth antegrade wave using 0.25 % (w/w) and 0.50 % (w/w) NaCMC in parts 1 and 2 respectively. Images adapted from Figure 8 and 9 of [9] with permission. S1, S2 and S3 represent sampling points along the DCM used in that study to measure drug dissolution.

pertaining to how the colonic contents move in response to normal and abnormal colon pathophysiology [247]. For example, erratic or dampened motility patterns of the colon wall (as a result of a functional gastrointestinal disorder, FGID), may not be effective for mixing and propulsion of the colonic contents. Colonic mixing phenomena mainly occur in the AC (before significant dewatering occurs), which is particularly difficult to access using manometry, and highly invasive. The influence of disease affecting the AC can therefore have a significant impact on the delivery of colon-targeted dosage forms. Reduced contractile activity of the AC walls may lessen the normal and shear forces arising from fluid motion and direct contact with the colonic walls.

Magnetic resonance (MR) tagging, a noninvasive and non-ionising imaging technique which is commonly used to assess cardiac function, has recently been applied to assess gastrointestinal motility [248–251]. MRI is a household name when it comes to hospital diagnoses, however parallel studies often take place in an MR-compatible model system known as a phantom. MRI has the capability to image fluid flows and solid deformations (moving boundaries) inside an opaque system, therefore offering the opportunity to evaluate DCM wall motion and luminal fluid flow in synchrony. The DCM offers the opportunity to act as a phantom for the human proximal colon. MRI of the DCM may permit evaluation of characteristics of intestinal flow to be analysed under a predetermined in vitro environment whilst also acting as a means of validation for the hydrodynamics inside the DCM by comparison with in vivo data.

Dissolution experiments have been carried out in the DCM under a single antegrade propagating pressure wave. The dissolution profile of the theophylline in viscous media was measured at from the three different sampling points, located at the beginning, at the middle and at the end of the DCM tube, shown in Figure 2.10 [9].

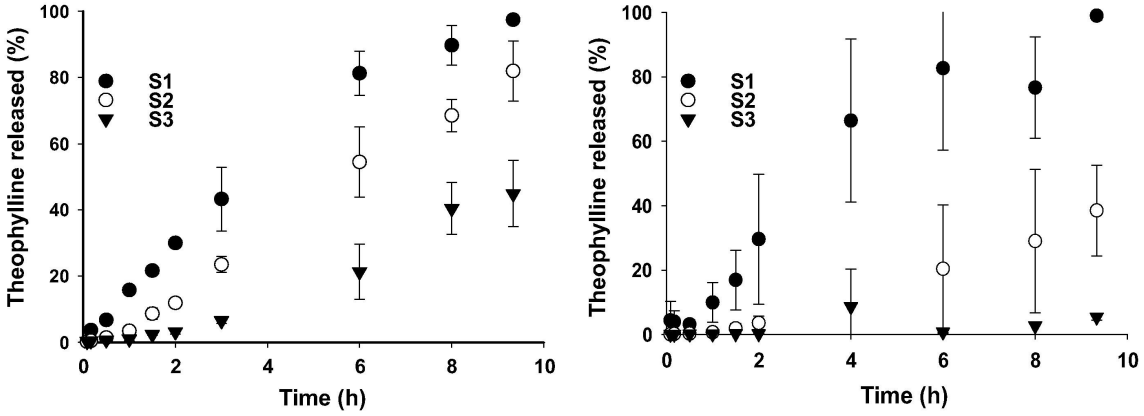

Figure 2.10: Dissolution curves of theophylline obtained from three different sampling points along the length of the DCM tube ($\bullet S1; \circ S2; \blacktriangledown S3, n = 6$). The dissolution experiments were performed in (left) 0.25 % and (right) 0.50 % NaCMC(700,000) (w/w) solutions adjusted at pH 7.4 using phosphate buffer at 37 °C. Images adapted from Figure 6 of [9] with permission.

It was found that there was an unequal distribution of the released drug along the length of the tube, which was augmented by media viscosity, resulting in a different release rate measured at each sample point. The differences in dissolution profile most likely reflect the ineffective transport of the drug along the tube, resulting in the formation of areas with high accumulation of the drug, especially at the beginning of the DCM tube, at which the tablet had been introduced. This highlights a) the importance of spatial information in measuring dissolution profiles in the DCM geometry and b) the need to develop a methodology for integrating dissolution profiles from multiple spatial coordinates into a single temporal dissolution profile that can be used to describe overall release characteristics and enable direct comparison of dissolution between the DCM and compendial apparatus. Further work is needed to investigate the discriminatory power of the DCM in producing different dissolution profiles under different mimic colonic motility patterns. Once more information is known about dissolution inside the DCM, there would be great value in trying to improve prediction of in vivo PK characteristics of CR formulations by integrating DCM dissolution profiles of CR dosage forms into PBPK models.

Concerning drug release of a dosage form to the colon, normal and shear stresses cause the break up and erosion of vehicles and the mixing profiles are paramount for understanding dispersion of the API. Quantification of the shear rates inside the human ascending colon has not been possible to date, therefore measurement of shear rates in the DCM with biorelevant geometry and motility may provide an insight. It is likely that the shear rate distribution in the DCM lumen and the range of shear rates present is highly different to compendial dissolution apparatuses, however shear rate information is currently unknown inside the DCM. Previously, in silico models have been used to estimate shear rates of similar in vitro systems such as the USPII and the TIM-1 [252, 253].

Chapter Three

Evolution of DCM design

3.1 Introduction

The DCM was invented by Stamatopoulos [8]. Since then, there has been interest from industry and academia as outlined in the business case in Section 1.6. However, for the model to deliver as an advanced biorelevant dissolution apparatus, there are aspects of the design that needed to be improved to enhance research output. Before these can be communicated, a more detailed background on the DCM is required.

3.1.1 Background on DCM manufacture and operation

A schematic of DCMv1 is shown in Figure 3.1. The tube consists of 10 individual silicone segments (green) bounded by parts that represent the caecum (pink) and the hepatic flexure (blue). The system is compressed and held in place using a clamp (black).

An individual silicone DCM segment is shown in Figure 3.2 (a). Each segment comprises three distinct pockets that mimic the haustra of the human colon. In the DCM, acrylic inserts (blue) are fitted into the pockets to maintain structural integrity during operation, as shown in Figure 3.2 (b). A side view of the segment is shown in Figure 3.2 (c).

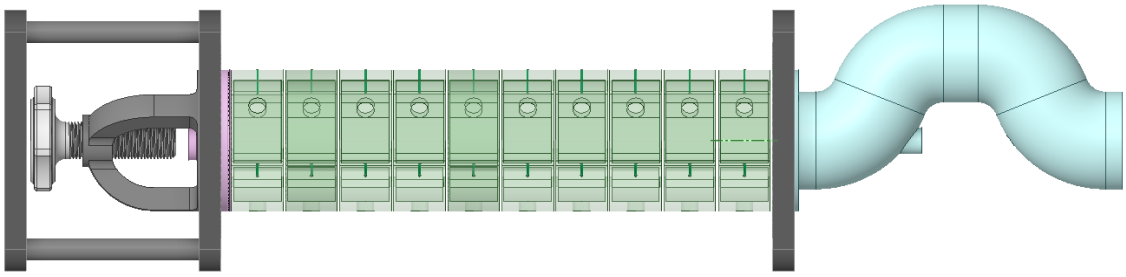

Figure 3.1: Schematic of the DCM without the hydraulic system

There are two holes passing through each haustra (6 per segment) where rods were passed through to connect and align adjacent segments and facilitate compression. A single port facilitates manual sampling of media from the lumen.

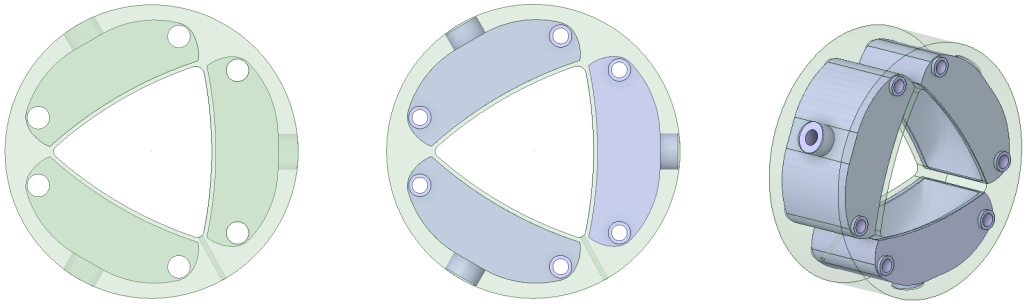

a b c

Figure 3.2: DCM v2 silicone mould without (a) and with (b) the acrylic haustra parts inserted

Each segment is hydraulically operated by a syringe as per Figure 3.3 (a simplified diagram). One syringe (Figure 3.3 (a)) is connected via tubing (Figure 3.3 (b)) to three ports on a DCM segment. This is a closed system filled with water (as an incompressible fluid). Displacement of the syringe displaces the water and causes an increase in internal pressure in the haustra, displacing the flexible membrane bounding the haustra and positively (contraction) or negatively (relaxation) occluding the lumen. Visually, this looks like an inflation or deflation of the haustra pocket. All three haustra of a segment move in synchrony since they are all connected to the same syringe.

Since the DCM comprises 10 segments, a system of ten syringes, shown in Fig-

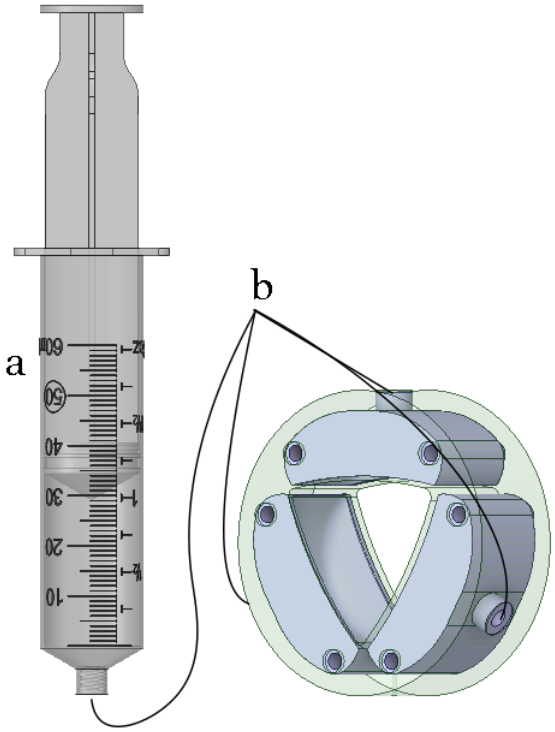

Figure 3.3: Diagram of a DCM segment: Each DCM segment has three haustra that are connected to the same syringe (a). The syringe and the connecting tubes (b, simplified to lines here) a full of water that causes the lumen-bounding membrane to displace with the syringe.

ure 3.4, controls the motility of the DCM. The position of the plunger of each syringe is controlled by a stepper motor (depicted as the black boxes in Figure 3.4).

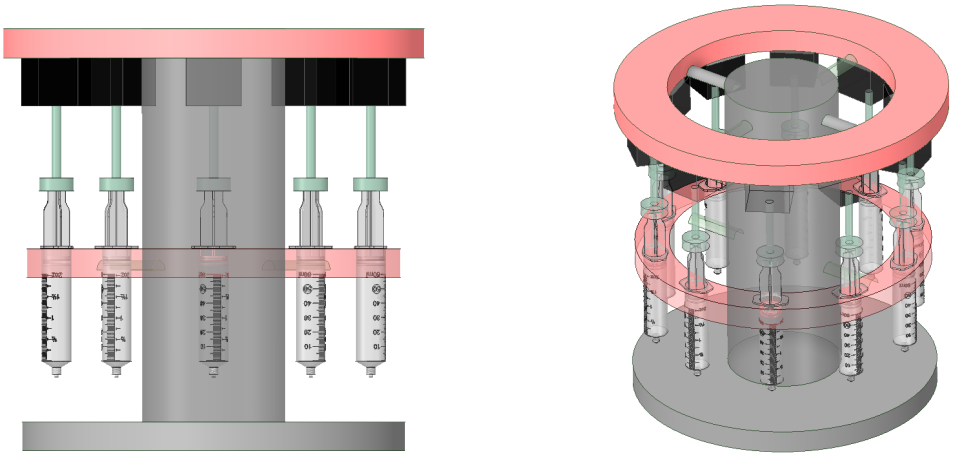

Figure 3.4: Schematic of the hydraulic control system; ten syringes (one per DCM segment) where the plunger of each syringe is connected to its own stepper motor (depicted as a black box).

The system is computer controlled, enabling each stepper motor to move predefined distances in synchrony with the others to produce patterned contractility in the DCM.

The segments are fabricated from silicone which offers the strength and flexibility required for the mimic intestine walls to occlude the lumen. To manufacture a segment, deaerated room temperature vulcanisation (RTV) silicone is poured into a mould of the unit and requires 3 - 4 hours to cure before the segment can be removed from the mould. A successful mould has no air bubbles, which weaken the structure and lead to damage. However, there are small channels in the mould where it is difficult to remove air bubbles if they have formed.

3.1.2 Design goals

In order for the DCM to deliver the desired research output, there was a range of design challenges to be overcome. These were handled in two distinct phases using computer

aided design (CAD) and additive manufacture techniques.

1. Design Phase one: MRI compatibility.
    - A high potential was identified for magnetic resonance imaging (MRI) flow studies using the DCM. For this, all metal parts needed to be replaced with non-metal counterparts.
2. Design Phase two: Improving performance and ease of integration into an industry workflow.
    - During normal operation there was a high risk and frequency of damage to the DCM that rendered it inoperable.
    - The DCM was required to be able to complete a campaign of at least eighteen dissolution experiments (six motility patterns with three repeats).
    - Repair requires complete replacement of the model which is highly resource-intensive.

3.2 Materials and methodology

3.2.1 Design phase one: MRI compatibility

In order to conduct MRI experiments, the metallic components from the DCM needed to be replaced with non-metallic counterparts. Metal parts included the clamping system, stability rods, caecum chamber and gaskets, all of which were fabricated from stainless steel 306 and manufacturing was outsourced with heavy lead times. This necessity was taken as an opportunity to move DCM part manufacture to in-house additive manufacturing.

Table 3.1: Material property comparison for DCM parts: Stainless steel (SS) 304 versus 3D printed alternatives. †Due to the strong chemical bonds in SLA printed parts, they are isotropic meaning that flexural strength is equivalent to tensile strength.

Property	**SS 304** [254]	**Tough 2k** [255]	**Clear** [256]	**PLA** [257]	**Nylon** [258]
Tensile Strength [MPa]	1,090	65†	65†	60	70
Elongation at failure [%]	70	48	6.2	6	90
E [GPA]	193	2.2	2.8	3.6	1.8
HDT at 0.45 MPa [°C]	» 37	63	58.4	49-52	160
Flexural modulus [GPa]	210	1.9	2.2	3.8	1.8
Flexural strength [MPa]	1,100	65†	65†	83	117

The clamping system was required to keep the DCM segments pressurised from the caecum to the hepatic flexure so that the lumen chamber was watertight. Any leaks from the lumen would decrease the operational volume of media in the lumen which could affect the hydrodynamics in an unpredictable manner and result in inaccurate drug concentration measurements. Therefore, it was important to choose a replacement material with high elongation, since clamping can deform the material, in addition to considering tensile strength (a material's resistance to failure under tension). To ensure pressure was applied and maintained uniformly around the circumference of the DCM tube, high Young's (E) and flexural moduli were also desirable (the resistance of a material to deform under tensile stress). Additionally, it was important to consider the heat deflection temperature (HDT) as the DCM components would need to maintain their function at 37 °C. For these reasons, the Formlabs Tough 2000 resin was selected to manufacture the clamping system using stereolithography (SLA) printing. Table 3.1 presents the material properties of Formlabs tough 2000 resin against stainless steel 306.

Polylactic acid (PLA) was chosen to replace the steel gaskets which seal any gaps

between DCM segments under compression. PLA is the most widely used 3D printing material [259]; an environmentally and economically responsible choice as it is a biodegradable polymer with non-toxic vapours that has a low melting point, requiring comparatively low energy to print via fused filament fabrication (FFF). Printing temperature was maintained low at 185 °C. Higher extrusion temperature results in parts with a greater stiffness due to higher fusion [260] which was not required. Layer thickness was high at 0.25 mm as tensile and yield strength increase largely following a small increase in layer thickness [261].

The 3D printed rigid siphon representing the hepatic flexure was redesigned to include a gasket-like part in order to remove the need for an extra gasket. For this part and the caecum at the opposite end of the DCM, the Formlabs Clear resin was selected, since mechanical strength was not as much of a concern whilst transparency of the material would add a view window at either end of the DCM. Most compendial USP dissolution apparatuses are transparent since it is highly valuable for an operator to be able to view processes inside a dissolution apparatus, such as fluid level, tablet behaviour and the agitation mode of the mimic intestine walls inside the DCM. Figure 3.5 displays schematics of the replaced parts.

a b c d e

Figure 3.5: DCM parts that require non-metal replacements: a) Caecum b) Clamp c) clamp bolt d) Elbow connector e) Hepatic flexure

Finally, metal fluid inlet/outlet ports were replaced by a Nylon-based connection procured from Industrial Specialties Mfg. & IS MED Specialties [262]. The part resem-

bled a swivel-elbow system comprising a male thread to fit the acrylic haustra piece and a hose barb connecting to the syringe pump system.

3.2.2 Design phase two: improving performance

In this phase of design work, the aims are to minimise or eliminate failure events and to decrease the time taken to repair the DCM if damage does occur.

Identification of risk factors for failure events

A single segment of DCM v1 is shown in Figure 3.6 (a). DCM v1 exhibited two common modes of failure for a segment: hydraulic fluid leaking from the holes (b) or the silicone membrane tearing or rupturing at weak spots identified and during inflation and deflation (c).

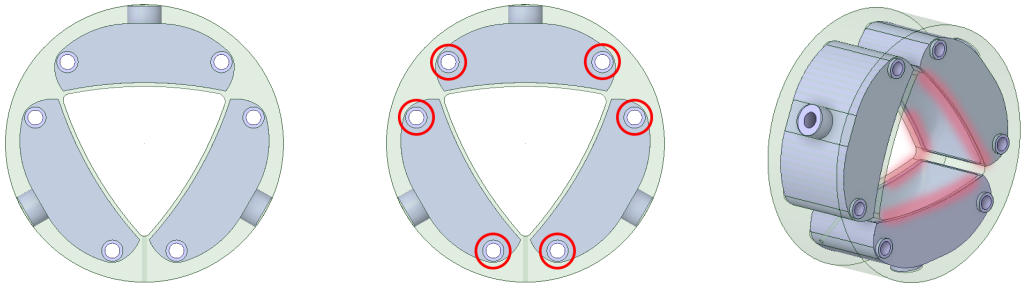

a b c

Figure 3.6: A single DCM segment (a) and the points of failure identified (b and c).

Both modes of failure led to changes in lumen media composition, affected concentration measurements and caused wall motility to fall out of calibration.

The most intuitive solution to minimise leaks was to design out the holes highlighted in 3.6 (b). The purpose of the holes was enable rods to be passed through and fastened to compress of all ten units to make the system watertight. To design out this

feature, a new method of fixing together the segments was explored using different compression methods.

It was identified that tears in the membrane were caused by the application of adhesive to seal the silicone to the acrylic haustrum, which restrained inflation of the pocket. Therefore a new method was required to make DCM segments watertight, avoiding the use of adhesive.

Areas for improvement of the repair process

DCM v1 relied on silicone adhesive to adhere adjacent DCM segments together, creating a watertight seal so media did not leak from the lumen. However, this meant that failure of a DCM segment required the entire DCM to be replaced, since it was difficult to make repairs inside the tube. Replacing the DCM typically consumed > 40 working hours and was expensive in material costs. This was due to a combination of the need to replace the entire DCM and the low success rate of moulding a DCM segment.

The success rate of the moulding process was low due to small channels where air bubbles commonly formed and were difficult to remove. Additionally, fabrication of mould parts was outsourced with excessive lead times. The parts were fabricated from acrylic, with CNC machined screw threads that had a high failure rate.

Re-design process for a DCM segment

Firstly, the DCM segments were redesigned to remove the holes, as shown in Figure 3.7 (b). The weak spots identified in Figure 3.6 (c) were due to the adhesive that was used to seal the silicone mould to the acrylic inserts at the corner points. No adhesive was used to adhere the silicone to the acrylic haustra pieces, for DCM v2. Instead of adhesive, the segments were kept watertight through an effective compression method, explored in the

following section, that was less restrictive to the silicone membrane during inflationary and deflationary motion during a mimicked motility pattern.

Additionally, DCM v1 had three sampling ports positioned at segments 1, 5 and 10. To improve understanding of the distribution of dissolved drug throughout the lumen of the DCM, the DCMv2 was designed to include three sampling ports in each of the ten segments, visible in Figure 3.7. Multiple ports per segment added the option to add separate lines for media replenishment in addition to sampling.

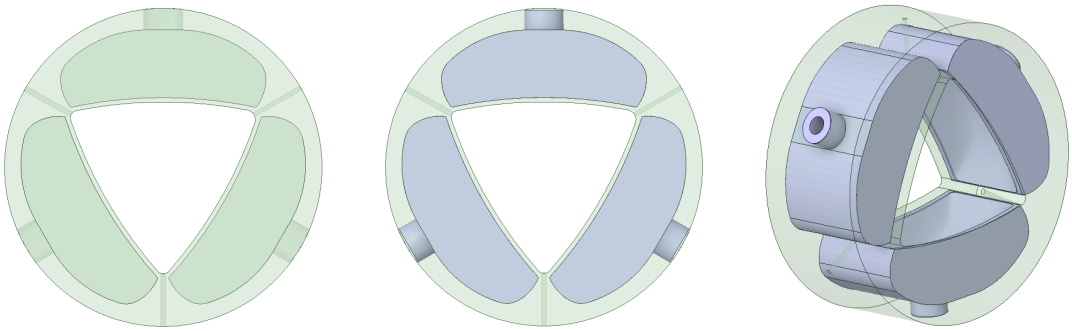

a b c

Figure 3.7: DCM v2 silicone mould (a), silicone mould with acrylic haustra parts inserted (b) and a side view (c).

The mould manufacturing process was taken in house using CAD and additive manufacturing techniques. The mould parts were printed using Formlabs Tough 2000 resin and including holes in the drawing with a larger diameter than the required screw thread. Brass threaded expansion inserts, procured from RS [263], were pressed into the mould parts before post-cure (these metal parts are for casting the mould only, not used in the actual DCM). The parts were then subjected to the standard UV cure process to consolidate the threaded insert within the mould. Moving the process in house made it possible to quickly and easily make modifications to the design of a segment. The outer silicone layer surrounding the haustra cavities was doubled. This increased the diameter of the smallest channel in the mould, enabling air bubbles to be quickly and easily removed before the silicone cured and increasing the success rate of the moulding process. Also,

this added strength to the membrane during inflation and deflation.

Finally, in attempt to overhaul the moulding process completely, prototypes for a 3D printed DCM segment using Formlabs Elastic 50 A v1 resin [264]. This was the 3D printing material (available at the time) with material properties closest to the silicone rubber from which the DCM v1 segments were fabricated (Table 3.2). If successful, this would also eradicate the need for the hasutrum-shaped inserts.

Table 3.2: Material properties of silicone rubber versus Formlabs Elastic 50A resin.

Property	**RTV Silicone rubber [265]**	**Formlabs Elastic 50 A v1 resin [266]**
Shore hardness	15 A	50 A
Tensile strength [MPa]	1.82	3.23
Elongation at failure [%]	640	160
Tear Strength [$kN\,m^{-1}$]	9.63	19.1

Modular solution

A modular approach to the DCM was explored to streamline the repair process by enabling a broken segment to be removed and repaired or simply replaced with a new, functional segment.

Alternative compression methods were explored since the holes for the support rods had been designed out and an effective means of compression was required to avoid the use of sealant. Firstly, a similar rod-enabled compression technique was explored, where the rods were relocated to outside of the DCM segments as shown in Figure 3.8 (b). However, this method was tricky and time-consuming to assemble and dissassemble. Ultimately, a new method was employed that used a reversible elasticated compression technique to fix DCM segments together that was more user-friendly and removed the need

for rods, screws and the clamp system, as shown by the the more minimal design shown in Figure 3.8 (c). The feasibility of this method was improved by the thicker membrane that provided extra material to deform and fill any air gaps when compressed, making the lumen watertight.

Statistics to assess performance

Moulding attempts were classified categorically as either successful or unsuccessful. Standard error was calculated according to Equation 3.1, where s_p represents the standard error, $\hat{p}$ is the statistical sample proportion and n is the sample size.

$$s_p = \sqrt{\frac{(\hat{p}\,(1-\hat{p}))}{n}} \tag{3.1}$$

Once constructed, performance of the model was assessed by the number of complete motility patterns until failure. Error was given as the mean range of motility patterns over which failure could have occurred, if the exact number was unknown. For example, if a segment failed had at an unknown time point within a known time frame of one hour, the error was given as $\pm$ 30 motility patterns, given an actuation frequency of two minutes.

3.2.3 Calibration of wall motion

Since the design of a DCM segment was modified, the relationship between syringe displacement and wall motion required recalibration.

Occlusion degree

Since the DCM v2 has a thicker membrane and may respond differently to the hydraulics, wall motion and luminal occlusion needs to be re-calibrated. The most significant parameters to control wall motion in the DCM are occlusion degree and occlusion velocity. As in the human colon, the haustra of the DCM are convex in shape. Occlusion degree (OD_x) therefore varies along the length of a segment. For means of calibration, occlusion degree was calculated with equation 3.2 using the ratio of cross-sectional area (A_x), measured at the central apex of the haustra (i.e., the maximum occlusion degree reached in the segment), to the cross-sectional area at the neutral position (A_N).

$$OD_x = 100\,(1 - \frac{A_x}{A_N}) \tag{3.2}$$

The control software (GutRig, developed by the School of Biosciences, University of Birmingham) was used to set syringe displacement to 0, 5, 10, 20, 25 and 28 mm using a stepper motor at a constant syringe speed of 15 mm s^{-1}, pausing for 5 s when a segment reached full contraction. An endoscope camera with a framerate of 60 s^{-1} (60 fps) fixed in position inside the DCM and used to capture the movement at 50 fps. A program was written in MATLAB that used image segmentation and binarisation techniques to find the area of the lumen in pixels. The change (%) in area of the lumen dictated the occlusion degree, according to Equation 3.2. Measurements were conducted in triplicate for each degree of syringe displacement.

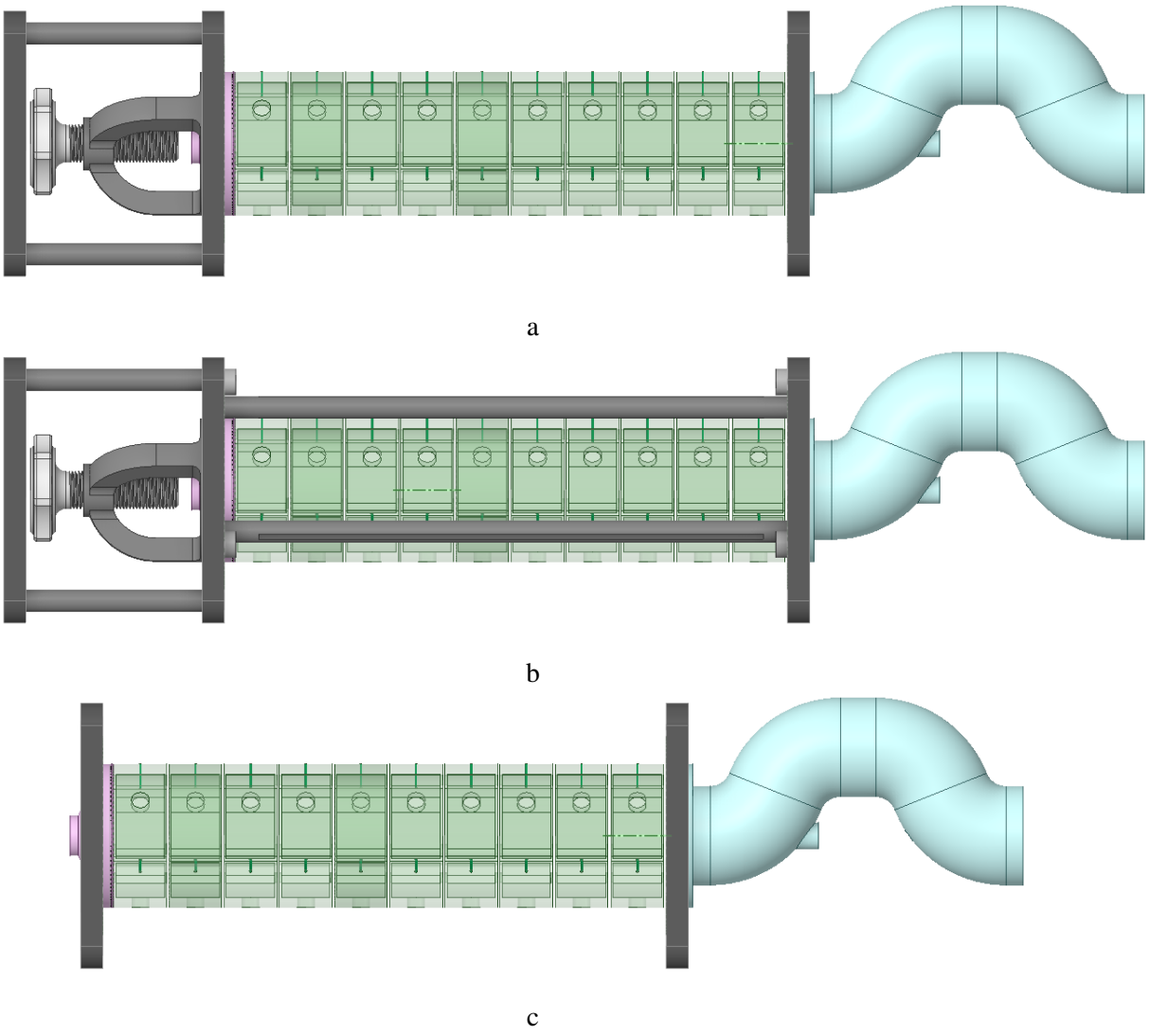

Figure 3.8: a) DCM v1 approach with rods that passed through the holes in each segment (shown in Figure 3.6 (b)), secured using the clamp system. b) Second method of compression after designing out the holes and relocating rods to the outside of the segments to secure the DCM together. c) DCM v2 using reversible elasticated compression.

Membrane displacement

Using the top of the membrane at the centre of the haustra as a point of reference, the displacement of the membrane was also measured, similar to the method used by [10].

Occlusion velocity

The relationship between occlusion velocity and displacement of the syringe was also re-calibrated. An iPhone camera with a frame rate of 60 s^{-1} was clamped in position, with a single DCM segment in direct view that was adhered to a ruler. This set up was clamped and held at the identical elevation and orientation to the DCM. The GutRig software was used to set syringe speed to 5, 10, 20, 25, 30, 40, 45 and 50 $mm\,s^{-1}$, and displacement to a constant 15 mm. The corresponding membrane speed for each syringe speed was measured and recorded for each of the three haustra in this segment.

3.3 Results and Discussion

3.3.1 Performance of the new design

Measurable performance criteria

Figure 3.9 presents four key performance criteria for the DCM, comparing the version of the DCM inherited at the beginning of the project, DCMv1, to the latest version, the DCMv2, which has undergone the design work detailed in Sections 3.2.1 and 3.2.2.

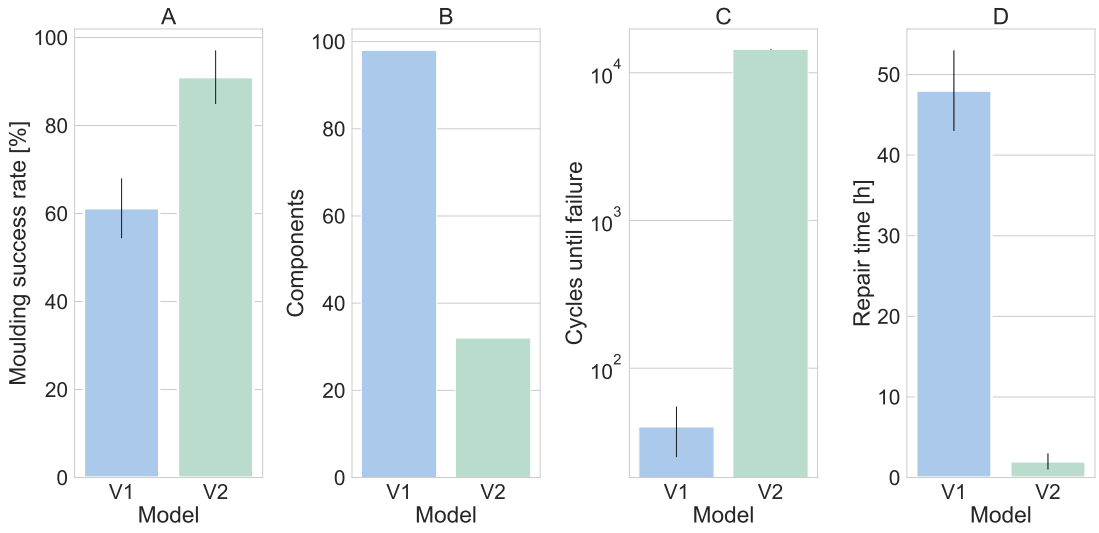

Figure 3.9: A comparison of key performance criteria between DCMv1 (n = 49) and v2 (n = 22). A) Success rate for casting silicone moulds. B) Number of individual components of the model. C) Number of motility patterns operated until the first failure (n.b. no error bar for C since n = 1, i.e., the DCMv2 hasn't broken to the date of authorship). D) The average number of working hours required to fix a failed segment from identification through to full replacement.

Changes made to the design of the mould improved the success rate of the moulding process from 61.2 % to 91.1 % (3.9 A). This reduced the manufacturing time and material costs. Increasing membrane thickness increased the minimum channel diameter in the

mould which was previously prone to bubble formation which weakened the silicone.

Design processes were switched from more conventional techniques to additive manufacturing (AM). Design for AM enabled part consolidation, reducing the number of component parts of the DCM from 98 to 32 (3.9 B). Consolidation has reduced assembly time and eliminated connections that were susceptible to leaks (contributing to the increased longevity (3.9 C) and diminished repair time (3.9 D) respectively).

The DCM is composed of 10 individual segments. The most frequent mode of failure of the DCM was puncturing or tearing of the silicone membrane of a segment during inflation / deflation of the haustrum according to a predefined motility pattern. These faults were difficult to fix and often required replacement of the entire system. To overcome these issues, the mechanism to consolidate the 10 units was modified from a permanent adhesive-based solution to a reversible compression method. Frequency of failure was reduced drastically with the first fault manifesting after $> 14,440$ contractions, as opposed to multiple iterations of design v1 that manifested multiple failures in < 80 motility patterns. This is illustrated in Figure 3.9 C.

Using the modular design, failure of a single segment could be resolved by simply substituting out the compromised segment. This drastically reduced the downtime required for repair, as shown in Figure 3.9 D.

A thicker membrane facilitated an easier casting process with a higher success rate since it became easier for any air bubbles that formed in narrow gaps to escape.

Transparency

Most commercially available compendial dissolution apparatuses use a transparent vessel which is highly valuable to the user. Printing the caecum and hepatic flexure from transparent materials added this feature to the DCM, with the ability to view the contents of the

DCM from outside, as shown in Figure 3.10. This enables the user to view wall motion, fluid levels and tablet displacement.

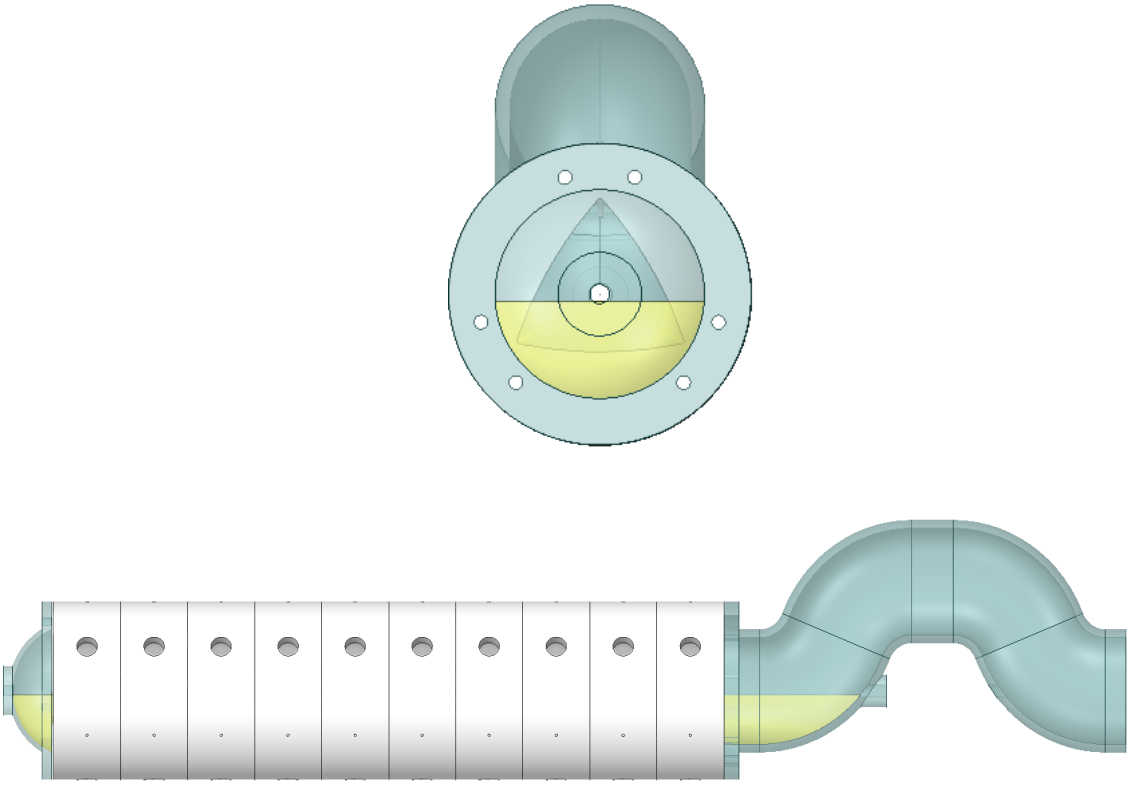

Figure 3.10: Schematic of the DCM partially filled with 100 mL of simulated fluid, visible through the transparent caecum and hepatic flexure printed from Formlabs Clear resin.

Sampling system

The DCM was successfully integrated into the Agilent 850-DS automated sampling system. This capability bolsters the DCM as an industry-ready dissolution apparatus that is easily introduced into a laboratory workflow. It is rare for aliquots of fluid samples to be withdrawn and replenished manually in industry.

Figure 3.11 displays a simplified diagram of the process, with a cross section of the DCM lumen filled with 100 mL fluid (3.11A). The automated media sampling & re-

plenishment (AMSR) system primes the sampling lines by withdrawing sufficient fluid to ensure the lines are full. This is essential to ensure an accurate volume of sample fluid can be collected. After priming, the AMSR system withdraws a predefined volume of fluid from the lumen (3.11B). This fluid is dispensed into vials for offline sampling. Finally, the media is replenished to its initial volume (3.11C).

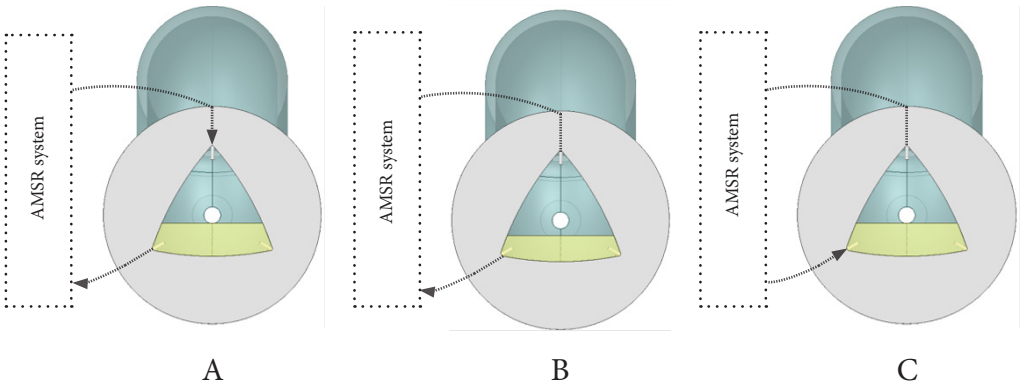

Figure 3.11: A) Priming - AMSR system primes the sampling lines by withdrawing sufficient fluid to ensure the lines are full. B) Sample withdrawal - a predefined volume of fluid is withdrawn from the lumen. C) Replenishment - an equal volume of fresh media is returned to the DCM lumen using the same lines that were used to withdraw the samples.

3.3.2 Segment printing

Unfortunately, as can be seen by Figure 3.12 the design was susceptible to cupping and resulted in a blowout of one or more of the haustral segments. Typically, cupping can be solved by changing the orientation or adding vent holes. For this design, cups could not be removed through reorientation. Vent holes couldn't be added as the haustra pockets need to be watertight. Additionally, the material properties of Elastic 50 A v1 were

too constraining and the desired profile of wall motion was infeasible. This method was subsequently abandoned.

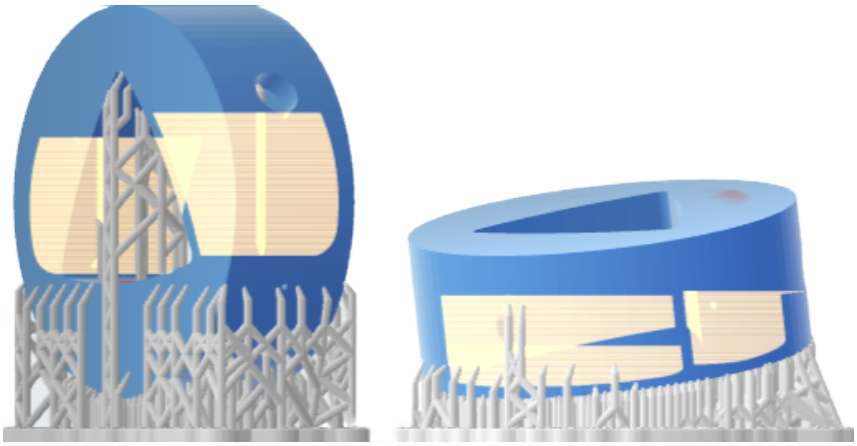

Figure 3.12: Two orientations of a single DCM segment ready to print, prepared using PreForm 3.22.1 (formlabs). Support material is coloured grey whilst blue indicates a viable part for print. Regions outlined in yellow are cups that may result in blowout or poor surface finish. Areas shaded orange may require extra support material for a successful print.

3.3.3 Wall calibration

Occlusion degree

The results are presented in Figure 3.13, where error bars represent the standard deviation of area measurement. Occlusion degree (OD) was found to increase linearly (Equation 3.3, correlation coefficient $R^2 = 0.997$) with syringe displacement (SD) over the range $12 \leq OD \leq 72$ which covers that reported in vivo (18 ± 10 and 59 ± 18 % under baseline and stimulated conditions respectively).

$$OD = 5.80SD - 44.03 \tag{3.3}$$

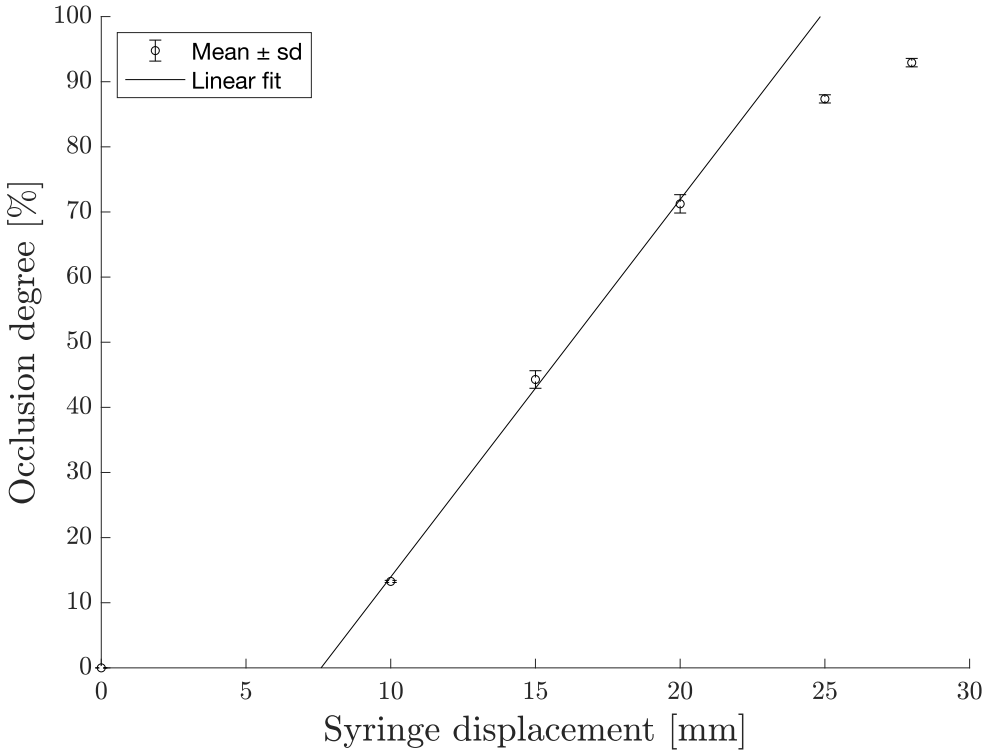

Figure 3.13: Calibration curve of lumen occlusion degree versus syringe displacement for the hydraulic system.

Membrane displacement

A linear relationship (Equation 3.4) was also established between membrane displacement (MD) and SD for the range $5 \leq SD \leq 20$ with a correlation coefficient of 0.996. The results are shown in Figure 3.14.

$$MD = 0.34SD + 0.73 \tag{3.4}$$

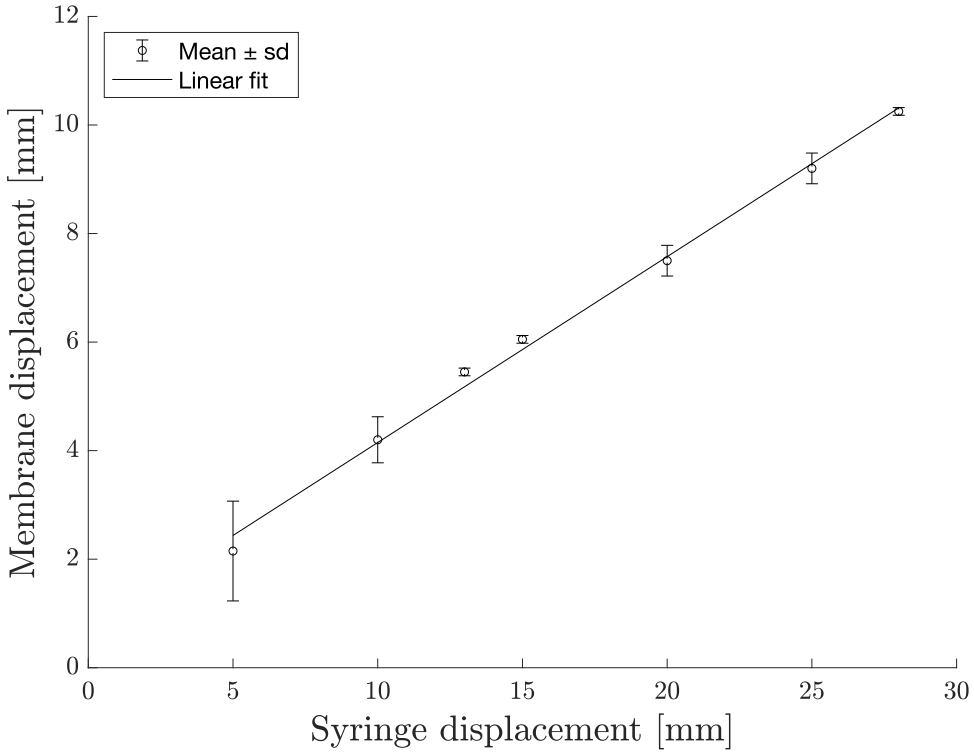

Figure 3.14: Calibration curve of membrane displacement inside the DCM lumen versus syringe displacement on the hydraulics system.

Occlusion velocity

Figure 3.15 displays the calibration curve obtained for occlusion velocity (OV) versus syringe speed (SS), where the error bars describe the intra-segment variation that may be

caused by slight manufacturing defects. A linear relationship (Equation 3.5) was obtained with a correlation coefficient of 0.997 over the range $5 \leq SS \leq 50$.

$$OV = 0.32 \times SS + 0.92 \tag{3.5}$$

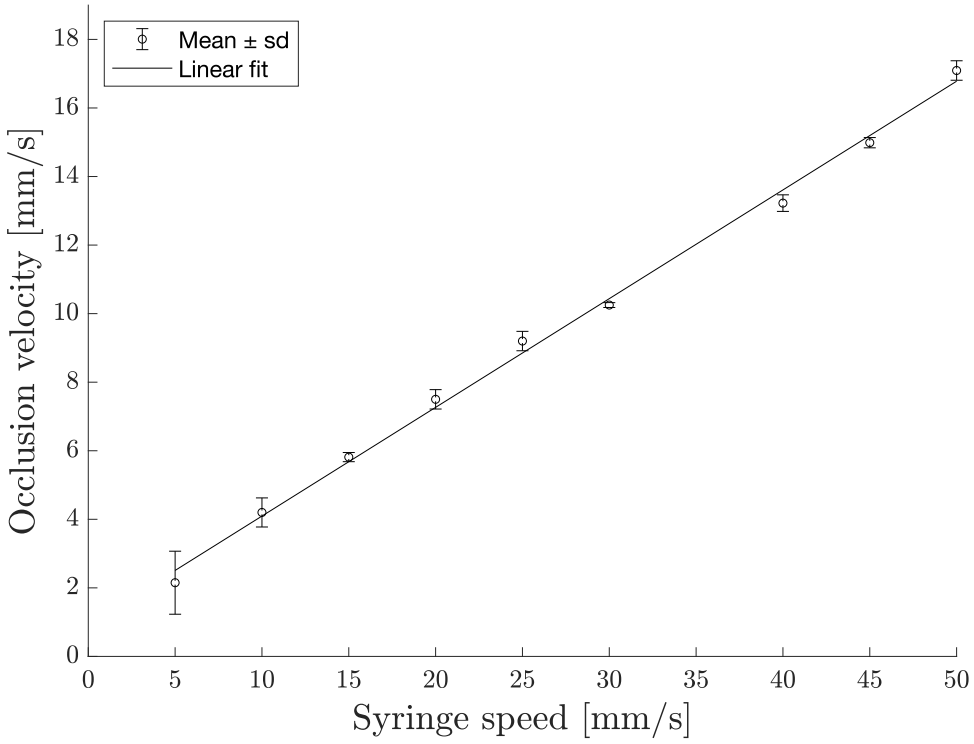

Figure 3.15: Calibration curve of the velocity of luminal occlusion inside the DCM versus syringe displacement on the hydraulics system.

3.4 Conclusions

Various issues that hindered operation of the DCM were outlined. This chapter set out the approaches for redesign of the model were and the methodology of how this was achieved. Implementing a modular approach the DCM significantly reduced the downtime associated with repair of a damaged segment by > 40 working hours. The design was somewhat simplified using additive manufacturing techniques to reduce the total number of component parts for the tube by > 60 %. The recorded operational hours of the DCM were increased by two orders of magnitude. Overall, this work produced a new iteration of the model that is more easily integrated into the workflow of a standard dissolution testing laboratory.

Chapter Four

Luminal Fluid Motion Inside an In Vitro Dissolution Model of the Human Ascending Colon Assessed Using Magnetic Resonance Imaging

This chapter was published in Pharmaceutics 13(10): 'Luminal Fluid Motion Inside an In Vitro Dissolution Model of the Human Ascending Colon Assessed Using Magnetic Resonance Imaging' [14]

4.1 Abstract

Knowledge of luminal flow inside the human colon remains elusive, despite its importance for the design of new colon-targeted drug delivery systems and physiologically relevant in silico models of dissolution mechanics within the colon. This study uses magnetic resonance imaging (MRI) techniques to visualise, measure and differentiate between different motility patterns within an anatomically representative in vitro dissolution model of the human ascending colon: the dynamic colon model (DCM). The segmented architecture and peristalsis-like contractile activity of the DCM generated flow profiles that were distinct from compendial dissolution apparatuses. MRI enabled different motility patterns to be classified by the degree of mixing-related motion using a new tagging method. Different media viscosities could also be differentiated, which is important for an understanding of colonic pathophysiology, the conditions that a colon-targeted dosage form may be subjected to and the effectiveness of treatments. The tagged MRI data showed that the DCM effectively mimicked wall motion, luminal flow patterns and the velocities of the contents of the human ascending colon. Accurate reproduction of in vivo hydrodynamics is an essential capability for a biorelevant mechanical model of the colon to make it suitable for in vitro data generation for in vitro in vivo evaluation (IVIVE) or in vitro in vivo correlation (IVIVC). This work illustrates how the DCM provides new insight into how motion of the colonic walls may control luminal hydrodynamics, driving erosion of a dosage form and subsequent drug release, compared to traditional pharmacopeial methods.

4.2 Introduction

Knowledge of luminal flow inside the human colon remains elusive, as this anatomical region is difficult to access and current techniques are generally invasive. Improved knowledge would enable a greater understanding of colonic physiology and pathology, enhancing the capability to design new or improved colon-targeted drug delivery systems. Targeted drug delivery to the ascending colon (AC) offers a promising opportunity for local administration of effective therapeutics for a range of conditions, such as inflammatory bowel disease, colon cancer and irritable bowel syndrome, all of which have enormous and increasing prevalence across the globe [267–269]. In the case of colorectal cancer (CRC), it is the fourth most commonly diagnosed and third most deadly cancer worldwide as of 2018 [267]. The combination of enhanced biorelevant in vitro and in silico dissolution testing could streamline the research and development process for new colon-targeted formulations [270, 271]. In silico models that can simulate luminal flow inside the colon enable the investigation of colonic drug delivery systems to interpret how flow parameters can affect the breakdown of different formulations and API release [238, 253]. Formulations can then be optimised by the use of quantitative simulations of how luminal flow affects mass transport phenomena of the API, including release and dissolution rates and distribution via convective transport inside the lumen.

Manometry techniques are used to measure intraluminal pressure activity during contractions of the colonic wall, with significant advances being made using high resolution manometry in recent years [41, 244–246]. However, little information is available pertaining to how the colonic contents move and particularly changes in movement based on motility patterns associated with both normal and abnormal colon pathophysiology [247]. For example, unsynchronised or reduced motility patterns of the colon wall (as a result of a functional gastrointestinal disorder, FGID), may not be effective for mixing and propulsion of the colonic contents. Colonic mixing phenomena occur in the AC (before significant dewatering occurs), which is particularly difficult to access using manometry,

and highly invasive. In this region, it is possible that the hydrodynamics can be affected by disorders that cause extreme variances in physical properties of the chyme. The influence of disease affecting the AC can therefore have a significant impact on the delivery of colon-targeted dosage forms. Reduced contractile activity of the AC walls may lessen the impact of normal and shear forces arising from fluid motion and direct contact with the colonic walls. Therefore, a technique to measure motion of the colonic walls and contents in conditions that incorporate extremes of disease would have great value in the development of patient-centric colonic delivery systems.

Magnetic resonance (MR) tagging, a noninvasive and nonionising imaging technique which is commonly used to assess cardiac function, has recently been applied to assess gastrointestinal motility [248–251]. MR tagging involves deliberately altering the MR imaging (MRI) signal along parallel lines or 'tags' in an organ inside the body, at a given time before acquiring an image. A comb of parallel black tags is 'drawn' on the tissue and if the tissue moves between the tagging process and the action of taking the MRI image, the black lines are observed to move with the tissue. This is captured on the MRI image as deformation of the black lines in the direction of motion, with the amount of deformation being proportional to the degree of motion. MR tagging velocimetry then involves the tracking of a tagged material or volume of fluid to estimate the local velocity from the displacement of tags between frames. It has been used to measure the velocity in fluid flows, primarily in blood vessels [272] and more recently in engineering systems [273, 274]. Pritchard *et al.* [35] and Wilkinson-Smith *et al.* [251] applied an MR tagging technique to the flow of the contents of the human AC. A principal output of their work was the definition of a coefficient of variance (CoV) parameter, that may successfully discriminate between healthy and constipated subjects based on the degree of mixing-related motion that occurred.

This research aims to use MR tagging to visualise, assess and discriminate between different motility patterns applied to an in vitro model of the human AC, the dynamic

colon model (DCM). The DCM (Figure 4.1) replicates the anatomy, physical pressures and motility patterns of the human AC [9, 10, 12]. Precise replication of well controlled, repeatable motility patterns and therefore hydrodynamic conditions permits an intensive analysis which is not possible in vivo as colonic motility is inherently erratic. Therefore, good performance in vitro would provide further validation for the CoV parameter in addition to enabling a rapid estimation of the intensity of hydrodynamic activity that a dosage form may be subjected to inside the luminal environment during dissolution testing. The biorelevant DCM is a valuable dissolution testing apparatus, since existing pharmacopeial dissolution testing apparatuses do not mimic the hydrodynamics of the AC [10, 153], as they were designed with simple architecture and mixing mechanisms to satisfy the need for the batch-to-catch quality control of dosage forms [275].

The DCM also enables tight control of biorelevant parameters, such as the viscosity and volume of the lumen contents, that may be affected by functional gastrointestinal disorders (FGIDs) [276] and are pivotal in the release of the API from a dosage form [277–279]. Different motility patterns can be applied reproducibly to investigate a range as well as extremes of motion; thus, the sensitivity of a formulation to these extremes can be understood which can help to understand the variability in product performance that may exist in health and disease. Thus, the biorelevance of the system can encompass the variability that may be observed in vivo by accurate replication of a range of motility patterns. The interplay between colonic environmental parameters and the applied motility pattern on the motion of the luminal contents can be evaluated using MR tagging within the DCM. Again, this is not possible within the in vivo colonic environment, which is also subject to the inherent variability of in vivo measurements and effects of respiratory motion. Therefore, validation of an MRI technique using the DCM provides researchers and clinicians an additional tool to understand how underlying abnormalities affect fluid flow within the colon.

This study also extends analysis (of the same tagged dataset) using MR tagging

velocimetry, to explore the in-plane measurement of velocity of the contents inside the DCM lumen arising from motility patterns that mimic antegrade cyclic propagating pressure waves (CPPWs). CPPWs are among the most abundant forms of motility observed in the unstimulated human AC [170]. Furthermore, the same approach will be applied to measure velocities of the contents of the human AC using a tagged sequence previously published by Pritchard *et al.* [35]. This will facilitate a direct comparison of luminal flow in the colonic environment with its in vitro counterpart. Additional understanding of the similarities and differences between in vitro and in vivo systems could be valuable to inform in vitro in vivo evaluation (IVIVE) or in vitro in vivo correlation (IVIVC) studies using the DCM. These can reduce the number of in vivo studies, that are costly in terms of both time and money, during the development of new pharmaceutical formulations. However, similarly to pharmacopeial dissolution apparatuses, the DCM is limited in that it cannot currently model absorption kinetics. Therefore, assumptions need to be made regarding permeability and dissolution–absorption relationships according to data from cellular models, such as Caco-2 or colonoids.

Phase contrast (PC) cine-MRI, described in detail in [280], is also used to measure blood flow [281]. To date, no nuclear magnetic resonance (NMR) velocimetry studies have been carried out on the human AC, nor on phantoms that closely replicate the geometry and flows inside the colonic environment. Both MRI techniques enable visualisation of the motion of the DCM wall and lumen contents. This work implements both techniques to measure the in-plane (MR tagging) and through-plane (PC cine-MRI) velocity of the contents of the DCM lumen synchronously with the movement of the DCM colonic walls; to develop an understanding of the hydrodynamic conditions a dosage form is subjected to during dissolution testing inside the DCM.

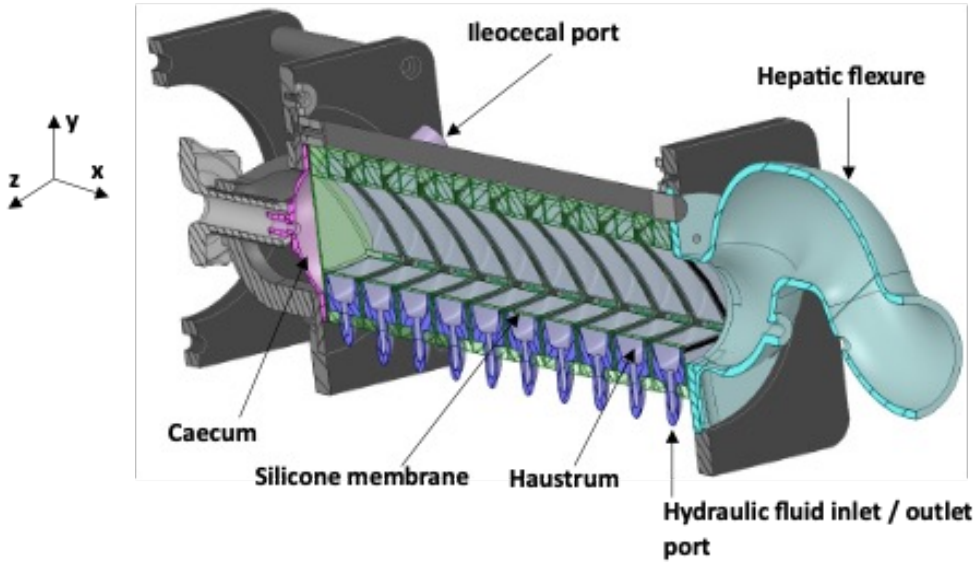

Figure 4.1: Schematic cross-sectional view of the Dynamic Colon Model (DCM). The DCM has a segmented appearance reflecting that of the human ascending colon: segment 1 is adjacent to the caecum, through to segment 10 adjacent to the hepatic flexure.

4.3 Methodology

The DCM was filled with liquid media and placed in the MRI scanner in the supine patient position. The liquid media were chosen to mimic a biorelevant viscosity based on previous studies [9, 10, 12], by using aqueous solutions of NaCMC (700,000 Mn); denoted as LOVIS (low viscosity, 0.25 (w/v) NaCMC, 13 m Pa s) or HIVIS (high viscosity, 0.50 (w/v) NaCMC, 98 m Pa s). Media volumes varied from 150 mL to 200 mL. The wall motility waves applied in this study were antegrade contractile waves travelling the entire length of the DCM (20 cm), in line with the default pattern previously applied [9, 10]. Propagation speeds of 0.8 cm s^{-1} and 0.4 cm s^{-1} were used. The former is the average propagation velocity of a cyclic antegrade wave in the fed state in the colon and the latter is the average propagation speed of a high amplitude propagating contraction (HAPC) [170]. The occlusion degree was fixed at 60 ± 5 for each pattern, higher than in previous reports, to further explore the graduation of fluid flow with wall contraction [10].

Scanning was carried out using a 3T Philips Ingenia Widebore scanner (Philips, Best, The Netherlands). Localiser scans were carried out prior to the tagging and PC scans for placement of these sequences across the DCM. Firstly, motion of the contents of the DCM lumen was visualised using a tagged balanced turbo field echo (bTFE) sequence. This sequence saturated predetermined regions of fluid inside the DCM by applying a radiofrequency pulse to null the signal of these regions. This resulted in dark horizontal stripes (tags) being superimposed onto the images, with 12 mm spacing between the centres of consecutive tags. The delay of 250 ms between the application of the tag lines and acquisition of the image allowed movement within the DCM lumen to be detected. The tags were approximately 5 mm thick. Sharpness and width of the tag lines are influenced by the time it takes to run the tagging pulses and this sequence uses a slightly longer pulse train than the default set for cardiac applications, which improves the definition of the edges of the tag. A shim box was placed over the area of interest to reduce the susceptibility to artefacts in the region in vitro, in line with the in vivo scan [35]. This

sequence had a repetition time (TR)/echo time (TE) of 2.44 / 1.22 ms, a flip angle (FA) of 45°, with a single sagittal slice, thickness of 15 mm, a field of view (FOV) of 259 mm (anterior–posterior (AP)), and 330 mm (head-feet (HF)) with a reconstructed resolution of 0.98•0.98 mm. In total, 100 scans were acquired at 600 ms intervals. Important imaging parameters are summarised in Table 4.1, including those used for the in vivo study, which the DCM sequence was based upon. After acquisition of a tagging sequence, a rest period of 10 s was allowed for the lumen media to stabilise before running subsequent sequences.

Table 4.1: MRI scanner parameters.

Parameter	**DCM PC cine-MRI**	**DCM Tagging**	**Human colon tagging [35]**
Scan duration [s]	60	60	20
TR [ms]	9.21	2.43	2.30
TE [ms]	7.60	1.22	1.15
FA [°]	10	45	45
FOV [mm^2]	177×200	259×330	$222 - 264 \times 330$
Recon resolution [mm^2]	1.14×1.14	0.98×0.98	0.98×0.98
Slice thickness [mm]	8	15	15
SENSE	2.0	1.5	1.5
No. dynamics	30	100	33
Temporal resolution [s]	2	0.6	0.6

Secondly, PC cine-MRI scans were acquired using a sequence modified from a standard PC flow sequence that normally acquires multiple flow measurements in arteries (and veins) across the cardiac cycle. This method is described in detail in [273]. For this study, a single fast field echo (FFE) image was generated using flow-sensitive gradients with a $TE = 7.6$ ms and $TR = 9.2$ ms. Each image of 101×101 voxels was generated with an in-plane reconstructed resolution of 1.136×1.136 mm and a slice thickness of 8 mm. This scan was then repeated over a 60 s period with a temporal resolution of 2 s resulting in a set of 30 images for each parameter combination. Three different slice locations along the length of the DCM were used sequentially, with 10 s rest periods between scans to investigate the spatial variation of the flow induced. The locations were at segments 2, close to the caecum, 6, the midpoint and 10, the hepatic flexure (see Figure 4.1). Following completion of all spatial locations for the default motility pattern, the protocol was repeated for the slower CPPW. After completion of all scans, media volume and/or media type (LOVIS or HIVIS) were changed, and the protocol repeated. Flow was encoded only in the streamwise direction (x-axis). To avoid aliasing, maximum velocities were encoded at ± 3 cm s^{-1}, 50 higher than the fastest propagating wave speed of 2 cm s^{-1} which has been shown by Stamatopoulos *et al.* [10] to be close to the maximum media velocity inside the lumen. Positive and negative velocities represent flow along the x-axis towards the hepatic flexure and caecum (depicted in Figure 4.1), respectively.

4.3.1 MR data analysis

Any movement of the lumen contents during the delay between the application of a tag and image acquisition changes the position of the tag lines on the image. However, if no motion occurred during the complete scan, the full set of sequential tagged images would be identical, with all tag lines remaining straight (as seen in Figure 4.2A). Motion of the luminal contents, in any direction, leads to changes in the signal intensity in the tagged contents from frame to frame. This variation forms the basis of the method proposed to assess motion inside the DCM.

To measure motion of the contents of the human AC, Pritchard *et al.* [35] analysed standard deviation maps within a region encompassing the AC, calculated over a sequence of tagged images. Applying this technique to the DCM, a region of interest (ROI), R, was drawn, enclosing the lumen at the neutral wall position (outlined in Figure 4.3B) to focus measurements on the motion of fluid inside the lumen rather than fluids inside the haustra, used for the pneumatic control of wall motion. Those voxels within R which experience variation in the signal intensity during the 60 s of data acquisition have a relatively large standard deviation of intensity, whereas static structures (DCM core structure) or motionless lumen contents have a standard deviation close to zero. Therefore, the resulting standard deviation map highlights any motion of the DCM lumen contents. The standard deviation map can also reveal where the motion is concentrated. The mean signal intensity (MIR) and standard deviation ($STDEV_R$) maps were calculated using MATLAB (R2019B, The MathWorks, Inc., Natick, MA, US) over 100 frames. The coefficient of variation (CoV) for the tagged scan was then estimated from:

$$CoV = 100 \times \frac{STDEV_R}{MI_R} \tag{4.1}$$

The predominant direction of flow (antegrade or retrograde) is revealed from the direction of tag displacement. If motility induces laminar flow inside the DCM or AC lumen, each frame would show a uniform displacement of each tag line, where tag displacement would

be proportional to flow velocity. Velocity estimates (v) of lumen contents were obtained from tagged MRI images of the DCM acquired in this study, and from in vivo sequences previously published in the supplementary material of the Pritchard *et al.* [35] study. This was described by the measured displacement (δx) of a point of the tag over a fixed period of time (Δt) - the delay of 250 ms between the application of the tag lines and acquisition of each image—as shown by Equation (2.2). Different parts of a tag can travel different velocities [282]. The average velocity of the tagged contents was calculated by measuring the displacement of the centroid of each tag between consecutive images, whilst the peak velocity was measured using the maximum displacement of each tag between consecutive images, i.e., tracking the displacement of the leading edge of each tag. Displacement could be accurately measured to within ± 1/2 voxel diameter, ± 0.49 mm, which translates to an uncertainty of $\pm 0.20\ \mathrm{cm\,s^{-1}}$ associated with TOF tagging velocity measurements.

$$v_x = \frac{\Delta x}{\Delta t} \tag{4.2}$$

The in vivo data available for assessment included one sequence with extreme motility obtained after stimulation by ingestion of a 500 mL dose of polyethylene glycol (Macrogol 3550) electrolyte solution (MOVIPREP®, Norgine Pharmaceuticals Ltd., Harefield, UK). Details of the participants are outlined in the study described in [35]. Using PC cine-MRI, the mean velocity of the DCM lumen contents was measured by taking the mean of all the weighted-average velocities measured in voxels that constitute the through-plane lumen cross-sectional flow area. Additionally, a second measure of the mean velocity was made by taking the mean of all the weighted-average velocities measured in voxels encompassed by the 'central flow region' of the lumen. This was to assess the impact of any stagnant regions of fluid close to the walls on the through-plane mean velocity. Furthermore, peak velocities were also measured by taking the mean of the 6 highest value voxels within each ROI. Due to the potential for high noise in individual voxel velocity measurements, PC cine-MRI peak velocity estimates should be made using

several voxels, rather than just one [283]. The standard deviation of the mean velocity calculated using each ROI was considered to be the error associated with the respective PC cine-MRI mean velocity measurement.

4.3.2 Statistics

A three-way analysis of variance (ANOVA) was performed to investigate the main effects of volume, viscosity and wave speed, in addition to their interaction effects, on CoV. Data were tested for normality using the Shapiro–Wilk test, and homogeneity of variances using Levene's test for equal variances. Post-hoc analysis employed Tukey's honest significant difference (HSD) test to assess significant differences in the mean of CoV between groups ($p < 0.05$).

4.4 Results and discussion

4.4.1 MR Tagging of Fluid Motion

The series of tagged images enabled visualisation and quantification of the motion of the DCM luminal contents, whilst simultaneously tracking the dynamic morphology of the interior DCM walls during motility, as shown in Figure 4.2 and supplementary video S1 of O'Farrell *et al.* [14]. Prior to initiation of a motility pattern, the DCM was at its 'baseline' state, as shown in Figure 4.2A. The DCM walls were clearly distinguishable against the media in the lumen and fluid inside the haustra, without the need for additional contrasting agents. Tags were straight, parallel and intact, showing no motion. Contraction of the first segment close to the caecum, synchronous with the relaxation of the second segment, drove a wave of antegrade flow along the positive x-direction (aboral), as shown by displacement of the tags in Figure 4.2, also indicated by the direction of the arrow above (B). The initial wave front travelled the length of the DCM (25 cm), identified as all tags were displaced. This sequence of segmental motion demonstrates how the DCM reproduces the widely accepted law of the intestine, wherein synchronised constriction and relaxation of the lumen results in a peristaltic wave [10].

Wall motility generated both antegrade and retrograde motion of the contents, as expected from in vivo observations [35]. As a wall segment contracted, for example, S6 in Figure 4.2C, the tagged contents on either side were displaced in opposite x-directions. Upon reaching maximum contraction, the principal flow direction of all immediately adjacent tags switched to retrograde as shown in Figure 4.2D. Arrows have been drawn on the images above the displaced tags to aid the visualisation. The data from this full tagging sequence is shown in supplementary video S1 of O'Farrell *et al.* [14]

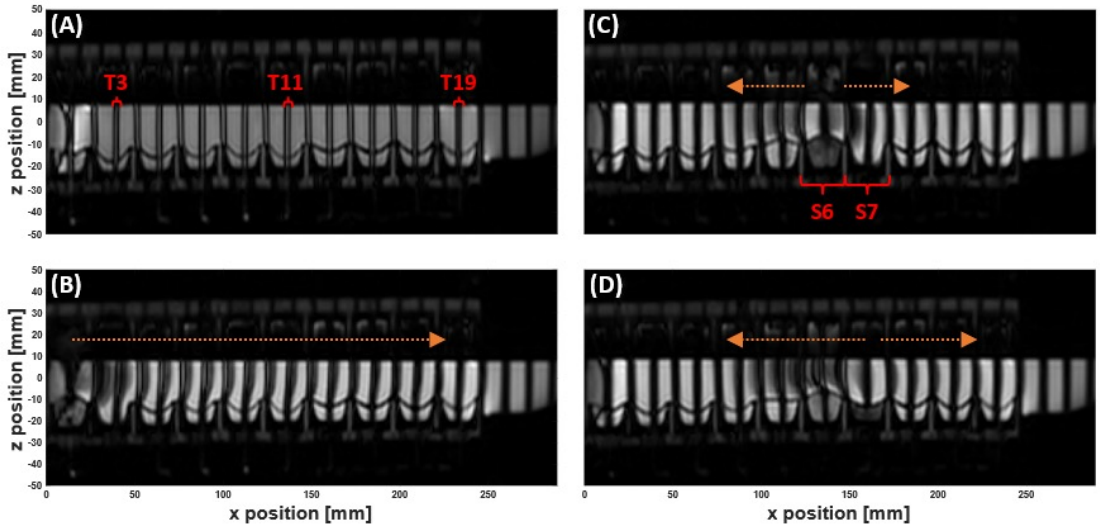

Figure 4.2: MR Tagging applied to the dynamic colon model (DCM) filled with 200 mL LOVIS fluid. 'Tags' are the dark stripes across the images. The DCM is orientated such that the caecum is at $x = 0$ mm, and the hepatic flexure begins at $x = 250$ mm. (A) Coronal image showing no movement inside the DCM before motility is initiated. The tags are straight, parallel and intact. (B) Tagged image during contraction of the first DCM segment. Tags are shifted in the positive x-direction showing a wave of antegrade flow travelling through the lumen. (C) and (D) Tagged images of the DCM during contraction of segment 6, showing antegrade flow in the immediately downstream tag at early stages of contraction (C) and stronger retrograde flow in all adjacent tags (D). The arrows drawn onto the images are to aid visualisation of the direction of tag displacement and therefore motion of the contents. Tags (T) 3, 11 and 19, and segments (S) 6 and 7 are labelled as these were the focus of velocimetry studies in Sections 4.3.2 and 4.3.3.

Figure 4.3 shows the mean (A) and standard deviation (B) maps of voxel intensity over the duration of the slower CPPW inside the DCM, with 200 mL LOVIS fluid inside the lumen. These relate to movement and blurring of the tags and therefore mixing-related motion of the contents. For all media, the standard deviation of voxel intensity varied along the x-axis; therefore, the level of motion experienced by the contents is nonuniform along the x-axis. This complements findings from dissolution studies inside the DCM, where different drug concentrations are found at different sampling points along the x-axis [9]. Low levels of motion were observed close to the caecum ($x = 0$ mm), increasing along the x-axis of the DCM lumen to a peak just after the midpoint, before decreasing close to the hepatic flexure ($x = 250$ mm). This indicates that the efficiency with which the DCM mixes and transports the contents may be low close to the start and end of a CPPW, suggesting that a solid dosage form may experience a slower eroding activity and therefore release rate in these regions. In this study, the beginning and end of the CPPW were fixed at the mimic caecum and hepatic flexure, respectively. This was based on clinical findings that showed an antegrade contractile wave ending at the hepatic flexure [10]; however, in vivo contractions can start and end in different locations [170]. A limitation of the model is that the hepatic flexure in the DCM is a rigid body, whereas in vivo it contracts to aid transfer of contents from the AC to the transverse colon, which may account for less intensive mixing phenomena observed in the DCM. Moreover, in vivo the AC is regularly receiving chyme from the ileum through the ileocecal valve which may increase mixing activity, compared to the DCM which acts as a closed system, rather than a flow-through style apparatus.

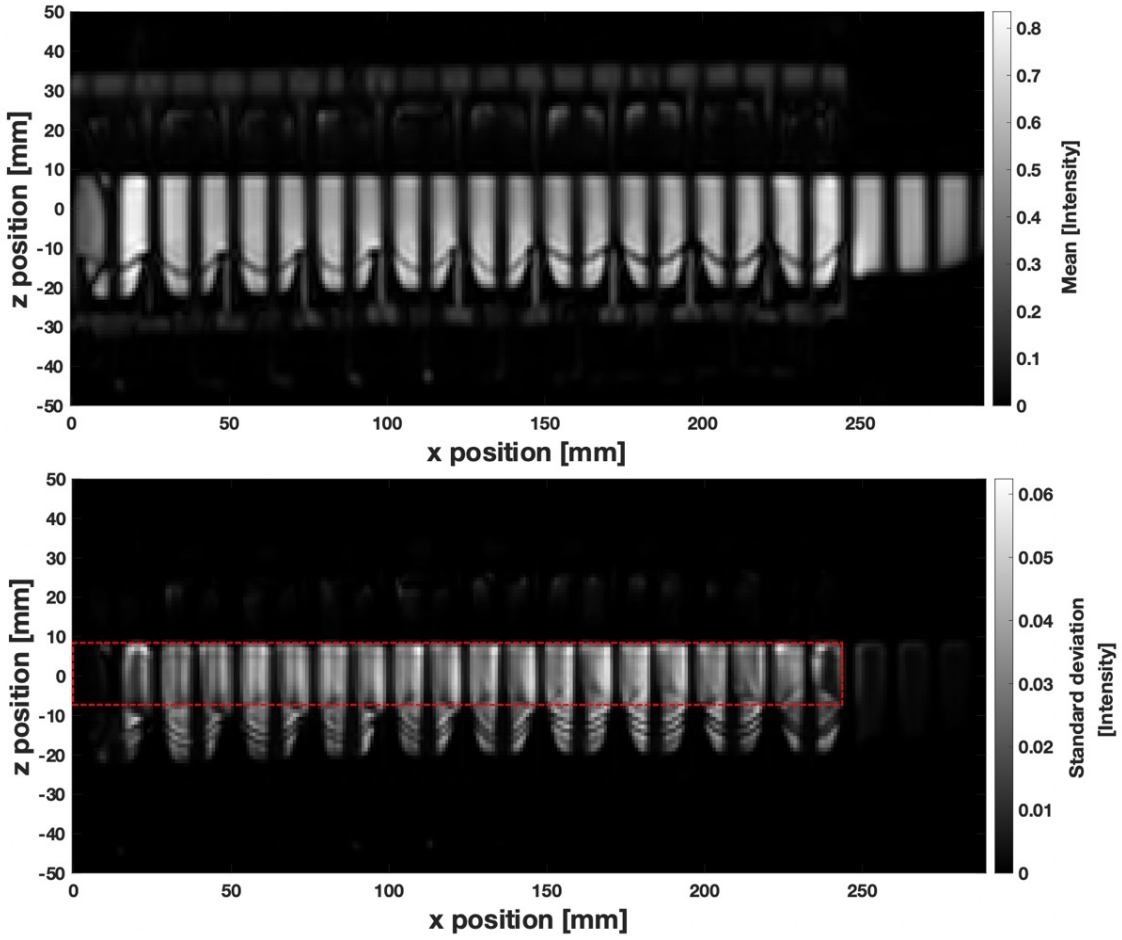

Figure 4.3: Processed images from tagged cine-MRI data showing (A) a mean voxel intensity map and (B) the corresponding voxel standard deviation map (calculated over 100 dynamic images). The red dashed line depicts the ROI, R, that encloses the DCM lumen.

The calculated average coefficient of variation (CoV) for all tagged scans are shown in Table 4.2, along with the post-hoc analysis of main effects. Data were found to be approximately normally distributed using the Shapiro-Wilk test for normality, with homogeneous variances. Effects of media volumes on the degree of mixing were not statistically significant ($p > 0.05$). However, the motility pattern and media viscosity were found to have statistically significant effects on the degree of mixing ($p < 0.05$). Interaction effects were not tabulated as all were found to be insignificant ($p > 0.05$), indicating that there was no combined effect for the motility pattern, media viscosity and volume on the degree of mixing under the experimental conditions in this study. However, differences are expected to be more extreme over a broader parametric range.

Table 4.2: Degree of mixing (CoV) scores reported from tagging experiments and Tukey's post-hoc assessment for significant differences (n = 4). All interaction effects were deemed insignificant ($p > 0.05$) so were not tabulated.

Media		Volume	CoV [%]
Slower CPPW ($0.4\,\mathrm{cm\,s^{-1}}$)			
	LOVIS	150 mL	32.16
		200 mL	30.23
	HIVIS	150 mL	26.52
		200 mL	25.68
Faster CPPW ($0.8\,\mathrm{cm\,s^{-1}}$)			
	LOVIS	150 mL	37.29
		200 mL	37.42
	HIVIS	150 mL	32.35
		200 mL	31.98

Post-hoc multiple comparisons of CoV using Tukey's HSD test

Factor	Level difference	Mean difference	p - value
Motility pattern	Slower - faster CPPW	6.113	$p < 0.05$
Media viscosity	LOVIS / HIVIS	5.142	$p < 0.05$
Media volume	150 − 200 mL	-0.752	$p < 0.05$

The above findings demonstrate that the tagging technique can discriminate between motility patterns based on the degree of mixing-related motion ($p < 0.05$) inside the DCM and reinforce findings made in vivo [35]. The degree of mixing-related motion significantly increased with the propagation speed of the contractile wave, supporting results by Thorpe *et al.* [284], where the distribution of 5-aminosalicylic acid (5-ASA) concentration increased with elevated levels of simulated motility within a colonic model. Levels of colonic motility differ based on disease and prandial states in vivo. For example, patients with chronic idiopathic constipation exhibit reduced colonic motor activity [285,

286], and the level of retrograde CPPWs increases in the fed state compared to fasted [170]. Thus, the DCM could be used to study relationships between the motion of the colonic walls and contents of the colon, and the resulting impact on drug release and distribution when replicating distinctive types of motility patterns from clinical observations. This information is essential to inform the disease-state-specific design of locally acting dosage forms for the colon, in addition to the administration recommendations for such a formulation (with or without a meal).

Tagging was also able to discriminate between media viscosities based on the degree of mixing-related motion ($p < 0.05$). This additional sensitivity enables further understanding of the pathophysiology of colonic flow and the mode of action of treatments for functional colonic diseases, such as laxatives. In silico modelling of tablet dissolution in the proximal colon has shown that the ability of a motility pattern to distribute a dissolved API along the proximal colonic axis is highly dependent on the viscosity of the contents [238]. Viscosity has also been widely shown to influence dissolution in vitro [9, 277, 287]. Therefore, tagging scans that can distinguish between the viscosity of the contents based on mixing-related motion may be useful to inform the effectiveness of how a locally acting drug may be distributed in the region containing the target area. This area is currently very poorly understood, and therefore additional information provided by tagging is valuable and could in turn aid the design and optimisation of patient-centred therapeutic formulations.

4.4.2 Velocimetry of Fluid Motion In Vitro Using MR Tagging

Figure 4.4 shows the measured average velocity of each MR tag over 100 consecutive images collected over the duration of the slow CPPW with 200 mL LOVIS fluid A inside the lumen. Figure 4.5 illustrates the local wall displacement at the location of odd-numbered tags, which were placed at the midpoint of each DCM segment, facilitating visualisation of how the contractile wave propagated along the x-axis of the DCM tube. For the slower CPPW, this analysis produced a quantitative overview of flow events along the entire DCM tube that occurred due to contractions in the walls of the DCM, enabling a comparison of flows induced by wall motility at different spatiotemporal locations along the in vitro colon model. There was no local wall motion at the location of even numbered tags as these were placed between segments where the walls are rigid, hence they were excluded from this plot.

Prior to motility of a given segment, the walls remained at the neutral position (0 mm displacement), whilst contents of the DCM lumen experienced a phasic cycling between low amplitude antegrade and retrograde velocities between the approximate limits of 0.80 and $-0.40\,\mathrm{cm\,s^{-1}}$ in a 'to and fro' motion. This showed that the media flow field was out of phase with the CPPW, i.e., a sloshing motion was observed, as reported in previous studies [9, 10]. During motility, each segment followed an identical motion sequentially from segments 1-10, which consisted of a relaxation stage at $0.80\,\mathrm{cm\,s^{-1}}$ to -3.20 ± 0.30 mm while the previous segment contracted, followed by a contraction stage where the haustra were inflated causing the walls to move at $0.80\,\mathrm{cm\,s^{-1}}$ via the neutral position to reach a maximum displacement of 10.40 ± 0.60 mm. The wall remained at the maximum displacement for 2 s before relaxing to the neutral position at $0.18\,\mathrm{cm\,s^{-1}}$

An extended period of antegrade motion of the contents was observed for each tag that aligned with contraction of the immediately upstream segment and relaxation of the immediately downstream segment which began simultaneously, as is clear from Figure

4.5. This was followed by a sharp burst of retrograde flow during contraction of the immediately downstream segment. This pattern was expressed most clearly by even-numbered tags and is consistent with clinical data that showed fast retrograde flows during the relaxation of the ascending colon wall after propagation of an antegrade wave (video S2, taken from [35]). This implies that the position of the tagged luminal contents along the x-axis with respect to wall activity, shown in Figure 4.5, was decisive in determining the principal direction of motion. An example of this flow behaviour is illustrated in the inset plot of Figure 4.4 and Figure 4.5, showing the velocity profile of tag 12, which lies between segments 6 and 7 (see Figure 4.2 parts (A) and (B)), during contractile activity of those adjacent segments which are delineated by the dashed lines in Figure 4.5. Part (a) encloses the antegrade velocity increase that coincides with the wall contraction of segment 6, and wall relaxation of segment 7, whilst part (b) highlights the subsequent negative velocity jet as the wall contraction of segment 7 commenced. Even-numbered tags either side of a segment, where the walls were rigid and maintained a constant lumen diameter, consistently experienced higher magnitudes of velocity and more dramatically changing velocity profiles, compared with a seemingly dampened version of this profile for odd-numbered tags located in the centre of a segment where contractile activity occurs. The highest average antegrade velocity was recorded to be $1.50 \pm 0.20\ \mathrm{cm\,s^{-1}}$ for tag 2 after contraction of the first segment. The average retrograde velocity peaked at $-1.50 \pm 0.20\ \mathrm{cm\,s^{-1}}$ for tag 11 at time $t = 34.8$ s. Given the extent of retrograde activity, it would be expected that the net aboral propulsion of suspended fluid contents would be poor when subjected to the CPPW, similar to previous observations from studies that applied faster propagating waves in low viscosity media [9, 10]. However, it is highlighted in Figure 4.4 that this motility pattern does not generate one continuous wave front in the contents that progress further along the x-axis of the DCM with each contraction, as in recent in silico studies [237]. This was expected as the CPPW was not a fully occluding event, therefore backflow was more prevalent post-contraction.

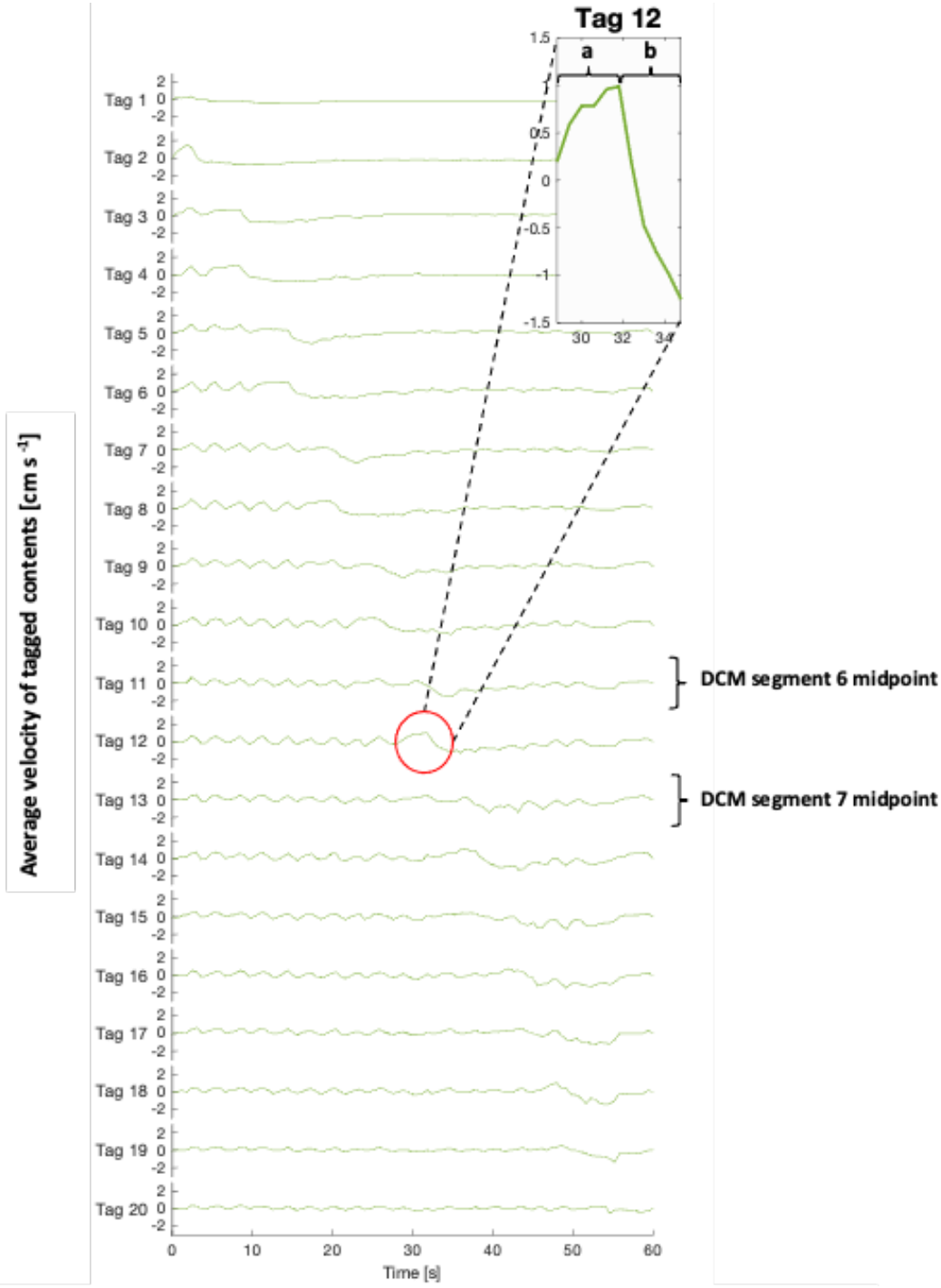

Figure 4.4: Average velocities of tagged DCM contents (200 mL LOVIS fluid) at each time point during a CPPW. Tag 1 is closest to the caecum, whilst tag 20 is closest to the hepatic flexure. The inset graph displays a magnified plot of tag 12 during (a) contraction of segment 6 and relaxation of segment 7 and (b) contraction of segment 7.

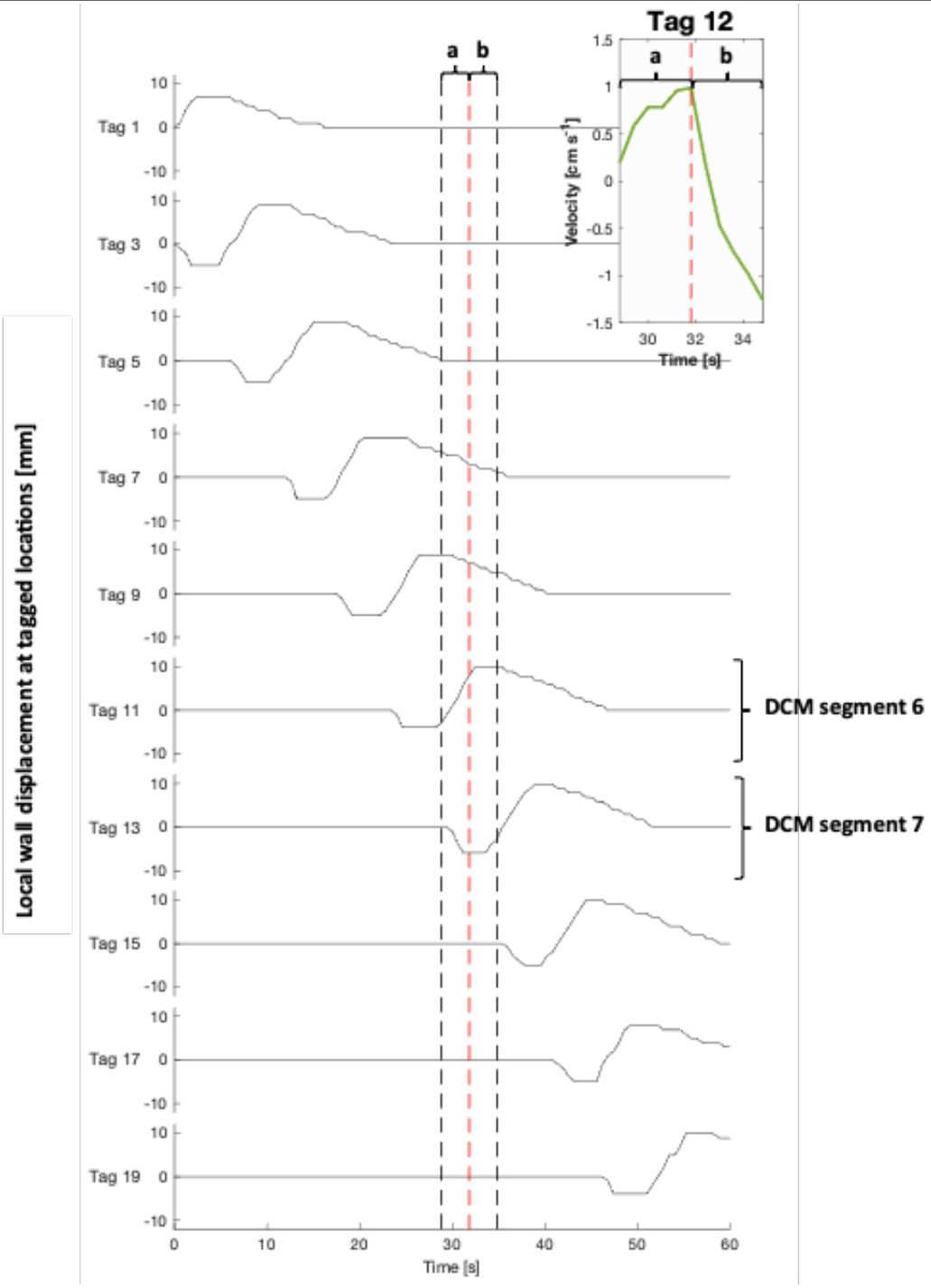

Figure 4.5: Local wall displacement at each tagged location during a CPPW. Note no local wall motion at even-numbered tags due to rigid walls, which have hence been excluded from this plot. Inset is a magnified plot of the velocity of the contents at tag 12, during (a) contraction of segment 6 and relaxation of segment 7 and (b) contraction of segment 7. The black dashed lines bound the time frame of the inset figure to aid visualisation of local wall motility surrounding tag 12 during the recorded flow event.

Identification of general flow and mixing patterns inside the lumen are valuable for the design of colon-targeted drug delivery systems. Many dosage forms that target the colon control drug release via erosion of the coating materials, which is controlled by luminal flow. The shear rates at the surface of these solid materials control the rate of erosion and hence drug release; therefore, understanding flow patterns is of high importance when designing medicines. For example, a recent simulation of drug release from a solid dosage form in the human ascending colon showed that motility patterns which provoked frequent single peaks in shear stress exerted on the surface of the dosage form, appeared to accelerate the release of the API [238]. Thus, any advances in knowledge of flows inside the DCM during the replication of motility patterns observed in healthy and diseased populations, enhances the value of this tool in the development of patient-centric formulations.

However, analysis proved challenging for the faster CPPW, as tags overlapped with one another, making it difficult to clearly distinguish the displacement of one tag from another without simplification that would greatly interfere with the data. Therefore, the tagging velocimetry methodology equipped with this particular parameter setup in this investigation was only suitable for analysis of the slower motility pattern. In the future, this could be solved through optimisation of the scanning parameters prior to the scan, based on the expected flow rates, for example, increasing the distance between the tags or decreasing the delay time between the application of the tag lines and acquisition of the image in order to capture higher velocity flows. In previous studies, MR tagging has been used to measure flows that are magnitudes stronger [282], using a single tag. Therefore, the use of a multiple tagged scan to identify regions of extreme flow due to erratic motility with pathological roots, followed by the application of a single tag to quantify the extent of the flows, could form a valuable clinical or research tool. Learnings from the in vitro model can inform in vivo studies, if the biorelevance of the motility patterns explored using the DCM is understood. Recent cine-MRI studies have shown that antegrade contractile waves in the unstimulated human AC propagate at 0.98 $\mathrm{cm\,s^{-1}}$ [10]. Since this is comparable to

the CPPW applied to the DCM in this in vitro study, the tagging technique may be well-suited to velocimetry of the colonic contents during unstimulated contractile activity in the human AC. However, when stimulated, a 2.2-fold increase in the propagation velocity was observed in the AC, with antegrade and retrograde waves propagating at 2.2 ± 3.3 $\mathrm{cm\,s^{-1}}$ and 2.2 ± 1.8 $\mathrm{cm\,s^{-1}}$, respectively. This is a faster propagation speed than the CPPWs in this study, although similar to previous motility patterns simulated using the DCM [10]. Therefore, since different flow velocities can be expected from either faster or slower motility patterns inside the DCM, and whether the AC is stimulated or unstimulated in vivo, parameters, such as tag spacing and the delay between tag application and image acquisition, should be tailored accordingly to facilitate optimum tagging velocimetry.

Figure 4.6A shows an image of the human ascending colon under baseline conditions with little to no motion, illustrated by the straight, parallel tags [35]. Figure 4.6B–D depicts a chronological selection of screenshots from Video S2, an in vivo tagged MRI sequence previously published by Pritchard *et al.* [35]. The opening sequence in video S2 begins with a contraction of the colonic walls close to the caecum, driving an antegrade wave of motion of the contents, with a residual velocity of 1.20 ± 0.20 $\mathrm{cm\,s^{-1}}$, clearly shown further along the colonic axis in Figure 4.6B. Subsequently, the walls of the colon relax, dilating the lumen and driving the contents back towards the caecum in a wave of backflow first observable closer to the midpoint in the early frames of Video S2 and in Figure 4.6C and peaking with the following sharp jet of 4.80 ± 0.20 $\mathrm{cm\,s^{-1}}$ shown in Figure 4.6D. The correlation between wall motion and flow events observed in this in vivo sequence is reproduced well in the DCM, as shown in Figure 4.2 and discussed in Section 4.3.1. This bolsters the DCM as a tool for enhanced biorelevant dissolution testing and demonstrates its suitability for the development of methods capable of achieving IVIVCs or performing IVIVE for colon-targeted formulations.

Thus, measurement of velocity of the tagged colonic contents under stimulated conditions in vivo was possible, with many tags remaining intact, permitting local velocity

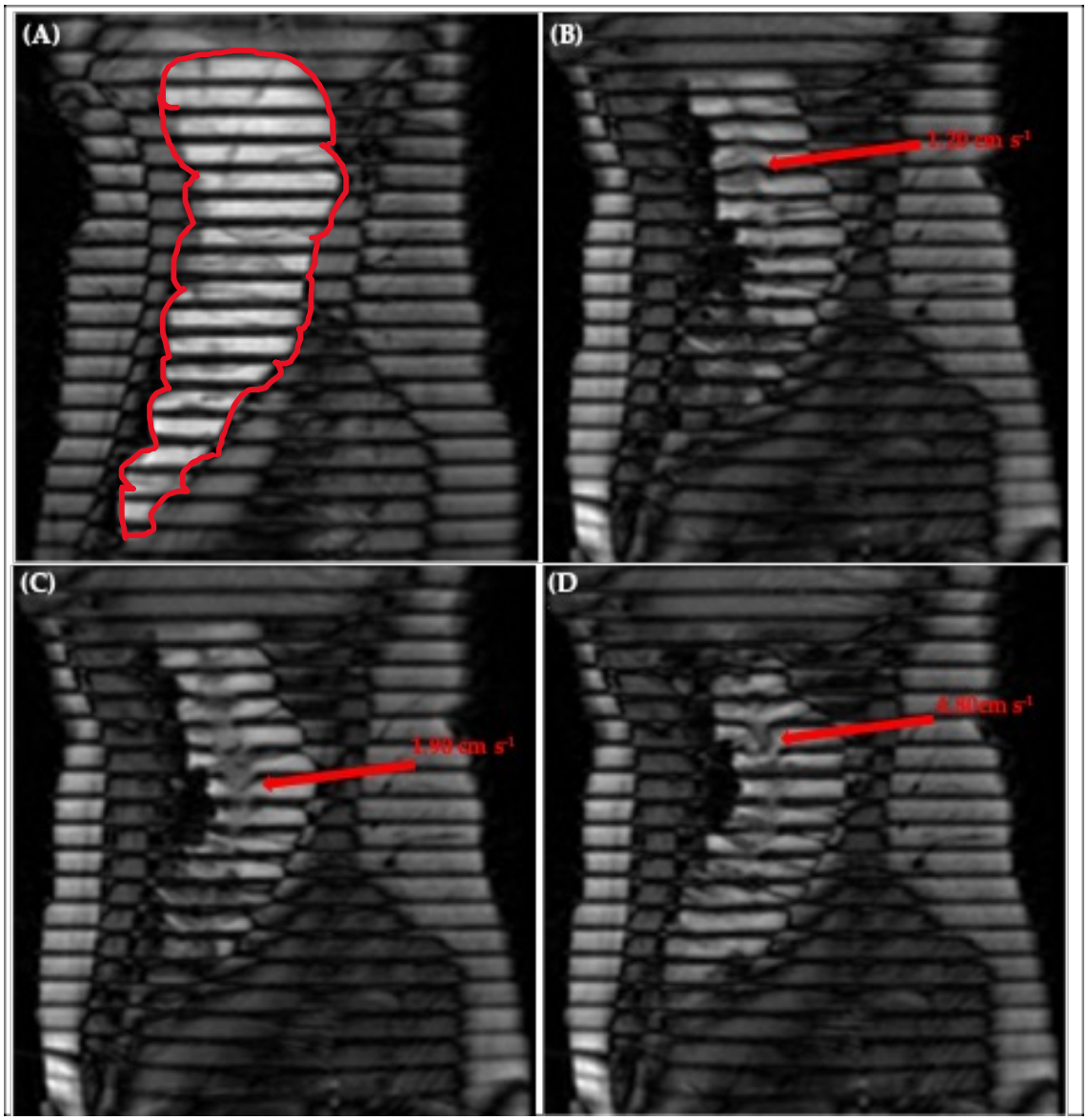

Figure 4.6: MR Tagging applied to the human ascending colon, outlined in red in (A), showing (A) little motion, (B) antegrade flow of 1.20/0.20 cm s^{-1} close to the hepatic flexure, (C) retrograde flow of 1.90/0.20 cm s^{-1} close to the midpoint of the AC and (D) retrograde 'jet' of 4.80 $\pm$ 0.20 cm s^{-1} close to the hepatic flexure. Images taken from supplementary video S2 of Pritchard *et al.* [35].

measurement at different spatiotemporal locations along the colonic axis. This facilitated the evaluation of regional and temporal similarities and differences. For example, both antegrade (1.20 ± 0.20 cm s^{-1}) and retrograde (4.80 ± 0.20 cm s^{-1}) flows were measured close to the caecum, whilst close to the midpoint of the human AC, retrograde flows of 1.90 ± 0.20 cm s^{-1} were recorded. Similar antegrade and retrograde activity has been reported in vivo by [170]. In conjunction with visualisation of how the walls moved in real time, this methodology therefore has the potential to further inform an understanding of colonic pathophysiology. A clear application would be to establish quantitative limits that identify regions suffering from dysmotility based on the magnitude of the velocity of the contents compared to values observed in the healthy AC. A key advantage of the tagged MRI technique is the coverage acquired—the ability to both visualise and measure flows across the entire AC in one scan.

Complex multidirectional flows were observed under stimulated in vivo conditions, manifesting as smearing of the tag lines, and simultaneous antegrade and retrograde flow of media at different points along the same tag, as shown in Figure 4.6C & D. These phenomena were not observed in the DCM, where tagged media typically flowed in a laminar antegrade or retrograde fashion. The DCM motility was programmed to replicate CPPWs in the healthy human colon, as opposed to the extreme stimulated conditions observed in the in vivo study of [35]. This involved a cyclic repetition of one antegrade CPPW in which all haustra in a segment contracted or relaxed in a specific, predefined order and with a fixed degree and rate of occlusion. In vivo, motility is governed by the enteric nervous system which results in a more complex motion than the controlled wall motility of the DCM. However, the in vivo motility observed by Pritchard *et al.* [35] included both antegrade and retrograde waves, with haustra contracting and relaxing asynchronously and with different degrees of occlusion, which due to the momentum of the contents, caused more complex multidirectional flows. Similar activity has been observed in vivo by Wilkinson-Smith *et al.* [251], where contractions in the AC wall were not continuous, but sporadic. Multidirectional motility patterns could be replicated in future work with the DCM to

more precisely mimic specific in vivo patterns for direct comparison. Furthermore, there are many other factors associated with administration of the stimulus that may affect the motility in vivo. For example, the rate of delivery of macrogol to the AC, the mixing of the macrogol with the contents of the colon upon arrival and the absorption rate of any fluid from the macrogol [251]. These factors, in addition to characteristics of the patient such as age [288], influence the volume of the contents of the AC, which is likely to trigger distension of the walls in vivo, hence driving the erratic motility. In vitro, the DCM was only partially filled (150–200 mL, 52–69 %), compared to the AC which was full of contents after the macrogol stimulus.

The complex flows caused blurring of the tag lines which can break in places, rendering the tagging method of flow quantification invalid. Ultimately, tagged MRI failed to accurately measure velocities at all tagged locations in extreme conditions in vivo, but was still able to measure velocities at individual tagged locations where the tags remained intact. However, it must be appreciated that these extreme conditions are among the least abundant motility types observed naturally in vivo, simply meaning that this technique forfeits its applicability to measure intracolonic flows under extreme conditions generated by stimulation or that may occur naturally in patients presenting with certain disease states, such as diarrhoea [170]. Nevertheless, this field is currently in its infancy and therefore revealing the upper limits of this technique is additional added value resulting from this work.

Due to the apparent randomness of the starting point for a propagating contraction in vivo, visible in the in vivo sequence (Supplementary Materials Video S2) and high-resolution manometry studies [170], it is important that preliminary scans apply multiple tags across the colonic axis, as in this study. However, as previously mentioned, the application of a single tag is useful when high flow velocities are expected. Therefore, single tag velocimetry analysis of areas already identified as having extreme motility from a prior multi-tag scan, could add value in a clinical or research setting by quantifying the degree

of extreme flow in patients presenting with a motility-related pathology.

4.4.3 PC Cine-MRI Velocimetry of the DCM Lumen Contents

Figure 4.7 presents a selection of morphological images with the associated spatially registered through-plane velocity maps superimposed over the lumen media, acquired using PC cine-MRI at the midpoint of segment 7, the cross section at Tag 11, and at different temporal locations. As highlighted in a recent review of in vitro models of the GI tract, the DCM is currently the only in vitro model to replicate peristaltic motility in a lumen with the segmented architecture of the human colon [12]. Therefore, understanding the streamwise velocity profile through a segment of the DCM at different stages of biorelevant motility adds insights to how intestinal wall motion influences the hydrodynamics that drive dissolution and mixing. The box drawn at the centre of Figure 4.7A outlines the area represented by the central flow region of the lumen. The idea of combining tagging and PC cine-MRI, for the acquisition of in-plane and through-plane motion information, has been explored previously byPerman *et al.* [289] and Kuijer *et al.* [290].

To account for the background signal, initial velocity measurements were taken using PC cine-MRI prior to any induced motility (neutral wall position) when it was known the luminal contents were at rest. The mean velocity over the cross-sectional lumen flow area was close to zero at 4.32×10^{-4} cm s^{-1} with a standard deviation of 6.40×10^{-3} cm s^{-1}. This standard deviation value was taken as the measurement error for a single voxel and hence the error for PC cine-MRI peak velocity measurements, and is three orders of magnitude smaller than the expected maximum signal (± 3 cm s^{-1}).

Overall, the morphological information and associated velocity maps acquired using PC cine-MRI accurately explained the flow phenomena in the tagged contents described in Figure 4.4. Figure 4.7A shows the cross section at tag 11 at $t = 8.0$ s. The DCM walls were at the neutral position and a low antegrade flow was focused around the centre of the lumen toward the free surface, in keeping with the positive peak in cyclic antegrade–retrograde flow recorded by the tagged dataset in Figure 4.4 at $t = 8.0$ s. Due

to the neutral position of the DCM walls, it can be confirmed that this flow was caused by the upstream wall displacement shown in Figure 4.5. There are clearly stagnant regions close to the walls. This suggests that any dosage form agglomerates that lie in the stagnant corners may not experience high peaks in shear forces arising from the flow; however, the proximity to the walls is likely to result in elevated normal forces exerted on the dosage form during contraction, which may accelerate break up and drug release. This kind of squeezing force is absent in typical pharmacopeial dissolution apparatuses, but is relevant for colon-targeted dosage forms due to the architecture of the colon and its wall movements.

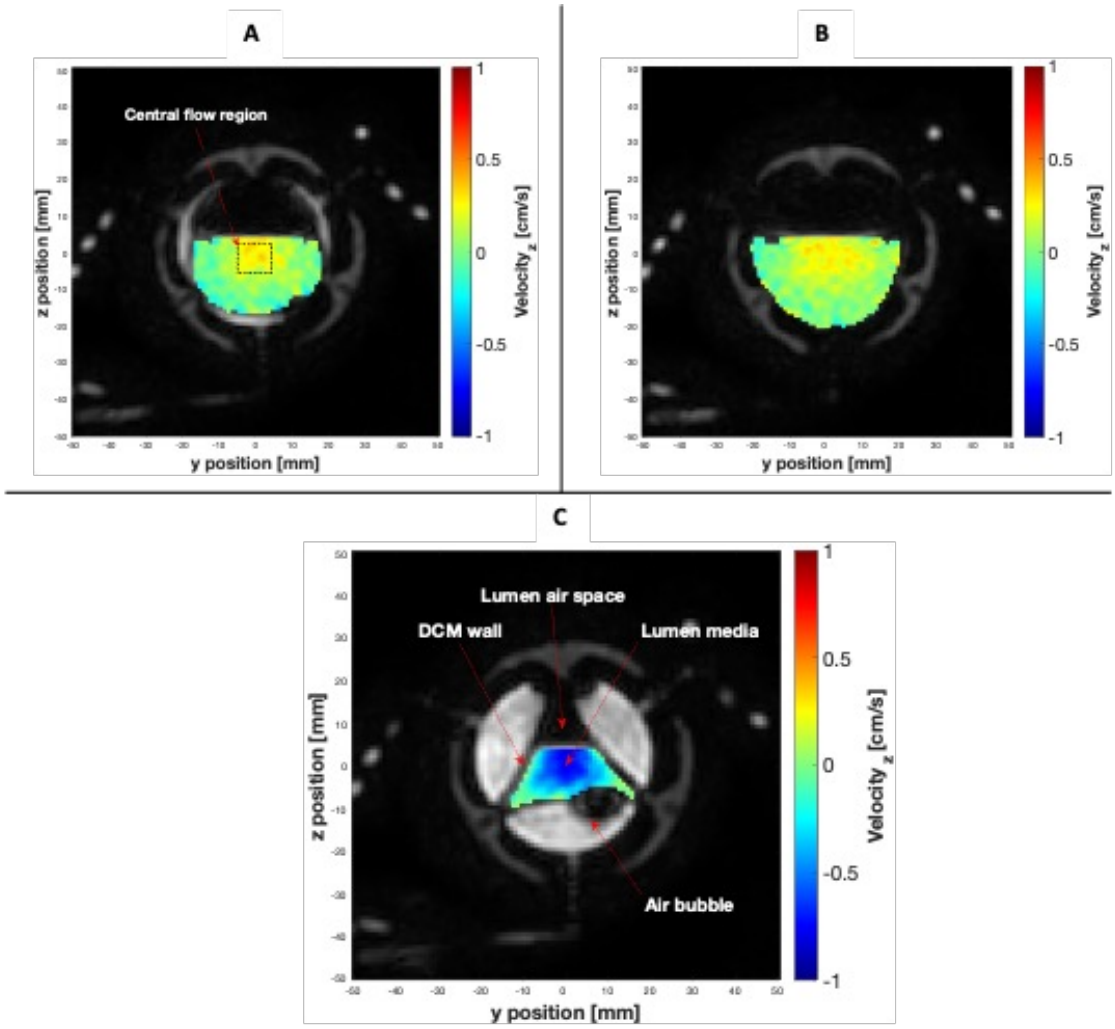

Figure 4.7: PC cine-MRI of the DCM, (velocity encoded in the x-axis). Simultaneous acquisition of morphological data and spatially registered flow at the cross section of tag 11, placed at the midpoint of segment 6. Parts A-C were produced by superimposing the two data sets at different stages of motility: neutral, during upstream motility (4.7A), relaxation (4.7B) and contraction (4.7C).

Figure 4.7B shows the cross section of tag 11 at $t = 28$ s, depicting the walls in a fully relaxed state, maximising the cross-sectional area of the lumen. This is in line with the beginning of an antegrade flow episode observed in the tagged dataset (Figure 4.4A). Flow was in the positive x-direction, driven by the immediately upstream DCM contraction, in keeping with the antegrade flow event recorded in the tagged contents. Again, the flow was concentrated in the centre of the lumen close to the free surface. During the relaxation of the walls immediately before the image in Figure 4.7B, the "pouring mode" described by Alexiadis *et al.* [236] may occur where significant flows in the z-direction take place; this is not shown, as velocity was encoded only in the x-direction. The tagged dataset in Figure 4 shows a strong peak in negative velocity at $t = 35.4$ s, aligning with the cross section captured in Figure 7C which shows the walls fully contracted at $t = 36.0$ s, occluding the lumen and forcing the contents backwards. An established velocity profile is evident, with the highest retrograde velocities in the centre of the lumen and steepest velocity gradients towards the walls.

The combination of antegrade flow and the "pouring mode" during relaxation of the walls, followed by occlusion of the lumen and strong backflow may subject dosage form agglomerates and the released API to stresses and mixing phenomena unique to the intestinal lumen. This is likely to result in tablet–liquid mass transfer coefficients that are highly dependent on the tablet location with respect to contractions of the mimic colonic walls and also on the frequency of contractions. Since the motility and architecture of the DCM are based on human anatomical data, this is probably a much closer representation of the in vivo situation than in typical pharmacopeial systems. For example, the USP2 and USP mini vessels, which typically operate under continuously mixed conditions using a paddle, form two flow loops above and below the paddle, with the tablet sitting in a relatively stagnant zone beneath the paddle [253, 277, 291]. The parabolic flow profile during pulsatile flow in the flow through cell (FTC), another internationally recognised pharmacopeial dissolution apparatus used to assess modified-and extended-release dosage forms [292], bares some semblance to flow in the partially filled DCM. However, the two are

not comparable due to the many dissimilarities including (but not limited to) phenomena common in partially filled pipes, such as the velocity drop phenomenon [293], vessel architecture, multidirectional flows due to the nature of peristaltic waves, and a dissimilar (higher) pulse rate in the FTC compared to a physiologically-relevant rate of peristaltic contractions in the DCM [10, 170].

Figure 4.8 presents a direct comparison of velocity data collected using both the PC cine-MRI technique and the tagging technique using 200 mL LOVIS fluid subjected to the 0.4 $\mathrm{cm\,s^{-1}}$ CPPW at the location of tags 3, 11 and 19. Additionally, wall motility was quantified by displacement from its neutral datum as shown by the black dashed line, measured by tracking the wall membrane in the magnitude component of PC cine-MRI images. This permitted tracking of the fluid velocity with respect to the wall motion and thus the consequences of the wall motility on the motion of the contents, to be evaluated directly. Comparison of the adjacent plots in Figure 4.8 facilitates visualisation of how the contents moved as the contractile wave propagated along the x-axis of the DCM tube.

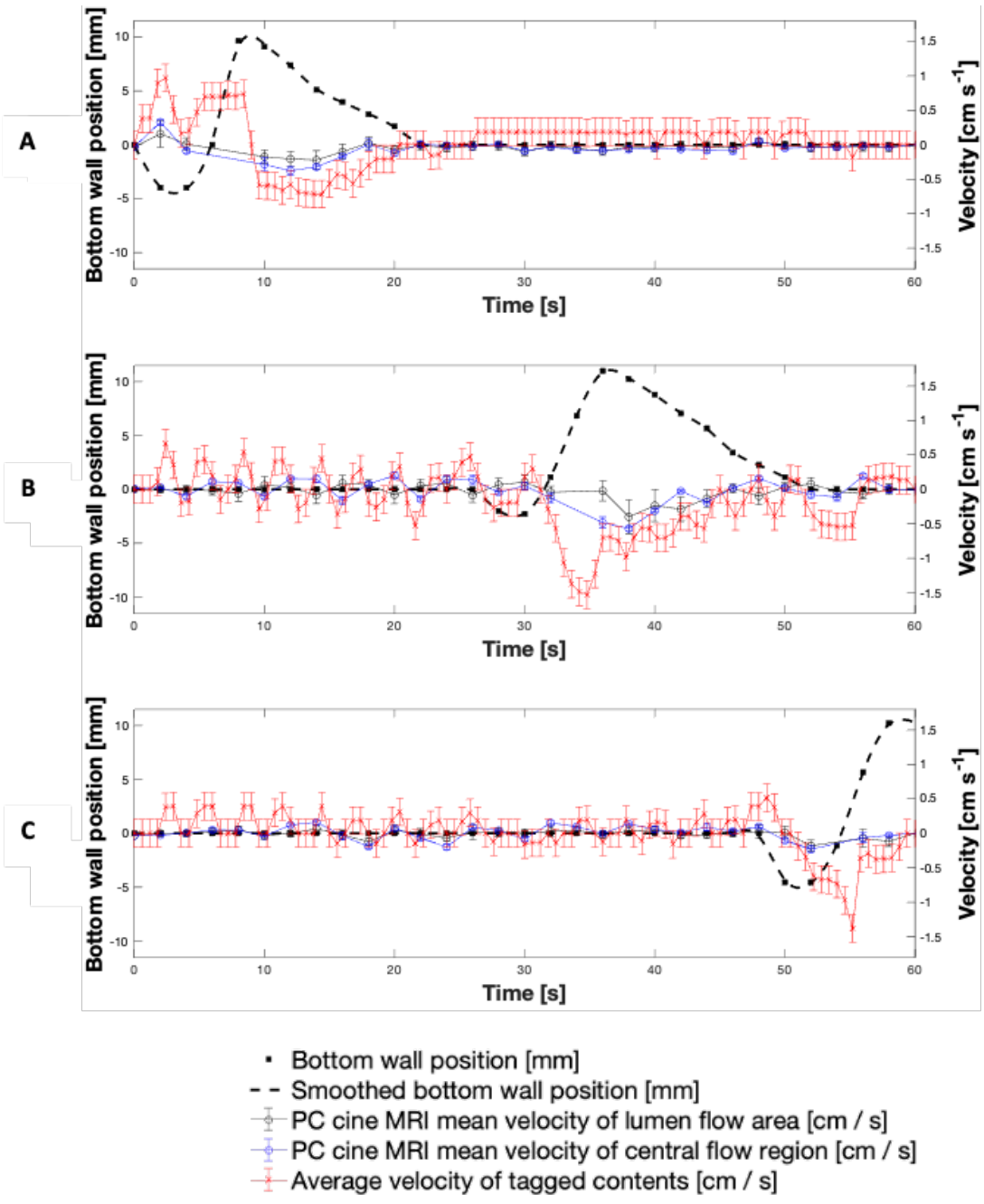

Figure 4.8: Average velocities measured using tagged and PC cine-MRI at the location of tags 3 (A), 12 (B) and 19 (C), alongside wall displacement at the corresponding location (dashed line).

Since the measurements were taken on different scans, the wall waves and therefore fluid flows were marginally out of phase, but overall, the average velocity-time profiles measured using the tagged methodology and the mean PC cine-MRI measurements were similar. Velocities measured using tagging were consistently higher in magnitude than the mean PC cine-MRI measurements; however, PC cine-MRI mean velocity measurements using the central flow region closely aligned with the tagged methodology. This shows that the average velocity of tagged contents more closely represented flow of the central plug of media enclosed by the region outlined in Figure 4.7A, rather than representing flow across the entire cross section at the tagged location. This, alongside the consistently higher velocity measurements, was likely to be due to the difference in the 2-dimensional plane in which measurements were taken and the discrete values that the tagging velocities were restricted within. PC cine-MRI measures flow through a cross section perpendicular to the flow, and therefore consideration of the entire luminal cross section involves a greater voxel coverage of stagnant regions towards the walls of the lumen where lower flows are abundant. Voxels containing these low flows were less significantly represented in the displacement of the centroid of a tag, compared to in PC MRI mean velocity estimation. This is because tag displacement is analysed in the 2D longitudinal axis, where voxels containing more extreme non-transversely uniform flows have an equal weight to a voxel containing a region that is stagnant through a larger proportion of the transverse plane. Therefore, the nature of the tagging technique affords it a higher intrinsic sensitivity to flows along the x-axis of the DCM. A deeper analysis of tagging versus PC cine-MRI measurements is presented in Appendix One A.1, whilst A.2 explains the absence of PC cine-MRI data points. The highest antegrade average flows were observed at the location of Tag 3 (shown in Figure 4.8A), close to the start of the CPPW, recorded as 0.90 ± 0.20 cm s^{-1} at t = 1.8 s using tagging, compared to 0.16 ± 0.19 cm s^{-1} and 0.33 ± 0.04 cm s^{-1} using PC cine-MRI measurements of the entire lumen and the central flow region, respectively at t = 2 s. After the local wall segment returned to the neutral position, all velocities remained approximately stable between the limits of -0.20 cm s^{-1} and 0.20 cm s^{-1}.

At the location of tags 11 and 19, fluctuation in the velocity prior to local wall motility consistently measured between approximately -0.50 to 0.50 ± 0.08 cm s^{-1} and -0.20 to 0.40 ± 0.08 cm s^{-1}, respectively. Average retrograde velocities consistently peaked immediately before or during local wall motility, with the fastest average retrograde velocity of -1.53 ± 0.20 cm s^{-1} at the location of tag 11 (shown in Figure 4.8B) at $t = 34.8$ s, compared to -0.40 ± 0.24 cm s^{-1} and -0.57 ± 0.02 cm s^{-1} at $t = 36.0$ s for PC cine-MRI analysis of the whole lumen flow area and central flow region, respectively. This finding is in line with CFD modelling of the colon by Sinnott *et al.* [233], which found that higher speed retrograde flow is visible local to the contracting region and extends further upstream than the contraction. Overall, velocities in the DCM during the 0.4 cm s^{-1} CPPW were much lower than in the pharmacopeial USPII and mini vessel, where they were 50-100 rpm and 50-200 rpm, respectively, and tangential velocities have been reported to reach 15 cm s^{-1} [253, 291]. On the other hand, the maximum velocities observed in the FTC are far lower than in the DCM, not breaching 0.4 cm s^{-1} even at the highest flow rate typically used in pharmacopeial dissolution testing (16 mL min^{-1}) [292].

Figure 4.9 shows the peak velocities recorded using each MRI technique under the same experimental conditions as for Figure 4.7. Typically, the peak velocities followed the same trend as the average velocity measurements and there was good agreement between tagging and central flow region PC cine-MRI peak velocity measurements. However, tagging consistently registered higher velocity measurements where highly localised regions of fast-moving media (typically around $z = 0$) caused sharp displacement of a tag. Voxel intensity is proportional to the volume of media displaced which varies along the z-axis, as shown by the velocity profiles in Figure 4.7. The highest antegrade velocity recorded was 1.60 ± 0.20 cm s^{-1} in tagged data and 0.76 ± 0.20 cm s^{-1} in PC cine-MRI; both faster than the speed of the propagating wave, 0.4 cm s^{-1}. Previously in positron emission particle tracking (PEPT) studies, Stamatopoulos *et al.* [10] recorded maximum antegrade velocities (2.20 cm s^{-1}) using a faster propagating wave (2 cm s^{-1}). Previous in vivo analyses of colonic motility using a magnetic pill revealed a broad spectrum of velocities [294,

295]. However, interpreting motion of the colonic contents from the observed motion of a tracer particle must be done carefully since the particle relaxation time can inhibit its ability to follow the fluid. This makes direct comparisons between datasets, either in vivo or in vitro, difficult [10]. Noninvasive methods such as MRI have a significant advantage in this regard.

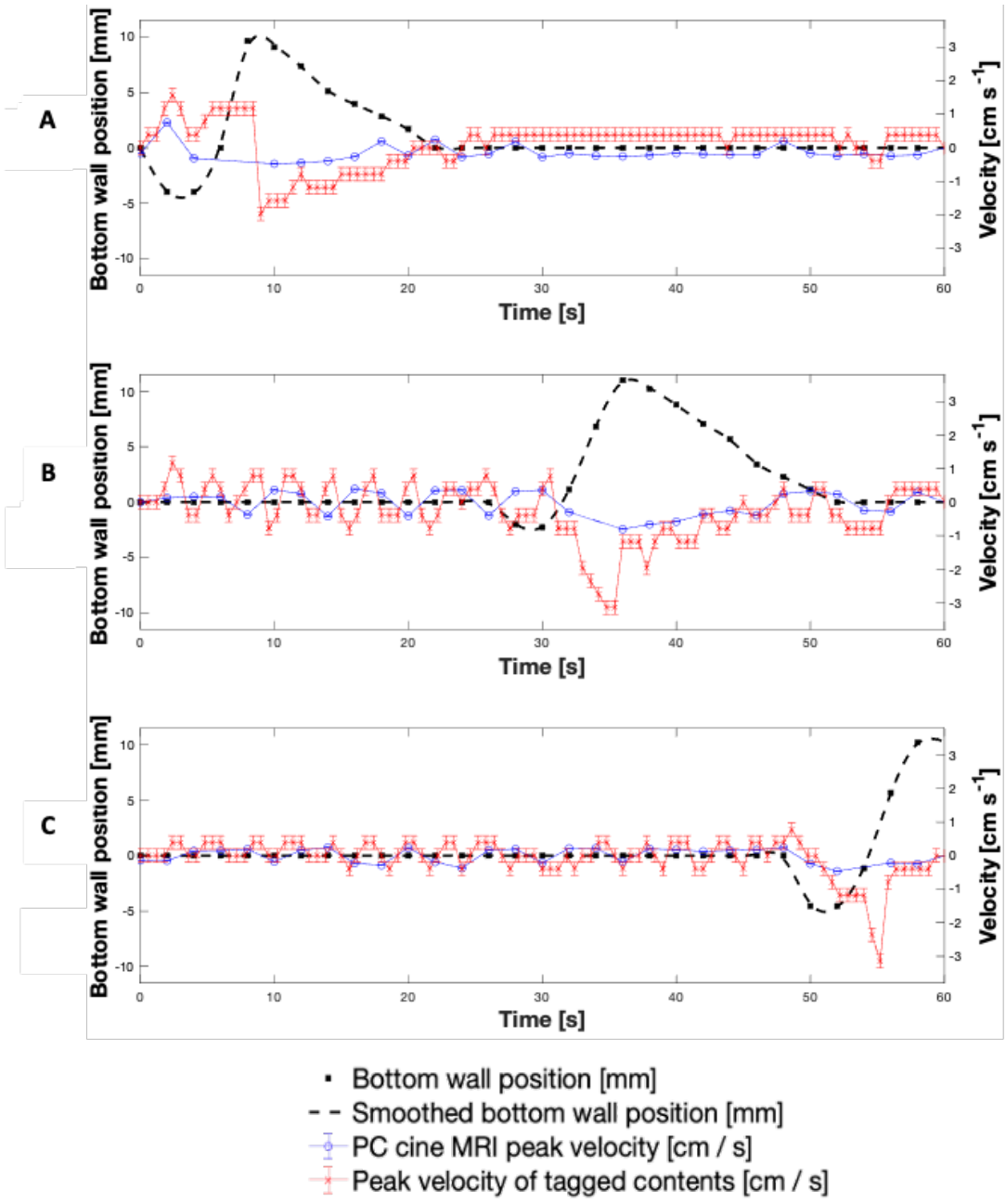

Figure 4.9: Peak velocities recorded using tagged and PC cine-MRI at the location of tags 3 (A), 12 (B) and 19 (C), alongside wall displacement at the corresponding location (dashed line).

Retrograde velocities inside the DCM have previously been reported to reach 4 $cm\,s^{-1}$ using 0.25 (w/v) NaCMC in previous PEPT studies [10]. The highest retrograde velocity observed in the DCM in this study was similar; -3.10 ± 0.20 $cm\,s^{-1}$ at $t = 55.8$ s during local contraction at tag 19 toward the later stage of the CPPW. This was likely to be influenced by gravitational forces as media rises up the hepatic flexure but does not cross it, causing it to fall back into the lumen with a strong backflow. This measurement is in line with the in vivo observation in Figure 4.6D, wherein the highest measured retrograde velocity (4.80 $cm\,s^{-1}$) occurred close to the hepatic flexure during relaxation of the colonic walls after a propagating contractile wave. Similarly, this could be due to a combination of the influences from relaxation of the walls and gravitational forces. The highest average retrograde velocity, -1.50 ± 0.20 $cm\,s^{-1}$, was observed at the position of tag 11 just past the midpoint of the DCM. Comparatively strong retrograde velocities in segment 2 and low antegrade velocities help to explain why Stamatopoulos *et al.* [9] observed theophylline extended-release dosage forms remaining closer to the caecum throughout dissolution experiments, with the highest drug release rates measured close to the caecum compared with downstream sampling points. These findings show ineffective aboral transport at early stages of the CPPW close to where a solid oral dosage form would enter the colon through the ileocaecal valve, consistent with previous findings which demonstrated poor overall propulsion of contents using low viscosity media [277]. The findings in this work strengthen conclusions made by previous studies [35, 251], that combining this technique with existing motility and volume measurements could improve classification between healthy subjects, and subjects whose colonic motility is absent or ineffective at mixing and transporting the contents. This has the potential to facilitate stratification of the functional type from irritable bowel syndrome (IBS) type disorders and contribute to the development of an understanding of local intracolonic environmental conditions, which are essential to optimise the delivery of therapeutics for patient-centred formulation design. However further investigation in such patient groups is needed to explore this possibility.

4.5 Conclusions

This work demonstrates that a noninvasive MR tagging method developed to assess human colonic motility and distinguish between colonic disease states, can differentiate between motility patterns and media viscosities in a biorelevant in vitro model of the human ascending colon. This adds value to the MR tagging technique in its ability to understand colonic pathophysiology, the effectiveness of treatments and the conditions that a colon-targeted dosage form may experience in vivo.

The same tagged dataset was used to directly measure the velocity of the luminal contents inside the in vitro model and a tagged sequence of the ascending colon in vivo, with simultaneous knowledge of how the walls move. It was demonstrated that the dynamic colon model (DCM) can induce flow that replicates the flow patterns observed in vivo, of a similar velocity magnitude. To reproduce the hydrodynamics of the human ascending colon is an essential capability for a biorelevant mechanical dissolution apparatus to be suitable for the development of methods facilitating IVIVE or IVIVC.

PC cine-MRI revealed the streamwise flow profiles observed inside the DCM lumen, which represents the segmented architecture of the ascending colon, at different stages of a biorelevant peristaltic wave. Flow profiles resembled flows in a partially filled pipe, but differed greatly to those observed in compendial dissolution apparatuses, such as USP2 and the flow through cell (USP4). Nevertheless, this visualisation elucidates the environment that a dosage form may be subjected to inside the DCM during dissolution studies which is vital in understanding how the motion of the mimic colon walls drive the hydrodynamic conditions that govern the erosion of a dosage form and the release and dissolution of the API. Additional insights into colonic flow gained through the model could be useful to inform in silico modelling of colonic drug release and dissolution.

Chapter Five

Simulating the Hydrodynamic Conditions of the Human Ascending Colon: A Digital Twin of the Dynamic Colon Model

This chapter was published in Pharmaceutics 14(1): 'Simulating the Hydrodynamic Conditions of the Human Ascending Colon: A Digital Twin of the Dynamic Colon Model' [15, 16]. This was a joint work with equal contribution from O'Farrell, C and Schutt, M., as indicated in the author list of the publication.

Please note: The methodology describing the development of the computer simulation was conducted by Schutt, M. The full contributions statement is given below.

Conceptualization, C.O. and M.S.; methodology (experimental), C.O., K.S., C.L.H., L.M. and S.S.; methodology (computation), M.S. and A.A.; formal analysis (experimental), C.O. and C.L.H.; formal analysis (computational), M.S.; data curation, C.O. and M.S.; writing—original draft preparation, M.S. and C.O.; writing—review and editing, C.O., M.S., K.S., L.M., C.L.H., S.S., M.J.H.S., H.K.B. and A.A.; visualization, M.S. and

C.O.; supervision, K.S., H.K.B., M.J.H.S. and A.A. All authors have read and agreed to the published version of the manuscript and contributions statement.

5.1 Abstract

The performance of solid oral dosage forms targeting the colon is typically evaluated using standardised pharmacopeial dissolution apparatuses. However, these fail to replicate colonic hydrodynamics. This study develops a digital twin of the Dynamic Colon Model; a physiologically representative in vitro model of the human proximal colon. Magnetic resonance imaging of the Dynamic Colon Model verified that the digital twin robustly replicated flow patterns under different physiological conditions (media viscosity, volume, and peristaltic wave speed). During local contractile activity, antegrade flows of 0.06 - 0.78 cm s^{-1} and backflows of -2.16 - -0.21 cm s^{-1} were measured. Mean wall shear rates were strongly time and viscosity dependent although peaks were measured between 3.05 - 10.12 s^{-1} and 5.11 - 20.34 s^{-1} in the Dynamic Colon Model and its digital twin respectively, comparable to previous estimates of the USPII with paddle speeds of 25 and 50 rpm. It is recommended that viscosity and shear rates are considered when designing future dissolution test methodologies for colon-targeted formulations. In the USPII, paddle speeds >50 rpm may not recreate physiologically relevant shear rates. These findings demonstrate how the combination of biorelevant in vitro and in silico models can provide new insights for dissolution testing beyond established pharmacopeial methods.

5.2 Introduction

In recent years, colon-targeted drug delivery has received increased attention due to regional conditions that present advantages for the delivery of certain types of pharmaceutical formulation compared to the small intestine [296, 297]. The hydrodynamics of the proximal colon are crucial for the design and optimisation of colon-targeted formulations, particularly in terms of disintegration, dissolution, and distribution of the dosage form. To gain a better understanding of the hydrodynamics and mixing conditions in the intestinal environment, in vitro, as well as in silico, studies have been carried out, focusing on both the colon [9, 10, 236–238] and the small intestine [233, 298]. In vitro dissolution apparatuses have historically been used for biopredictive testing. Although pharmacopeial dissolution apparatuses permit the control of media properties, the vessels bear little semblance to colonic geometry and use simplified mixing methods that fail to reproduce the hydrodynamic conditions of the human colon in vivo [277, 291]. The Dynamic Colon Model (DCM), depicted in Figure 5.1, is a biorelevant in vitro model that replicates the architecture of the proximal colon and reproduces peristaltic/segmental activity [9, 10].

The design of the DCM was based on clinical data obtained from MRI images of the human (adult) proximal colon in vivo. The DCM is able to mimic the motor patterns of the colon, which mostly occur as propagating pressure waves (PPWs): one of the identified motor patterns in the colon [170]. The DCM is the most physiologically relevant in vitro colon model to date as it is the only model that replicates peristaltic motility in a lumen with the segmented architecture of the human colon [12]. A recent study has shown that when a PPW is applied to the DCM, the motion of the walls causes the contents of the lumen to flow in a way that closely reproduces the flow in the human proximal colon [14], verifying the hydrodynamics of the model. In Vitro and in silico models that are based on in vivo data offer affordable alternatives to in vivo studies. Furthermore, in vivo studies are conducted, where possible, using healthy volunteers, and this population does not represent the extremes of GI variability which are of interest in the design of a dosage form.

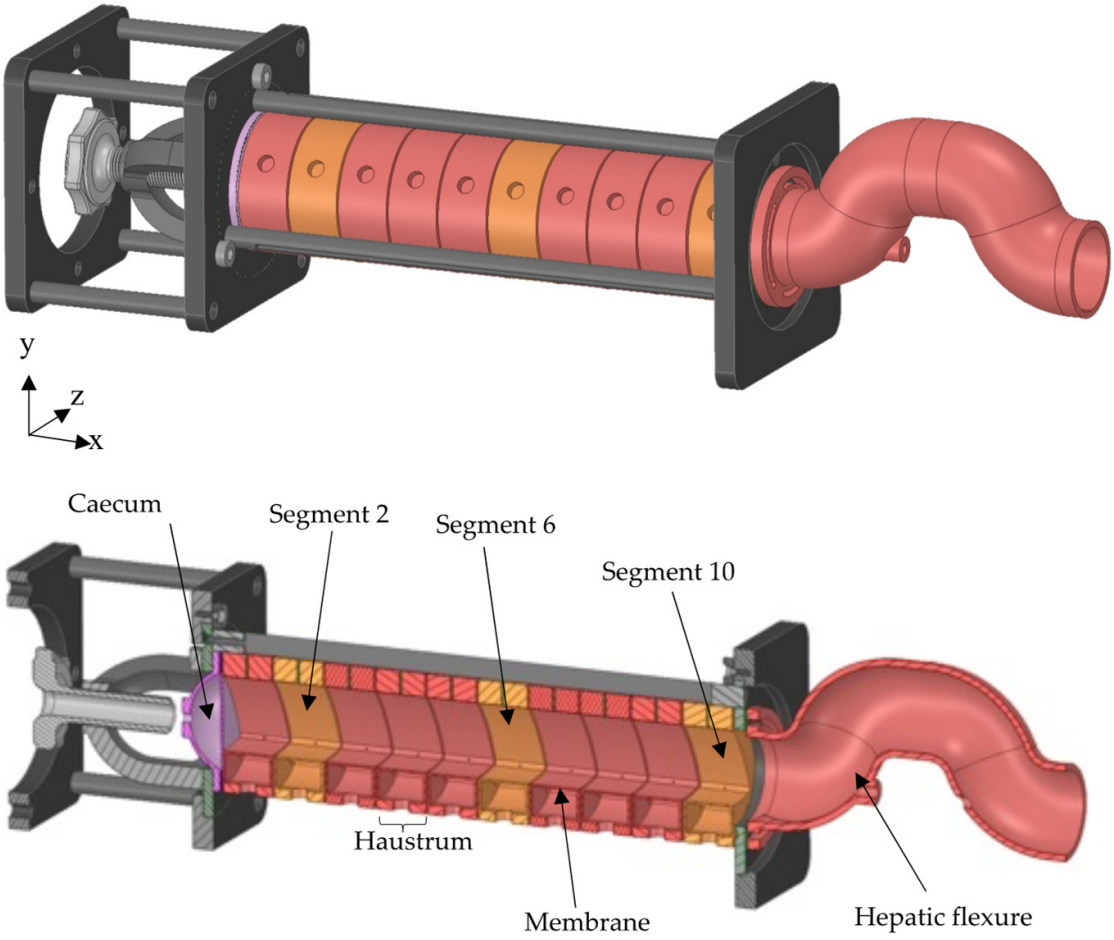

Figure 5.1: Schematic of the Dynamic Colon Model (DCM), Adapted from [14], MDPI, 2021. The DCM has a segmented appearance reflecting that of the human proximal colon: segment 1 is adjacent to the caecum, through to segment 10 adjacent to the hepatic flexure.

The DCM can reproducibly replicate extreme GI motion. More advanced in vitro models that are physiologically representative offer the possibility of a deeper insight into in vivo conditions and therefore better understanding of the physical laws governing colonic space. This is especially important for pharmaceutical research and the development of new formulations of modified release solid oral dosage forms that reach the colon, as these data are necessary to predict release behaviour in the colonic environment. Over the last few years, several in silico models of the human proximal colon have been developed [236, 237] based on a computational technique called Discrete Multiphysics (DMP) [299, 300]. Recently, this approach has been applied to the pharmaceutical field and used to model drug release from a solid dosage form under the influence of different in vivo motility patterns [238]. The major advantage of in silico models is that they are resource-saving compared to in vitro models and especially to in vivo experiments. Additionally, in silico models are highly versatile and provide additional insights that are difficult to acquire using common measurement techniques, often at resolutions that are equally unattainable. However, in vitro models are essential to make sure all relevant variables occurring in the real environment are accounted for, and to generate sufficient data to inform the development and the validation of their digital counterpart. Therefore, the quality and quantity of the data describing the colonic environment will always depend on the power of in vitro and in silico models. Together, myriad runs can be conducted, generating a high data output at low cost. This data is crucial for the pharmaceutical industry to create effective therapeutic delivery vehicles. This study describes the development and validation of a digital twin (DT) of the DCM (DCMDT) using a particle modelling approach. The DCMDT is depicted in Figure 5.2.

The DCMDT is a digital informational construct of the physical DCM that exists in virtual space. It replicates the design and motility of the DCM and is similarly compatible with a range of fluids, which is achieved by modifying the physical properties of the computational fluid particles. Further details on the modelling methodology are given in Section 5.2.2. The environmental conditions inside the lumen of the proximal colon are

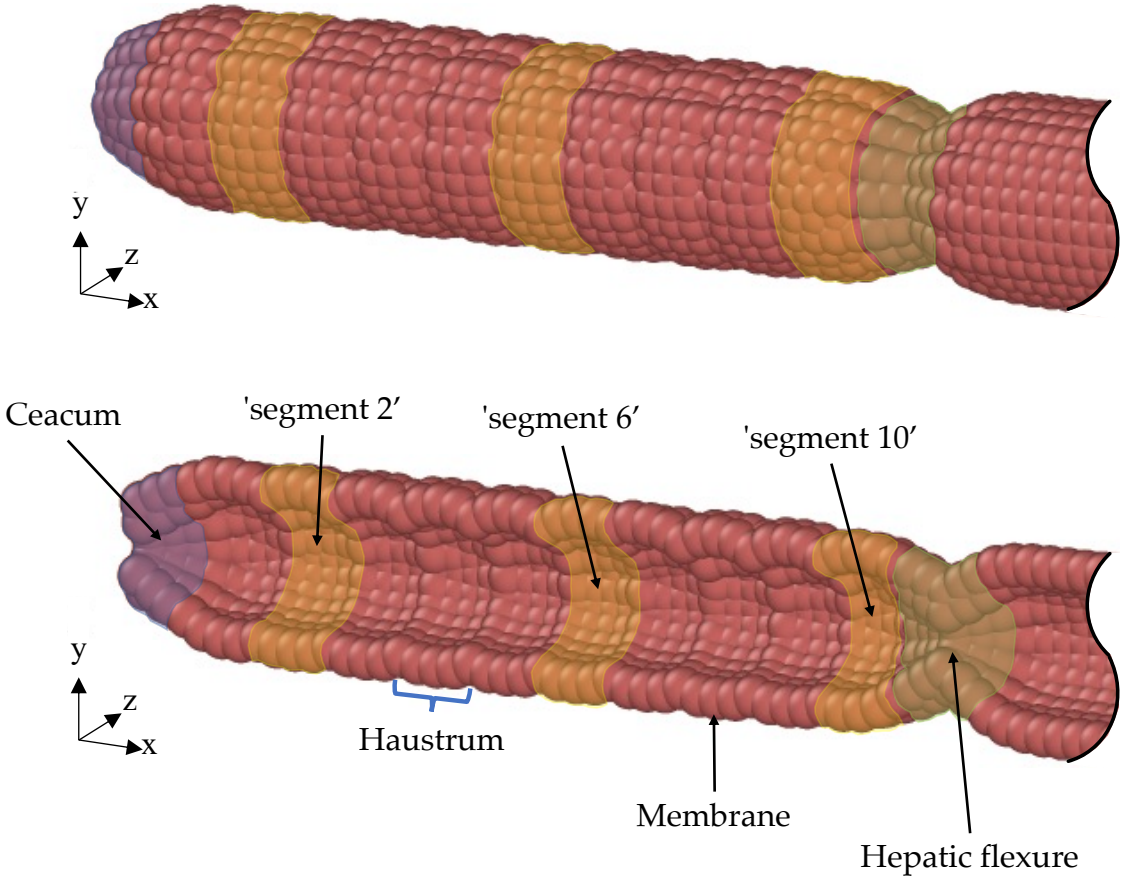

Figure 5.2: Schematic view (top) and a cross-sectional view (bottom) of the computational model (DCMDT). The DCMDT comprises 10 sections reflecting the DCM. Segment 1 is adjacent to the caecum and segment 10 is adjacent to the hepatic flexure. The hepatic flexure is modelled as a reduction to create a backpressure, guided by the in vivo situation.

controlled by a range of factors, including but not limited to disease state, microbiota, prandial state, ingested food contents, and importantly, the inherent interindividual variation [278]. The dynamic interplay of these influences can affect a wide range of parameters, which can ultimately be manipulated in the in vitro or/and in silico models. For example, media volume can change with prandial state and could affect the sink conditions of a formulation, resulting in accelerated or hampered release of the active pharmaceutical ingredient (API) which can influence bioavailability [298] [296]. Functional gastrointestinal disorders may affect the motility of the colonic walls; dampened motility may cause lower shear rates to be exerted on the surface of the dosage form, leading to incomplete release of the API. Contents of solid or liquid food ingested may affect the viscosity of the contents of the proximal colonic lumen [278]. A more viscous fluid demonstrates greater resistance to flow and may cause a different velocity profile in the lumen, affecting the transport and shear forces acting on a dosage form [9, 10]. The DCM and its DT permit the manipulation of these parameters individually, under fixed conditions, to scrutinise the effects. Thus, this study investigates how the interplay of media viscosity, media volume, and wall motility influence flows inside the DCM (Figure 5.1) and the DCMDT (Figure 5.2). This will facilitate assessment of the ability of the DCMDT to replicate the wall motion and the relationship this has with the flow of the contents. Flow analysis will cover the velocity and shear rate distributions at different locations along the models. Shear rates within the fluid determine the shear stresses exerted by the fluid on the surface of a dosage form in the colonic lumen, which governs the erosion of solid oral dosage forms inside the colon [238]. The ability of the DCMDT to extract shear rate data under a multitude of conditions with relative ease could establish it as a highly valuable tool to inform the design of formulations that are sensitive or insensitive to motion.

5.3 Methodology

5.3.1 Experimental work

Experimentally, a simulated antegrade PPW travelling from the caecum to the hepatic flexure was applied to the DCM and the velocity of the contents and the shear rate in the lower layer of fluid closest to the bottom wall were measured. The study investigated the effects of three factors: propagation speed of the contractile wall wave, media viscosity, and volume on the results as a full factorial design. In vitro measurements were made using phase contrast (PC) cine-MRI. In the DCM, volume was varied from 150 to 200 mL, corresponding to filling levels of approximately 60 % and 80% respectively. Viscosity was controlled by varying aqueous sodium carboxymethyl cellulose (NaCMC) concentration. The low viscosity fluid (LOVIS) consisted of 0.25 % (w/v) NaCMC aqueous solution whilst the high viscosity fluid (HIVIS) was a 0.50 % (w/v) NaCMC aqueous solution. Details of the fluids used are given in Section 5.2.2.2. The motility pattern was varied by controlling the speed of the propagating wave along the DCM wall, varied between 0.4 and 0.8 cm s^{-1}. The occlusion degree was fixed at 60 ± 5 % for each pattern.

5.3.2 MRI protocol

Scanning was carried out using a 3T Philips Ingenia widebore scanner (Philips, Best, The Netherlands). Localiser scans were carried out prior to the tagging and PC scans for placement of these sequences across the DCM. PC scans were conducted using a sequence adapted from a standard PC flow sequence that usually acquires multiple flow measurements in blood vessels throughout the cardiac cycle, described in detail in [273]. In this work, a single fast field echo (FFE) image of 101•101 voxels was generated using flow-sensitive gradients. The scan was repeated for each parameter combination investigated. The parameters from the MRI scanner are shown in Table 5.1.

Table 5.1: MRI scanner parameters.

Parameter	**Value**
Scan duration [s]	60
TR [ms]	9.21
TE [ms]	7.60
FA [°]	10
FOV [mm^2]	177×200
Recon resolution [mm^2]	1.1×1.1
Slice thickness [mm]	8
SENSE	2.0
No. dynamics	30
Temporal resolution [s]	2

Three different slice locations along the length of the DCM were used to investigate the spatial variation of the flow induced; at segment 2, close to the mimic caecum, segment 6, midpoint and segment 10, hepatic flexure (see Figure 5.1) sequentially with 10 s rest periods between scans. Following completion of all spatial locations for the default motility pattern, the protocol was repeated for the slower PPW. After completion of all scans, media volume and/or media type (LOVIS or HIVIS) were changed, and the protocol repeated. The flow was encoded only in the streamwise direction (x-axis). Maximum velocities were encoded at ± 3 cm s^{-1} based on previous work by O'Farrell *et al.* [14]. Positive and negative velocities represent flow along the x-axis towards the hepatic flexure and caecum (depicted in Figure 5.1) respectively. To account for the background signal, initial velocity measurements were taken using PC cine-MRI prior to any induced motility (neutral wall position) when it was known the luminal contents were at rest. The mean velocity over the cross-sectional lumen flow area was close to zero at $4.32 \bullet 10^{-4} cms^{-1}$ with a standard deviation of $6.40 \bullet 10^{-3} cms^{-1}$. This standard deviation value was taken as the measurement error for a single voxel and hence accumulates in the error for PC cine-MRI

mean velocity measurements.

5.3.3 Modelling approach

The DCMDT employs Discrete Multiphysics (DMP), similar to Schütt *et al.* [237]. DMP is a meshless particle-based simulation technique where computational particles are used instead of a computational grid. DMP couples different particle-based modelling techniques, such as Smoothed Particle Hydrodynamics (SPH) Lattice Spring Model (LSM), and Discrete Element Method (DEM). The model in this study only accounts for SPH and LSM. SPH is used to model the fluid by calculating the viscous and pressure forces between the particles that represent the fluid. LSM is used to calculate the elastic forces between the particles that represent the solid walls of the DCM. The particle types and details of the model are highlighted in the cross section of the partially filled DCMDT in Figure 5.3. This partially filled state reflects the average situation where gas is also present in the colon.

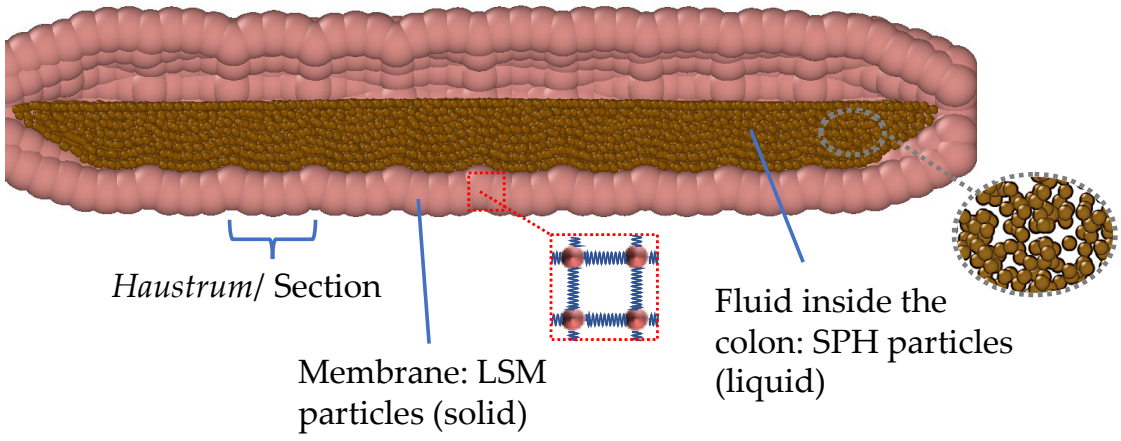

Figure 5.3: Particle representation of the model showing the colon haustra, the flexible membrane, and the fluid inside the colon.

Further details on the DT and the simulation parameters are given in Section 5.2.2. For a general overview on the DMP theory and how it can be applied to a variety of applications such as biological flows and/or fluid–structure interactions [236, 237, 301–307],

solidification and dissolution [308–310], machine learning [311, 312], and composite materials [312], the reader can refer to the available literature (e.g., DMP: [299, 300], SPH: [313], LSM: [314–316]). For technical details and how it is applied to the large intestine, the reader is referred to [236, 237, 317].

The DCMDT replicates the geometry and segmental appearance of the DCM, which is a biorelevant model of the human proximal colon (see Figure 5.1) [9, 10]. It is composed of a cylindrical body with a total length of 0.622 m and an inner diameter of $4.0 \bullet 10^{-2} m$. Only 0.24 m of the total model represents the DCM whereas the remaining part serves as a 'drain tank' (Figure 5.4).

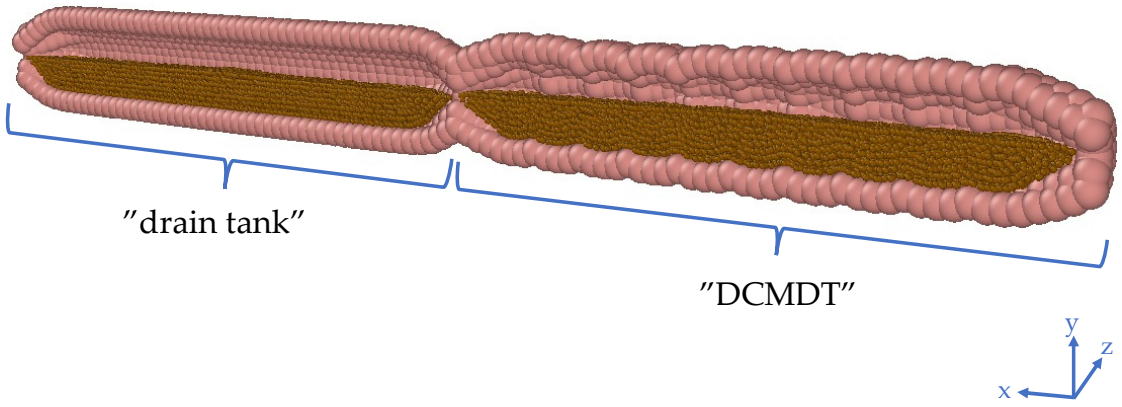

Figure 5.4: Cross section of the digital twin of the DCM and the 'drain tank'. The antegrade direction in this image is from the right to the left.

In the DCM, an antegrade PPW propels the fluid towards a rigid siphon that represents the hepatic flexure at the end of the DCM (see Figure 5.1); the sharp bend between the proximal and the transverse colon. Here, the fluid rises up the rigid siphon and falls back down when the PPW ends and the haustra return to the neutral position. The DCMDT is a closed system that mimics the presence of the hepatic flexure by separating the DCM-like compartment from the drain tank by constriction, enabling a small portion of fluid to escape the DCMDT lumen, if necessary, whilst still generating a back pressure when the wave reaches the end of the lumen. The DCM consists of 10 individual segments of equal size. Each segment consists of three chambers, representing the sack-like haustra on the

human colon, which are controlled simultaneously to contract and relax the wall for each segment. In the DCMDT, the membrane is also divided into 10 segments of equal size. Each segment consists of 3 circular rings of 25 LSM 'wall' particles, one of which can be seen in Figure 5.5a.

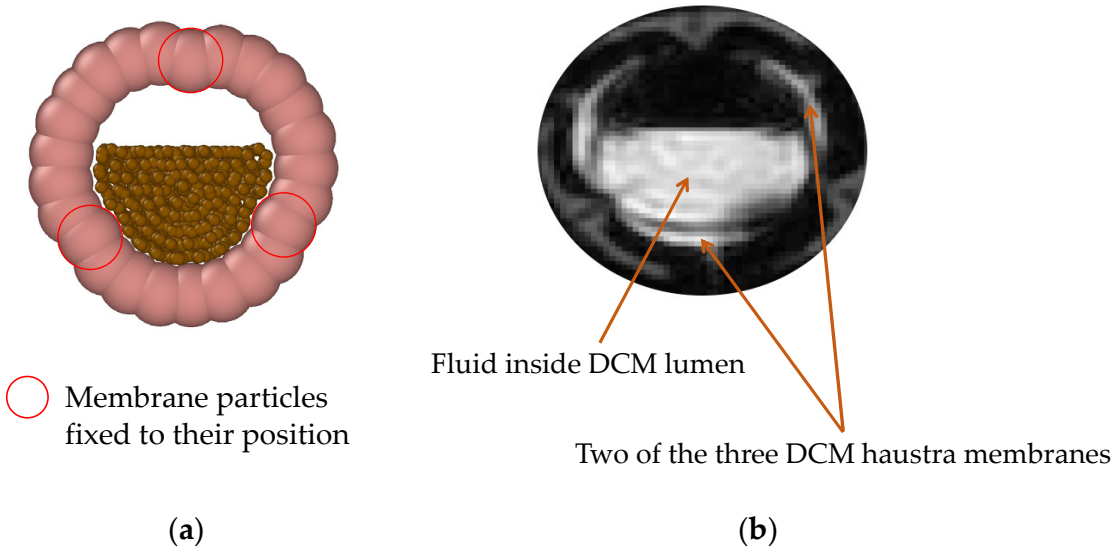

Figure 5.5: Morphology of a model colon segment during relaxation, where (a) is the computational model and (b) is a segment of the DCM.

To mimic the shape of the DCM segments during the relaxation and contraction phases, three particle rows along the DCMDT are fixed in position as highlighted in Figure 5.5a. This prevents them from moving during relaxation or contraction and consequently creates a similar three chamber system. Membrane motion is segmental in that the rings inside each segment move together as one body through the radial axis, contracting and relaxing in response to the application of a positive or negative radial force and mimicking contraction and relaxation of the DCM membrane respectively. The radial motion of adjacent segments can be synchronised to replicate any DCM motility pattern in terms of contraction/relaxation pattern, luminal occlusion degree, and the speed that a contractile wave propagates along the colonic axis.

5.3.4 DCMDT and Computational Simulation Parameters

Membrane Design and Motility

The membrane is modelled similarly to [237]. The DCMDT membrane is represented by 975 LSM particles in total which are tethered to their initial position using a Hookean spring, so that the membrane particles return to their initial position after the activation by a radial force (i.e., contraction or relaxation). This also fixes the model in the domain during the simulation. Additionally, particles in close proximity are interconnected with an additional Hookean force. Analogously, the forces are calculated using Hooke's law:

$$F_{i,j} = k(r_{i,j} - r_0) \tag{5.1}$$

where $F_{i,j}$ represents the present spring force between particle i and j, and k is the Hookean constant. The current distance between the particles i and j is represented by $r_{i,j}$, while r_0 is the equilibrium distance between these particles. This creates a lattice structure that replicates the properties of an elastic solid [314]. This approach has been used previously to model biological membranes [304, 318]. The Hookean coefficient used for the lattice is $K_{M,b}$, the coefficient used for the tethered springs is $k_{M,p}$. An additional viscous force

$$F_i = -k_{M,v} \cdot v_i \tag{5.2}$$

where v_i is the velocity of the particle, is added to the membrane particles to improve the stability of the simulation and simultaneously confer viscoelastic properties to the membrane as in [318]. Once the forces acting on each particle are calculated, the particles move according to the Newton equation of motion

$$m_i \cdot \frac{dr_i}{dt} = \sum_j^N F_{ij} \tag{5.3}$$

where r_i is the position of particle i. The pattern of force application to the simulated wall follows that of the DCM, wherein the rate of relaxation from peak contraction to neutral position is slower than the rates of initial relaxation and contraction. This is intended to mimic the viscoelasticity of the intestinal wall in vivo. Further details of the simulated membrane are shown in Table 5.2.

Table 5.2: Model parameters of the digital colon membrane.

Parameter	**Value**
SPH	
Total number of membrane particles (one layer)	2500
Number of membrane particles (DCMDT)	975
Mass of each particle, m $[kg]$	3.89×10^{-4}
LSM	
Hookean coefficient (bonds), $K_{M,b}$ $[Jm^{-2}]$	0.1
Hookean coefficient (position), $K_{M,p}$ $[Jm^{-2}]$	0.012
Viscous damping coefficient, $K_{M,v}$ $[m]$	1.0×10^{-2}
Equilibrium distance, r_0 $[m]$	6.283×10^{-3}

Fluid

Two different fluid volumes of 150 and 200 mL (i.e., 60 % and 80 % respectively) were modelled with SPH particles. A resolution analysis to determine the number of SPH particles representing the fluid was carried out in [237]. The model also accounts for two different fluid viscosities, a LOVIS and a HIVIS fluid. The aqueous NaCMC solutions (see Section 5.2.1) used in the DCM lumen demonstrated a response to shear that follows the power law model ($R^2 = 0.999$). Therefore, the shear stress τ can be calculated according to Equation (5.4):

$$\tau = K\dot{\gamma}^n \tag{5.4}$$

where K is the consistency index, γ the shear rate and n the power law exponent. The parameters describing the fluids used are provided in Table 5.3.

Table 5.3: Rheological parameters of the simulated luminal fluid.

Fluid	K $[Pa\ s^n]$	n [*]
Low viscosity fluid (LOVIS)	0.04	0.87
High viscosity fluid (HIVIS)	0.20	0.74

Figure 5.6 shows how the rheology of the simulated HIVIS and LOVIS fluids compares to the power law model fitted to the experimental data.

An approximately linear viscoelastic region was identified between $0 - 40s^{-}1$ corresponding to a constant viscosity. Therefore, the fluid modelled in the DCMDT was assumed to be Newtonian for simplicity, with a viscosity equal to the gradient of the linear viscoelastic region; $26mPas$ ($R^2 = 0.9959$) for the model LOVIS and $85mPas$ ($R^2 = 0.9806$) for the model HIVIS fluid.

Fluid Structure and Global Boundary Conditions

In the SPH framework the continuum domain is discretised into a finite number of points which can be thought of as particles, which are characterised by their mass, velocity pressure, and density. The SPH equations of motion result from the discrete approximations of the Navier–Stokes equation. SPH is based on the mathematical identity:

$$f(r) = \int\int\int f(r\prime)\delta(r - r\prime)dr\prime \tag{5.5}$$

where $f(r)$ is any scalar function defined over the volume V. The vector r is posi-

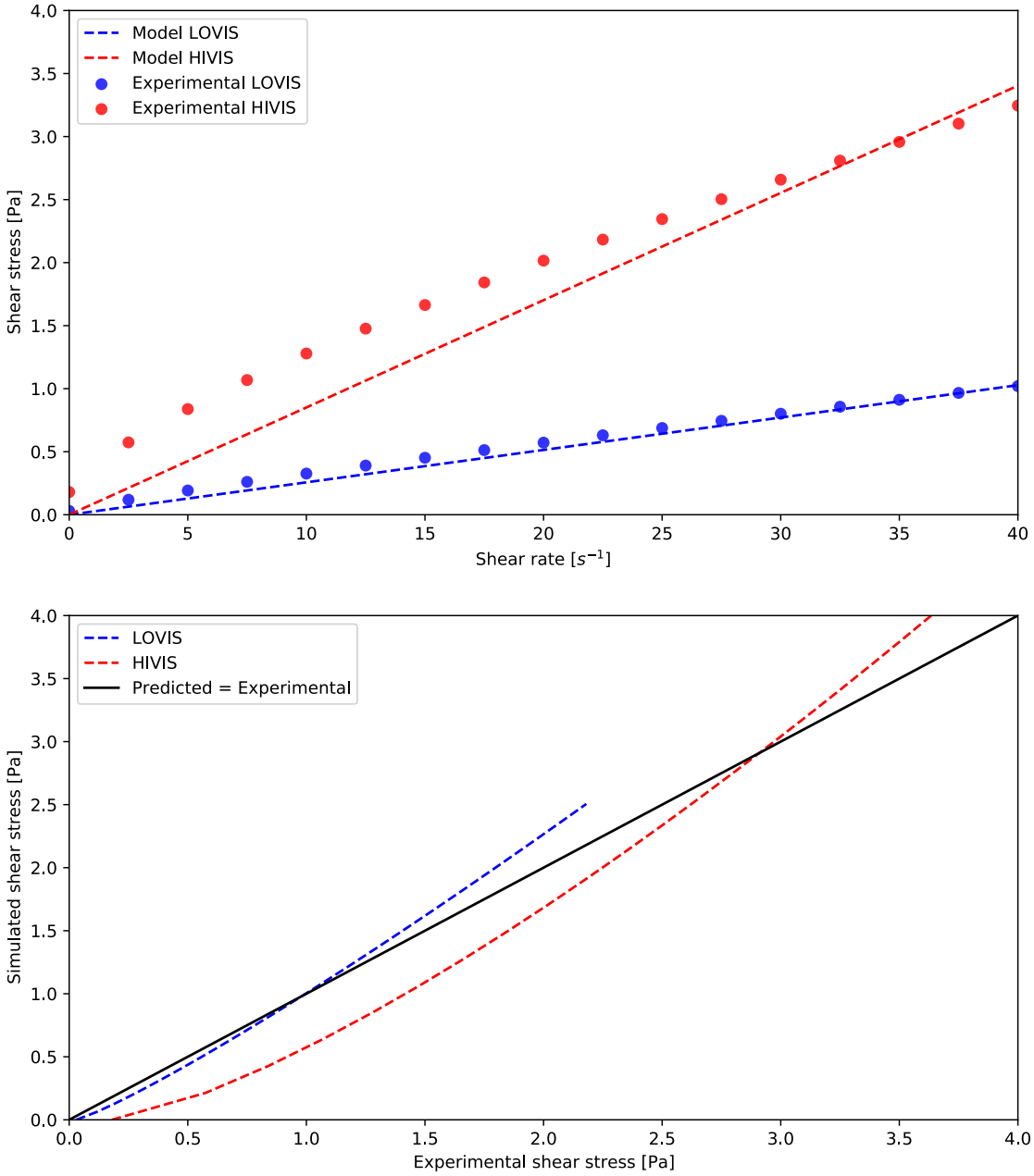

Figure 5.6: Rheological behaviour of LOVIS and HIVIS fluids in the DCM and their simulated counterparts in silico. Rheological measurements were carried out at 25 °C.

tion vector defined in the space V. $\delta(r)$ is the three-dimensional delta function and approximated in the SPH formulations by a smoothing kernel W and its characteristic width or smoothing length h:

$$\lim_{h\to\infty} W(r,h) = \delta r\prime \tag{5.6}$$

A variety of kernel functions can be found in literature. In this study, the so-called Lucy kernel function [319] is used. By replacing the delta function by a kernel or smoothing function W, Equation (5.5) becomes

$$f(r) \approx \int\int\int f(r\prime)W(r-r\prime)dr\prime \tag{5.7}$$

The discretisation over a series of particles of mass $m = \rho(r\prime)dr\prime$, the identity equation results in

$$f(r) \approx \sum_i \frac{m_i}{\rho i} f(r_i)W(r-r_{i,h}) \tag{5.8}$$

here, m^i is the mass and ρ_i is the density of i^{th} particle, where i ranges over all particles within the smoothing kernel W (i.e., $|r-r_i| < h$). Equation (3.8) represents the discrete approximation of a generic continuous field and can be used to approximate the Navier–Stokes equation

$$m_i\frac{dv_i}{dt} = \sum_j m_i m_j \left(\frac{P_i}{\rho_i^2} + \frac{P_j}{\rho_i j^2} + \Pi_{ij}\right)\nabla_j W_{i,j} + F_i \tag{5.9}$$

where v_i is the velocity of particle i, P is the pressure, $W_{i,j}$ is the concise form of $W(r_j - r_i, h)$, the term ∇j is the gradient of the kernel with respect to the coordinate r_j. F_i, accounts for a body force (e.g., gravity) and $\Pi i, j$ denotes the viscous forces. For the tensor $\Pi_{i,j}$ there are different expressions available in the literature; here we use [320]

$$\Pi_{i,j} = -\alpha h \frac{c_0}{\rho_{i,j}} \frac{v_{i,j} r_{i,j}}{\rho_{i,j}^2 + bh^2} \tag{5.10}$$

where α and b are dimensionless parameters to ensure the stability of the simulation. c_0 is the reference speed of sound at zero applied stress and $v_{i,j}$ represents the relative velocity and $\rho_{i,j}$ is the density of particle i and j, respectively. The constant b is used with $b \approx 0.01$. With the following relation, the artificial viscosity can be recognised as an effective kinematic viscosity η. The value of α is chosen depending on the desired effective kinematic viscosity in the simulation, accordingly [321]:

$$\upsilon = \frac{\alpha h c_0}{10} \tag{5.11}$$

To calculate the pressure forces between the fluid particles the Tait equation is used. This equation is also used to link the density ρ and the pressure P and correspondingly fulfil Equation (3.9):

$$P = \frac{c_0^2 \rho_0}{7} [\left(\frac{\rho}{\rho_0}\right)^7 - 1] \tag{5.12}$$

Here, $\rho 0$ the reference density at zero applied stress. Further details of the fluid properties are shown in Table 5.4.

To imitate the solid–fluid interactions (i.e., between the wall and the boundary layer of luminal fluid) a repulsive potential is used. This potential is used for the purpose of avoiding overlap between solid and liquid particles. A soft potential of the following form is used:

$$E_{ij} = A \left[1 + \cos \frac{\pi r_{ij}}{r_c}\right] with r_{ij} < r_c \tag{5.13}$$

Table 5.4: Model parameters of the simulated luminal fluid.

Parameter	**Value**
SPH	
Number of particles (150 mL / 60% filling level)	11,507
Number of particles (200 mL / 80% filling level)	18,076
Mass of each particle, $m_{F,low\ viscosity}$ $[kg]$	1.324×10^{-5}
Mass of each particle, $m_{F,high\ viscosity}$ $[kg]$	1.328×10^{-5}
Density, $\rho_{F,low\ viscosity}$ $[kg\ m^{-3}]$	1017
Density, $\rho_{F,high\ viscosity}$ $[kg\ m^{-3}]$	1020
Dynamic viscosity, $\eta_{F,low\ viscosity}$ $[mPa\ s]$	26
Dynamic viscosity, $\eta_{F,high\ viscosity}$ $[mPa\ s]$	85

where A is an energy constant, $r_{i,j}$ represents the distance between particle i and j and r_c is the cut-off distance. The no-slip boundary conditions between the solid and fluid particles are approximated by viscous forces similar to those of Equation (3.10), but applied to the interaction between the solid and the fluid particles.

Model parameters of the DCMDT used in the simulations are presented in Table 5.5.

Table 5.5: Fundamental DCMDT model parameters.

Parameter	**Value**
SPH	
Artificial speed of sound, c_0 $[m\ s^{-1}]$	0.1
Time-step, Δt $[s]$	5×10^{-4}
Smoothing length, h $[m]$	4.71×10^{-3}
Momentum-smoothing length, h_M, $[m]$	9.42×10^{-3}

5.3.5 Software

The computational simulations in this study were performed using the University of Birmingham BlueBEAR HPC service [322], running the simulations on 10 cores with 40 GB of memory, resulting in a simulation time of about 10 min each. The open-source code LAMMPS [323, 324] is used for the numerical calculations and the open-source code OVITO [325] for the visualisation of the results from the computational simulations. MATLAB [326] is used for the visualisation of the experimental data and the postprocessing of the DCMDT data as well as the experimental data.

5.3.6 Method of Analysis

MRI data analysis

Using PC cine-MRI, the mean velocity of the DCM lumen contents was measured by taking the mean of all weighted-average velocities measured in voxels that constitute the through-plane lumen cross sectional flow area (denoted as 'MRI' in Figure 5.7, Figure 5.8, Figure 5.9, Figure 5.10, Figure 5.11 and Figure 5.12). Additionally, peak velocity was estimated by taking the mean of the five voxels in the centre of the lumen (denoted as 'MRI (peak)' in Figure 5.7, Figure 5.10, Figure 5.11 and Figure 5.12), to assess the impact of any stagnant regions of fluid close to the walls on through-plane mean velocity. Furthermore, peak velocities were also measured by taking the mean of the four highest value pixels within each region of interest (ROI). Due to the potential for high noise in individual pixel velocity measurements, MRI peak velocity estimates should be made using several pixels, rather than just one [283]. The standard deviation of the mean velocity calculated using each ROI was considered to be the error associated with the MRI mean velocity measurement.

Since velocity was encoded only in the streamwise direction, x, as this is the prin-

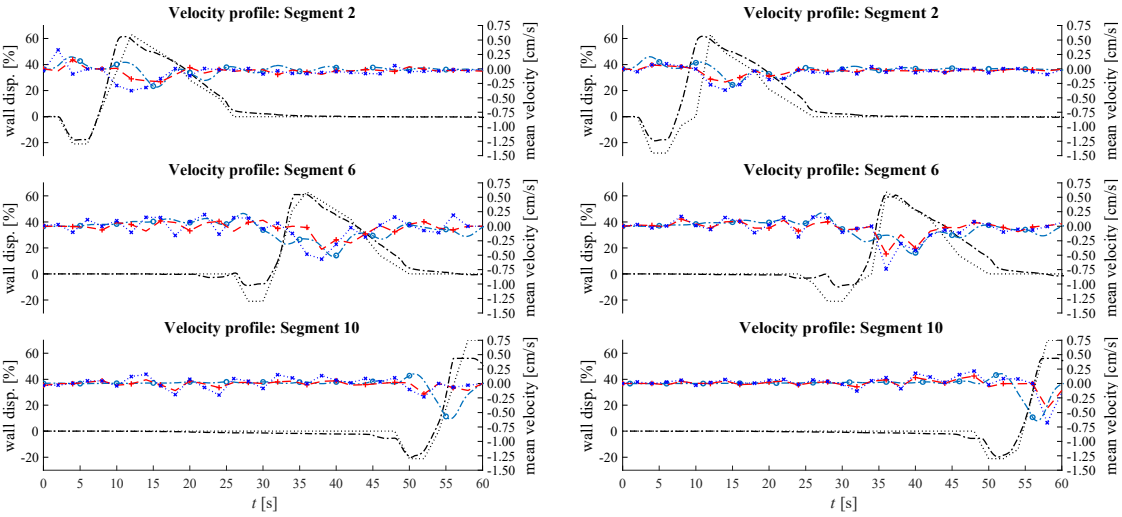

Total Sum of Squares TSS [cm^2 s^{-2}]

	Segment 2	Segment 6	Segment 10
DCMDT / MRI	0.23	0.59	0.67
DCMDT / MRI (peak)	0.76	0.75	0.96
MRI / MRI (peak)	0.42	0.85	0.14

(**a**)

Total Sum of Squares TSS [cm^2 s^{-2}]

	Segment 2	Segment 6	Segment 10
DCMDT / MRI	0.18	0.42	1.01
DCMDT / MRI (peak)	0.29	0.66	1.42
MRI / MRI (peak)	0.07	0.17	0.12

(**b**)

Figure 5.7: Comparison of the fluid velocities and wall displacement profiles of the DCM and the DCMDT with 60 % fluid volume and slower propagating PPW. Parts (a,b) compare the mean fluid velocities with LOVIS and HIVIS respectively.

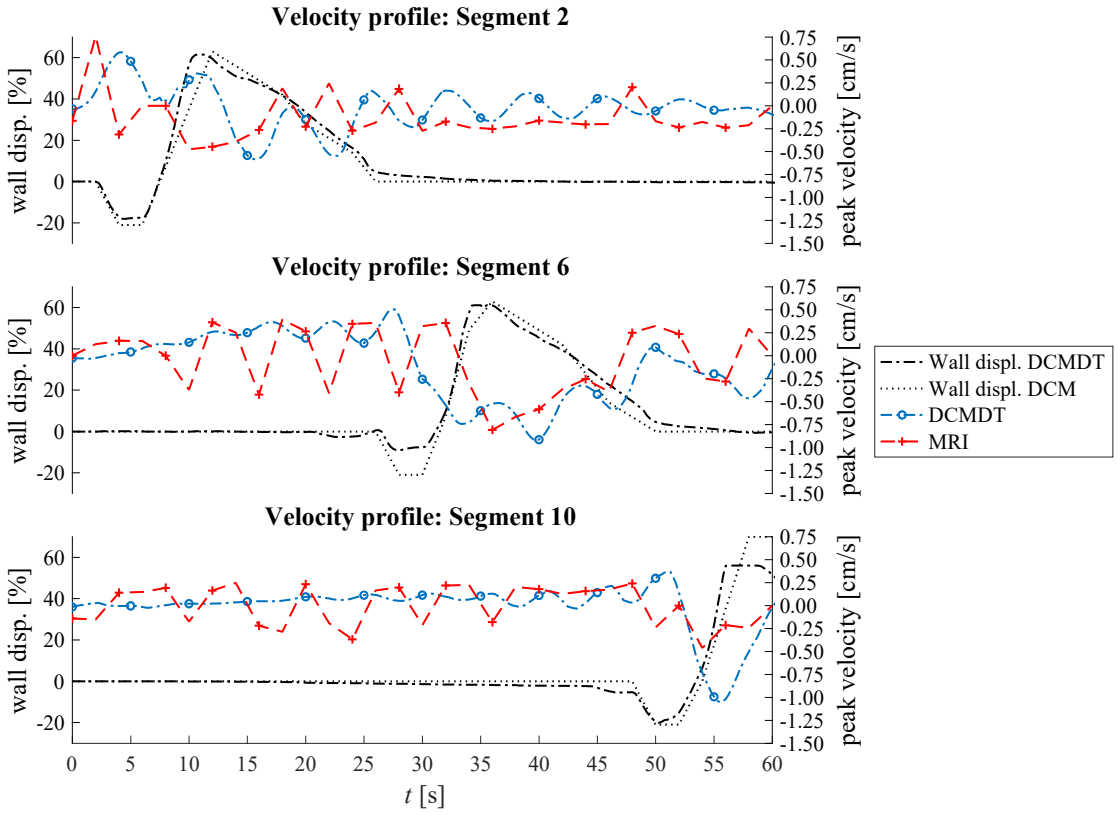

Total Sum of Squares TSS [cm^2 s^{-2}]

	Segment 2	Segment 6	Segment 10
DCMDT / MRI	4.76	5.40	2.63

Figure 5.8: Comparison of the maximum fluid velocities and wall displacement profiles of the DCM and the DCMDT with low fluid volume, low fluid viscosity, and a slow propagating PPW.

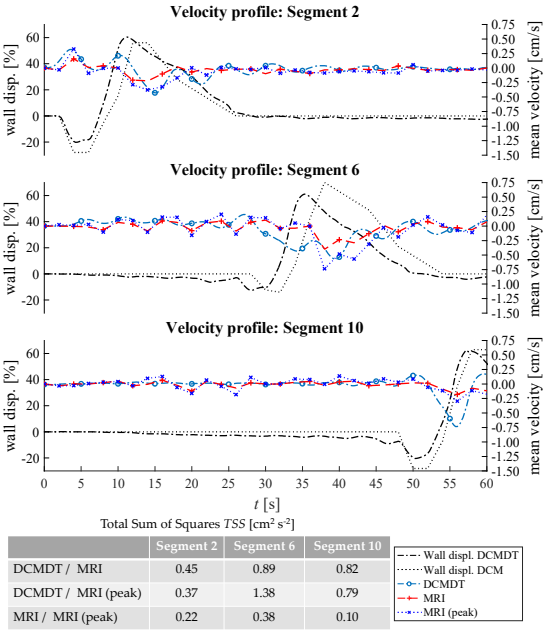

Total Sum of Squares TSS [cm^2 s^{-2}]

	Segment 2	Segment 6	Segment 10
DCMDT / MRI	0.45	0.89	0.82
DCMDT / MRI (peak)	0.37	1.38	0.79
MRI / MRI (peak)	0.22	0.38	0.10

(**a**)

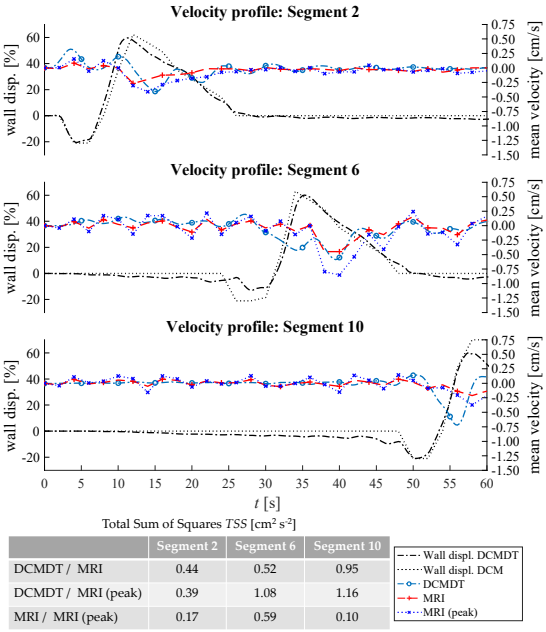

Total Sum of Squares TSS [cm^2 s^{-2}]

	Segment 2	Segment 6	Segment 10
DCMDT / MRI	0.44	0.52	0.95
DCMDT / MRI (peak)	0.39	1.08	1.16
MRI / MRI (peak)	0.17	0.59	0.10

(**b**)

Figure 5.9: Comparison of the fluid velocities and wall displacement profiles of the DCM and the computational model with high fluid volume and slow propagating PPW. In (a) the mean fluid velocities with low fluid viscosity and in (b) the mean fluid velocities with high fluid viscosity are compared.

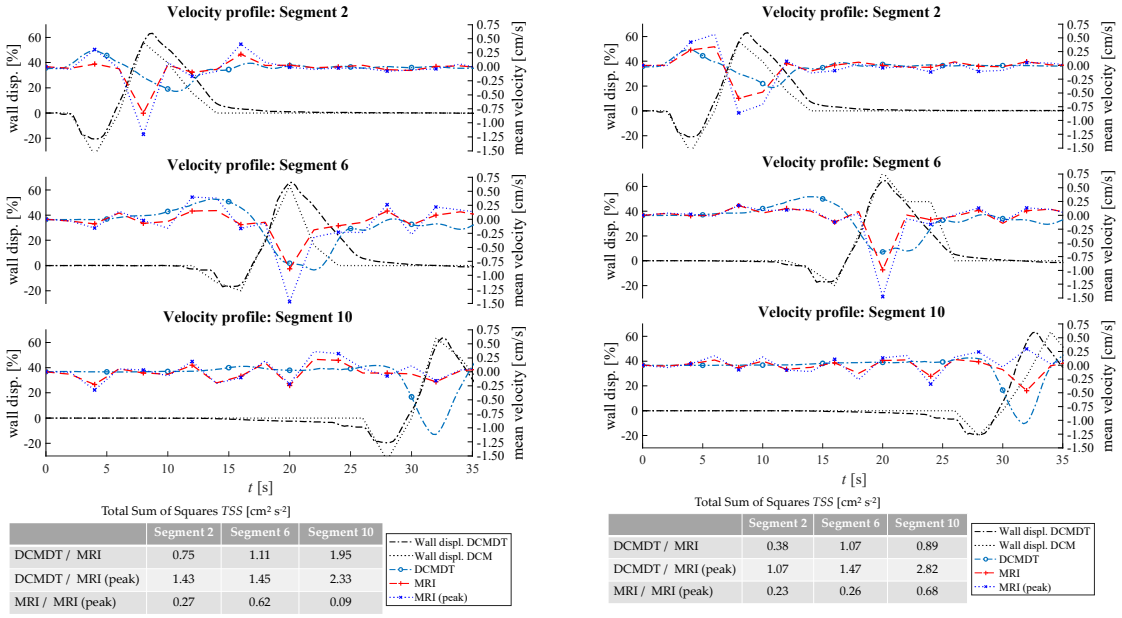

Total Sum of Squares TSS [cm² s⁻²]

	Segment 2	Segment 6	Segment 10
DCMDT / MRI	0.75	1.11	1.95
DCMDT / MRI (peak)	1.43	1.45	2.33
MRI / MRI (peak)	0.27	0.62	0.09

(**a**)

Total Sum of Squares TSS [cm² s⁻²]

	Segment 2	Segment 6	Segment 10
DCMDT / MRI	0.38	1.07	0.89
DCMDT / MRI (peak)	1.07	1.47	2.82
MRI / MRI (peak)	0.23	0.26	0.68

(**b**)

Figure 5.10: Comparison of the fluid velocities and wall displacement profiles of the DCM and the DCMDT at low fluid volume and a fast propagating PPW. In (a) the mean fluid velocities with low fluid viscosity and in (b) the mean fluid velocities with high fluid viscosity are compared.

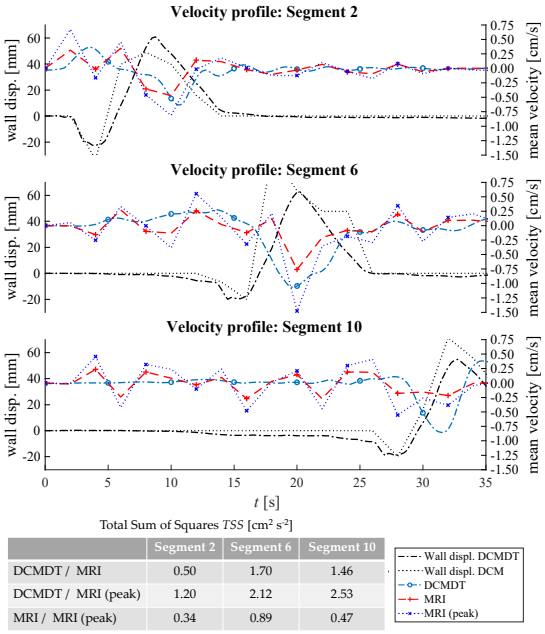

Total Sum of Squares TSS [cm^2 s^{-2}]

	Segment 2	Segment 6	Segment 10
DCMDT / MRI	0.50	1.70	1.46
DCMDT / MRI (peak)	1.20	2.12	2.53
MRI / MRI (peak)	0.34	0.89	0.47

(**a**)

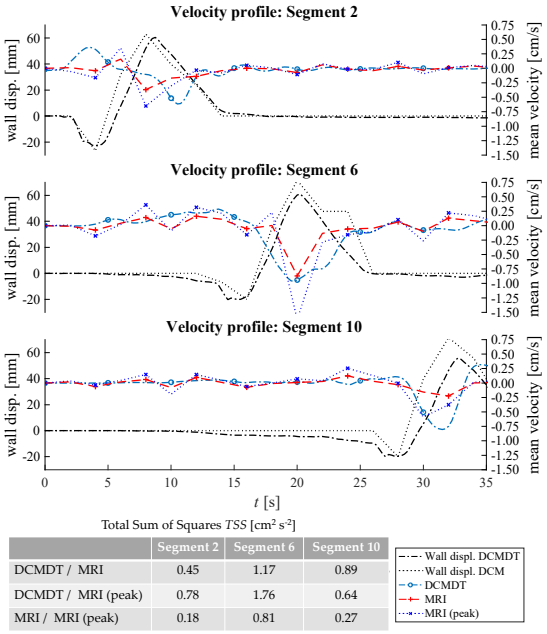

Total Sum of Squares TSS [cm^2 s^{-2}]

	Segment 2	Segment 6	Segment 10
DCMDT / MRI	0.45	1.17	0.89
DCMDT / MRI (peak)	0.78	1.76	0.64
MRI / MRI (peak)	0.18	0.81	0.27

(**b**)

Figure 5.11: Comparison of the fluid velocities and wall displacement profiles of the DCM and the DCMDT with high fluid volume and a fast propagating PPW. In (a) the mean fluid velocities with low fluid viscosity and in (b) the mean fluid velocities with high fluid viscosity are compared.

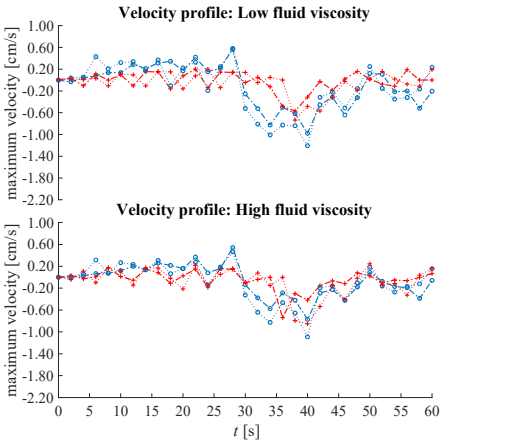

Total Sum of Squares TTS [cm^2 s^{-2}]

	LV	HV
DCMDT 60 % / DCMDT 80 %	1.41	0.69
MRI (peak) 60 % / MRI (peak) 80 %	1.50	1.54
DCMDT 60 % / MRI (peak) 60 %	3.53	1.71
DCMDT 80 % / MRI (peak) 80 %	5.25	2.15

(**a**)

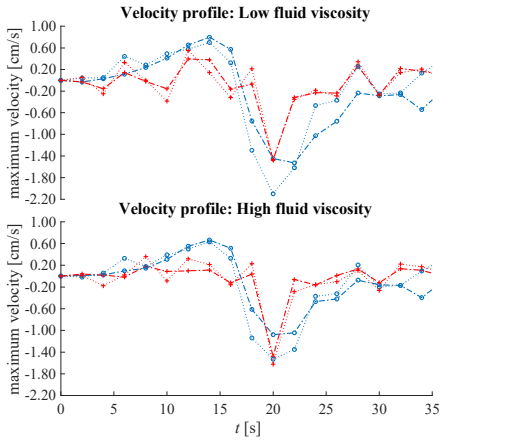

Total Sum of Squares TTS [cm^2 s^{-2}]

	LV	HV
DCMDT 60 % / DCMDT 80 %	2.46	1.20
MRI (peak) 60 % / MRI (peak) 80 %	0.31	0.33
DCMDT 60 % / MRI (peak) 60 %	5.16	3.22
DCMDT 80 % / MRI (peak) 80 %	6.52	4.30

(**b**)

Figure 5.12: Comparison of the fluid velocities at different fluid volumes and different fluid viscosities of segment 6. (a) represents data for the slower propagating PPW and (b) for the faster propagating PPW (b). In the table for the Total Sum of Squares, the following abbreviations are used: LV—low viscosity, HV—high viscosity.

cipal direction of flow and it was assumed that the z and y components of velocity were of negligible magnitude. $v_{\perp i}$ is the measured streamwise component of velocity of the fluid in pixel i. The measured value represents the weighted average of streamwise velocity inside the area entrapped within the pixel, which is dictated by the spatial resolution of the scanner. The flow rate through the pixel can therefore be determined by the following equation where q_i is flow rate through pixel i, and a_i is the area of pixel i.

$$q_i = v_{\perp i} a_i \tag{5.14}$$

The shear rate distribution can be mapped by evaluating the spatial gradient of the velocity distribution. Encoding velocity only in the streamwise direction simplifies the problem, eliminating the components of the shear rate tensor that involve measured velocity of the element of fluid inside pixel i in the z-direction, $v_{\perp z,i}$ and in the y-direction, $v_{\perp y,i}$ Additionally, the gradient of streamwise velocity with respect to the change in x-direction becomes unattainable as velocity values in only a single slice are obtained, therefore $\frac{\delta v_{\perp x,i}}{\delta_{x,i}}$ also assumes a zero value. Equation (3.15) presents the simplification of the shear rate tensor acting on a pixel, where γ_i is the shear rate acting on pixel i and ∇v_i is the velocity vector across pixel i.

$$\gamma_i = (\nabla v_i)^T = \begin{bmatrix} \frac{\delta v_{\perp x,i}}{\delta x_i} & \frac{\delta v_{\perp y,i}}{\delta x_i} & \frac{\delta v_{\perp z,i}}{\delta x_i} \\ \frac{\delta v_{\perp x,i}}{\delta y_i} & \frac{\delta v_{\perp y,i}}{\delta y_i} & \frac{\delta v_{\perp z,i}}{\delta y_i} \\ \frac{\delta v_{\perp x,i}}{\delta z_i} & \frac{\delta v_{\perp y,i}}{\delta z_i} & \frac{\delta v_{\perp z,i}}{\delta z_i} \end{bmatrix} = \begin{bmatrix} 0 & 0 & 0 \\ \frac{\delta v_{\perp x,i}}{\delta y_i} & 0 & 0 \\ \frac{\delta v_{\perp x,i}}{\delta z_i} & 0 & 0 \end{bmatrix} \tag{5.15}$$

To obtain values for the nonzero components of the shear rate tensor for each pixel, the velocity gradient was obtained using Equations (5.16) and (5.17). All voxels are of equal size and have a square face, where $\delta_{y,i}$ is equal to $\delta_{z,i}$, so the spatial difference is denoted as L, the length of one voxel.

$$\gamma_{z,i} = \frac{v_{\perp z,i+1} - v_{\perp z,i-1}}{L} \tag{5.16}$$

$$\gamma_{y,i} = \frac{v_{\perp y,i+1} - v_{\perp y,i-1}}{L} \tag{5.17}$$

where $\gamma_{z,i}$ and $\gamma_{y,i}$ are the z and y components of streamwise shear rate across pixel i. To map the shear rate distribution, the nonzero components for each pixel in the ROI were computed using a convolution matrix that performed the operations in Equations (5.16) and (5.17) on each voxel. The remaining shear rate components can then be resolved as in Equation (3.18) to give the overall shear rate acting over the voxel i by using the Frobenius norm.

$$||\gamma_i|| = \sqrt{\left(\frac{\delta v_x, i}{\delta z_i}\right)^2 + \left(\frac{\delta v_x, i}{\delta y_i}\right)^2} \tag{5.18}$$

DCMDT Data analysis

In the DCMDT, the shear rates were calculated from the stress tensor shown in Equation (3.19). The components *sigma* define the local normal stress and τ the local shear stress in the x, y-plane, x, z-plane, and y, z-plane respectively. Because only the velocity component in the streamwise direction (x-direction) is available from the DCM data, the stress tensor can be simplified. The simplification reduces the stress tensor to the local stress on the yx-, and z, x-plane, assuming zero values for all other elements. This facilitates comparison to the experimental data:

$$\tau = \begin{bmatrix} \sigma_x & \tau_{x,y}\tau_{x,z} \\ \tau_{y,x} & \sigma_y\tau_{y,z} \\ \tau_{z,x} & \tau_{z,y}\sigma_z \end{bmatrix} = \begin{bmatrix} 0 & 0 & 0 \\ \tau_{y,x} & 0 & 0 \\ \tau_{z,x} & 0 & 0 \end{bmatrix} \tag{5.19}$$

The remaining shear stress components were condensed into a single value using the Frobenius norm:

$$||\tau|| = \sqrt{(\tau_{y,x})^2 + (\tau_{z,x})^2} \tag{5.20}$$

For simplicity, a Newtonian fluid was used in the computational part. Thus, for the calculation of the shear rate γ, the following relationship between shear stress, shear rate and fluid velocity was used:

$$\dot{\gamma} = \frac{\tau}{\eta} \tag{5.21}$$

where τ is the shear stress and η the dynamic viscosity of the fluid.

In Vitro and In Silico Comparison Data Analysis

For each combination of parameters, the total sum of squares (TSS) between the different velocity data sets was calculated to evaluate the correlation of the experimental and computational data and the difference between the mean and peak measurements inside the DCM:

$$TSS_j = \sum_{i=1}^{n} (y_{j,i} - x_{j,i})^2 \tag{5.22}$$

where $y_{j,i}$ and $x_{j,i}$ are the discrete datapoints of a data set j which should be compared (i.e., computational data and experimental data). The TSS is calculated for each colon section and data set j separately. The main effects of three factors—wave speed, media viscosity and volume—on the response and mean shear rate at the bottom wall during local contractile activity were estimated and visualised using a main effects plot (see Figure 5.14). Main effects plots (also known as a design of experiment mean plot) are

an efficient data visualisation technique that help to identify differences between mean values of experiment parameters and thus depict how individual luminal parameters may influence the shear rate.

5.4 Results and discussion

5.4.1 Wall motion

Figures 5.7-11 show the mean displacement (denoted as 'Wall displ.') of the mimic intestinal wall beside the consequential velocity profiles of the lumen contents in both the DCM and the DCMDT over the course of a PPW. In both models, the PPW starts at segment 1 (left-hand side), and propagates to segment 10, over the course of 60 s for the slower wave and 35 s for the faster wave. Positive and negative wall displacement represent contraction and relaxation respectively. Figure 5.7, Figure 5.8, Figure 5.9, Figure 10 and Figure 11 demonstrate that the motility pattern of the DCMDT generally corresponded very well with that of the DCM in segments 2, 6 and 10, following an almost identical course of relaxation to -20% occlusion, contraction to 60 % occlusion and subsequently a slower relaxation back to the neutral position. This shows that the computational model is suitable to replicate the contractile nature of the DCM walls and can be synchronised to follow the same peristaltic PPW along the colonic axis.

5.4.2 Velocity Profile of the Contents

To verify, the DCMDT can mimic the DCM under a range of environmental conditions and the fluid velocity profiles were compared with those measured in the DCM in all combinations of PPW speed, media viscosity, and luminal fluid volume. In all cases, the DCMDT generated flows of the contents that followed the same pattern as the contents of the DCM. Before a PPW began, the contents were stationary with no measurable velocity. Low fluctuations in velocity between approximately 0.25 and -0.25 cm s^{-1} occurred prior to local wall displacement. Initial relaxation of the walls and contraction of the immediately upstream segment caused positive flows, propelling the contents towards the mimic hepatic flexure. Subsequently, contraction of the walls reversed the fluid direction and drove fluid

backwards towards the caecum at greater velocities. The fluid–structure interactions modelled in the DCMDT were therefore suitable to reproduce the complex series of antegrade propulsion and back mixing observed in the DCM [10, 14]. Both models show similarity to the in vivo situation as the velocity of the human ascending colonic contents is also not constant and exhibits periods of rhythmic back and forth motion [327]. Overall, the PPW generated mean fluid velocities in the DCMDT of similar magnitude to that of the DCM. The mean fluid velocities at lower fluid viscosity conditions were slightly noisier than at higher fluid viscosities (for example Figure 5.7a versus Figure 5.7b). The DCM produced mean (Figure 5.7, Figure 5.9, Figure 5.10 and Figure 5.11) and peak (Figure 5.8) velocities of slightly higher magnitude during the fluctuations above and below the datum outside of the period of local wall contraction. Where small deviations in wall displacement were observed, there was no significant effect on mean velocity of the contents in either the DCM or the DCMDT. More detailed flow phenomena were captured in the DCMDT than the DCM as the experimental data were comparatively low in temporal resolution compared to the DCMDT (2 s versus 0.25 s in this study, respectively) which highlights a clear advantage of using the digital twin. The mean fluid velocities using HIVIS were considerably less noisy than with LOVIS due to enhanced dampening of residual oscillatory motion caused before and after the contractile wave passes. Figure 5.7 shows the results obtained when the lumen was filled to 60 % capacity and the slower PPW (0.4 $\mathrm{cm\,s^{-1}}$) was applied. At the lower fill volume of 60 % , the slow motility wave (Figure 5.7) generated particularly similar mean fluid velocities in segment 2, close to the caecum as demonstrated by the low TSS values of 0.23 and 0.18 for LOVIS and HIVIS fluids respectively. In segment 10, the LOVIS experimental data did not show the strong backflow phenomenon that typically occurred during the contraction phase, which, on the other hand, was evident in the DCMDT. For the parameter combination shown in Figure 5.7a (i.e., low fluid volume, low fluid viscosity and slow PPW), the peak fluid velocities that occurred in the experiment and the computation are presented in Figure 5.8. The peak velocities fluctuated in a wavelike pattern similar to the mean velocities. Despite the similarities between the DCM

and the DCMDT upon visual analysis, TSS values were relatively high. This was due to the slight phase offset between the wavelike flow pattern of the DCM and the DCMDT which arose from marginally different initiation times. Next, the fill volume of the lumen was increased to 80 % (Figure 5.9). When volume was increased to 80, TSS values were < 1.4 with no significant deviations between the experimental and computational data. This shows that the simulation is robust at the elevated volume when the slower PPW is applied. At this stage, a limitation of the DCM and its DT is that the 'neutral' volume of the lumen is fixed, so when varying the fill volume of fluid inside the lumen below 100 %, an air space is present at the top of the lumen. In vivo, the capacity of the ascending colon adapts according to the volume of its contents; the walls of the colon reduce their tone and encase the contents fully, leaving no air gap (unless gas is present as a product of microbial activity). However, the focus of this paper is to demonstrate that the digital twin can reproduce flows inside the DCM under different luminal conditions. Future in silico models of the human ascending colon could better represent the in vivo situation by incorporating this morphological response to the volume of the contents to understand how this may affect the flow of the contents. The fluid volume was then reduced back to 60 and the faster PPW was applied (Figure 5.10). A faster PPW involved a faster occlusion rate which caused greater mean fluid velocities compared to the slower PPW seen in Figure 5.7. The experimental data shown in Figure 5.10a segment 2 and segment 6 and Figure 5.10b segment 2 exhibited a slightly higher mean fluid velocity ahead of the wall wave compared to the slower PPW. These elevated positive velocities were also accurately reproduced by the DCMDT in addition to the greater magnitude of backflow velocity. Both models also showed a higher fluid velocity in segment 6 at high fluid viscosity Figure 5.10b. Inside the DCM, media viscosity influenced the flow pattern, with a lower viscosity fluid causing more erratic wave-like behaviour. From the statistical analysis in Figure 5.10a, it can also be seen that the DCMDT data do not fully capture this fluid behaviour in the DCM. This could be attributed to shear rates at the extremes of, or outside of the linear viscoelastic region of the NaCMC solutions, causing the behaviour of the real fluid to deviate from that

of the simulated fluid in the DCMDT. A small contribution may also result from small irregularities between the segments in the DCM that are not captured in the DCMDT.

In Figure 5.11, the faster PPW was maintained but fill volume was increased from 60 to 80. In this case, there were no significant changes in mean velocity in the DCM that arose from increasing the fill volume from 60 to 80. The DCMDT performed well to capture this as shown by a relatively low TSS. Generally, mean velocities were slightly higher in the DCM than in the DCMDT. Comparison of Figure 5.12 parts (a) and (b) demonstrates the influence of propagating wave on the velocities achieved by the contents of the lumen, which follows intuition that a faster wave produces higher velocities in both the DCM and the DCMDT. The antegrade velocities were less affected than the retrograde peak during local wall contraction. A lower fill volume increased the degree of retrograde velocity experienced in the DCM, and this was replicated in the DCMDT also. Increasing fluid viscosity in the DCMDT decreased average retrograde velocity during local wall contraction, however, there was no significant effect in the DCM.

5.4.3 Shear Rates

Figure 5.13 presents the mean shear rate over time in the same cross section, and the maximum shear rate recorded for each of the same parameter combinations. In the DCM, mean shear rate spiked during local contraction of the walls at approximately 6 s and 20 s for the fast wave in segments 2 and 6 respectively in Figure 5.13A,B. Subsequently, shear rate dropped sharply, returning to low levels where small fluctuations between 0.01 s^{-1} and 3 s^{-1} were seen for the remainder of the motility wave. For the slow wave, local contractile activity occurred around 6 s and 40 s in segments 2 and 6 respectively, causing a lower, broader peak in average shear rate.

In the digital twin, a similar trend was observed in that there was a peak in average shear rate during a local wall contraction. However, instead of returning to low levels

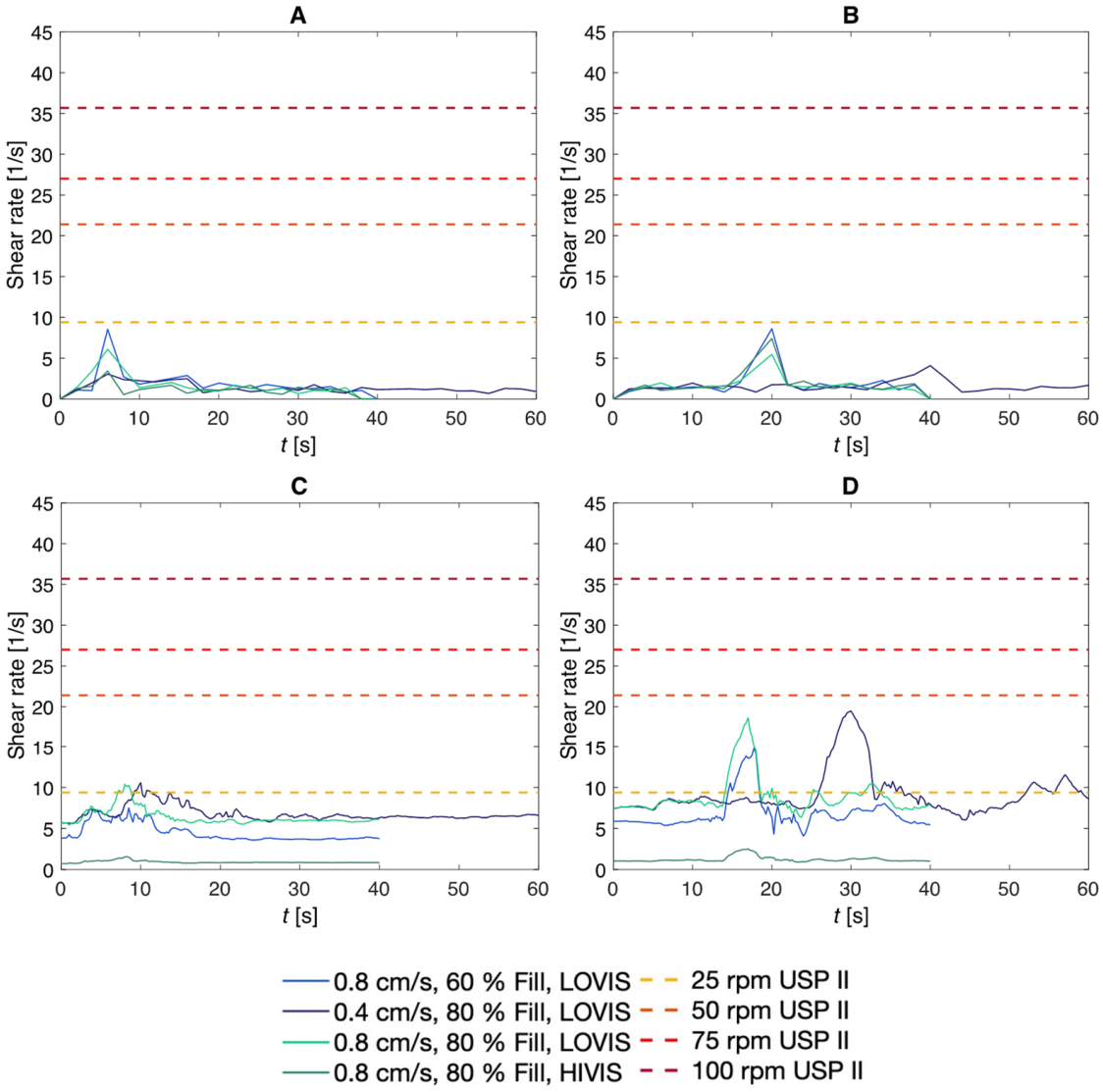

Figure 5.13: Average shear rates versus maximum shear rates for each parameter combination, where (A) represents DCM 'segment 2', (B) DCM 'segment 6', (C) DCMDT 'segment 2', and (D) DCMDT 'segment 6'. USPII shear rate data was reproduced from [252], Elsevier, 2018.

immediately, the average shear rate in segment 2 (Figure 5.13C) followed the general trend of decreasing post-contraction but periodically peaking to progressively lower shear rates as the subsequent segments contract. This effect was most prominent with the slow wave at a low viscosity and the greater volume of 80, which also gave rise to the highest mean wall shear rates in segment 6, peaking at 19.48 s^{-1} and in segment 2 at a height of 10.60 s^{-1}. In segment 6, shear rates were considerably higher than in segment 2, however, the periodic increases in shear rate following the highest peak arising from local contraction were irregular and less well defined. This suggests that a tablet located close to the caecum might experience more frequent peaks in shear rate and may erode faster, according to findings from a recent in silico study which suggested that is not the average shear rate that is important for tablet disintegration in the colon, but individual shear rate peaks that lead to accelerated tablet disintegration [238]. In both segments 2 and 6, shear rates were considerably lower when the lumen contained the higher viscosity fluid, HIVIS. Even though the DCMDT and DCM data show deviations in their course, the order of magnitude of the computational and the experimental data agree well. The mean bottom wall shear rate in both the DCM and the digital twin were highly variable and time-dependent, in contrast to inside the USPII modelled by Hopgood *et al.* [252]. In the USPII model, tablet surface shear rates were approximately constant for a given paddle speed and increased linearly from 9 s^{-1} at 25 rpm to 36 s^{-1} Hopgood *et al.* [252] at 100 rpm [252]. At no combination of parameters covered in this study does the shear rate at the wall in the DCM or DCMDT reach that of the USPII at 50 rpm (21.4 s^{-1}) or higher. This finding suggests that a constant paddle rotational speed greater than 50 rpm may bear low physiological relevance when studying the dissolution of colon-targeted dosage forms in the USPII. The spatiotemporal dependence of wall shear rate in the DCM is in line with observations in a CFD simulation of the TIM-Automated Gastric Compartment, which is a similar advanced biorelevant in vitro dissolution apparatus modelling the stomach [252]. Clearly, Figure 5.13 showed that mean wall shear rate in both models had some dependence on the speed of the propagating wave, media viscosity and media volume. The main effects plot in

Figure 5.14 scrutinises this further, giving a clearer idea about the relative significance of these parameters on the mean wall shear rate.

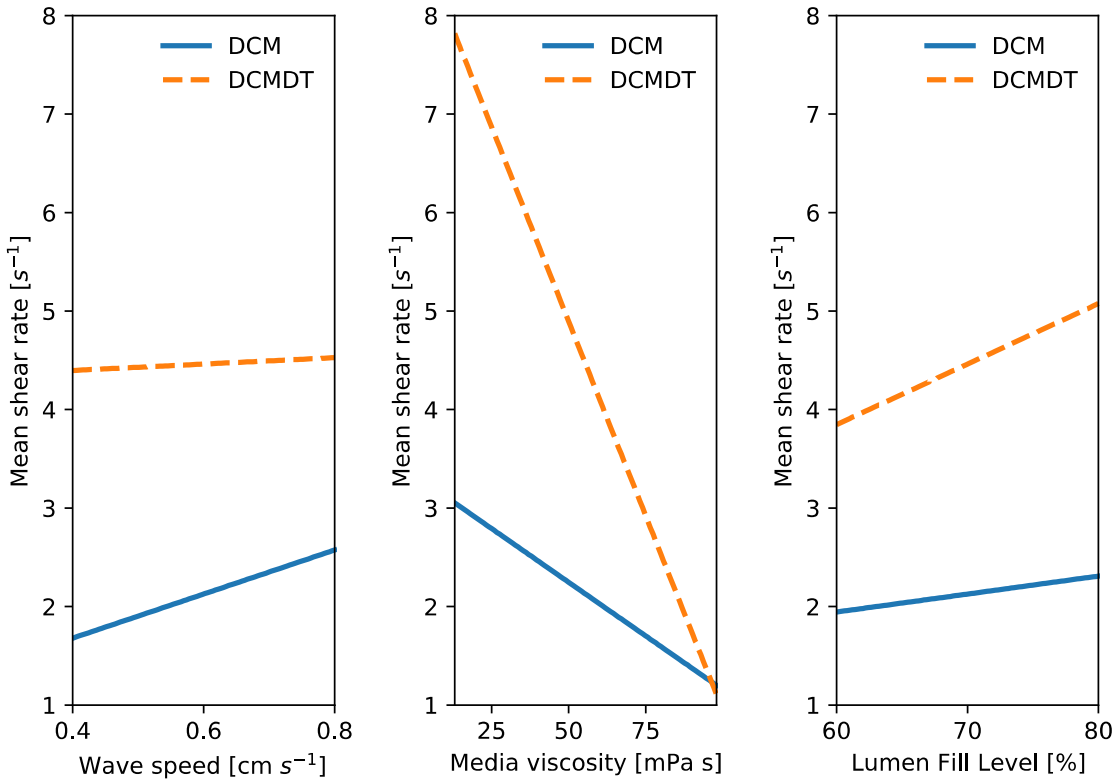

Figure 5.14: Main effects of wave speed, media viscosity and volume on mean shear rate at the bottom wall during local wall contraction at segment 6 in the DCM and the DCMDT. $N = 4$ mean data points at each level (low and high).

In all plots, the DCMDT is shown to represent the same type of effect as the DCM. Weak positive effects of wave speed and media volume and a strong positive effect of media viscosity on mean shear rate at the bottom wall during local wall contraction were evident. This shows that the DCMDT can model the influences of changes in wave speed, media viscosity, and volume on magnitude of luminal flow velocity. Effects were more pronounced in the DCMDT than the DCM. Over the parametric range studied in this work, only the effect of media viscosity on mean shear rate was significant ($p < 0.05$) in both models. This demonstrates that media viscosity is a key parameter to consider when designing a biorelevant media for dissolution testing, since shear rate influences dissolution

rate. Furthermore, this may mean that colonic disease states that alter media viscosity may divert the intended release profile towards a dose-dump-type scenario or the opposite, insufficient release and therefore administration of therapeutic molecules to the target site in vivo. Although the main effects of wave speed and media volume on mean shear rates are insignificant at between 0.4λ0.8 cm s^{-1} and 60λ80 % fill level, the main effects plot suggests that these parameters may demonstrate some influence on shear rate over a broader range of levels. Considering wave speed, a recent study in the DCM showed that wave propagation speed increases the velocity of the contents due to the higher level of kinetic energy imparted to the luminal fluid [14]. Intuitively, this may cause steeper velocity gradients and therefore higher shear rates. Future work should therefore consider a wider range of wave propagation speeds. The range of speeds in this study (0.4λ0.8 cm s^{-1}) covers fed cyclic antegrade (0.8 ± 0.3 cm s^{-1}) and fed short single antegrade (0.5 ± 0.3 cm s^{-1}) [170]. However, long single waves have been reported to propagate at (2.0 ± 0.8 cm s^{-1}) [170]. Other factors are at play in a motility pattern other than propagation velocity, for example, high amplitude propagating sequences (HAPSs, 0.4 ± 0.1 cm s^{-1} [170], 0.71 (0.29 – 5.15, solid-state catheter, 0.76 (0.22 – 6.06, water perfused catheter [328]), 1.11 ± 0.1 cm s^{-1} [329]) which have a similar velocity, exhibit a higher pressure amplitude as a result of higher occlusion rate and/or degree, which is likely to influence shear rate. Also, it is unknown how a retrograde propagating contractile wave affects flow in the DCM or its digital twin. Increasing volume influences the pressure and gravitational forces associated with fluid inside the lumen during a contraction, which is likely to influence shear rates. Future hydrodynamic investigations could explore the effect of orientation of the DCM and DCMDT and the associated influence of gravity on shear rates.

As already mentioned, the size of the DCM segments is fixed so that the membrane does not adjust to the current amount of intestinal content. This feature is also difficult to visualise in practice. However, the DT might offer a feasible way to represent the in vivo environment in a more realistic way by implementing this feature to investigate how this effects shear rates, along with adding in the complexities of gravity by standing the model

up so that the hepatic flexure is above the caecum — as is the case in ambulatory life.

5.5 Conclusions

The alignment of advanced in vitro and in silico models of in vivo systems is a promising approach to begin addressing the gaps in knowledge that currently hamper the progression of drug delivery and disease therapy. This study describes the development of a digital twin of the Dynamic Colon Model, a biorelevant dissolution apparatus representing the human proximal colon. The capabilities of the digital twin were verified using fluid velocity and shear rate data obtained through MRI imaging of the in vitro model. The DCMDT presents an addition to the available toolbox of in silico frameworks to model the fate of orally ingested dosage forms inside the gastrointestinal tract. In the colon, hydrodynamic parameters such as shear rates are pivotal in the disintegration and dissolution of a solid dosage form, particularly erodible matrices. Both models permit modification of a range of physiologically relevant parameters that describe the colonic environment and influence the hydrodynamic conditions inside the respective mimic lumen. This study investigated the effects that the propagation speed of a contractile wall wave, media viscosity, and media volume have on the mean wall shear rate inside the Dynamic Colon Model. It was found that media viscosity had a significant negative effect on wall shear rate, whilst weak positive effects were seen by propagating wave speed and media volume, which are anticipated to be enhanced at more extreme levels. The digital twin was able to replicate these effects, meaning that it is robust over a range of physiologically relevant parameter combinations and may be useful to model particular disease states and the effect these may have on the delivery of colon-targeted dosage forms. The findings in this paper indicate that viscosity is important to consider when designing a biorelevant media for dissolution testing of colon-targeted dosage forms. Additionally, constant paddle rotational speed greater than 50 rpm may bear low physiological relevance when studying the dissolution of colon-targeted dosage forms in the USPII dissolution apparatus. However, to consolidate the findings of this study, further work needs to be done that also considers the different motility conditions (i.e., wave speeds, direction of propagation and occlusion

degrees) found in the colonic environment.

Chapter Six

The effect of biorelevant hydrodynamic conditions on drug dissolution from extended-release tablets in the Dynamic Colon Model

This chapter was published in Pharmaceutics 14(10): 'The Effect of Biorelevant Hydrodynamic Conditions on Drug Dissolution from Extended-Release Tablets in the Dynamic Colon Model'.

6.1 Abstract

The in vitro release of theophylline from an extended-release dosage form was studied under different hydrodynamic conditions in a United States Pharmacopoeial (USP) dissolution system II and a bespoke in vitro tubular model of the human colon, the Dynamic Colon Model (DCM). Five biorelevant motility patterns extracted from in vivo data were applied to the DCM, mimicking the human proximal colon under baseline conditions and following stimulation using polyethylene glycol or maltose; these represent the lower and upper bounds of motility normally expected in vivo. In the USPII, tablet dissolution was affected by changing hydrodynamic conditions at different agitation speeds of 25, 50 and 100 rpm. Applying different motility patterns in the DCM affected the dissolution profiles produced, with theophylline release at 24 h ranging from 56.74 $\pm$ 2.00 % (baseline) to 96.74 $\pm$ 9.63 % (maltose-stimulated). The concentration profiles of theophylline were markedly localized when measured at different segments of the DCM tube, highlighting the importance of a segmented lumen in intestine models and in generating spatial information to support simple temporal dissolution profiles. The results suggested that the shear stresses invoked by the unstimulated, healthy adult human colon may be lower than those in the USPII at 25 rpm and thus insufficient to achieve total release of a therapeutic compound from a hydroxyethyl cellulose matrix. When operated under conditions mimicking the colonic response to oral administration of maltose or PEG solution in vivo, drug release in the DCM was between that achieved at 25 and 50 rpm in the USPII.

6.2 Introduction

Understanding and replicating the gastro-intestinal environment using in vitro and in silico models is of great importance for the development and evaluation of orally administered dosage forms. Whilst the hydrodynamic conditions within the GI tract are an important factor governing drug release, they are not replicated in commonly used dissolution apparatus, such as the ubiquitous United States Pharmacopoeial (USP) dissolution system II. This comprises a cylindrical vessel with a hemispherical base and a vortexinducing paddle. Although some apparatus have been developed to change pH dynamically in accordance with transit through the GI tract [130, 131], there has again been no attempt to replicate the hydrodynamic conditions [330]. Some dosage forms are designed to release drug over an extended period of time, or to reach specific regions of the GI tract. To achieve this, it is common to include polymeric excipients that serve to control release by erosion, which is driven by hydrodynamics [331].

Historically, the rate of drug release from polymeric matrices has been fitted using the power law model by Korsmeyer and Peppas (1983) (Equation (6.1)).

$$\frac{M_t}{M_\infty} = Kt^m \tag{6.1}$$

Here, the ratio of M_t to M_∞ denotes the remaining fraction of the initial mass of undissolved drug at time t and K is the rate constant that depends upon the micro- and macro-structural features of the dosage form. The exponent, m, is used to characterise the different mechanisms of release. The dynamic colon model (DCM), shown in Figure 6.1, is an advanced in vitro model of the human proximal colon that replicates segmental peristaltic motility [12]. It is the only model known to the authors to reproduce peristaltic motility of the colon in a segmented luminal architecture. The DCM can be programmed to mimic different intestinal motility patterns observed in vivo. This permits in vitro analysis

of different motility parameters such as occlusion degree and rate, isolated single contractions versus wave contractions and direction of propagation. Previously, the dissolution of theophylline from an extended-release dosage form in the DCM was studied under application of a high amplitude pressure wave (HAPW) [9]. The HAPW was applied once every 5 min over the course of 8 h. However, this aggressive motility represented a highly extreme version of the in vivo situation, where a HAPW occurs only 4–10 times per 24 h in the unprepared (no medical procedures to empty the contents of the bowel e.g., no laxative drink) human colon [332–334]. In addition, a low amplitude cyclic antegrade propagating wave (CPPW) travelling the 28 cm length of the DCM (mimicking from caecum to hepatic flexure) has been used in previous studies [10, 14, 15]. Its motility was based on observations from a high resolution manometry study on healthy volunteers by Dinning *et al.* [170]. CPPWs have also been reported to propagate in the retrograde direction.

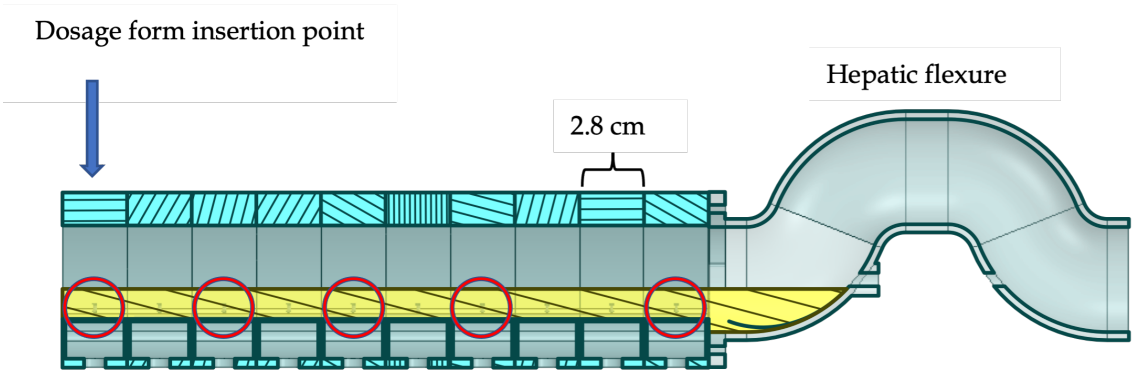

Figure 6.1: Cross section of the DCM partially filled with 100 mL fluid. Circled are the sample ports S1, S3, S5, S7 and S10 from left to right. The DCM comprises of 10 identical, modular segments of length 2.8 cm. A dosage form is introduced at segment one. Adjacent to the final segment, segment 10 at the opposite end of the tube is the mimic hepatic flexure.

In recent years, both high-resolution manometry and magnetic resonance imaging (MRI) have illustrated the variability of peristaltic contractions inside the colon. These include three patterns observed using cine-magnetic resonance imaging (cine-MRI) of healthy adult human subjects at a resting 'baseline' state and under stimulation by oral

administration of either polyethylene glycol (PEG) electrolyte solution or maltose [10, 168, 335]. These motility patterns have also been applied to an in silico model of the human proximal colon as reported by Schütt *et al.* [238]. Simulated colonic motor patterns with the highest frequency of single shear stress peaks were shown to cause a higher rate of drug release from a solid oral dosage form, whilst dampened motility led to slower drug release due to less advection to maintain a concentration gradient of the drug [238]. However, these simulations were based upon a homogenous dosage form containing only one compound (a simulated API), modelled using a lattice spring model of solid particles, rather than the complexity of a real tablet with a range of excipients and particle-particle or particle-fluid interactions within the overall structure. This limitation is of particular relevance when considering an erodible modified release tablet that would be applied to the colon. By simulating physiologically derived motor patterns in vitro, it becomes possible to understand the capability of a patient's colonic motor patterns to influence release of a therapeutic from a drug delivery vehicle. Furthermore, it facilitates assessment of the sensitivity or resistance of the formulation to the shear forces that are likely to be present in the human colon. The aim of this study is to evaluate the effect of simulated colonic motor patterns within the DCM on the dissolution of theophylline from an erodible extended-release formulation. This has required the integration of the new motility profiles into the DCM and the application of these motility profiles to the tablet of interest, Uniphyllin Continus® (UC) 200 mg theophylline ER tablets.

Table 6.1: Uniphyllin Continus® 200 mg tablet formulation information.

Formulation	Product name	Lot	Dosage	Excipients
ER theophylline	Uniphyllin Continus	251186	200 mg	Hydroxyethyl cellulose, povidone (K25), magnesium stearate, cetostearyl alcohol, macrogol 6000, talc

6.3 Methodology

6.3.1 Materials

Sodium carboxymethyl cellulose (NaCMC) 700,000 MW and potassium phosphate mono- (KH_2PO_4) and dibasic (K_2HPO_4) were purchased from Merck. Uniphyllin Continus® 200 mg prolonged release theophylline tablets (Napp Pharmaceuticals) were purchased from New Castle Healthcare NHS pharmacy, described in Table 6.1 [13, 336].

6.3.2 Calibrating the DCM for Replication of Colonic Motor Patterns

To develop the motility patterns in the DCM using previously published in vivo data, it was necessary to first convert the available in vivo parameters, namely the occlusion degree and occlusion velocity, into a form that is useful for the DCM.

6.3.3 Integrating occlusion degree

The DCM consists of ten segments, each of which comprises three haustra which combine to form a circular unit. When a segment contracts or relaxes, all three constituent haustra move synchronously. As in the human colon, the haustra of the DCM are convex in shape,

so the occlusion degree varies along the length of a segment. The occlusion degree was calculated from Equation 6.2, using the ratio of cross-sectional area measured at the central apex of the haustra (i.e., the maximum occlusion degree reached in the segment), to the cross-sectional area at the neutral position.

$$OD = 100 \times \left(1 - \frac{A_x}{A_N}\right) \tag{6.2}$$

Within the DCM, the haustra are contracted or relaxed using a hydraulic system controlled by syringe drivers. An in-house software was used to set syringe displacement to 0, 5, 10, 20, 25 and 28 mm using a stepper motor at a constant syringe speed of 15 mm s^{-1}, pausing for 5 s when a segment reached full contraction. An endoscopic camera fixed in position inside the DCM was used to capture the motion at 50 50 fps. At each position, the occlusion degree was calculated using MATLAB to find the area of the lumen in pixels after binarizing the images. This was conducted in triplicate for each degree of syringe displacement. Using the top of the membrane at the centre of the haustra as a point of reference, the displacement of the membrane was also measured, similar to the method used by Stamatopoulos *et al.* [10]. A linear relationship (Equation (6.3)) was established between syringe displacement (SD) and membrane displacement (MD) with a correlation coefficient of 0.996.

$$MD = 0.3425SD + 0.7246 \tag{6.3}$$

Occlusion degree was found to increase linearly with syringe displacement (SD) over the range of occlusion degrees that have been reported in vivo 18 $\pm$ 10 and 59 $\pm$ 18 % under baseline and stimulated conditions, respectively (Equation (6.4), with a correlation coefficient of 0.997).

$$OD = 5.80SD - 44.03 \tag{6.4}$$

6.3.4 Integrating occlusion velocity

The occlusion velocity was related to the displacement of the syringe that hydraulically inflated and deflated the haustra. An iPhone camera with a frame rate of 60 fps was clamped in position, with a single DCM segment in direct view that was adhered to a ruler with graduations of 1 mm. This set up was clamped and held at the identical elevation and orientation to the DCM. The in-house software was used to set syringe speed to 5, 10, 20, 25, 30, 40, 45 and 50 mm s^{-1}, and displacement to a constant 15 mm. The corresponding membrane speed for each syringe speed was measured and recorded for each of the three haustra in this segment.

A linear relationship (Equation (6.5)) was obtained between occlusion velocity (OV) and syringe speed (SS) with a correlation coefficient of 0.997.

$$OV = 0.32SS + 0.92 \tag{6.5}$$

6.3.5 Application of the DCM Motility Patterns

Table 6.2 shows the motility parameters for each pattern used, with the in vivo parameter shown for comparison. Figure 6.2 shows a graphical representation of the wall motion for each pattern. The patterns included a zero-motility state applied as a control. The motility patterns in this study were developed from analysis by Stamatopoulos *et al.* [10] of in vivo cine-MRI data produced by Marciani *et al.* [168] and Hoad *et al.* [335] as well as using data from high resolution manometry [170]. All of these were also simulated computationally in [238], except for a retrograde version of the CPPW applied here. Wave travel distance

was measured as the distance between the start of the first segment contracting to the end of the last segment contracting; i.e., if one segment has a length of 2.8 cm (Figure 6.1), a wave that involves contraction of three adjacent segments travels a distance of 8.4 cm. The time taken was calculated from the time that the first segment begins to contract to the time at which the final segment in the sequence reaches its point of maximum contraction. The repetition period of all patterns was set to 120 s as used by Schütt *et al.* [238], representative of the in vivo data presented in Stamatopoulos *et al.* [9]. Over the 24 h duration of the experiments, there were therefore 720 cycles per experiment. The motility patterns contained propagating waves in either direction and isolated single contractions. However, they differed in the location of contraction with respect to the point of tablet introduction, occlusion degree and occlusion rate. Higher occlusion rates are associated with sharper peaks in recorded luminal pressure when the contents have a greater viscosity than water [9, 337]. This causes more sudden disturbances to the fluid contents of the lumen, likely producing higher shear rates and therefore increased capacity for tablet erosion. During a propagating contraction, the DCM replicated the sequential peristaltic wall motion that is well documented in vivo, wherein a segment remained contracted until the following segment reached full contraction. The wall then returned back to its neutral position at a 0.26-fold slower speed than the occluding event, to mimic the viscoelastic properties of the colon wall in line with in vivo observations [10]. This causes the pressure profile generated to tail off in line with in vivo high-resolution manometry [10, 41]. This overall propagating wave motion of the wall has been shown to create a strong backflow inside the DCM [14]. Isolated single contractions were followed by immediate relaxation at the same ratio of 0.26 and 0.91 times the contraction speed in stimulated and baseline conditions, respectively. During a propagating contraction, the occlusion degree during relaxation was set constant at -10 %, equating to a 3.5 mm outward displacement of the membrane and a syringe displacement of -6 mm. Figure 6.2 shows the occluding behaviour of each motility pattern used in this study. Each segment is colour coded, with the warmer colours tending towards the caecum, S1 being red, moving through cooler colours culminating in purple

for S10. Therefore, adjacent contractions that transition to warmer and cooler colours with increasing distance from the caecum represent antegrade and retrograde propagating waves, respectively.

Table 6.2: Motility parameters of the static, baseline, CPPW (A = Antegrade, R = Retrograde) and stimulated (PEG or maltose) motility patterns applied to the DCM in this study, including the in vivo range where in vivo data is available

Parameter + in vivo data if available/applicable	**Static**	**Baseline [170]**	**CPPW [168]**	**Stimulated (PEG) [168]**	**Stimulated (maltose) [168]**
			Single contraction		
Occlusion degree (%)	0	25	-	60	60
Membrane displacement (mm)	0	4.80	-	6.87	6.87
Occlusion velocity (mm s^{-1})	0	1.55	-	12.98	12.98
Syringe displacement (mm)	0	11.91	-	17.95	17.95
Syringe velocity (mm/s)	0	1.97	-	38	38
			Wave		
Occlusion degree (%)					
Stimulated = 59 ± 18, Baseline = 18 ± 10	0	20.00	40.00 (S1: 23.15)	A: 75, 55, 50 R: 75, 50	A: 75, 55, 50 R: 75, 50
Membrane displacement (mm)	0	4.51	7.12 (S1: 23.99)	A: 7.76, 6.58, 6.28 R: 7.76, 6.28	A: 7.76, 6.58, 6.28 R: 7.76, 6.28
Occlusion velocity (mm s^{-1}) Stimulated = 36 ± 1.7 Baseline = 1.4 ± 1.1	0	1.55	10.80 (S1: 10.80)	12.98 for all	12.98 for all
Syringe displacement (mm)	0	11.05	18.6771 (S1: 12.45)	A: 20.54, 17.09, 14.67 R: 20.54, 14.67	A: 20.54, 17.09, 14.67, R: 20.54, 14.67
Syringe velocity (mm s^{-1})	0	1.97	31.13	38 for all	38 for all
Wave velocity (cm s^{-1}) Stimulated A = 2.2 ± 3.3, Stimulated R=2.2 ± 1.8, Baseline = 0.98 (A only)	0	0.37	A: 3.72 R:3.62	A: 4.25, 5.05, 5.26, R: 4.25, 5.14	A: 4.76, 5.31, 5.54, R: 6.09, 5.54
Propagation distance (cm) Stimulated A = 5.3 ± 1.4, Stimulated R = 6.6 ± 2.2, Baseline = 3.9 (A only)	0	8.4	28	A: 11.2, 8.40, 8.40 R:11.20, 11.2	A:5.60, 8.40, 8.40 R:11.20, 8.40
Cyclic frequency min (2–6 min [170])	-	2	2	2	2

6.3.6 Motility index

The motility index (MI) is a parameter established by [168] for the purpose of comparing the level of colonic motility observed between different subjects and stimulated versus unstimulated conditions using cine-MRI sequences. This was described using Equation (6.3), where $k = \frac{t}{t_{iv}}$. The duration of the time window that is to be analysed is reresented by t. This window is broken down into smaller episodes of constant duration t_{iv}. Based on the motility observed, Marciani *et al.* [168] chose to analyse 20 s intervals within a period of 120 s ($K = 6$).

$$MI = \sum_{K=1}^{K} \left(t_{iv} \times N_{seg}\right)_k \tag{6.6}$$

The number of segments, N_{seg}, was also derived from analysis of MRI data and depended on visible motility and interpatient variability. Considering in vitro and in silico models, the number of segments is well-defined in the geometry of the system and does not rely on imaging capabilities and unpredictable in vivo motility to distinguish between segments. Stamatopoulos *et al.* [9] and [337] demonstrated occlusion velocity to be key in generating pressure during non-occluding events. Therefore, a modified version of the motility index, MI_{DCM} (described by Equation (6.4)), was introduced, whose derivation is given in Appendix Two B1 - B4. The MI_{DCM} is a dimensionless index that is sensitive to both occlusion velocity and frequency of contractile activity that causes individual peaks in shear stress, which Schütt *et al.* [238] reported to be an effective predictor of dissolution ability. MI and MI_{DCM} values for each pattern are presented in Table 6.3.

$$MI_{DCM} = \frac{1}{\omega \times L} \sum_{K=1}^{K} \left(v \times N_{seg}\right)_k \tag{6.7}$$

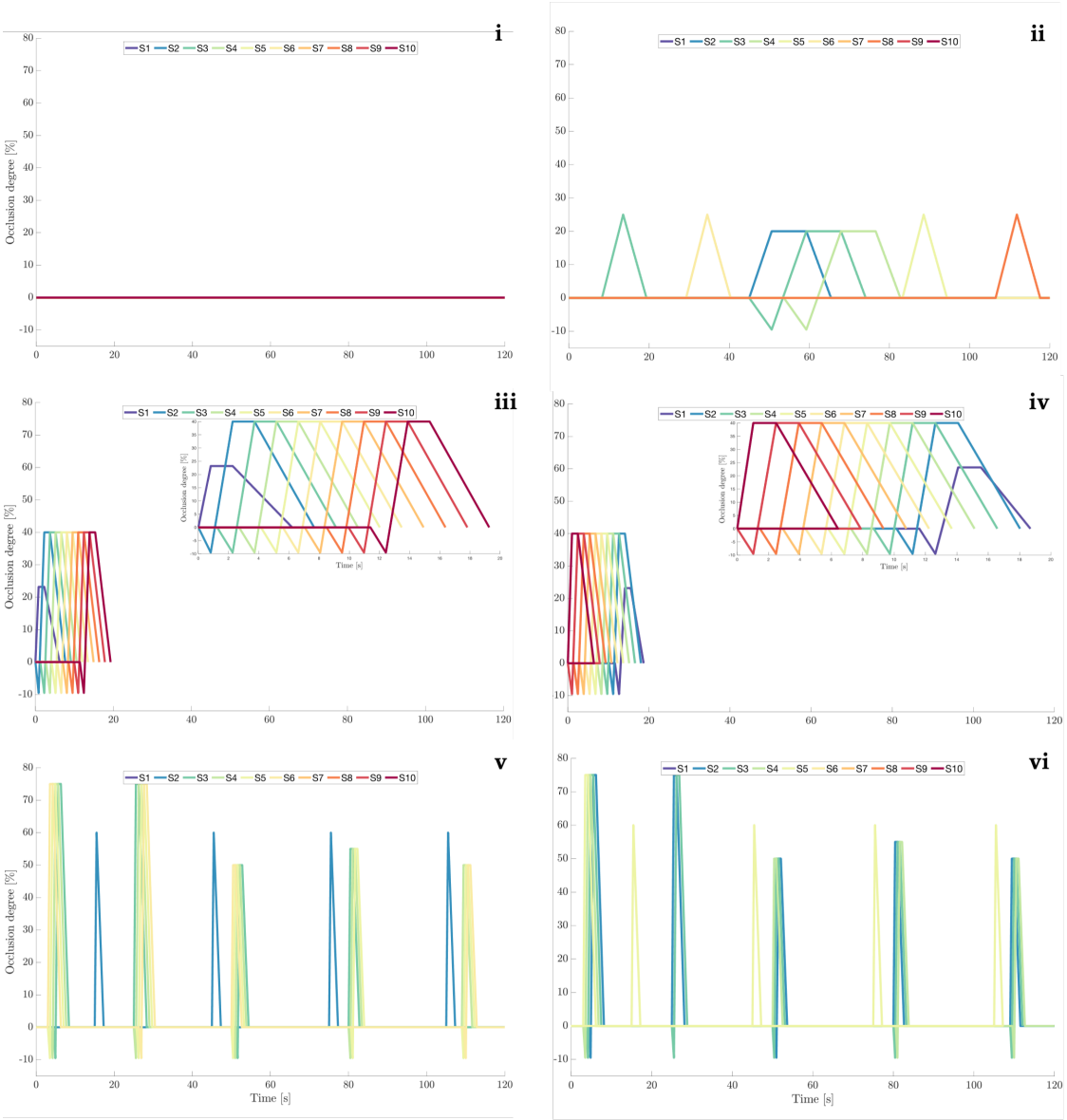

Figure 6.2: Graphical representation of the motility patterns applied to the DCM. i) Static, ii) Baseline [10, 168], iii) Antegrade CPPW, iv) Retrograde CPPW, v) PEG stimulated motility [10, 168] and F) Maltose stimulated motility [170]. Inset figures are placed in C and D to show the motility of each CPPW in more detail.

Table 6.3: Comparison of the existing motility index (MI) and the MI_{DCM} of the motility patterns applied to the DCM.

Pattern	**MI [segment × s]**	**MI_{DCM}**
Static	0	0
Baseline	180	0.0033
CPPW	200	0.016
Stimulated (PEG)	440	0.085
Stimulated (maltose)	380	0.073

6.3.7 Dissolution experiments

Analysis of drug concentration

Drug concentration was measured by UV-Visible spectrophotometry (Biochrom Libra S12) at 270 nm using a quartz cuvette with 10 mm optical path at 22 °C. Absorbance at 270 nm was compared against a calibration curve that was linear between 2 - 20 $\mu g\,mL^{-1}$ (correlation coefficient of 0.999) obtained through testing a serial dilution of standard solutions ($N = 4$).

Dissolution experiments in the USPII

Preliminary dissolution experiments ($N = 4$) were conducted in the Agilent 708-DS USPII system (Agilent Technologies, USA) using conventional 1 L capacity vessels to verify the shear sensitivity of the tablets. Agitation speed was fixed at 25, 50 or 100 rpm. USPII vessels were filled with 900 mL pH 7.4 aqueous phosphate buffer. Tablets were simultaneously dropped into the vessels using a dosage drop device (Agilent Technologies, USA). The temperature of the vessels was maintained at 37 ± 0.1 °C using an Agilent 708-DS USPII water bath. One sample location was used per vessel as per USP chapter <711>

Dissolution [338]. Samples 1 mL in size were removed at 0.25, 0.5, 1, 2, 3, 4, 6, 8, 10, 12, 16 and 24 h and filtered using 0.45 µ/metre polyethersulfone (PES) syringe filter membranes (Whatman, Cytiva, Marlborough, MA, USA) before storage in amber vials for a maximum of 24 h until analysis. Dissolution media was replenished immediately after sample withdrawal using the 850-DS automated sampling system (Agilent Technologies, Santa Clara, CA, USA).

Dissolution experiments in the DCM

The DCM was partially filled with $V_L = 100$ mL of 0.25 % (w/w) NaCMC solution adjusted to pH 7.4 using phosphate buffer as illustrated in Figure 6.1, in line with previously published dissolution experiments [9]. Theophylline is highly soluble in water and does not exhibit a strongly pH-dependent dissolution within the pH range observed in the human proximal colon [13, 336]. The temperature of the fluid inside the DCM lumen was maintained at 37 ± 0.3 °C. The tablet was directly inserted into the ileocecal port of the DCM, highlighted in Figure 6.1. Immediately following tablet insertion, a motility pattern (see details in Table 6.1) was applied and repeated at a frequency of one cycle per 120 s lasting 24 h. At 0.25, 0.5, 1, 2, 3, 4, 6, 8, 10, 12, 16 and 24 h, = 1 mL of sample fluid was withdrawn from 5 different sample ports (SP) simultaneously along the length of the DCM, SP1, SP3, SP5, SP7 and SP10, circled in Figure 6.1. Samples were filtered using a 0.45 µm PES syringe filter and analysed. Over the course of the experiment, 5 mL was removed and replenished at each of the twelve timepoints, corresponding to 60 % turnover of dissolution media, this needed to be accounted for in the analysis of cumulative drug release.

6.3.8 Dissolution profile calculations

The DCM was oriented horizontally, as in the supine position typically assumed by subjects during the manometric, scintigraphic and MRI procedures that informed design of the model [9, 10, 14]. Thus, the fluid was distributed throughout the lumen such that 8.9 mL fluid was present in each of the ten segments and 11 mL fluid resided in the hepatic flexure (see Figure 6.1). The assumption was made that the concentration of dissolved theophylline was homogeneous within a segment. The volume of each segment after sampling V_S, was 8.5 mL with $V_{HF} = 10.45$ mL in the hepatic flexure. The result, denoted ($C_{S(t)}$), was the measured concentration, C, in segment S at time t. Firstly, this value was used to estimate the mass of dissolved theophylline removed from the system by the sampling procedure at segment S and time t, ($m_S(t)$) using Equation (6.8).

$$m_{S(t)} = V_r C_{S(t)} \tag{6.8}$$

This equation makes the reasonable assumption that the concentration of dissolved theophylline was homogeneous within a 1 mL sample vial. Therefore, the total mass of dissolved drug removed from the DCM lumen $m_{sampled}$ at timepoint t was given by:

$$m_{sampled(t)} = c m_{S(t)} \tag{6.9}$$

where $S \varepsilon 1, 3, 5, 7, 10$ (i.e., each of the five sample ports used). Over the course of the experiment, the cumulative sum of mass removed was used to estimate the total dissolved drug that had been removed in saturated sample fluid until that time point. Therefore, the cumulative sum of mass removed, $m_{sampled}$, from $t = 0$ until $t = t$ resulted in the total mass removed, $m_{removed(t)}$, from the lumen up until time point t (Equation (6.10)).

$$m_{removed(t)} = m_{sampled(t)} + \sum_{t=1}^{t=T-1} m_{sampled(t)} \tag{6.10}$$

The mass of dissolved drug residing in each sampled segment was given by Equation (6.11):

$$m_{s(t)} = V_S C_{S(t)} \tag{6.11}$$

By plotting the concentration profile along the length of the DCM at each time-point, the distribution of dissolved drug was modelled and the concentration in intermediate segments was estimated. The total drug present in the lumen at time t, $m_{L(t)}$, was given by Equation (6.12):

$$m_{L(t)} = \sum_{S=1}^{S=10} m_{s(t)} + C_{HF(t)} V_{HF} \tag{6.12}$$

where $C_{HF(t)}$ is the concentration of dissolved drug estimated in the hepatic flexure at time t. Ultimately, to calculate the fractional drug release and fit to a power law model, the remaining mass of undissolved drug was given by Equation (6.13):

$$m_t = m_{L(t)} + m_{removed(t)} \tag{6.13}$$

6.3.9 Comparison of dissolution profiles

The model-independent dissimilarity factor, f_1, described by Equation (6.14), was applied to analyse the difference between a test (T) and reference (R) dissolution profile at each time point [339]. Two curves are deemed similar if $0 \leq f_1 \leq 15$ (%).

$$f_1 = 100 \times \left(\frac{\sum_{t=1}^{n} |R_t - T_t|}{\sum_{t=1}^{n} R_t} \right) \tag{6.14}$$

The similarity between dissolution curves was tested by the model-independent similarity factor, f_2, approach, where $50 \leq f_2 \leq 100$ suggests that two dissolution profiles are similar [340]. An f_2 value of 50 means that there is an average of 10 % difference between mean dissolution (%) at all specified time points [341].

$$f_2 = 50 \log \left[\frac{100}{1 + \sqrt{\frac{\sum_{t=1}^{n} (A_{t,x} - A_{t,y})^2}{n}}} \right] \tag{6.15}$$

6.3.10 Tablet position inside DCM

Using an endoscope camera, the segmental position of the tablet in the DCM was recorded after the dissolution experiment was completed.

6.4 Results and Discussion

6.4.1 Motility

When establishing the parameters for motility, the primary concern was ensuring that the parameters chosen were within the observed ranges in vivo. However, technical limitations of the DCM meant that not all in vivo parameters could be matched. For example, when stimulated (using PEG or maltose), occlusion velocity was reported to be 36 ± 1.7 mm s^{-1} in vivo. However, this correlated to a mean syringe speed of 109.63 mm s^{-1} which is beyond the capabilities of the stepper motors employed. The maximum operable syringe speed for the syringe distances travelled in this study was 38 mm s^{-1}. However, previous experiments have demonstrated that pressures within the range of those measured using high resolution catheters in the ascending colon in vivo have been recorded for non-occluding events in the DCM at occlusion rates as low as 4.3 mm s^{-1} [170, 342]. Additionally, occlusion velocities this high may only occur a few times per day in vivo. Therefore, the pressure events generated by the motility patterns in this study were considered to be biorelevant.

6.4.2 USPII Dissolution profiles

Figure 6.3 presents dissolution profiles of theophylline from UC tablet in the USPII at different agitation speeds. The profile generated at 25 rpm is significantly different to those obtained at 50 and 100 rpm: f_1 = 18.2 and 55.7 %, f_2 = 56.1 and 33.0 %, respectively. The profiles generated at 50 and 100 rpm were also significantly different with f_1 = 31.8 and f_2 = 45.0 %. Dissolution rate and drug release increase with rpm, demonstrating that the overall release and the release rate are sensitive to shear rate. The consequent erosion of the gel layer contributes significantly to release from these HEC matrix formulations.

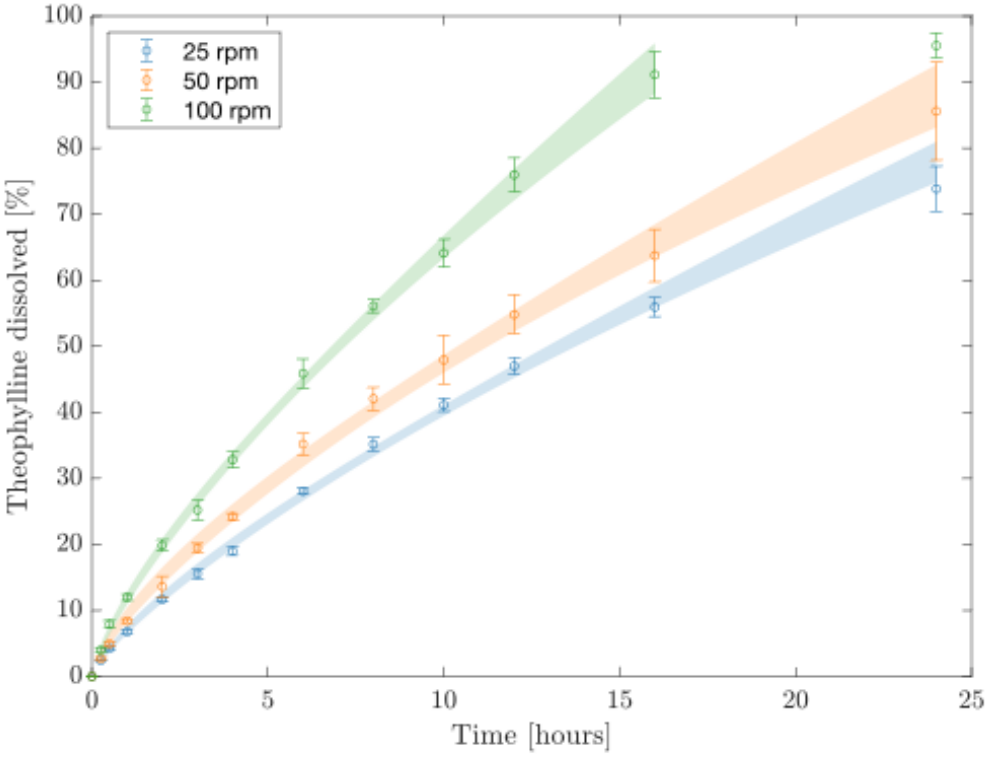

Figure 6.3: Dissolution profiles of theophylline from UC 200 mg tablets in the USPII apparatus at 25, 50 and 100 rpm.

6.4.3 DCM Tablet position

When the static and baseline motility patterns were applied, the tablet remained in the same position throughout, therefore the base of the tablet was not exposed to fluid. Conversely, when the CPPWs and stimulated patterns were used, the orientation of the tablet had changed after the experiment. Insertion of the intact tablet at the ileocaecal junction assumes that the dosage form reaches the proximal colon intact which is an unlikely situation in vivo. Nevertheless, the impact of the different in vivo-relevant motility patterns on dissolution behaviour of an erodible tablet has been demonstrated.

6.4.4 Segmental DCM dissolution profiles

Standard drug dissolution/release profiles in the pharmaceutical industry are presented as a single profile with no spatial information, as in Figure 6.3. However, the lumen of the DCM, much like the intestine in vivo, is not perfectly mixed. This means that information to describe how drug concentration varies with location is key to understanding how much API has been released from the tablet and how effective the motility pattern is at distributing the dissolved compound. Samples were withdrawn from five locations along the DCM to obtain the distribution of dissolved API along the DCM tube over 24 h. Figure 6.4 presents the concentration profiles of dissolved theophylline measured at S1, S3, S5, S7 and S10, progressively further from the point of tablet insertion, whilst the respective inset figure shows the location of the sampled segment.

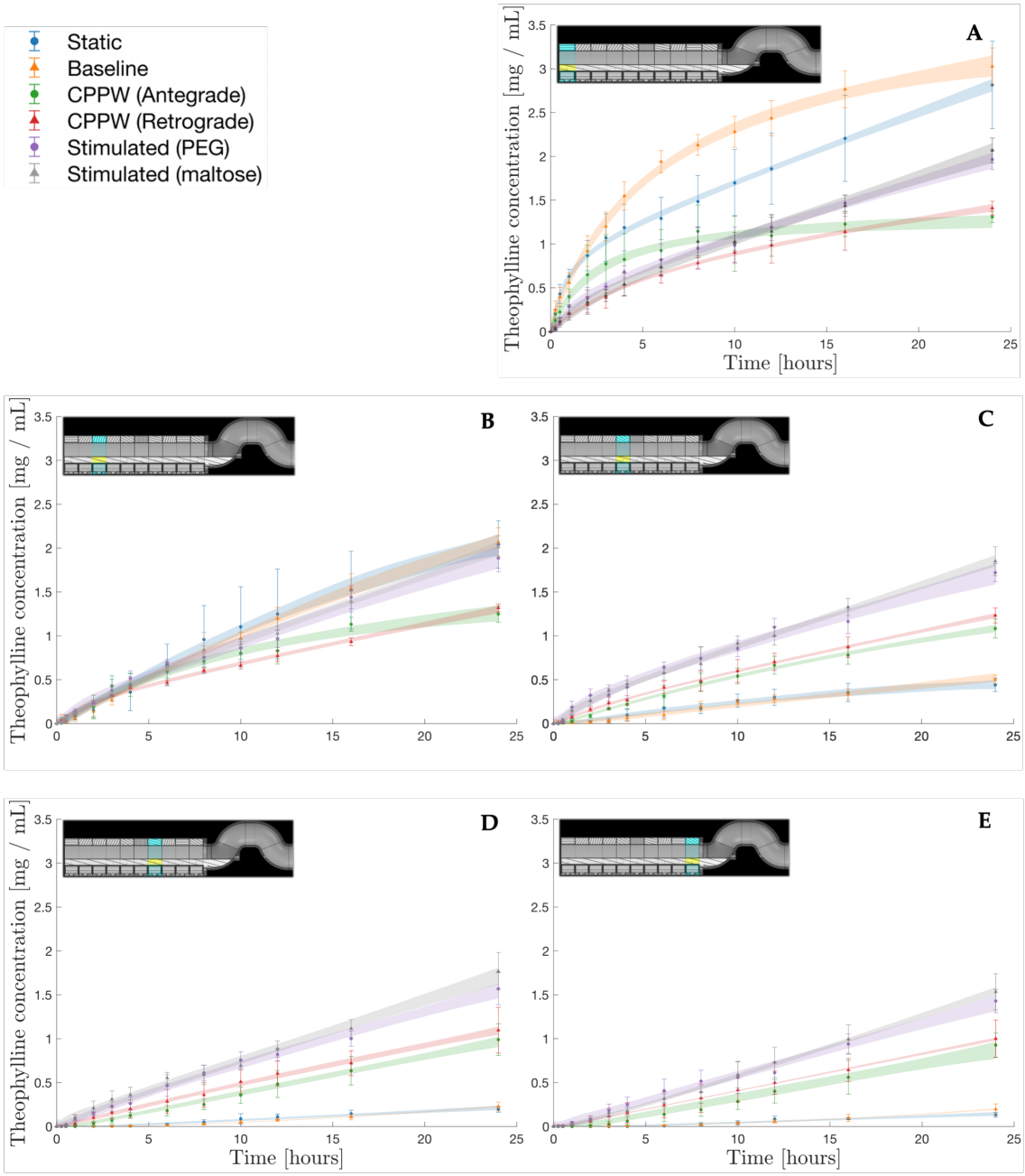

Figure 6.4: Concentration profiles of theophylline in segments S1 (A), S3 (B), S5 (C), S7 (D) and S10 (E) of the DCM under different motility patterns.

Besides from the DCM, the architecture of most advanced in vitro models of the colon takes the form of a single tube [12]. The most advanced physiologically based pharmacokinetic (PBPK) models use oversimplified first order transit rate models that consider the colon to be a single homogeneously mixed compartment. It is well-documented that the colon contracts in a segmental fashion wherein there is likely to be regional differences in both mixing behaviour and thus drug concentration. This has been demonstrated using the DCM in this study where mimicked in vivo motility involved frequent contractions (to different degrees of occlusion) whilst other segments remained stationary. The spatiotemporal information in Figure 6.4 demonstrates clearly that a drug concentration profile is highly dependent on the segments of the DCM lumen from which measurements are taken (Figure 6.4). If the DCM were a perfectly mixed system each segment should yield 2 mg mL^{-1} of theophylline. This demonstrates the importance of a segmented lumen in models of the colon, thus, there is a need to update the PBPK models to include a segmented colon. Furthermore, the segmental and cumulative dissolution data from the DCM could be integrated into PBPK models of the colon to better predict overall exposure; particularly for erodible formulations where motility is critical for drug release. This is relevant as it was observed that operating motility patterns with a low DCM motility index (MI_{DCM}, see Appendix 2 for derivation) can cause the contents of some segments to be somewhat stagnant. Operating patterns with such low motility may therefore encounter potential solubility effects on the rate of release measured in segments containing the tablet body, especially considering vehicles with a poorly soluble payload.

S1 was the point of tablet insertion. Figure 6.4a presents the concentration profiles of theophylline measured at S1, representing measured dissolution in the fluid immediately surrounding the tablet, which did not move from its insertion point for the duration of the experiments. The highest concentration reached in S1 was under static (2.82 $\pm$ 0.50 mg mL^{-1}) and baseline (3.07 $\pm$ 0.21 mg mL^{-1}) conditions. When the DCM was static, drug release from the dosage form and distribution along the DCM was driven primarily by diffusion. This led to accumulation around the point of tablet insertion and high local drug

concentration. Mass transport in the static model was not purely diffusive however, since the media sampling and replenishment process introduced advective mixing, although this was minimised by operating sampling/replenishment syringe pumps at low flow rates (6 mL/min). Under baseline conditions, there were single, isolated contractions in S3, S6, S5 and S8, in chronological order. Additionally, there was a propagating pressure wave (PPW) from S2 to S4. This baseline contractile activity had a low MI_{DCM}, involving low occlusion degrees (25 %) and slow occlusion rates (1.5 mm s^{-1}) compared to the other patterns (refer to Table 6.2). Under such lethargic wall motion, it is unlikely that sufficient energy was imparted to the fluid to mix the area of high drug accumulation in S1, with the segments of the DCM closer to the hepatic flexure via advective transport through the viscous dissolution media. This was proven by the very low concentrations reached in S5, S7 and S10 (Figure 6.4c–e), where the baseline and static concentration profiles were very similar and significantly lower than in all other motility conditions.

Furthermore, it is possible that the baseline contractions promoted back-mixing rather than antegrade propagation of the contents. However, it is evident that the rate of increase of concentration in S1 was higher under baseline conditions compared to static. This suggests that the local mixing is caused by proximate wall motion: the PPW from S2 to S4 and the isolated contraction at S3, was sufficient to either impart sufficient shear stress to erode the outer layers of the dosage form or mix the contents within S1. To elaborate on the latter, it was assumed that the concentration within a segment was homogeneous. However, the robustness of this assumption is proportional to the mixing of the system; in a perfectly mixed system it holds true whilst in a stagnant system, such as the static DCM, it is less valid. The baseline pattern may have been sufficient to disturb the fluid surrounding the tablet and mix the contents of S1 such that the sample withdrawn from SP1 gave a more accurate reflection of how much drug had dissolved from the tablet. It is likely that there was a steep concentration gradient radiating from the tablet body outwards in these patterns with low MI_{DCM}, exacerbated by the viscosity of the dissolution media used. This could mean that the highest concentrations in S1 under the low MI_{DCM} static

and baseline conditions were not reflected by the concentration measurements taken from SP1.

Although the static and baseline patterns showed the highest concentrations of dissolved theophylline in S1 (Figure 6.4), these data also exhibited the highest variability. This could be due to a limitation of the UV-VIS methodology used where samples with a higher concentration were diluted to a higher extent, which increases the scale of any initial error due to an increased number of measurements required using the pipette.

Theophylline concentrations in S1 were generally lowest under the CPPWs, reaching 1.31 ± 0.06 and 1.41 ± 0.08 mg mL^{-1} at 24 h under the antegrade and retrograde waves, respectively. Figure 6.4 clearly shows a constant increase in concentration at S3, S5, S7 and S10 for the antegrade and retrograde CPPWs. After only 1 h, concentration of theophylline measured at S5, S7 and S10 was significantly higher than for the baseline pattern for both CPPWs. This clearly demonstrates that these patterns were effective at mixing along the length of the tube, significantly more so than the baseline motility pattern. Concentrations at S1 after 24 h were not significantly different between the antegrade and retrograde CPPWs. Interestingly however, there were significant differences in the course taken by the concentration profiles. The rate of increase in theophylline concentration measured at S1 was much higher for the antegrade pattern until $t = 10$ h, where a plateau was reached whilst the concentration profile generated by the retrograde CPPW followed the same trajectory (at a lower rate of increase) as the stimulated patterns until $t = 8$ h. This suggests that the antegrade wave may not have been as effective as the retrograde wave in driving advective transport of dissolved drug along the DCM tube, away from the tablet lying in S1. This is reinforced by the consistently lower mean drug concentrations measured at S5, S7 and S10, however the differences were not statistically significant ($p < 0.05$). Additionally, this hypothesis is supported by a previous MRI study of the DCM that showed that the highest magnitude velocities generated by an antegrade CPPW were backflows (retrograde) rather than in the direction of wave propagation [14].

Considering the patterns mimicking stimulated activity, the rate of increase of drug concentration at S1 followed similar trajectory to the retrograde CPPW, lower than the static, baseline and antegrade patterns, until $t = 8$ h. At this point, the concentration continued to increase at an almost constant rate until the peak at 24 h. The concentration at S3, S5, S7 and S10 also constantly increases over the duration of the experiment, consistently reaching higher values than in the CPPWs. This infers that in addition to extensive mixing capabilities, the hydrodynamics caused by the higher $\mathrm{MI_{DCM}}$ stimulant-driven patterns generated a higher erosive effect than the CPPWs, constantly releasing and dissolving drug from the tablet body and mixing it throughout the DCM.

At S1 after 24 h, the concentration of theophylline measured under application of the stimulated patterns lied in between the static and baseline patterns and the CPPWs, at 1.96 ± 0.11 and 2.07 ± 0.14 for PEG and maltose, respectively. These values are close to 2 mg $\mathrm{mL^{-1}}$ which would be expected for a homogenously mixed lumen and complete drug release. At S10 however, drug concentration was lower, reaching 1.43 ± 0.13 and 1.53 ± 0.21, therefore this situation was not realised. The highest release measured at S7 and S10 was from the Maltose stimulated pattern, closely followed by the PEG stimulated pattern. This demonstrates that the stimulated motility patterns were effective at distributing dissolved drug throughout the DCM. In these patterns with the highest MI_{DCM}, wave propagation speed and frequency were higher, though wave propagation distance was shorter, travelling a maximum of 4 segments compared to 10 in the CPPWs. This proves that inside the DCM it is not necessary for a contractile wave to propagate the length of the system (such as in the CPPWs) to effectively transport and mix fluid contents across the entire length of the tube.

The concentration profiles generated by the stimulated motility patterns at S7 and S10 increased with time in a linear modality, as did that of the baseline and CPPW patterns. However, in the maltose stimulated motility pattern there was a discrepancy in the linear trend at $t = 6$ h. In the DCM, this type of artefact may be caused by dispersed

tablet material that have become detached from the principal tablet body and were local to the sample point when samples were taken. The likelihood of this occurring is bound to increase with the eroding capabilities of the motility pattern. This type of discrepancy is likely to be more prevalent in the DCM than in typical USPII apparatus, due to a higher sample point to media volume ratio.

6.4.5 Cumulative theophylline dissolution profiles in the DCM

The cumulative dissolution profile generated under each motility pattern is shown in Figure 6.5. This profile was built from the segmental concentration measurements, from which the distribution of the dissolved drug throughout the model could be estimated to evaluate the total mass of dissolved theophylline in the DCM lumen. The shaded regions represent the 95 % confidence intervals for the power law models fitted to the experimental data, further explained in Table 6.4.

Table 6.4: Power law model fitted to release profiles in the DCM under different motility patterns. The constants are presented as mean (95% confidence interval) and relevant regression statistics are presented including root mean square error (RMSE) and standard square error (SSE). Adjusted correlation coefficient (adj. R^2) equalled 1.00 for all fits.

Motility pattern	**K**	**m**	**RMSE**	**SSE**
Static	4.51 (3.95, 5.06)	0.77 (0.72, 0.81)	0.98	9.47
Baseline	5.58 (4.65, 6.51)	0.74 (0.68, 0.80)	1.57	24.57
Antegrade	5.14 (4.65, 5.63)	0.80 (0.76, 0.83)	0.90	8.17
Retrograde	4.75 (4.47, 5.03)	0.83 (0.81, 0.85)	0.55	3.07
Stimulated (PEG)	6.42 (5.76, 7.08)	0.86 (0.82, 0.89)	1.29	16.74
Stimulated (maltose)	5.85 (5.11, 6.59)	0.90 (0.84, 0.94)	1.59	25.30

In the early stages of dissolution where $t < 3h$, all profiles were similar to the static

and baseline patterns, suggesting that diffusive mass transport governed release from the tablet. Subsequently, the importance of erosion becomes evident as the dissolution profiles under mimic stimulated conditions deviated significantly from the static and baseline waves. This is likely to align with hydration time of the HEC gel layer. From this point onwards, the hydrodynamics becomes important and the potential of the DCM to discriminate drug release profiles based upon physiologically relevant motility patterns is highly pertinent. The ability to recreate motility conditions demonstrates the power of the DCM to replicate inter- and intrasubject variability in motility, including extremes, and how this may influence colonic drug delivery. However, the authors recognise that in vivo the tablet would be subjected to the conditions of the upper GI tract prior to reaching the colon and that these aspects are not recreated in this study. A future study that included a biorelevant mimic of the conditions including the hydrodynamics of the upper GI tract that enabled delivery of the hydrated tablet without disruption of the swollen gel layer would be a great extension of this work.

The baseline motility was able to release 56.74 ± 2.00 % of theophylline from the formulation over 24 h, significantly higher than achieved by the static DCM 49.98 ± 4.14 %. However, the spatial information provided by Figure 6.4 showed that it was highly ineffective at transporting dissolved API along the DCM tube to segments beyond S3. When directly compared, the dissolution profiles generated from the antegrade and retrograde CPPWs were not statistically different (f_1 = 5.5 %, f_2 = 76.4 %). However, when compared to the profile measured under static conditions, the antegrade CPPW was not significantly different to the static profile (f_1 = 19.4 %, f_2 = 54.3 %) whilst the retrograde CPPW was different (f_1 = 31.2 %, f_1 = 48.0 %). This shows that the advective motion generated by a retrograde CPPW is sufficient to elevate the release and distribution of the drug inside the DCM beyond simple diffusion. However, the mean release achieved by the retrograde wave was significantly higher than the antegrade wave at t = 24 h. Although the wave parameters of the antegrade and retrograde contractions were equal, the propagation distance of the wave and the location of the wave front relative to the tablet

position are drastically different. This is likely to be the leading contributing factor to the significantly higher mean release at $t = 24$ h under the retrograde CPPW. Additionally, O'Farrell *et al.* [14] showed the nature of a CPPW with 40 % occlusion degree to cause high velocities in the opposite direction to wave propagation, which may be attributed to the increased rate of dissolved theophylline transport along the length of the DCM. Furthermore, in one experiment using the retrograde motility pattern, a large fragment of tablet had been eroded from the bulk tablet body and was located at the hepatic flexure from $t = 16 - 24$ h. This suggests that motility patterns which include more frequent retrograde propagating pressure waves may be more effective at achieving higher release of a therapeutic from a dosage form located towards the early stages of the proximal colon. Figure 6.5 shows a decrease in rate of increase of theophylline concentration from $t = 3$ h in both the antegrade and retrograde CPPWs, compared to the stimulated profiles which maintain a steady rate of increase. This suggests that insufficient shear was generated in the CPPWs to maintain the release rate observed in the profiles generated by the stimulated patterns. The same conclusion can be drawn from the baseline pattern. After $t = 16$ h, the shear stresses generated by the baseline and CPPWs appeared to be insufficient to cause breakdown and release of the drug that lies in the core of the tablet body, since the stimulated motility patterns produced significantly higher release than all others. The maltose stimulated pattern performed best in achieving highest release of theophylline.

Comparing the PEG and maltose stimulated patterns, there was no significant difference between the release profiles obtained ($f_1 = 6.00$ %, $f_2 = 70.70$ %). However, the mean concentration was consistently higher for the maltose-stimulated pattern at most time points. Although the PEG-stimulated pattern had a higher motility index, different features of the pattern may have caused the lower release. For example, S2 was the closest segment to the tablet insertion point in both patterns. However, in the PEG-stimulated pattern, S2 only exhibited isolated contractions, compared to the maltose-stimulated pattern, where S2 was involved in propagating wave contractions. This might suggest that the flows of the contents of the lumen generated by propagating waves are more effective

at eroding a dosage form in the local vicinity. Furthermore, it has been shown that the location of the contents with respect to contractile activity is vital in determining the velocities imparted to that fluid and therefore the shear rates experienced [14]. Propagating pressure waves in the PEG-stimulated motility pattern involved S6 rather than S2 in the maltose-stimulated pattern. This may have caused lower peaks in flow around the tablet located at S1, since contractions in S6 are further from the tablet and more fluid lies in between the contracting segment and the tablet to dampen the flow.

The findings from this study align with those from the in silico study by Schütt *et al.* [238] that the mimicked motor patterns based on stimulants were significantly more effective at releasing a water-soluble drug from an erodible vehicle. Stimulated motility patterns had a higher MI_{DCM} and thus exhibited faster occlusion rates and a higher frequency of waves and single contractions, in addition to higher occlusion degrees. This means that there would be a higher number of peaks in shear stress per 120 s cycle; Schütt *et al.* [238] predicted that drug release from a computationally simulated dosage form was significantly impacted by the number of shear stress peaks. This is likely to also be a contributing mechanism in vitro. Higher occlusion rates have been shown to generate higher pressures inside the DCM [10], which (through conservation of energy) would cause higher velocities of the contents and subject a dosage form to more intense agitation and higher shear rates, achieving higher release. Comparisons between the hydrodynamics experienced by the tablet in this study and the in silico study are limited though, since the solid dosage form modelled by Schütt *et al.* [238] was neutrally buoyant whereas the UC tablets sunk in the DCM fluid and had less surface exposed to high shear rates in the fluid. Overall, the findings from this study suggest the in silico model may have value for testing whether a particular motility pattern, combinations of patterns or changes in motility parameters have a significant effect on drug release. This could be conducted as a first step to prioritise in vitro trials.

As previously discussed, the significant difference in release resulting from the

change in rpm of the USPII apparatus demonstrated by Figure 6.3 shows that this formulation is shear-sensitive. However, the dissolution profiles inside the DCM in Figure 6.5 show that extended-release formulations that reach the colon may need to have greater sensitivity to lower shear rates. If a significant portion of the API remains in the vehicle when a prolonged release formulation reaches the colon, the polymer gel layer may be too resistant to shear to release sufficient API for effective treatment. It may be beneficial for formulators to use in vitro tools that model different regions of the GI tract for different stages of release, for example an inner core that is more sensitive to shear after 5.3 h, when a formulation typically reaches the ascending colon (median colon arrival time in healthy adult humans, 95 % confidence interval 4.51 - 5.48 h Padmanabhan *et al.* [100]). From these findings, it may be more applicable run the USPII apparatus with a pulsed agitation, stepping between 0 - 25 rpm with intermediate steps representing shear rates expected in vivo. This is similar to the stress test device developed by Garbacz *et al.* [342] based on physiological pressures a dosage form may experience during GI transit. However, precise information regarding in vivo shear rates is not currently available [13]. Future work with the DCM should use a combination of baseline and stimulated patterns in the same dissolution experiment in order to more accurately reflect the range of motility a healthy human subject may experience day-to-day after ingesting a solid oral dosage form. It may also be possible to evaluate the difference of DCM orientation on baseline dissolution, by rotating the DCM through 0 – 90 °at predetermined intervals to mimic the influence of gravity and human physical activity. This would likely cause a change in positioning or orientation of the tablet, exposing the side of the tablet that constantly in contact with the lower DCM wall in this study.

The knowledge gained from overall release profiles can also be used to further understand the segmental concentration profiles. Figure 6.4 showed plateauing behaviour of the S1 antegrade concentration profile from $t = 6$ h, suggesting a decrease in the rate of theophylline release. However, it is clear from Figure 6.5 and Table 6.4 that total release was not close to 100 %. Therefore, the plateau could be due to the introduction of solu-

bility effects as local concentration gradients between the gel layer of the tablet and the surrounding fluid in S1 were diminished and the fluid approached the aqueous solubility of theophylline (5.5 mg mL^{-1}). This would retard the rate of mass transport by diffusion. Another possibility is that diffusion from the outer layers of the tablet was complete and the rateof diffusion from the inner core was slow and crystalline theophylline was essentially 'locked up' and inaccessible without erosion of the outer layers, due to a low MI_{DCM}.

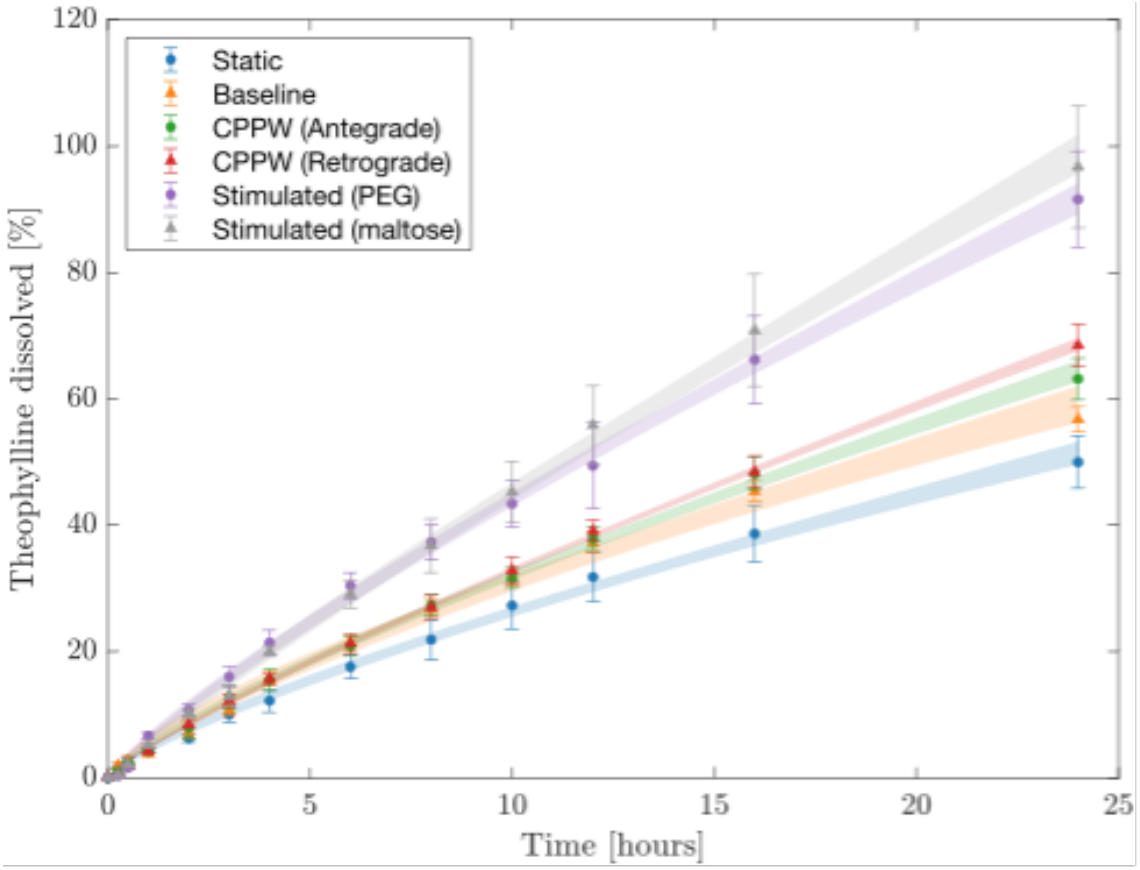

Figure 6.5: Cumulative release profiles in the DCM under different motility patterns. The shaded regions represent the 95 % confidence interval around the mean value predicted by the model (Table 6.4).

A power law model was fitted to the overall release profiles obtained in the DCM under different motility patterns (Figure 6.5), with $R^2 > 0.999$ for all profiles, as shown in Table 6.4. Similar to in the Korsmeyer-Peppas model, the exponent, m, generally increased with MI_{DCM} and is likely to be related to the frequency and intensity of shear experienced in an environment that exhibits colon-like pulsatile, peristaltic hydrodynamics. There is some discrepancy in this trend as the PEG stimulated pattern had a higher MI_{DCM} than the maltose stimulated pattern but a lower m and overall release. This suggests a contributing factor of the locality of the contractile activity with respect to the tablet, as previously discussed.

Table 6.5 presents the release comparison at $t = 4$, 10 and 24 h for each DCM motility pattern versus the USPII at 25, 50 and 100 rpm. Release at 4 h was generally higher in the USPII and discrepancy between the USPII and DCM increased with rpm, with 38.98 – 62.79 % greater release under 100 rpm compared to the DCM. Overall discrepancy between the DCM and USPII was most extreme at $t = 10$ h, with the DCM showing > 30 % less release than the USPII when all motility patterns were compared at agitation speeds of 50 and 100 rpm. This indicates that the release rate in the USPII under these conditions was considerably higher between $t = 4$ and $t = 10$ h. After 24 h, the DCM had had sufficient time to reduce the gap between release achieved in the systems. The static, baseline and CPPWs never achieved higher release than the USPII at any agitation speed. At $t = 4$, 10 and 24 h, release was higher under mimic stimulated conditions in the DCM compared with the USPII operated at 25 rpm, however it is unrealistic that the human proximal colon would display this level of stimulated activity for a continuous period of 24 h. These findings suggest that operation of the USPII at 25 rpm and above generates hydrodynamics conditions that may be too intensive to be representative of unstimulated human colon. However, the stimulated colon may generate hydrodynamic conditions that lie somewhere between 25 and 50 rpm. This data builds upon previous conclusions that the use of > 50 rpm in the USPII is not recommended for colon-targeted dosage forms [14].

Table 6.5: Release (Q) at t = 4, 10 and 24 h in the DCM and USPII (grey cells). Red: > 50% discrepancy between the DCM and the USPII. Blue and yellow: 10–50% positive and negative difference respectively. Green: results lie within 10% of one another. '↑' shows release in the DCM was higher than USPII, and vice versa. Statistical similarities ($p \leq 0.05$) are indicated at each timepoint by the same superscript.

	DCM	USPII		
		25 rpm	50 rpm	100 rpm
		Q_4		
USPII	-	18.97 [d]	24.20	32.81
Static	12.21 [a]	↓ −35.64%	↓ −49.55%	↓ −62.79%
Baseline	15.68 [b]	↓ −17.34%	↓ −35.21%	↓ −52.21%
CPPW (Antegrade)	15.52 [b]	↓ −18.19%	↓ −35.87%	↓ −52.70%
CPPW (Retrograde)	15.69 [b]	↓ −17.29%	↓ −35.17%	↓ −52.18%
Stimulated (PEG)	21.42 [c]	↑ +12.92%	↓ −11.49%	↓ −34.72%
Stimulated (maltose)	20.02 [c,d]	↑ +5.54%	↓ −17.27%	↓ −38.98%
		Q_{10}		
USPII	-	41.11 [h]	47.95 [g]	64.10
Static	27.29 [e]	↓ −33.62%	↓ −43.08%	↓ −57.43%
Baseline	31.68 [f]	↓ −22.94%	↓ −33.93%	↓ −50.58%
CPPW (Antegrade)	31.65 [f]	↓ −23.01%	↓ −33.99%	↓ −50.62%
CPPW (Retrograde)	32.84 [f]	↓ −20.12%	↓ −31.51%	↓ −48.77%
Stimulated (PEG)	43.40 [g,h]	↑ +5.57%	↓ −9.49%	↓ −32.29%
Stimulated (maltose)	45.26 [g]	↑ +10.09%	↓ −5.61%	↓ −29.39%
		Q_{24}		
USPII	-	73.84 [k]	101.15 [m]	95.54 [m]
Static	49.98	↓ −32.31%	↓ −50.59%	↓ −47.69%
Baseline	56.74 [i]	↓ −23.16%	↓ −43.91%	↓–40.61%
CPPW (Antegrade)	63.17 [i,j]	↓ −14.45%	↓ −37.55%	↓ −33.88%
CPPW (Retrograde)	68.47 [j,k]	↓ −7.27%	↓ −32.31%	↓ −28.33%
Stimulated (PEG)	91.60 [m]	↑ +24.05%	↓ −9.44%	↓ −4.12%
Stimulated (maltose)	96.74 [m]	↑ +31.01%	↓ −4.36%	↑ +1.26%

Table 6.4 highlighted that the baseline and CPPW patterns did not exceed 70 % release over 24 h, this suggests that the HEC gel layer in UC tablets may be overly resistant to the shear stresses that may be present in the unstimulated colon. Higher release was achieved in the USPII at 25, 50 and 100 rpm. Although conclusions cannot be drawn on the shear rates likely to have occurred from this comparison, since a constant shear is applied in the USPII and shear in the DCM has a high spatiotemporal dependence [15, 16]. Previous MRI studies of the DCM found velocities to vary from -2.16 – 0.78 cm s^{-1} and shear rate fluctuating between 0–8 s^{-1} when slower CPPWs were applied (0.4 and 0.8 cm s^{-1}) at the same volume and viscosity as in this study.

The variability in the overall release profile in the DCM was high compared to the USPII, likely due to the increased number of steps included in data processing. However, there was similarly high variability in direct measurements, e.g., the concentrations presented in Figure 6.4. This may better reflect the level of variation in vivo due to position of the tablet in relation to contractions and potential to experience elevated shear from being squeezed between contracted haustra, amongst many other factors. Regarding use of the f_2 approach to classify profiles as statistically indifferent/different from one another in this study, caution must be taken around the level of significance used. This method is typically used to compare dissolution profiles between products, rather than of the same product using different dissolution methods [339]. However, since the same formulation and dissolution media are used in all experiments and the dosage form is intended for extended release, it would be highly unusual for the product to exhibit $>$ 10 % difference at the earlier stages of dissolution. Additionally, the majority of official guidance from governing bodies worldwide regarding acceptance criteria for f_2 comparisons are for immediate release formulations rather than extended-release formulations where time is integral for matrix hydration, gel formation and erosion to take place.

6.5 Conclusions

The in vitro dissolution of theophylline from Uniphyllin Continus 200 mg ER tablets was assessed in the USPII and the dynamic colon model (DCM). In the DCM, different motor patterns previously identified in vivo were replicated using the DCM: baseline conditions for a healthy adult human, antegrade and retrograde cyclic propagating pressure waves (CPPWs) and the stimulated (using PEG or maltose) colon. The intensity of hydrodynamics induced by motility patterns was measured using a motility index that incorporated luminal occlusion rate and the number and frequency of segmental contractions.

Release from the ER tablets was sensitive to agitation speed in the USPII dissolution apparatus. The integration of biorelevant motility into the DCM provided predictions on the extent as well as variability of drug release that may be anticipated from an ER formulation subjected to intestinal hydrodynamics, as a function of motor pattern and position.

Mimicked baseline contractions were highly ineffective at advective transport of dissolved drug along the DCM tube and maximum release was $>$ 20 % lower than in the USPII at 25 rpm. Operating patterns with such low motility may encounter potential solubility effects on the rate of release measured in segments containing the tablet body, especially considering vehicles with a poorly soluble payload. Motility patterns which include more frequent retrograde propagating pressure waves may be more effective at achieving higher release of a therapeutic from a dosage form located towards the early stages of the proximal colon (compared to antegrade propagating waves). When mimicking the stimulated colon, a higher theophylline release was achieved than in the USPII at 25 rpm, although it is unrealistic to maintain these conditions for 24 h in vivo. Operation of the USPII at a constant rate of 25 rpm and above generates hydrodynamics conditions that may be too intensive to be representative of unstimulated human colon.

Chapter Seven

Application of the DCM as a biopredictive tool for controlled release theophylline formulations through integration into physiologically-based biopharmaceutics modelling (PBBM)

7.1 Introduction

Physiologically Based Biopharmaceutics Modelling (PBBM) techniques have been highly successful for prediction of PK profiles of orally administered immediate release (IR) formulations. In IR formulations, the dosage form is typically designed to achieve drug release almost instantaneously upon reaching the stomach and absorption is completed in the proximal small intestine. In vivo pharmacokinetic (PK) parameters are then estimated according to the physicochemical properties of the drug molecule in combination with the GI physiology. However, PBBM approaches face difficulty with controlled release (CR) formulations, wherein drug release is controlled by the presence and action of excipients, for example, polymeric compounds in CR hydrophilic matrix formulations. Release from these formulations is dependent on the kinetics of multiple processes such as hydration, swelling and erosion of the polymer to control drug release.

A significant portion of drug release may occur in the colon [17, 80, 343–345]. Inside the colon, hydrodynamic forces arising from the interplay between motor patterns, gastrointestinal (GI) fluid volumes and viscosities drive erosion of the tablet and are significant in controlling drug release. However, the colon is well documented to exhibit irregular motility patterns [35, 41, 346], lower fluid volumes [27], elevated media viscosity and a lack of bile salts [13]. These factors present a significant hindrance to dissolution compared to regions of the upper GI tract. Moreover, absorption is limited by a lower surface area. It is therefore unsurprising that colonic absorption has been recognised as a challenge in current biopharmaceutics modelling capabilities [347, 348]. Intracolonic dosing studies using remote controlled capsules that deliver a solution of drug to the colon have been carried out to measure colonic absorption [349, 350]. This chapter aims to contribute to the understanding of colonic absorption modelling by integrating in vitro release profiles measured inside the Dynamic Colon Model (DCM) or USP dissolution apparatus into commercially available PBBM platforms. The DCM is an in vitro model of the human proximal colon, with a geometric and hydrodynamic design rooted in in vivo MRI

data. In vitro, the colonic environment is not accurately captured by compendial dissolution apparatuses, such as the United States Pharmacopeial (USP) Apparatus II (USP II) which consists of a vessel with a hemispherical base stirred by a constantly revolving bi-winged paddle. There are key differences based on the frequency and magnitude of spikes in shear rate in vivo which are the driving force for drug release from polymeric matrix CR formulations via erosion. Chapter 6 demonstrated that inter- and intrasubject variability in mimicked colonic motor patterns has a significant influence on the dissolution of theophylline from Uniphyllin Continus® (UC) 200 mg CR tablets (Napp Pharmaceuticals) inside the DCM [17]. This chapter aims to clarify whether this variability in hydrodynamic conditions may translate to similar variability in absorption by building and validating a PBB model of oral theophylline administration and then importing the dissolution profiles as different release profiles. A 400 mg UC formulation is also investigated to understand how observations translate with dosage. Since there is no absorptive component in the DCM, yet dynamic fluid secretion and absorption processes occur in vivo, theophylline was selected as the model drug to avoid any potential solubility/permeability limited process which can affect the dissolution rate in the DCM.

Since PBBM platforms cannot currently model the interplay of excipients with the dynamic GI environment which controls release from orally administered CR formulations, the standard approach is to import in vitro release data for use as an in vivo release profile for simplicity. However, this methodology is designed with USP equipment in mind, where the concentration of dissolved drug is universally measured in samples collected from a single, predefined and reproducible location over a period of time. USP vessels are assumed to be homogenously mixed, however it is well documented that the validity of this assumption decreases drastically with increasing fluid viscosity [277]. This is a particularly important factor to consider when modelling colonic dissolution.

For CR formulations that transit through multiple environments in the GI tract during their extended release, the need to account for regional differences in absorption and

dissolution adds complexity. The nature of the DCM in terms of its orientation and geometry (which reflects that of the human AC) means that acquiring spatial information is essential to understand how dissolved drug concentration varies as a function of space and motility inside a model intestinal environment. Spatiotemporal dissolution data from the DCM may be valuable for improving in silico predictions of absorption in the lower GI tract. Following the standard methodology, the DCM provides the opportunity to construct a high-resolution global dissolution profile of drug from a CR dosage form using an average of the concentration measurements taken at each point in space per unit time that is likely to better describe in vivo release than using the USPII. Further, raw concentration data measured at different segments of the DCM offers the opportunity to develop regional release profiles along the length of the DCM. Since different compartments exist in silico for the lower GI tract (e.g., caecum and AC) with distinct properties (surface area, pH, volume, etc.) that govern absorption, spatial release data from the DCM may be manipulated to produce individual release profiles for the caecum and AC to improve the predictivity of PK characteristics of CR formulations in the lower GI tract.

7.2 Methodology

7.2.1 Dissolution experiments

Chapter 6 presented dissolution profiles of the UC tablet (200 mg) obtained from USP II filled with 900 mL pH 7.4 phosphate buffer at 25, 50 and 100 rpm and from the DCM II filled with 900 mL 0.25 (w/v) NaCMC solution buffered to pH 7.4, under six different motility patterns [17].

Following the same protocol, dissolution experiments were also conducted for UC 400 mg tablets using the USP II (900 mL) and the DCM. This involved experiments at 25, 50 and 100 rpm in the USPII and using two different motility patterns: baseline and a

retrograde propagating wave, in the DCM. To ensure potential solubility challenges were avoided, the sample volume was doubled from 1 mL per sample point, to 2 mL (Figure C.1 (Appendix 3) shows how sample size may be used to mimic in vivo colonic water absorption). Media replenishment was modified accordingly to account for this change.

7.2.2 PBB model development

A PBB model of theophylline absorption, distribution, metabolism and elimination was built using GastroPlus® v9.8.2 (SimulationsPlus). For in vivo studies where sufficient information about the population was available, specific population based pharmacokinetic (PBPK) models were built based on that population. PK parameters of theophylline were derived from the non-pregnant populations reported in Habib *et al.* [351], Lombardo *et al.* [352] and Abduljalil *et al.* [353] as shown in Table 7.1.

Table 7.1: PK parameters used in the GastroPlus® PBB model.

PK parameter	Value	Source
Blood to plasma ratio	0.815	[351]
Fraction unbound in plasma (F_U)	0.5	[352]
Effective permeability P_{eff}	7.2×10^{-4}	[354]
Diffusion coefficient D	0.853	[354]

7.2.3 Distribution and clearance optimisation and model validation

In Gastroplus®, theophylline was dosed as intravenous (IV), oral solution (OS) or oral tablet (OT) according to the clinical study. The distribution of theophylline throughout bodily tissues was described using a full physiologically based pharmacokinetic (PBPK) model. Clinical data for IV infusions were used to optimise the clearance and distribution

parameters for theophylline [355–358]. The performance of the established model to predict theophylline PK was then validated using clinical data for oral solutions and tablets. The information in Table 7.2 was used to inform PBPK models to predict the data in each clinical study.

Table 7.2: Past clinical studies and the associated virtual clinical trial parameters used to build and validate the PBBM model of theophylline. Admin. = administration.

Trial code	**Dosage form**	**Theophylline dose**	**Admin. duration**	**N trials**	**Subject information**
IV A [355]	Single IV infusion	7.3 mg kg^{-1}	30 mins	20	14 (0 % women) aged 19 - 35 years
IV B [356]	Single IV infusion	7.3 mg kg^{-1}	30 mins	20	20 (50 % women) aged 24 - 57 years
IV C [357]	Single IV infusion	240 mg	45 mins	20	10 (100 % women) aged 22 - 26 years
IV D [358]	Single IV infusion	151.2 mg	20 mins	20	13 (0 % women) aged 20 - 39 years)
OS A [359]	Single oral dose (solution)	3.4 mg kg^{-1}	-	20	10 (56 % women) aged 18 - 36 years)
OS B [360]	Single oral dose (solution)	5 mg kg^{-1}	-	20	12 (0 % women) aged 23 - 39 years)
OS C [361]	Single oral dose (solution)	5 mg kg^{-1}	-	20	10 (50 % women) aged 22 - 35 years)
OS D [356]	Single oral dose (solution)	7.6 mg kg^{-1}	-	20	10 (50 % women) aged 22 - 57 years)
OT A:D [362]	Single oral dose (tablet)	125, 250, 375 and 500 mg	-	20	10 (50 % women) aged 22 - 35 years)

7.2.4 Optimising the PBB model for colonic absorption

Next, the PBB model was optimised for colonic absorption, guided by clinical data. In both available clinical studies of colonic delivery of theophylline, the experiments were reported to fail for all but one participant. The C_p-time data was available for the Staib *et al.* [350] study, but not for the Clear *et al.* [349] study without inaccurate estimations using a plot digitiser due to the scale of the axes compared to the plotted data. Therefore, the C_p-time profile observed in Staib *et al.* [350] following direct administration of theophylline solution to the AC using an ingestible tracked capsule was used to guide optimisation of the PBB model for colonic absorption of theophylline. To mimic intracolonic dosing, the transit times of the GI compartments prior to the caecum were set to 0.00001 h, forcing the tablet to be intact when it reaches the caecum.

Initially, the default human caecum and AC transit times (4.19 and 12.57 h respectively) and absorption scale factors (ASFs) (0.352 and 0.823) were used. Next, the caecum compartment was removed to explore the effect of just using the AC compartment on colonic absorption. Predictions were considered successful if the observed PK profile fell within the 95^{th} and 5^{th} percentile of predicted data and predicted PK parameters were within 0.5- to 2-fold of the observed data [363].

Ultimately, the PBB model was adjusted to predict absorption using two methods: model 1 manipulated the ASF value to 1.68 (the surface area to volume ratio of the DCM partially filled with 100 mL). Model 2 used the optimisation module in GastroPlus to optimise for ASF.

7.2.5 Modelling CR formulations

In Gastroplus® the CR dosage form can be modelled as either a 'CR' integral tablet, where drug is considered to be dissolved instantaneously upon release, or as a 'CRU' integral

tablet, where released drug is undissolved. Therefore, the same dissolution profile measured in vitro can be treated as either a release or dissolution profile via this setting. Since theophylline is a highly soluble drug that may dissolve within the hydrated polymeric tablet before release by diffusion or erosion, UC 200 mg tablets were modelled using the 'CR integral tablet'. Finally, to capture the prolonged duration of release from CR formulations, AC transit time was extended to 32 hours, which is in line with figures in the literature [13, 364]. To support this further, Staib *et al.* [350] showed that intracolonic dosing of theophylline in the descending colon is not significantly different than in the AC, therefore the AC in Gastroplus® is essentially representing the entire colon in this model.

7.2.6 Importing global and regional dissolution profiles to the PBB model

The in vitro dissolution profiles of UC 200 mg tablets measured in the USP II and DCM (in Chapter 6) under a range of hydrodynamic conditions were separately imported to the modified ACAT model of Gastroplus® as in vitro release profiles required for modelling a CR tablet.

Release profiles were imported using one of two ways: Using the standard methodology of importing the dissolution profile measured in vitro as the global release profile, the tablet begins releasing drug immediately following oral administration. In the default Gastroplus® ACAT model, there is a transit time of 3.47 hours from the oral cavity until the caecum. Since the dissolution experiments were carried out using the DCM, this means that release under mimicked colonic conditions (pH, fluid volume, geometry and hydrodynamics) in the DCM is used to describe the first 3.47 hours of release in the upper GI tract, followed by the caecum (default 4.19 hours) and the colon compartment that was optimised according to the methodology described above.

The second method applies only to the DCM, is referred to as the 'regional ap-

proach' from herein and is described as follows. The in vitro release profile measured at segment 1 of the DCM was imported as the in vivo release profile of the caecum in Gastroplus®. To achieve this, the transit times of the GI compartments prior to the caecum were set to 0.00001 h, forcing the tablet to be intact when it reached the caecum. The caecum transit time was then set to the 36.19 h, the total that is seen in the optimised ACAT model above (4.19 h caecum plus 32 h AC) and the AC transit time was set to zero. This translates as a significant portion of the tablet residing in the caecum for an extended period of time during release. The simulation was then run to obtain an in vivo absorption profile for the caecum.

The same process was followed for the AC (transit time until AC = 0.00001 h, transit time of AC = 36.19 h), where release in the AC was described by the concentration measurements taken at segments 3, 5, 7 and 10, including interpolated measurements at segments 2, 4,6, 8 and 9. The absorption profiles for the caecum and AC were summed at each time point to obtain an absorption profile that was informed by regional concentration measurements inside the DCM.

7.2.7 Implementing the PBB model

In the reference UC tablet clinical trials, there were N = 12 subjects for the UC 200 mg study and N = 6 subjects for the 400 mg study [365]. Given the low number of subjects, simulations were carried out using the Gastroplus® (PEAR) population simulator modelling a healthy population of 26 humans; 50 % male; 50 % female; aged from 20 – 50 years; weight between 50 – 85 kg.

7.2.8 PBBM of absorption in the lower GI tract under different motility patterns

In Gastroplus®, the lengths of the caecum and AC are 13.19 and 27.65 cm respectively. The DCM is 28 cm long. Using the same ratio of AC to caecum, 0.48, as used in Gastroplus®, concentration measurements from S1 – S4 in the DCM would be assessed as the caecum. However, the DCM was designed to replicate the anatomy and hydrodynamics of the AC, it is essentially the same length (28 cm) as the AC in Gastroplus® (27.65 cm). Although there is no direct replication of the caecum, dosage forms are inserted into the DCM through a mimic ileocaecal junction (ICJ), located in the middle of segment 1 and the bulk of the tablet typically resides there for the entire duration of the dissolution experiment [17] unless a high amplitude propagating pressure wave (HAPW) is mimicked [9].

In this research, the concentration profiles measured at segment one of the DCM, inferior to the tablet insertion point, were integrated into Gastroplus® as release data for a CR tablet in the caecum. Data from segment 2 until the hepatic flexure were integrated to Gastroplus® to inform release in the AC. Similar to the in vivo situation, the caecum is continuous with the AC in this set up.

Since the human colon exhibits a range of motility patterns through the day, an average release profile was established using a weighted average of the different profiles obtained under different motility patterns. A weighted average profile was calculated according to the frequency of different motility patterns observed in vivo.

7.2.9 Comparison of dissolution profiles following deconvolution of in vivo data

Another method for comparing in vivo PK data with in vitro dissolution profiles is to run a mechanistic deconvolution of the observed C_p-time profile in Gastroplus® to obtain an in vivo release profile that would be predictive of a clinical C_p-time profile. However, problems arise due to clinical C_p-time data only being available for a single dose on day 6, with no information to describe the drug plasma concentration in the first 6 days [365]. For this approach, the data was translated forward by 120 h and the concentrations were divided by the estimated accumulation ratio (AR). Two key approaches exist to estimating the accumulation ratio. The first is according to Equation 7.1:

$$AR = \frac{1}{1 - e^{-k*\tau}} \tag{7.1}$$

Where τ is the dosing interval (24 hours in this study) and k is the elimination rate constant, described by equation 7.2:

$$K_L = \frac{Cl}{V} \tag{7.2}$$

Where Cl is the clearance (2.72 $L\,h^{-1}$) and V is the volume of distribution (29.96 L). The resulting value for AR is 1.13 using this method.

The second approach is based on the ratio between exposure parameters observed clinically at steady state for a single dose and for a multiple dose. However, since this information is unavailable for the 200 mg tablet, single dose data was extracted from the Simcyp model at that successfully predicted this data, giving AR = 1.6 [20]. Other approaches include taking ratios of key PK parameters, such as the area under the plasma concentration (C_p)-time curve (AUC) and the trough in the C_p-time curve (C_{min}), so there

is inherently a variability in the AR value that can be reached. In this work, the highest and lowest values of AR (1.6 and 1.13) were taken forward to examine the extent to which calculation methodology can affect the deconvoluted dissolution profile and subsequently the prediction of the 6-day data when that deconvoluted profile is imported at a CR profile. The translated data is presented in Figure 7.1.

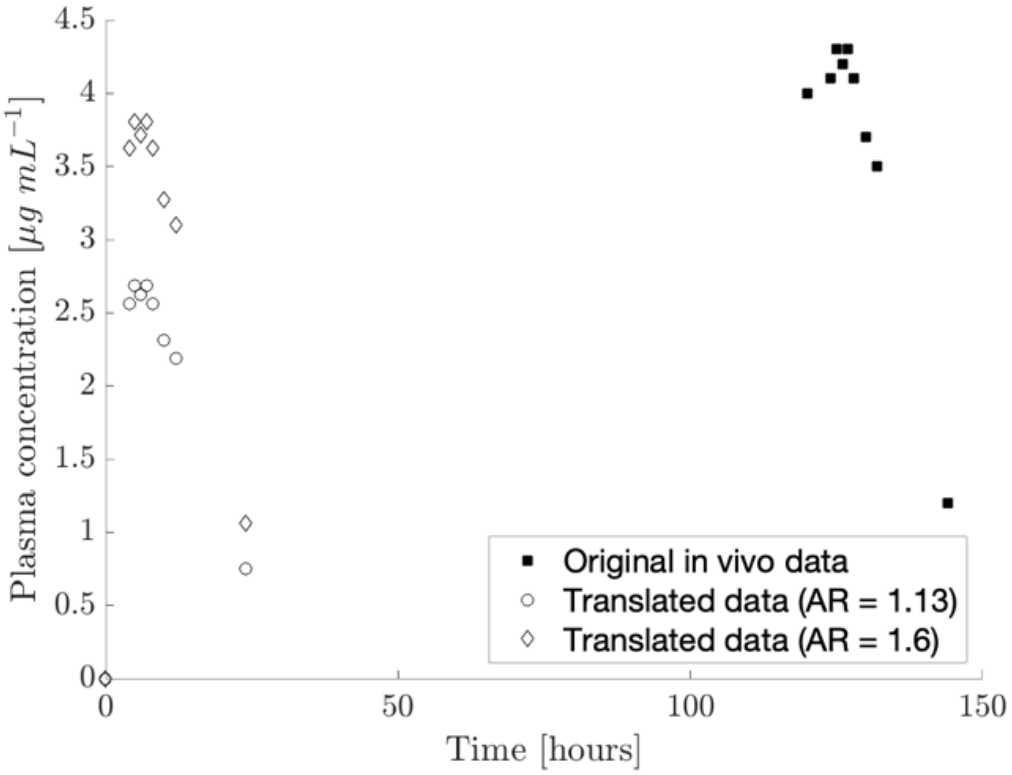

Figure 7.1: Original clinical data for a single dose of UC 200 mg administered on day 6 plotted alongside the translated dataset for administration at t = 0 hours. [365]

7.2.10 Statistics

PBPK model predictions were considered successful and acceptable if the measured C_p-time profile in vivo fell within the 5th and 95th percentile of predicted data (90 % prediction error) and the predicted PK parameters fell within 0.5- to 2-fold of the observed data. Calculations were made from the data generated by the population simulator in Gastroplus®

for the representative population.

The ratio of observed (obs) to predicted (pred) values for PK parameters was used to assess the performance of the PBB model.

7.3 Results and Discussion

7.3.1 Model development and validation

Figure 7.2 presents the mean C_p-time predictions made by simulations of theophylline administration using the PBB model developed in Gastroplus® for twelve sets of in vivo data. Firstly, IV data (Figure 7.2 IV A to D) was used to optimise the partition coefficient K_p (16.0 and 0.13) and clearance (2.40 and 0.31 L h-1) for the liver and kidneys respectively. The model was then further validated using oral solution (OS) data (Figure 7.2 OS A to D) and oral tablet (OT) data (Figure 7.2 OT A to D). Generally, the observed and predicted datasets were well aligned, shared a similar form and the observed data fell within the 90 % prediction window (shaded). Table 7.3 presents a comparison of the predicted PK parameters from the PBBM simulations against the observed data where available. All predicted PK parameters fell within the 0.5- to 2-fold interval of observed data. Overall, the model was considered to successfully predict all cases of clinical data for theophylline known to the authors.

7.3.2 Optimising the model to predict colonic absorption

Staib *et al.* [350] studied the regional absorption of theophylline solution using an ingestible capsule that released the contents on demand. This data was used to optimise the PBB model for colonic absorption. Figure 7.3 shows the predicted absorption following simulations of theophylline IR solution administration to the caecum (A) and AC (B). Both models overpredicted the in vivo data. Simulated caecal administration better predicted maximum plasma theophylline concentration (C_{Max}) and AUC than AC administration using the default parameters in the Gastroplus® ACAT model. However, to further improve the predictions, it was necessary to remove the caecum compartment in order to maintain a good replication of the high absorption rate observed (without using unreasonably low

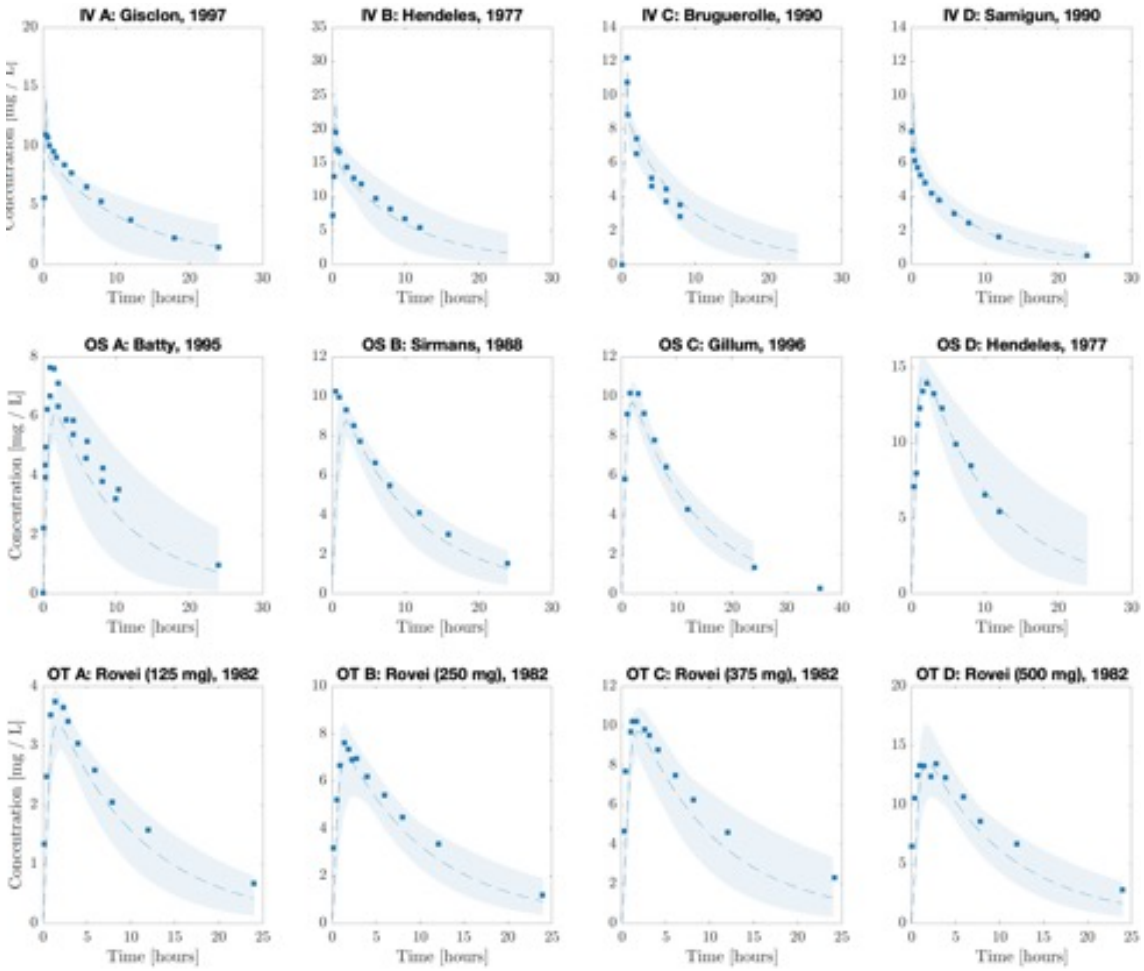

Figure 7.2: PBBM predictions of IV, OS and OT clinical studies. The shaded bands show the 90 % prediction error around the mean prediction (dashed line).

Table 7.3: Observed and predicted key PK parameters for theophylline.

Study	C_{Max} [mg L^{-1}]			**AUC** [mg h L^{-1}]		
	Obs	Pred	Ratio	Obs	Pred	Ratio
IV:A	10.7 ± 1.3	14.2 ± 12.4	1.32	126 ± 30	101 ± 24	0.80
IV:B	NA	24.0 ± 2.6	NA	184 (95 – 287)	149 ± 25	0.81
IV:C	10.7	11.3 ± 1.8	1.05	176 ± 35	76 ± 19	1.00
IV:D	NA	9.9⁄1.3	NA	NA	51 ± 11	NA
OS:A	NA	6.0 ± 0.6	NA	86	71 ± 18	0.83
OS:B	NA	9.1 ± 0.8	NA	134 ± 34	103 ± 15	0.77
OS:C	10.9 ± 1.1	9.8 ± 0.6	0.90	140 ± 24	116 ± 14	0.83
OS:D	15.3 (13.0 – 20.0)	14.8 ± 0.7	0.97	173 (88 – 283)	158 ± 39	0.91
OT:A	4.1 (3.0 – 6.7)	3.4 ± 0.4	0.83	52 (31 – 94)	36 ± 7	0.69
OT:B	8.0 (5.0 – 12.1)	7.0 ± 0.9	0.88	106 (69 – 172)	75 ± 13	0.71
OT:C	10.5 (6.7 – 15.0)	9.9 ± 0.9	0.94	161 (75 – 272)	104 ± 27	0.65
OT:D	15.1 (10.7 – 20.5)	13.8 ± 1.8	0.92	210 (136 – 373)	144 ± 27	0.68

ASF, < 0.1, essentially rendering it obsolete, but present). The ASF was optimised using the optimisation module in GastroPlus® where it was found that ASF = 0.6 provided the best fit ($R^2 = 0.93$).

The colonic absorption model achieved C_{Max} of 1.86, which is 1.25- fold of the in vivo prediction. AUC was 1.49- to 2.01- fold of the observed value. The distribution phase was not captured well by any model, which seemed to be the main cause of the overprediction of AUC. However, the model showed good predictivity in the 8 other clinical studies (N = 109) used for validation (Figure 7.2), therefore the results of this small scale clinical study by Staib *et al.* [350] (N = 1 for AC administration and N = 3 for oral administration) carry less significance. Thus, the focus of this development work was on replicating the colonic absorption phase of the data, rather than the distribution and clearance which have been validated as previously described. Staib *et al.* [350] observed the AUC of the C_p-time profile following intracolonic administration to be 79 – 87 % of the AUC in the oral administration study. Similarly, Clear *et al.* [349] showed that intracolonic administration of IR theophylline formulation led resulted in an AUC 85 % of the AUC and C_{Max} of 61 % for oral administration of the same IR tablet. The PBB model optimised for colonic absorption had an AUC and C_{Max} of 78 and 71 % of the predicted exposure following administration of an oral solution. The results are similar, but again since N = 1 for both clinical studies, may not be a reliable means of validation.

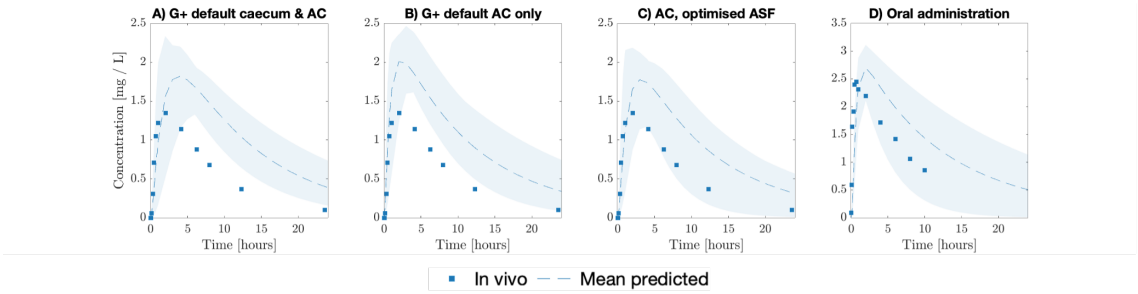

Figure 7.3: Optimisation of Gastroplus® PBB model for colonic absorption using existing clinical data [350].

The PBB model optimised for colonic absorption (Figure 7.3C) was implemented

going forward.

7.3.3 Predicting theophylline absorption by integrating USP II dissolution data under different paddle speeds

The in vitro dissolution profiles (presented in Chapter 6) of UC 200 mg tablets in the USPII and DCM under a range of hydrodynamic conditions were separately imported to the modified PBB model as in vitro release profiles for a CR tablet. The DCM motility patterns are as described in Chapter 6.

Standard dissolution experiments are typically carried out in the USP II, with concentration measurements taken at a single, standardised spatial coordinate. This produces a one-dimensional concentration profile, where dissolved drug concentration varies as a function of time only. Hence, the standard CR methodology in Gastroplus® is to import a single in vitro dissolution profile as an in vivo release profile where the tablet begins releasing drug immediately following oral administration. However, when using advanced in vitro dissolution apparatus that mimic particular regions of the GI tract, this may result in inaccurate PK characteristics. Figure 7.4 shows the predicted absorption profiles of theophylline using dissolution profiles from the USP II under different paddle speeds as in vivo release profiles. Predicted absorption rate increased significantly with paddle speed, as expected since the in vitro release profiles were so different. Figure 7.6 displays the predicted fraction absorbed, f_a. Although the dissolution rate increased after t = 3 h in vitro, this was not mirrored by the absorption profiles since after t = 3.47 h, when the simulation predicted the tablet to be in the caecum, where the ASF (0.38) is significantly lower than the compartments in the duodenum (2.80), jejunum I and II (2.75 and 2.73) and ileum I, II and III (2.70 2.65 and 2.58, respectively), calculated using the Opt LogD Model SA / V 6.1. This reflects the known differences in absorptive capacity between the small and large intestine in vivo. Figure 7.5 illustrates the predicted regional absorption profile

of theophylline following the release profiles in the USP II under the different agitation speeds. Clearly, the most significant portion of theophylline is predicted to be absorbed in the colon.

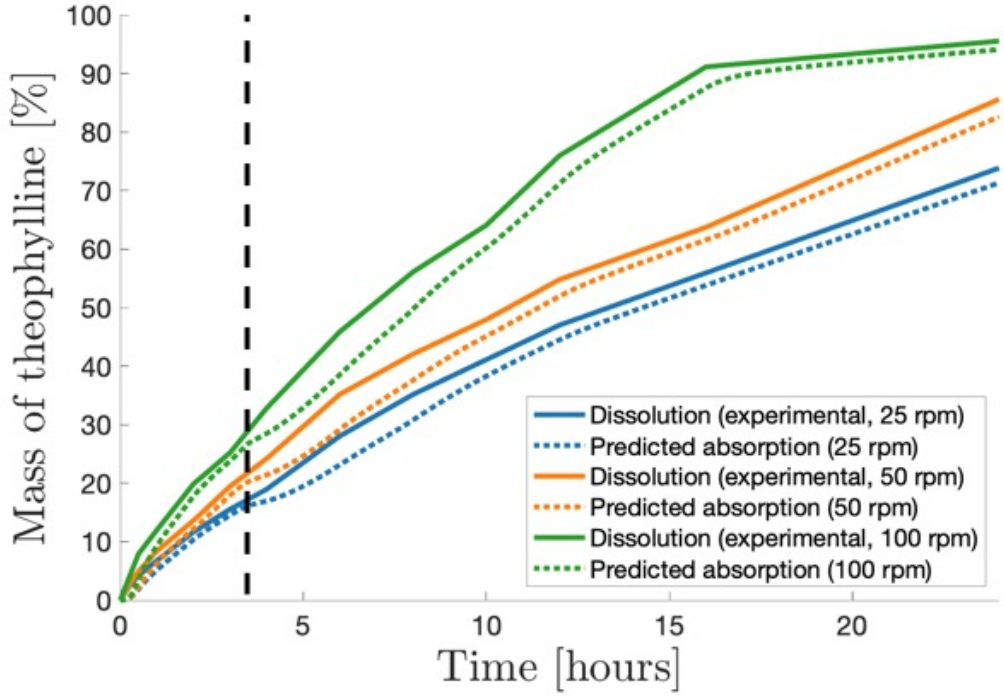

Figure 7.4: Effect of USP II paddle speed on predicted absorption of theophylline from UC 200 mg tablets when importing mean dissolution data [17] to the PBB model.

7.3.4 Predicting theophylline absorption by integrating DCM dissolution data under different motility patterns

Using the DCM, it is necessary to withdraw samples from various locations along the length of the DCM to understand how dissolved drug concentration varies as a function of space. Chapter 6 showed that the motility pattern significantly influenced the concentration profile of dissolved theophylline measured at different segments of the DCM lumen

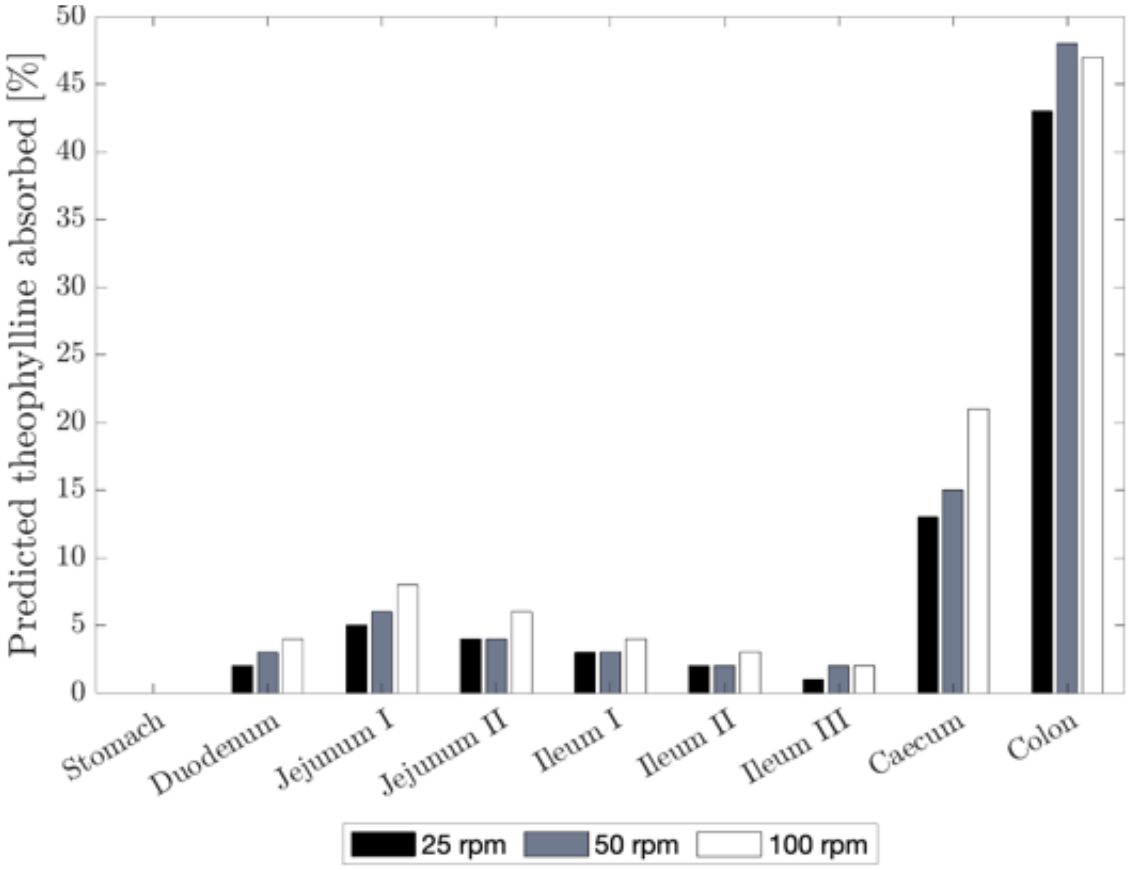

Figure 7.5: Regional absorption in the 24 hours following oral administration of the UC 200 mg tablet having imported USP II dissolution profiles into the PBB model.

due to the ability of peristaltic patterns to transport dissolved drug away from the tablet body and homogenise the contents of the lumen. An average of these segmental concentration profiles can be used to obtain an estimate of the total drug dissolution profile inside the DCM overall; the precision of which increases with the number of spatial sample points. The overall dissolution profiles measured under the baseline, antegrade and retrograde waves were similar over 24 h, these are presented in Figure 7.6. However, the regional in vitro dissolution profiles of these motility patterns varied. The distribution of theophylline throughout the DCM lumen was more homogenous under the action of the antegrade and retrograde propagating waves, as these patterns facilitated advective transport of dissolved theophylline along the length of the DCM tube. Contrarily, the baseline motility pattern led to higher accumulation of theophylline around segment 1, the 'caecum' of the DCM tube, where the tablet body remained for the duration of the dissolution experiment.

Thus, dissolution profiles measured from different segments could be used to model in vivo release in different compartments of the lower GI tract to improve predictivity of the PK characteristics of CR formulations. Figure 7.6 also displays the predicted theophylline absorption profiles from UC 200 mg tablets using the standard methodology (global release profile) and by importing the release information as separate regional release profiles. Since the DCM only models the lower GI environment, intracaecal and intracolonic dosing was mimicked for the 'regional' approach, such that the tablet immediately reached the caecum or AC and begins release according to the equivalent segmental profiles.

Figure 7.6 shows that the dissolution profiles, originally presented in Chapter 6, are sensitive to colonic hydrodynamics. Since only the fraction of drug that has dissolved is available for absorption, the predicted absorption profiles are clearly also inherently sensitive to colonic hydrodynamics. This demonstrates the importance of the segmented lumen of the DCM in mimicking colonic motor patterns observed in vivo, since this enables understanding of how different levels of shear, tablet erosion and dissolved drug distribution may translate to absorption in vivo. Further, this demonstrates the ability to predict PK

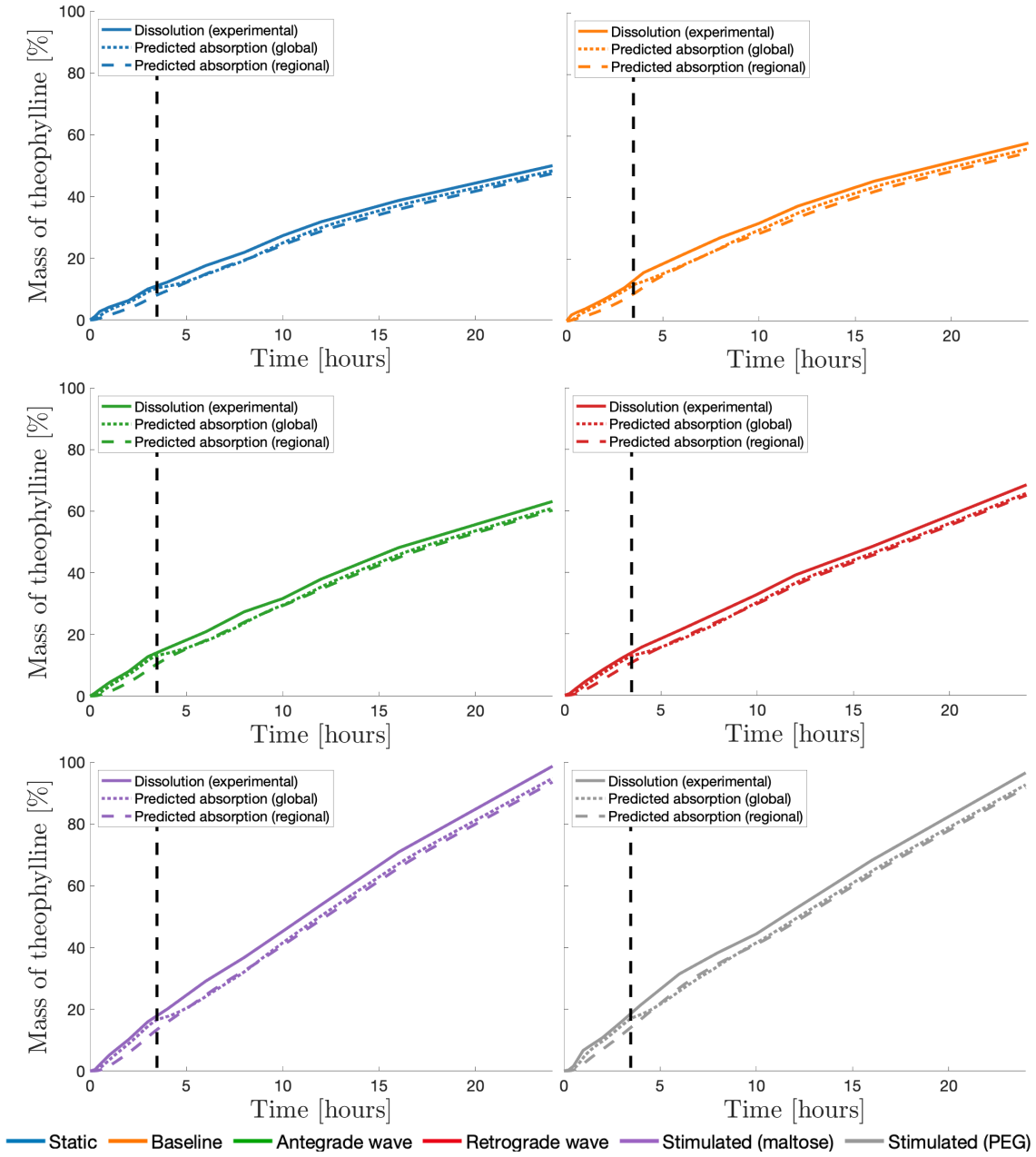

Figure 7.6: In vitro dissolution profiles of theophylline from UC 200 mg tablets in the DCM and predicted absorption profiles from importing the dissolution data as global or regional release profiles in separate simulations. The dashed line t = 3.47 h represents the default duration of transit from oral administration to the caecum in the Gastroplus® ACAT model.

data for populations that have known levels of motility, such as dampened motility, wherein the baseline pattern is likely to be better predictive than the stimulated patterns.

This is especially true for non-disintegrating CR dosage forms where unreleased drug material appears to remain locked up in the tablet body that is not easily fragmented due to the viscous gel layer formed upon hydration.

Typically, the mass of theophylline absorbed lagged behind the mass dissolved by 2 – 3 % from t = 10 h onward using both simulation approaches. So, the total fraction absorbed, f_a, presented in Table 7.4, was consistently lower for the regional approach, however not significantly different than the global method.

Table 7.4: Mean total predicted theophylline fraction absorbed $f_{a,total}$ over the 24 hours following oral administration of a single dose of UC 200 mg tablet using the global (USP II and DCM) and regional approaches (DCM) to dissolution data integration.

	USP II			DCM					
	25	50	100	Static	Baseline	Antegrade	Retrograde	Maltose	PEG
Global	0.73	0.84	0.94	0.49	0.57	0.62	0.67	0.97	0.95
Regional	-	-	-	0.48	0.44	0.61	0.65	0.94	0.92

The key observation, however, is the difference in absorption rate between time t = 0 and t = 3.47 h (marked on the plots) between, the global and regional approach. Following the global method, the UC 200 mg tablet is administered orally and exposed to the upper GI tract according to the default transit times in the Gastroplus® ACAT model; predicted absorption profiles closely follow the associated dissolution profiles. Contrarily, the regional approach assumes intracolonic administration of the tablet. This is clarified by Figure 7.7 which presents the simulated compartmental breakdown of the predicted fraction of drug absorbed, f_a, after importing the global (left) and regional (right) release profiles. Following the global approach, a significant fraction of drug is absorbed in the upper GI tract, where the absorptive capacity is higher than in the caecum or AC (where the optimised ASF is 0.6 and the default is 0.73) as previously discussed.

On the other hand, the regional approach assumes the UC 200 mg tablets are immediately dosed to the colon. Colonic absorption lagged up to 15 (retrograde wave) to 20 % (static) behind the predicted absorption using the global approach in this time frame. Absorption rate was slowest for the static and baseline motility patterns where a lack of mixing capability (demonstrated by the elevated concentration profiles in segment 1 in Chapter 6) resulted in accumulation of dissolved drug in the caecum, which has the lowest ASF of all GI compartments that have absorptive capabilty in Gastroplus®. This was despite the elevated concentration gradient across the caecum wall. Furthermore, although the enhanced f_a in the colon compartment is also attributable to the extended transit time of the colon in the global approach, this is not the case for the regional model, which used equal transit times for the caecum and colon. This was based on in vitro observations in Chapter 6, where the tablet body remained at the point of insertion since no HAPW was mimicked, which can transport the tablet body along the length of the DCM [9].

With local toxicity in mind, the high accumulation of drug in the caecum region does not seem to lead to particularly high concentrations locally due to the low amount of drug released overall under baseline conditions. Comparably low index motility patterns (antegrade and retrograde waves) that better homogenised the continuous caecum-AC lumen led to higher predicted absorption rates. This is despite a homogenised lumen being hampered by low concentration gradients across the gut wall (the driving force for absorption). It remains unknown how this interplay would translate in vivo where the available surface area for absorption also increases with homogeneity of the lumen, since the distribution of water and drug according to a segmented luminal architecture is not replicated in the ACAT model.

These findings may translate significantly for subjects with impaired motility. A dosage form entering colonic space through the ileocaecal valve may reside in the caecum for an extended duration whilst dissolved drug accumulates locally and is not distributed throughout the continuous caecum-AC lumen. The result being a lower absorption rate

than predicted using standard PBB methodology, would lower the C_{Max} in vivo and may hinder drug efficacy.

In this work, the regional approach used a biorelevant in vitro dissolution tool that mimics the proximal colon to predict how theophylline absorption may vary based on colonic hydrodynamic conditions, from a dosage form that arrives to the colon intact. This provided valuable insights for colonic absorption from formulations which are demonstrated not to release drug before reaching the colon, or formulations where release phenomena do not begin to unfold in the upper GI tract. However, for many CR formulations, some release is likely to occur in the upper GI tract (such as the UC 200 mg tablet in this study). Therefore, it is recommended that future work involves an upper GI preconditioning step for CR formulations, prior to introduction to the DCM, to achieve the most accurate regional prediction model.

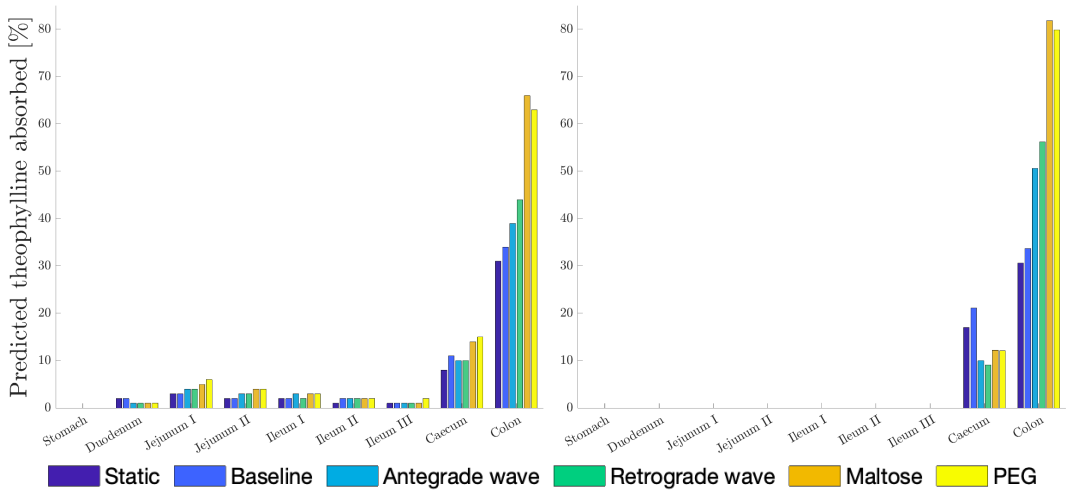

Figure 7.7: Compartmental absorption of theophylline using the global (left) and regional (right) approaches to importing DCM dissolution profiles from UC 200 mg tablets under different motility patterns.

This effect may be augmented here compared to the in vivo situation, since the AC compartment was used to model absorption in the entire colon, yet the default ACAT settings for fluid volume were used (10 %), which are the highest in the colonic region. Therefore, when integrating the regional dissolution profiles into the caecum and AC of

the ACAT model in Gastroplus®, there may have been a lower concentration gradient from free water in the lumen, across the mucosa and into the surrounding enterocytes.

Table 7.4 presents the mean f_a over the entire GI tract 24 h after administration of a single dose of the UC 200 mg tablet. Overall f_a was similar for the USPII at 100 rpm (0.94) and the DCM under stimulated conditions (0.97 and 0.95) when using the global and regional (0.94 and 0.92) approaches. However, the total f_a under baseline, antegrade and retrograde conditions did not exceed 0.70, while the USP II achieved 0.73 and 0.84 fractional release at 25 and 50 rpm respectively. The losses of theophylline ($100(1 - f_a)$ %) under baseline, antegrade and retrograde conditions were 43 & 56, 38 & 39, and 33 & 35 % using the global and baseline approaches respectively. This finding is in line with clinical observations by Clear *et al.* [349] where the amount of drug recovered from the Intelisite capsule post-defaecation was in the range of 34 – 54 % in most participants. These losses were not captured by the USP II and the DCM under mimic stimulated conditions. Figures 7.5 and 7.7 show that for all simulations of the USP II and DCM, the colon was the GI compartment in which the significant majority of absorption took place. This demonstrates that knowledge and understanding of the often-overlooked colon is paramount for improving the predictivity of PBB models for CR formulations. Further compartmentalisation of the colon in PBBM platforms could improve the predictivity of CR formulations where a significant portion of drug absorption occurs in the colon. The ASF is higher in the AC that the caecum, which would be similar in the transverse and distal colon according to Staib *et al.* [350], if calculated using the same Opt LogD Model SA / V 6.1. However, the introduction of a more detailed luminal environment of the transverse and descending colon may result in lower absorption compared to the caecum, such as progressive changes in media viscosity and volume from the caecum to the descending colon.

Although the motility patterns in this study were derived from in vivo magnetic resonance imaging (MRI) and high-resolution manometry studies, it remains unknown which combination of these patterns best describes a population of humans. In disease

states that are documented to exhibit lower motility, the absorption profile predicted from the baseline profile may be most accurate, which demonstrates a significant reduction in absorption for populations with such disease states. Absorption would be further hindered by comorbidities that reduce the surface area of the colon, such as Coeliac disease. Considering the static and baseline patterns, it is certainly possible that release and absorption may be higher in vivo than these predictions since passage through the ICJ and the occurrence of high amplitude propagating waves is likely to exert significant stress on a dosage form to erode the hydrated gel layer. However, passage though the ICJ occurs only once and the frequency of HAPWs is low at 3 – 4 per 24 h. The pylorus is less likely to have a significant eroding effect since hydration may have been insufficient before the gastric emptying time to facilitate significant erosion.

7.3.5 Predicting PK profiles for UC 200 mg tablets

Figures 7.8 and 7.9 present the resulting predicted C_p-time profiles after administration of a single dose of UC 200 mg each day for a 6-days, alongside the in vivo data [365]. Table 7.3 presents the PK characteristics predicted by the PBB model when importing dissolution profiles from the USP II and DCM and USP II for UC 200 mg tablets. Significant differences in the predictions of C_p-time profile, C_{Max} and AUC were observed with changes to the hydrodynamic conditions in both the USP II and DCM, where C_{Max} and AUC increased with rpm and MI_{DCM} respectively. This shows that important PK characteristics are sensitive to changes in hydrodynamic conditions that the CR dosage form is exposed to.

The PBB models built on the in vitro release profiles underpredicted the in vivo C_p-time data, although the closest predictions were achieved when integrating the more intense hydrodynamic conditions; in the USP II at 100 rpm and the DCM under stimulated motility. However, the SimCYP® PBB models published by Stamatopoulos et al. 2023

predicted the in vivo data well using the same in vitro dissolution profiles. In Gastroplus®, when modelling repeat doses of a CR tablet, any remaining unreleased material is immediately excreted upon administration of the next dose. Since the in vitro dissolution profiles do not show complete release before 24 h, a significant portion of the drug material is excreted before it can be released, resulting in significantly lower C_{Max}. This presents a limitation of using Gastroplus® for repeat dosing of CR tablets where complete release may exceed 24 h.

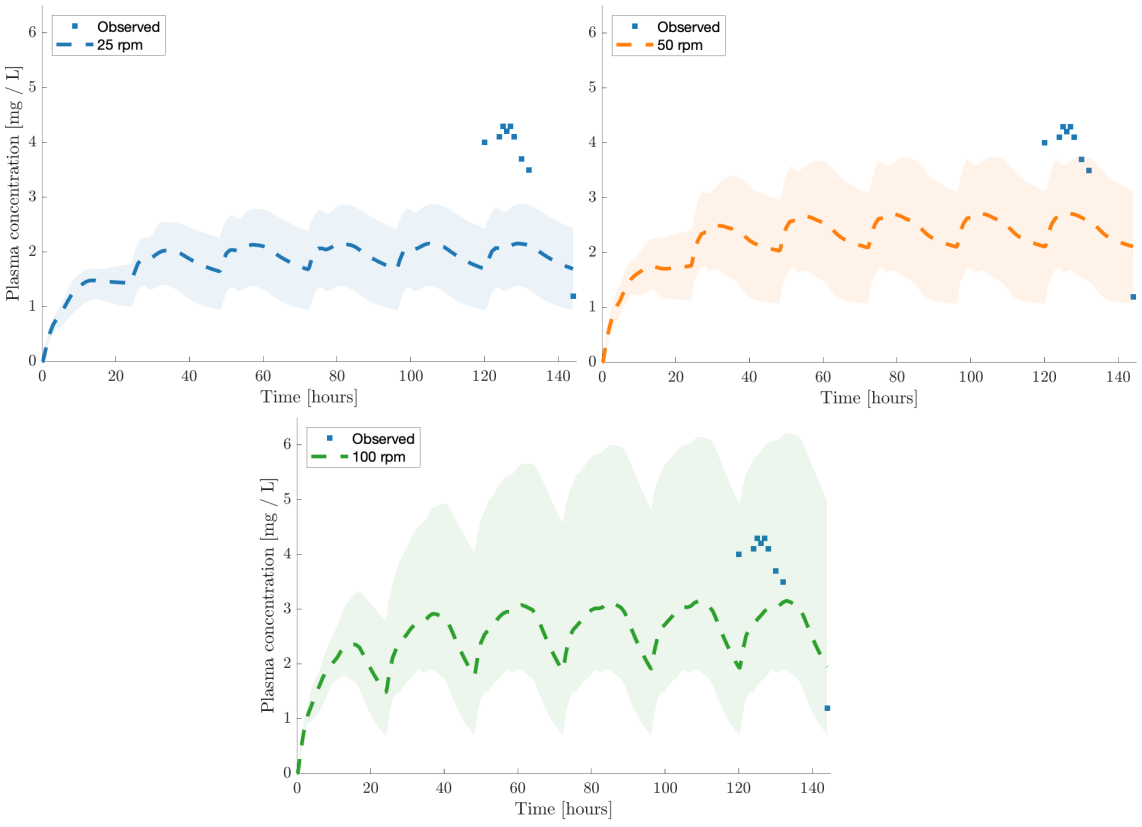

Figure 7.8: Predicted C_p-time data of theophylline from UC 200 mg tablets guided by in vitro dissolution profiles measured in the USP II under agitation speeds. Simulated administration of theophylline follows the nature of the clinical study: twice daily (b.i.d) for 5 days, with a single dose on day 6. The shaded region marks the 5^{th} to 95^{th} percentile of the predicted theophylline plasma concentration.

It can be assumed that the f_a of theophylline in the multiple day dosing simulations

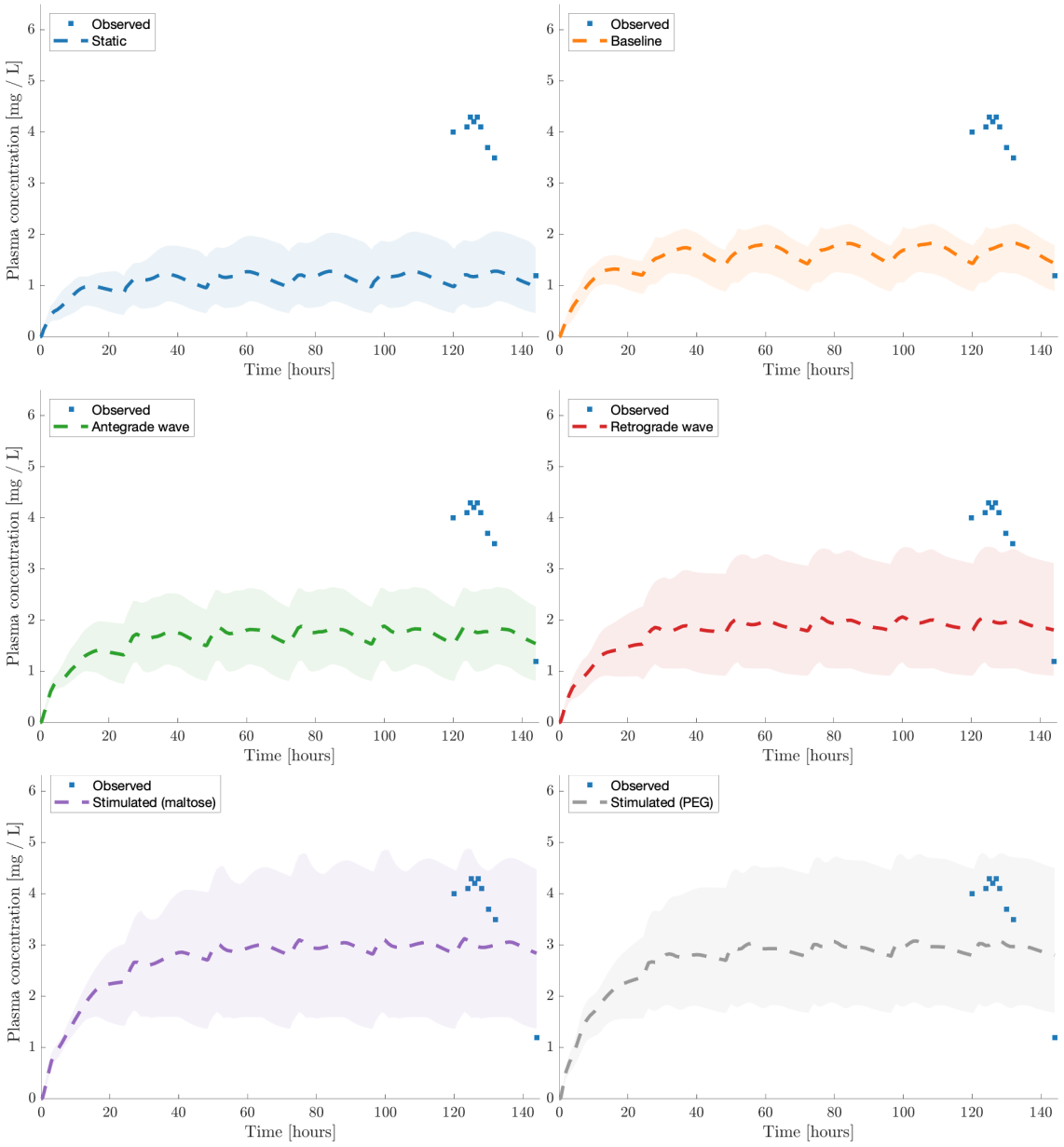

Figure 7.9: Predicted C_p-time data of theophylline from UC 200 mg tablets guided by in vitro dissolution profiles measured in the DCM under different motility patterns. The shaded region marks the 5^{th} to 95^{th} percentile of the predicted theophylline plasma concentration.

is not significantly different from the values presented in Table 7.3 for the 24 h simulation, due to the excretion of unreleased material at the 24 h mark (when the following dose is administered). Since the $f_a > 90$ % for the DCM under mimic stimulated conditions, it is likely that the PBB model would have underpredicted the observed PK data regardless of this limitation, despite validation of the model using a range of clinical studies where the distribution and clearance phases were captured well.

Due to this CR formulation limitation, simulations of multiple day dosing were not carried out using the regional approach implemented to probe absorption above. Additionally, the summative nature of the methodology would lead to inaccurate reproduction of the elimination phase since this is driven by the concentration in systemic circulation.

Figure 7.10 presents the predictions of the in vivo C_p-time data by the default Simcyp® model implemented by Stamatopoulos et al. , having optimised the ADAM for colonic absorption and imported the USP II and DCM dissolution profiles. In these predicted data, plasma concentrations of theophylline reach significantly higher levels, since in Simcyp® any remaining unreleased drug material is not immediately excreted after a subsequent dose. This setting may also be a contributing factor to why the clearance has a shallower gradient and better fits the in vivo data than the Gastroplus® model presented in this work. This was the first demonstration of the DCM being integrated into an in silico PBPK platform to improve predictivity compared to the USP II, which (alongside the stimulated patterns in the DCM) significantly overpredicts the in vivo data.

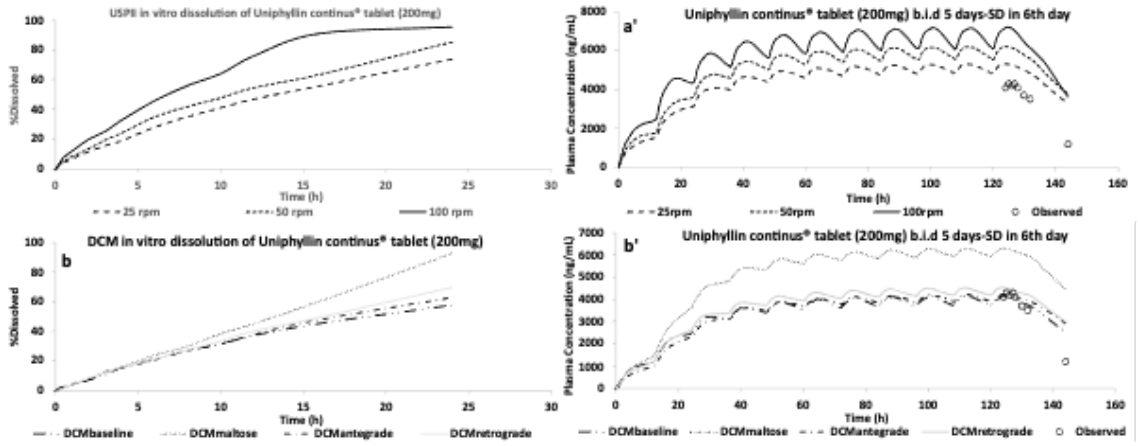

Figure 7.10: Average in vitro dissolution profiles of UC 200 mg tablet in USP II (a) and DCM (b) and the corresponding predictions (a' and b') of the plasma concentration of theophylline by the Simcyp™ model. This follows administration of Uniphyllin Continus® tablet (200 mg) b.i.d for 5 days, with a single dose (SD) on day 6. This figure is taken from Stamatopoulos *et al.* [20] with permission.

7.3.6 Correlating in vivo dissolution profiles of UC 200 mg tablets with in vitro dissolution data using a mechanistic deconvolution approach

In order to overcome the repeat dose problem in Gastroplus® a different approach to understanding the in vivo predictivity of dissolution in the DCM was taken. Instead of comparing predicted exposure data with the in vivo data, where limitations of the software prevent an accurate comparison, the in vivo data was translated from 6-day multiple dose data to single dose data from 0 – 24 h. Then, this data was mechanistically deconvoluted using the Gastroplus® in vitro in vivo correlation (IVIVC) module, to obtain an estimated in vivo release profile that can be directly compared against the dissolution profiles obtained in vitro. This would enable direct comparisons of the dosage form performance in the USP II and DCM and in vivo. Figure 7.11 A presents the upper and lower bounds of deconvoluted dissolution profiles using the established methodology for calculating AR. Figure 7.11 B shows the predicted C_P-time profiles when importing these deconvoluted release profiles

to the PBB model as CR release profiles. Clearly, two very different exposure profiles are obtained, with $AR = 1.6$ significantly underpredicting the clinical data ($C_{Max} = 3.14$ $\mu g\,mL^{-1}$ at $t = 126.89$ h, $AUC_t = 272.52$ [$\mu g\,h\,mL^{-1}$]) and $AR = 1.13$ predicting well. Additionally, significantly lower portion of the drug load is released according to AR = 1.6. However, there are similarities in the nature of the profiles that should be examined, which are distinctly different to the in vitro observations and CR dosage form theory.

Compared to the in vitro data collected in the DCM and USP II, the deconvoluted dissolution profiles exhibit a faster release, approaching plateau after just 7 h (compared to over 24 h when using DCM motility patterns). The rapid dissolution exhibited in the deconvoluted profiles caused a sharp increase in plasma concentration, with the same rate of clearance; thus, the fraction of theophylline eliminated from systemic circulation increased faster, causing the underprediction for $AR = 1.6$. Although most of the data are predicted well using $AR = 1.13$, the absorption phase is not. The gradient is steeper than for the observed data. This is because the associated dissolution profile achieved over 80 % release after only 5 h. From the in vitro experiments, this is clearly an unrealistic release profile for the UC 200 mg tablets under biorelevant conditions. It is likely that the released drug accumulates in the colon and the plasma concentration profile responds with a slow increase due to the lower absorption rate in the colon. This hypothesis is supported by findings by Clear *et al.* [349] where colonic absorption of theophylline was slow compared to the small intestine. The result is that intended by a CR formulation, a sustained level of API in systemic circulation over the dosing interval. This is reflected in the predictions made from importing the DCM in vitro release profiles, where C_{trough} never fell below 1.25 and the absorption phase from C_{trough} to C_{Max} was extended, compared to a low level (< 1.00) of C_{trough} for $AR = 1.13$, which does not align with the purpose of a CR tablet: to achieve a sustained level of API in systemic circulation.

This shows that the methodology of deconvoluting multiple dose in vivo data and applying an estimated accumulation ratio may be flawed for understanding the relationship

between a deconvoluted in vitro release profile and clinical data for CR dosage forms.

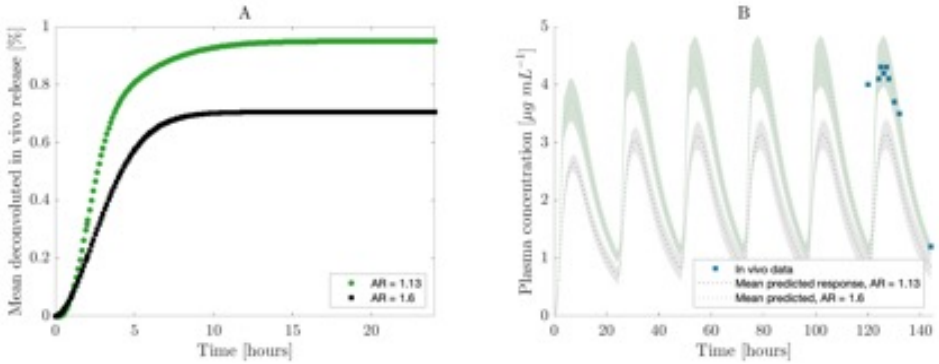

Figure 7.11: A) Deconvoluted in vivo release profile following oral administration of a single dose of UC 200 mg tablet. B) Predicted clinical response following oral administration every 24 h for 6 days. The Gastroplus® model was applied with the estimated deconvoluted single dose in vivo release profile input as an in vitro CR release profile. In vivo data is for the 6th day.

7.3.7 Dissolution profiles of UC 400 mg tablets

Figure 7.12 shows the dissolution profiles of UC 400 mg tablet obtain from DCM and USP II under different motility patterns and agitation speeds, respectively. As expected, release rate and extent were highest in the USP II at 100 rpm. Release slowed after 16 h approaching a plateau and 98 % release at 24 h. Under all other conditions, release steadily increased over the period of 24 h linearly with no sign of reaching a plateau. The lowest release was exhibited under the DCM at baseline, whilst the retrograde pattern was almost indistinguishable from the profile measured in the USP II at 25 rpm. Lower release was observed in comparison to the 200 mg tablets, for which the dissolution profiles are presented in Chapter 6 and Figure 7.6. Locally to the tablet body, higher concentrations of drug were present which may have hindered diffusion of theophylline through the gel matrix into the surrounding media. Additionally, the 400 mg tablets are larger (16.0 x 7.0 x 5.1 mm, 550 $\pm$ 10 mg, $n = 3$) than the 200 mg tablets (11.7 x 5.5 x 4.1 mm, 265 $\pm$ 10 mg,

$n = 3$). This ultimately presents a greater length of diffusion pathway for theophylline, as the distance for water to penetrate is greater and the time taken to form a gel layer that extends to the core of the tablet would be longer. Furthermore, there is more polymer to be eroded in order to achieve complete release under the same hydrodynamic conditions.

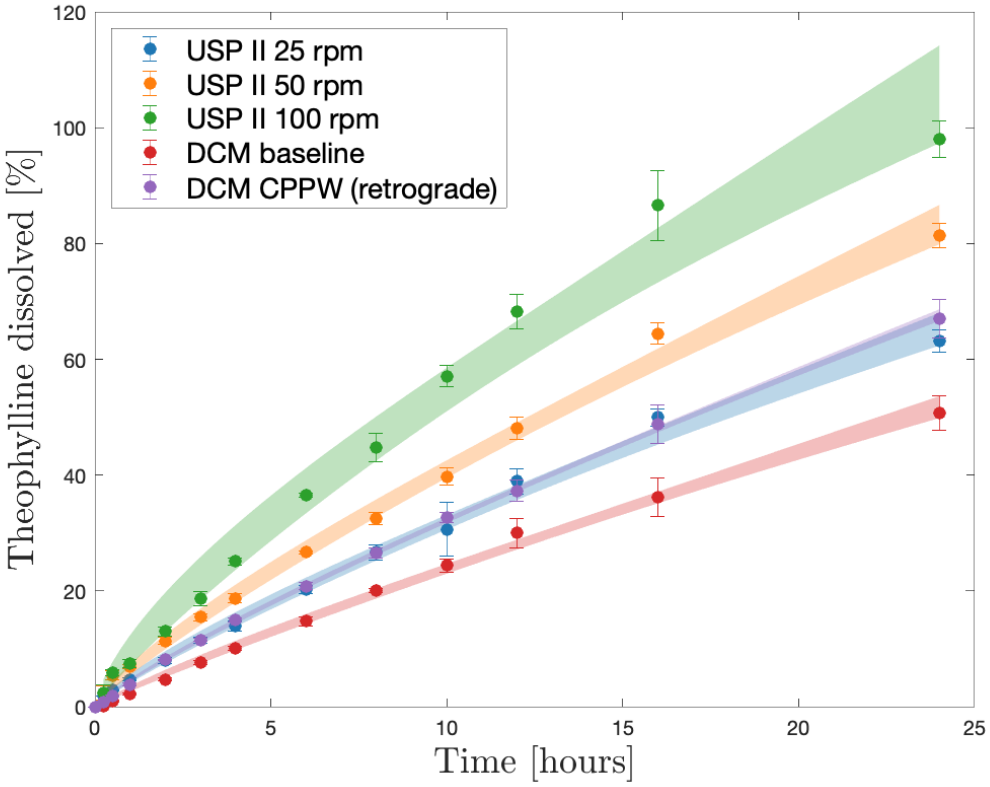

Figure 7.12: Dissolution profiles of UC 400 mg tablets in the USP II and DCM under different hydrodynamic conditions. Power law model is fit to the mean data with the 90 % prediction error interval shaded. Error bars represent the standard deviation of the concentration measurements.

7.3.8 Predicting PK profiles for UC 400 mg tablets

Figure 7.13 presents the predicted theophylline exposure profiles for UC 400 mg tablets when importing dissolution profiles from the USP II (A) and the DCM (B). The absorption phase in vivo is very fast compared to the predictions from importing USP II profiles and DCM profiles. This is likely due to the size of the tablet (which is larger than the 200 mg tablet) causing an extended gastric retention time; leading to elevated release in the stomach and absorption in the upper GI tract.

Furthermore, big tablets that do not disintegrate quickly may be emptied from the stomach mainly by the strong contractions of migrating motor complexes (MMC) in fasted subjects [366]. Therefore, these dosage forms may experience elevated erosion in vivo, resulting in more API to be released in the small intestine and available for absorption resulting in more theophylline to be released in the small intestine and get absorbed. Hence, using the DCM to describe the in vivo dissolution profile of large CR tablets might not be appropriated and a preconditioning dissolution step should be added to the protocol before the tablet is introduced into the DCM to simulate dissolution in the lower GI tract as a final step.

Predictions using the USP II dissolution profiles were reasonably good, showing that the USP II may be suitable for predicting release in the upper GI tract. Table 7.4 presents the PK characteristics predicted by the PBB model when importing dissolution profiles from the USP II and DCM and USP II for UC 200 mg tablets.

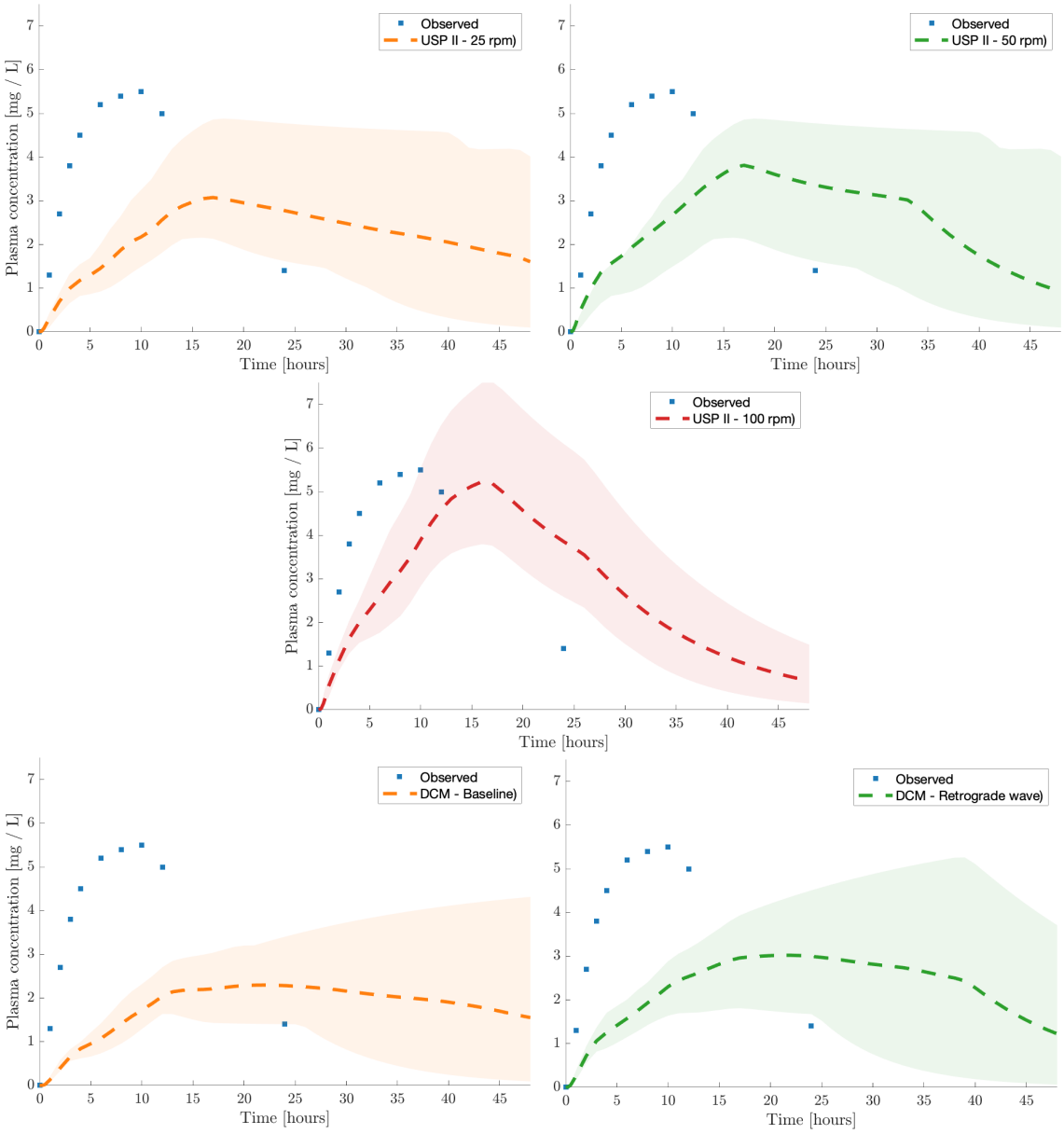

Figure 7.13: PBBM prediction of UC 400 mg tablets using the USP II and DCM with different paddle speeds and motility patterns respectively. The shaded region marks the 5^{th} to 95^{th} percentile of the predicted theophylline plasma concentration.

Table 7.5: Mean simulated and observed (Obs) and ratio () of PK parameters of theophylline following oral administration of UC 400 mg tablets in healthy adult volunteers. C_{Max} is expressed in mg mL^{-1}, $t_{C_{Max}}$ in h and AUC_{τ} in mg mL h^{-1}.

	Obs	USP II			DCM	
		25	50	100	Baseline	Retrograde
C_{Max}	5.5	3.24 (0.59)	4.19 (0.76)	5.54 (1.00)	2.50 (0.45)	3.16 (0.57)
$t_{C_{max}}$	10	16.5 (1.65)	16.74 (1.67)	16.3 (1.63)	39.8 (3.98)	38.4 (3.84)
AUC_{τ}	110.5	90.2 (7.8)	129.9 (11.3)	134.4 (11.7)	98.8 (8.60)	123.6 (10.7)

Stamatopoulos *et al.* [20] also applied the dissolution profiles obtained in this chapter to the prediction of UC 400 mg multiple dose data. However, due to the limitation of multiple day dosing of CR formulations and the difficulty predicting the larger sized tablet using the DCM profiles (Figure 7.12), this Chapter did not include an attempt to model this clinical data in Gastroplus®.

7.4 Conclusions

A PBB model for theophylline was developed and successfully predicted a range of clinical PK data. Despite this, the model underpredicted the PK data for UC 200 and 400 mg tablets when importing in vitro release profiles from the DCM and USP II. Predicted absorption primarily occurred in the colon.

PBB models that predict drug exposure from CR formulations that release a significant portion of their drug load in the colon should account for the different levels of erosion and drug dispersion expected from biorelevant motility patterns. These CR formulations tract may be improved by the designing polymeric release control system to be sensitive to intestinal hydrodynamics rather than the intense mixing conditions within USP apparatus. Further discretisation of colonic compartments in commercially available PBBM platforms may be valuable for modelling release from CR formulations. In addition, incorporation of the fluid viscosity may be useful due to the dewatering effect of the colon. Repeat dose CR formulations may require in silico models to have the capability to handle two dosage forms in separate gastrointestinal compartments simultaneously to achieve the level of release observed in vivo.

A segmented lumen is key for an in vitro and in silico dynamic model of the human colon to reproduce motility patterns, erosive capabilities and dissolved drug distribution, all of which influence the predicted absorption profile.

This study reinforces findings that a preconditioning step to simulate exposure of a CR dosage form to the upper GI tract may be required to improve the PBBM predictivity of tablets above a certain size threshold that may have extended gastric emptying time. However, the DCM may be a suitable tool for biopredictive evaluation of smaller CR formulations where absorption mainly occurs in the colon.

Chapter Eight

Conclusions

8.1 Conclusions

An existing model of the human proximal colon, the Dynamic Colon Model (DCM) underwent critical design work to become significantly more robust and ready for use as a biorelevant dissolution apparatus. Implementing a modular approach significantly reduced the downtime associated with repair of a damaged segment, the design was somewhat simplified using additive manufacturing techniques to reduce the total number of component parts for the tube by > 60 %. The recorded operational hours of the DCM were increased by over two orders of magnitude.

A combination of MRI techniques were applied to map and quantify velocities and shear rates in the fluid occupying the DCM lumen, with simultaneous knowledge of how the walls moved. It was demonstrated that the dynamic colon model (DCM) can induce flow that replicates the flow patterns observed in vivo. Also, velocities were confirmed to be representative of those measured in the human AC. To reproduce the hydrodynamics of the human ascending colon is an essential capability for a biorelevant mechanical dissolution apparatus to be suitable for the development of methods for testing extended release dosage forms that reach the colon.

Hydrodynamics of the DCM differ greatly from USP apparatus. Flow profiles partly resembled flows in a partially filled pipe, but differed greatly to those observed in compendial dissolution apparatuses, such as USP2 and the flow through cell (USP4). Nevertheless, this visualisation elucidated the environment that a dosage form may be subjected to inside the DCM during dissolution studies which is vital in understanding how the motion of the mimic colon walls drive the hydrodynamic conditions that govern the erosion of a dosage form and the release and dissolution of the API. Data from the DCM was used to develop and validate a digital twin of the system.

A noninvasive MR tagging method previously developed to assess human colonic motility and distinguish between colonic disease states, was extended and applied to suc-

cessfully differentiate between motility patterns and media viscosities in a biorelevant in vitro model of the human ascending colon. This adds value to the MR tagging technique in its ability to understand colonic pathophysiology, the effectiveness of treatments and the conditions that a colon-targeted dosage form may experience in vivo.

The in vitro dissolution of theophylline from was assessed in the USPII and the dynamic colon model (DCM). In the DCM, different motor patterns previously identified in vivo were replicated using the DCM: baseline conditions for a healthy adult human, antegrade and retrograde cyclic propagating pressure waves (CPPWs) and the stimulated (PEG or maltose stimulus) colon. The intensity of hydrodynamics induced by motility patterns was measured using a motility index that incorporated luminal occlusion rate and the number and frequency of segmental contractions.

Release from the ER tablets was sensitive to agitation speed in the USPII dissolution apparatus. The integration of biorelevant motility into the DCM provided predictions on the extent as well as variability of drug release that may be anticipated from an ER formulation subjected to intestinal hydrodynamics, as a function of motor pattern and position.

Mimicked baseline contractions were highly ineffective at advective transport of dissolved drug along the DCM tube and maximum release was $>$ 20 % lower than in the USPII at 25 rpm. Operating patterns with such low motility may encounter potential solubility effects on the rate of release measured in segments containing the tablet body, especially considering vehicles with a poorly soluble payload. Motility patterns which include more frequent retrograde propagating pressure waves may be more effective at achieving higher release of a therapeutic from a dosage form located towards the early stages of the proximal colon (compared to antegrade propagating waves). When mimicking the stimulated colon, a higher theophylline release was achieved than in the USPII at 25 rpm, although it is unrealistic to maintain these conditions for 24 h in vivo. Operation of the USPII at a constant rate of 25 rpm and above generates hydrodynamics conditions

that may be too intensive to be representative of unstimulated human colon.

Lastly, the clinical significance of dissolution data in the DCM was explored. A PBB model was developed for theophylline in Gastroplus® and predictivity of clinical data was explored when the model was informed by the DCM, versus the USP II. Although the model underpredicted clinical data, these data fell within the 5^{th} to 95^{th} percentile (acceptance criteria) of predictions, demonstrating preliminary success of using the DCM as a biopredictive tool. Although the DCM did not significantly improve predictivity of the PBB model in Gastroplus, it was demonstrated that this was likely a due to current features of the software used. Useful insights were gained in understanding how impaired or stimulated intestinal motility may affect absorption.

8.2 Future work

Improvements could be made to the biorelevance of dissolution experiments by using an upper GI preconditioning step before introducing a tablet to the DCM to mimic dissolution in the distal GI tract. More work is required to reproduce in vivo motility in the colon over an extended period, such as including a variety of motility patterns in one experiment; currently beyond the technical capacity of the DCM.

It may be possible to evaluate the difference of DCM orientation on baseline dissolution, by rotating the DCM through 0–90°at predetermined intervals to mimic the influence of gravity and human physical activity. This would likely cause a change in positioning or orientation of the tablet, exposing the side of the tablet that constantly in contact with the lower DCM wall in this study.

Further MRI experiments could quantify flow of particles, coupled with wall and fluid motion, in addition to dissolution from the particle (or mimic tablet) using a contrast agent to form an ultimate map of flow phenomena in the lumen.

It may be useful to test the performance of colon-targeted formulations with different release trigger mechanisms inside the DCM. In the future, there may also be opportunities to integrate features of the micro-environment into the DCM. It may be valuable to observe the development of human epithelial cells integrated into the walls of the lumen.

It may be of great value to develop a bespoke in silico system of ordinary differential equations (ODEs) that could handle multiple dosage forms simultaneously, with further compartmentalisation while these features are unavailable in commercially available software. Further, to develop a model with the capacity to recreate the dynamic changes in colonic fluid composition and motility during transit, include elements of the microbiota and mimic absorption through inclusion of a colonic epithelial cell line. An achievable means of doing the latter in a shorter time scale could be to perform colon epithelium

permeation experiments and combine the results with DCM dissolution data to estimate the fraction of drug that makes it to the portal vein in vivo.

References

1. Burisch, J., Jess, T., Martinato, M. & Lakatos, P. L. The burden of inflammatory bowel disease in Europe. *Journal of Crohn's and Colitis* **7,** 322–337. ISSN: 18739946 (2013).

2. Ng, S. C. *et al.* Geographical variability and environmental risk factors in inflammatory bowel disease. *Gut* **62,** 630–649. ISSN: 1468-3288 (Electronic) 0017-5749 (Linking). https://www.ncbi.nlm.nih.gov/pubmed/23335431 (2013).

3. Narula, N. *et al.* Association of ultra-processed food intake with risk of inflammatory bowel disease: prospective cohort study. *BMJ,* n1554. ISSN: 1756-1833 (July 2021).

4. Hou, J. K., Abraham, B. & El-Serag, H. Dietary Intake and Risk of Developing Inflammatory Bowel Disease: A Systematic Review of the Literature. *American Journal of Gastroenterology* **106,** 563–573. ISSN: 0002-9270 (Apr. 2011).

5. Park, K. T. *et al.* The Cost of Inflammatory Bowel Disease: An Initiative From the Crohn's & Colitis Foundation. *Inflammatory Bowel Diseases* **26,** 1–10. ISSN: 1078-0998 (Jan. 2020).

6. Schneider, F. *et al.* Resolving the physiological conditions in bioavailability and bioequivalence studies: Comparison of fasted and fed state. *European Journal of Pharmaceutics and Biopharmaceutics* **108,** 214–219. ISSN: 09396411 (2016).

7. Camilleri, M. & Linden, D. R. Measurement of Gastrointestinal and Colonic Motor Functions in Humans and Animals. *Cellular and Molecular Gastroenterology and Hepatology* **2,** 412–428. ISSN: 2352345X (2016).

8. Stamatopoulos, K. *Development of a Biorelevant Dynamic Colon Model of Human Proximal Colon: a Tool for Designing Colon - Specific Drug Delivery Systems* PhD thesis (2016).

9. Stamatopoulos, K., Batchelor, H. K. & Simmons, M. J. H. Dissolution profile of theophylline modified release tablets, using a biorelevant Dynamic Colon Model (DCM). *Eur J Pharm Biopharm* **108,** 9–17. ISSN: 1873-3441 (Electronic) 0939-6411 (Linking). https://www.ncbi.nlm.nih.gov/pubmed/27531624 (2016).

10. Stamatopoulos, K. *et al.* Dynamic Colon Model (DCM): A Cine-MRI Informed Biorelevant In Vitro Model of the Human Proximal Large Intestine Characterized by Positron Imaging Techniques. *Pharmaceutics* **12.** ISSN: 1999-4923 (2020).

11. Sarna, S. K. & Shi, X.-Z. in *Physiolog of the Gastrointestinal Tract* (ed Johnson, L. R.) 4th (Academic Press, Burlington, 2006).

12. O'Farrell, C., Stamatopoulos, K., Simmons, M. & Batchelor, H. In vitro models to evaluate ingestible devices: present status and current trends. *Advanced Drug Delivery Reviews.* ISSN: 0169409X (2021).

13. Stamatopoulos, K., O'Farrell, C., Simmons, M. & Batchelor, H. In vivo models to evaluate ingestible devices: Present status and current trends. *Advanced Drug Delivery Reviews* **177.** ISSN: 0169409X (2021).

14. O'Farrell, C. *et al.* Luminal Fluid Motion Inside an In Vitro Dissolution Model of the Human Ascending Colon Assessed Using Magnetic Resonance Imaging. *Pharmaceutics* **13.** ISSN: 1999-4923 (2021).

15. Schütt, M. *et al.* Simulating the Hydrodynamic Conditions of the Human Ascending Colon: A Digital Twin of the Dynamic Colon Model. *Pharmaceutics* **14.** ISSN: 1999-4923 (2022).

16. Schütt, M. *et al.* Correction: Schütt et al. Simulating the Hydrodynamic Conditions of the Human Ascending Colon: A Digital Twin of the Dynamic Colon Model. Pharmaceutics 2022, 14, 184. *Pharmaceutics* **14.** ISSN: 1999-4923 (2022).

17. O'Farrell, C., Simmons, M. J. H., Batchelor, H. K. & Stamatopoulos, K. The Effect of Biorelevant Hydrodynamic Conditions on Drug Dissolution from Extended-Release Tablets in the Dynamic Colon Model. *Pharmaceutics* **14,** 2193. ISSN: 1999-4923 (Oct. 2022).

18. O'Farrell, C., Hall, T. J., Grover, L. M. & Cox, S. C. Formulation of an antibacterial topical cream containing bioengineered honey that generates reactive oxygen species. *Biomaterials Advances* **133,** 112664. ISSN: 27729508 (Feb. 2022).

19. Schütt, M., Stamatopoulos, K., Batchelor, H. K., Simmons, M. J. H. & Alexiadis, A. Development of a digital twin of a tablet that mimics a real solid dosage form: Differences in the dissolution profile in conventional mini-USP II and a biorelevant colon model. *European Journal of Pharmaceutical Sciences* **179.** ISSN: 09280987 (2022).

20. Stamatopoulos, K., O'Farrell, C., Simmons, M. J. H., Batchelor, H. K. & Mistry, N. Use of In Vitro Dynamic Colon Model (DCM) to Inform a Physiologically Based Biopharmaceutic Model (PBBM) to Predict the In Vivo Performance of a Modified-Release Formulation of Theophylline. *Pharmaceutics* **15,** 882. ISSN: 1999-4923 (Mar. 2023).

21. Anatomy Medicine. *The Caecum* 2022. https://anatomy-medicine.com/.

22. Mahadevan, V. Anatomy of the caecum, appendix and colon. *Surgery (Oxford)* **38,** 1–6. ISSN: 02639319 (2020).

23. Erdogan, A. & Lee, Y. Y. in *Clinical and Basic Neurogastroenterology and Motility* 113–126 (2020). ISBN: 9780128130377.

24. Murray, K. *et al.* Magnetic Resonance Imaging Quantification of Fasted State Colonic Liquid Pockets in Healthy Humans. *Mol Pharm* **14,** 2629–2638. ISSN: 1543-8392 (Electronic) 1543-8384 (Linking). https://www.ncbi.nlm.nih.gov/pubmed/28648070 (2017).

25. Schiller, C. *et al.* Intestinal fluid volumes and transit of dosage forms as assessed by magnetic resonance imaging. *Aliment Pharmacol Ther* **22,** 971–979. ISSN: 0269-2813 (Print) 0269-2813 (Linking). https://www.ncbi.nlm.nih.gov/pubmed/16268972 (2005).

26. Placidi, E. *et al.* The effects of loperamide, or loperamide plus simethicone, on the distribution of gut water as assessed by MRI in a mannitol model of secretory diarrhoea. *Aliment Pharmacol Ther* **36,** 64–73. ISSN: 1365-2036 (Electronic) 0269-2813 (Linking). https://www.ncbi.nlm.nih.gov/pubmed/22582872 (2012).

27. Pritchard, S. E. *et al.* Fasting and postprandial volumes of the undisturbed colon: normal values and changes in diarrhea-predominant irritable bowel syndrome measured using serial MRI. *Neurogastroenterol Motil* **26,** 124–130. ISSN: 1365-2982 (Electronic) 1350-1925 (Linking). https://www.ncbi.nlm.nih.gov/pubmed/24131490 (2014).

28. Nilsson, M. *et al.* Quantification and variability in colonic volume with a novel magnetic resonance imaging method. *Neurogastroenterology & Motility* **27,** 1755–1763. ISSN: 13501925 (2015).

29. Sandberg, T. H. *et al.* A novel semi-automatic segmentation method for volumetric assessment of the colon based on magnetic resonance imaging. *Abdominal Imaging* **40,** 2232–2241. ISSN: 0942-8925 1432-0509 (2015).

30. Coletta, M. *et al.* Effect of bread gluten content on gastrointestinal function: a crossover MRI study on healthy humans. *British Journal of Nutrition* **115,** 55–61. ISSN: 0007-1145 1475-2662 (2015).

31. Lam, C. *et al.* Colonic response to laxative ingestion as assessed by MRI differs in constipated irritable bowel syndrome compared to functional constipation. *Neurogastroenterol Motil* **28,** 861–870. ISSN: 1365-2982 (Electronic) 1350-1925 (Linking). https://www.ncbi.nlm.nih.gov/pubmed/26871949 (2016).

32. Murray, K. A. *et al.* Corticotropin-releasing factor increases ascending colon volume after a fructose test meal in healthy humans: a randomized controlled trial. *The American Journal of Clinical Nutrition* **103,** 1318–1326. ISSN: 0002-9165 1938-3207 (2016).

33. Nilsson, M. *et al.* Opioid-induced bowel dysfunction in healthy volunteers assessed with questionnaires and MRI. *European Journal of Gastroenterology & Hepatology* **28,** 514–524. ISSN: 0954-691X (2016).

34. Bendezú, R. A. *et al.* Colonic content: effect of diet, meals, and defecation. *Neurogastroenterology & Motility* **29.** ISSN: 13501925 (2017).

35. Pritchard, S. E. *et al.* Assessment of motion of colonic contents in the human colon using MRI tagging. *Neurogastroenterol Motil* **29.** ISSN: 1365-2982 (Electronic) 1350-1925 (Linking). https://www.ncbi.nlm.nih.gov/pubmed/28439942 (2017).

36. Poulsen, J. L. *et al.* Colorectal Transit and Volume During Treatment With Prolonged-release Oxycodone/Naloxone Versus Oxycodone Plus Macrogol 3350. *Journal of Neurogastroenterology and Motility* **24,** 119–127. ISSN: 2093-0879 2093-0887 (2018).

37. Southwell, B. R., Clarke, M. C. C., Sutcliffe, J. & Hutson, J. M. Colonic transit studies: normal values for adults and children with comparison of radiological and scintigraphic methods. *Pediatric Surgery International* **25,** 559–572. ISSN: 1437-9813 (2009).

38. Abuhelwa, A. Y., Foster, D. J. R. & Upton, R. N. A quantitative review and meta-models of the variability and factors affecting oral drug absorption—part I: gastrointestinal pH. *The AAPS Journal* **18,** 1309–1321. ISSN: 1550-7416 (2016).

39. Rao, S. S. C., Kavelock, R., Beaty, J., Ackerson, K. & Stumbo, P. Effects of fat and carbohydrate meals on colonic motor response. *Gut* **46,** 205–211. ISSN: 0017-5749 (2000).

40. Corsetti, M. *et al.* First translational consensus on terminology and definitions of colonic motility in animals and humans studied by manometric and other techniques. *Nature Reviews Gastroenterology & Hepatology* **16,** 559–579. ISSN: 1759-5045 1759-5053 (2019).

41. Chen, J.-H. *et al.* Intraluminal pressure patterns in the human colon assessed by high-resolution manometry. *Scientific Reports* **7.** ISSN: 2045-2322 (2017).

42. Diakidou, A. *et al.* Characterization of the Contents of Ascending Colon to Which Drugs are Exposed After Oral Administration to Healthy Adults. *Pharmaceutical Research* **26,** 2141–2151. ISSN: 0724-8741 1573-904X (2009).

43. Vertzoni, M. *et al.* Biorelevant Media to Simulate Fluids in the Ascending Colon of Humans and Their Usefulness in Predicting Intracolonic Drug Solubility. *Pharmaceutical Research* **27,** 2187–2196. ISSN: 0724-8741 1573-904X (2010).

44. Cummings, J. H. Short chain fatty acids in the human colon. *Gut* **22,** 763–779. ISSN: 0017-5749 (1981).

45. Koziolek, M. *et al.* Investigation of pH and Temperature Profiles in the GI Tract of Fasted Human Subjects Using the Intellicap® System. *Journal of Pharmaceutical Sciences* **104,** 2855–2863. ISSN: 00223549 (Sept. 2015).

46. Henze, L. J. *et al.* Characterization of gastrointestinal transit and luminal conditions in pigs using a telemetric motility capsule. *European Journal of Pharmaceutical Sciences* **156,** 105627. ISSN: 09280987 (Jan. 2021).

47. Koziolek, M. *et al.* Characterization of the GI transit conditions in Beagle dogs with a telemetric motility capsule. *European Journal of Pharmaceutics and Biopharmaceutics* **136,** 221–230. ISSN: 09396411 (Mar. 2019).

48. Rawla, P., Sunkara, T. & Barsouk, A. Epidemiology of colorectal cancer: incidence, mortality, survival, and risk factors. *Gastroenterology Review* **14,** 89–103. ISSN: 1895-5770 (2019).

49. Langer, R. New methods of drug delivery. *Science* **249,** 1527–1533. ISSN: 0036-8075 (1990).

50. Benoit, D. S. W. & Overby Jr, C. T. *KRS, Ackun-farmmer MA. 2.5. 12-Drug Delivery Systems. Fourth Edi. Biomaterials Science* 2020.

51. Crouwel, F., Buiter, H. J. C. & de Boer, N. K. Gut microbiota-driven drug metabolism in inflammatory bowel disease. *Journal of Crohn's and Colitis* **15,** 307–315. ISSN: 1873-9946 (2021).

52. Friend, D. R. New oral delivery systems for treatment of inflammatory bowel disease. *Advanced Drug Delivery Reviews* **57,** 247–265. ISSN: 0169409X (2005).

53. Klotz, U. & Schwab, M. Topical delivery of therapeutic agents in the treatment of inflammatory bowel disease. *Advanced Drug Delivery Reviews* **57,** 267–279. ISSN: 0169409X (2005).

54. Banerjee, A. *et al.* Strategies for targeted drug delivery in treatment of colon cancer: current trends and future perspectives. *Drug Discovery Today* **22,** 1224–1232. ISSN: 13596446 (2017).

55. Guo, Y. *et al.* Advances in Pharmaceutical Strategies Enhancing the Efficiencies of Oral Colon-Targeted Delivery Systems in Inflammatory Bowel Disease. *Molecules* **23.** ISSN: 1420-3049 (Electronic) 1420-3049 (Linking). https://www.ncbi.nlm.nih.gov/pubmed/29973488 (2018).

56. Lee, S. H., Back, S.-Y., Song, J. G. & Han, H.-K. Enhanced oral delivery of insulin via the colon-targeted nanocomposite system of organoclay/glycol chitosan/Eudragit®S100. *Journal of Nanobiotechnology* **18.** ISSN: 1477-3155 (2020).

57. Tubic-Grozdanis, M. *et al.* Pharmacokinetics of the CYP 3A substrate simvastatin following administration of delayed versus immediate release oral dosage forms. *Pharm Res* **25,** 1591–1600. ISSN: 0724-8741 (Print) 0724-8741 (Linking). https://www.ncbi.nlm.nih.gov/pubmed/18213452 (2008).

58. Wang, J., Yadav, V., Smart, A. L., Tajiri, S. & Basit, A. W. Stability of peptide drugs in the colon. *Eur J Pharm Sci* **78,** 31–36. ISSN: 1879-0720 (Electronic) 0928-0987 (Linking). https://www.ncbi.nlm.nih.gov/pubmed/26111980 (2015).

59. Yadav, V., Varum, F., Bravo, R., Furrer, E. & Basit, A. W. Gastrointestinal stability of therapeutic anti-TNF alpha IgG1 monoclonal antibodies. *Int J Pharm* **502,** 181–187. ISSN: 1873-3476 (Electronic) 0378-5173 (Linking). https://www.ncbi.nlm.nih.gov/pubmed/26892815 (2016).

60. Zhang, W., Michalowski, C. B. & Beloqui, A. Oral Delivery of Biologics in Inflammatory Bowel Disease Treatment. *Frontiers in Bioengineering and Biotechnology* **9.** ISSN: 2296-4185 (2021).

61. Brayden, D. J., Hill, T. A., Fairlie, D. P., Maher, S. & Mrsny, R. J. Systemic delivery of peptides by the oral route: Formulation and medicinal chemistry approaches. *Advanced Drug Delivery Reviews* **157,** 2–36. ISSN: 0169-409X (2020).

62. Crouwel, F., Buiter, H. J. C. & de Boer, N. K. Gut Microbiota-driven Drug Metabolism in Inflammatory Bowel Disease. *Journal of Crohn's and Colitis* **15,** 307–315. ISSN: 1873-9946. https://doi.org/10.1093/ecco-jcc/jjaa143 (2020).

63. Enright, E. F., Gahan, C. G. M., Joyce, S. A. & Griffin, B. T. Focus: microbiome: the impact of the gut microbiota on drug metabolism and clinical outcome. *The Yale journal of biology and medicine* **89,** 375 (2016).

64. Flowers, S. A., Evans, S. J., Ward, K. M., McInnis, M. G. & Ellingrod, V. L. Interaction between atypical antipsychotics and the gut microbiome in a bipolar disease cohort. *Pharmacotherapy: The Journal of Human Pharmacology and Drug Therapy* **37,** 261–267. ISSN: 0277-0008 (2017).

65. Hatton, G. B., Madla, C. M., Rabbie, S. C. & Basit, A. W. Gut reaction: impact of systemic diseases on gastrointestinal physiology and drug absorption. *Drug Discovery Today* **24,** 417–427. ISSN: 1359-6446 (2019).

66. Haiser, H. J., Seim, K. L., Balskus, E. P. & Turnbaugh, P. J. Mechanistic insight into digoxin inactivation by Eggerthella lenta augments our understanding of its pharmacokinetics. *Gut microbes* **5,** 233–238. ISSN: 1949-0976 (2014).

67. Van Kessel, S. P., Auvinen, P., Scheperjans, F. & El Aidy, S. Gut bacterial tyrosine decarboxylase associates with clinical variables in a longitudinal cohort study of Parkinsons disease. *npj Parkinson's Disease* **7.** ISSN: 2373-8057 (2021).

68. Wu, H. *et al.* Metformin alters the gut microbiome of individuals with treatment-naive type 2 diabetes, contributing to the therapeutic effects of the drug. *Nature Medicine* **23,** 850–858. ISSN: 1546-170X (2017).

69. Hakozaki, T. *et al.* The Gut Microbiome Associates with Immune Checkpoint Inhibition Outcomes in Patients with Advanced Non–Small Cell Lung CancerGut Microbiome Impact on ICI Efficacy in Patients with NSCLC. *Cancer Immunology Research* **8,** 1243–1250. ISSN: 2326-6066 (2020).

70. Routy, B. *et al.* Gut microbiome influences efficacy of PD-1–based immunotherapy against epithelial tumors. *Science* **359,** 91–97. ISSN: 0036-8075 (2018).

71. Tekade, R. K. *Basic fundamentals of drug delivery* ISBN: 0128179104 (Academic Press, 2018).

72. Koutsamanis, I. *et al.* Controlled-Release from High-Loaded Reservoir-Type Systems—A Case Study of Ethylene-Vinyl Acetate and Progesterone. *Pharmaceutics* **12.** ISSN: 1999-4923 (2020).

73. Yang, W.-W. & Pierstorff, E. Reservoir-Based Polymer Drug Delivery Systems. *SLAS Technology* **17,** 50–58. ISSN: 24726303 (2012).

74. Nokhodchi, A., Raja, S., Patel, P. & Asare-Addo, K. The role of oral controlled release matrix tablets in drug delivery systems. *Bioimpacts* **2,** 175–187. ISSN: 2228-5652 (Print) 2228-5652 (Linking). https://www.ncbi.nlm.nih.gov/pubmed/23678458 (2012).

75. Goldoozian, S., Mohylyuk, V., Dashevskiy, A. & Bodmeier, R. Gel Strength of Hydrophilic Matrix Tablets in Terms of In Vitro Robustness. *Pharmaceutical Research* **38,** 1297–1306. ISSN: 0724-8741 1573-904X (2021).

76. Timmins, P. *et al.* Advances in mechanistic understanding of release rate control mechanisms of extended-release hydrophilic matrix tablets. *Therapeutic Delivery* **7,** 553–572. ISSN: 2041-5990 2041-6008 (2016).

77. Timmins, P. *et al.* Probing the Impact of Porosity on Swelling Kinetics of Hydrophilic Matrices. *British Journal of Pharmacy* **2.** ISSN: 2058-8356 (2017).

78. Tripathi, K. & Feuerstein, J. D. New developments in ulcerative colitis: latest evidence on management, treatment, and maintenance. *Drugs in Context* **8,** 1–11. ISSN: 17404398 (2019).

79. Adepu, S. & Ramakrishna, S. Controlled Drug Delivery Systems: Current Status and Future Directions. *Molecules* **26.** ISSN: 1420-3049 (2021).

80. Amidon, S., Brown, J. E. & Dave, V. S. Colon-Targeted Oral Drug Delivery Systems: Design Trends and Approaches. *AAPS PharmSciTech* **16,** 731–741. ISSN: 1530-9932 (2015).

81. Palugan, L., Cerea, M., Zema, L., Gazzaniga, A. & Maroni, A. Coated pellets for oral colon delivery. *Journal of Drug Delivery Science and Technology* **25,** 1–15. ISSN: 17732247 (2015).

82. Crowe, J. S. *et al.* Oral delivery of the anti-tumor necrosis factor α domain antibody, V565, results in high intestinal and fecal concentrations with minimal systemic exposure in cynomolgus monkeys. *Drug Development and Industrial Pharmacy* **45,** 387–394. ISSN: 0363-9045 1520-5762 (2018).

83. Ashford, M., Fell, J. T., Attwood, D., Sharma, H. & Woodhead, P. J. An in vivo investigation into the suitability of pH dependent polymers for colonic targeting. *International Journal of Pharmaceutics* **95,** 193–199. ISSN: 03785173 (1993).

84. Lin, C. *et al.* Exploring Different Strategies for Efficient Delivery of Colorectal Cancer Therapy. *International Journal of Molecular Sciences* **16,** 26936–26952. ISSN: 1422-0067 (2015).

85. Bak, A., Ashford, M. & Brayden, D. J. Local delivery of macromolecules to treat diseases associated with the colon. *Advanced Drug Delivery Reviews* **136-137,** 2–27. ISSN: 0169-409X. http://www.sciencedirect.com/science/article/pii/S0169409X1830259X (2018).

86. Maroni, A., Moutaharrik, S., Zema, L. & Gazzaniga, A. Enteric coatings for colonic drug delivery: state of the art. *Expert Opinion on Drug Delivery* **14,** 1027–1029. ISSN: 1742-5247. https://doi.org/10.1080/17425247.2017.1360864 (2017).

87. Ibekwe, V. C. *et al.* An Investigation into the In Vivo Performance Variability of pH Responsive Polymers for Ileo-Colonic Drug Delivery Using Gamma Scintigraphy in Humans. *Journal of Pharmaceutical Sciences* **95,** 2760–2766. ISSN: 0022-3549. https://doi.org/10.1002/jps.20742 (2006).

88. Ibekwe, V. C. *et al.* Interplay Between Intestinal pH, Transit Time and Feed Status on the In Vivo Performance of pH Responsive Ileo-Colonic Release Systems. *Pharmaceutical Research* **25,** 1828–1835. ISSN: 1573-904X. https://doi.org/10.1007/s11095-008-9580-9 (2008).

89. Yu, A. *et al.* Measurement of in vivo Gastrointestinal Release and Dissolution of Three Locally Acting Mesalamine Formulations in Regions of the Human Gastrointestinal Tract. *Molecular Pharmaceutics* **14,** 345–358. ISSN: 1543-8384 1543-8392 (2016).

90. Rowland, I. *et al.* Gut microbiota functions: metabolism of nutrients and other food components. *European Journal of Nutrition* **57,** 1–24. ISSN: 1436-6207 1436-6215 (2017).

91. Kotla, N. G. *et al.* Bioresponsive drug delivery systems in intestinal inflammation: State-of-the-art and future perspectives. *Advanced Drug Delivery Reviews* **146,** 248–266. ISSN: 0169409X (2019).

92. Hashem, F. In Vitro and In Vivo Evaluation of Combined Time and pH- Dependent Oral Colonic Targeted Prednisolone Microspheres. *British Journal of Pharmaceutical Research* **3,** 420–434. ISSN: 22312919 (2013).

93. Navarro-Ruíz, E. *et al.* Multiparticulate Systems of Meloxicam for Colonic Administration in Cancer or Autoimmune Diseases. *Pharmaceutics* **14.** ISSN: 1999-4923 (2022).

94. Patel, M. M. Cutting-edge technologies in colon-targeted drug delivery systems. *Expert Opinion on Drug Delivery* **8,** 1247–1258. ISSN: 1742-5247 1744-7593 (2011).

95. Park, H. J. *et al.* Colon-targeted delivery of solubilized bisacodyl by doubly enteric-coated multiple-unit tablet. *European Journal of Pharmaceutical Sciences* **102,** 172–179. ISSN: 09280987 (2017).

96. Foppoli, A. *et al.* In vitro and human pharmacoscintigraphic evaluation of an oral 5-ASA delivery system for colonic release. *International Journal of Pharmaceutics* **572.** ISSN: 03785173 (2019).

97. Liu, F., Moreno, P. & Basit, A. W. A novel double-coating approach for improved pH-triggered delivery to the ileo-colonic region of the gastrointestinal tract. *Eur J Pharm Biopharm* **74,** 311–315. ISSN: 1873-3441 (Electronic) 0939-6411 (Linking). https://www.ncbi.nlm.nih.gov/pubmed/19932177 (2010).

98. Varum, F. J., Hatton, G. B., Freire, A. C. & Basit, A. W. A novel coating concept for ileo-colonic drug targeting: proof of concept in humans using scintigraphy. *Eur J*

Pharm Biopharm **84,** 573–577. ISSN: 1873-3441 (Electronic) 0939-6411 (Linking). https://www.ncbi.nlm.nih.gov/pubmed/23348235 (2013).

99. Maurer, J. M. *et al.* ColoPulse tablets perform comparably in healthy volunteers and Crohn's patients and show no influence of food and time of food intake on bioavailability. *Journal of Controlled Release* **172,** 618–624. ISSN: 01683659 (2013).

100. Padmanabhan, P. *et al.* Gastrointestinal pH and Transit Time Profiling in Healthy Volunteers Using the IntelliCap System Confirms Ileo-Colonic Release of ColoPulse Tablets. *PLoS One* **10.** ISSN: 1932-6203 (2015).

101. Gareb, B., Dijkstra, G., Kosterink, J. G. W. & Frijlink, H. W. Development of novel zero-order release budesonide tablets for the treatment of ileo-colonic inflammatory bowel disease and comparison with formulations currently used in clinical practice. *International Journal of Pharmaceutics* **554,** 366–375. ISSN: 03785173 (2019).

102. Gareb, B. *et al.* Towards the Oral Treatment of Ileo-Colonic Inflammatory Bowel Disease with Infliximab Tablets: Development and Validation of the Production Process. *Pharmaceutics* **11.** ISSN: 1999-4923 (2019).

103. Macfarlane, G. T. & Englyst, H. N. Starch utilization by the human large intestinal microflora. *Journal of Applied Bacteriology* **60,** 195–201. ISSN: 00218847 (1986).

104. Ibekwe, V. C., Khela, M. K., Evans, D. F. & Basit, A. W. A new concept in colonic drug targeting: a combined pH-responsive and bacterially-triggered drug delivery technology. *Alimentary Pharmacology & Therapeutics* **28,** 911–916. ISSN: 0269-2813. https://doi.org/10.1111/j.1365-2036.2008.03810.x (2008).

105. Turanlı, Y. & Acartürk, F. Preparation and characterization of colon-targeted pH/Time-dependent nanoparticles using anionic and cationic polymethacrylate polymers. *European Journal of Pharmaceutical Sciences* **171.** ISSN: 09280987 (2022).

106. Cai, X. *et al.* Colon-targeted delivery of tacrolimus using pH-responsive polymeric nanoparticles for murine colitis therapy. *International Journal of Pharmaceutics* **606.** ISSN: 03785173 (2021).

107. Mohamed, J. M., Alqahtani, A., Ahmad, F., Krishnaraju, V. & Kalpana, K. Pectin co-functionalized dual layered solid lipid nanoparticle made by soluble curcumin for the targeted potential treatment of colorectal cancer. *Carbohydrate Polymers* **252.** ISSN: 01448617 (2021).

108. Samprasit, W., Opanasopit, P. & Chamsai, B. Mucoadhesive chitosan and thiolated chitosan nanoparticles containing alpha mangostin for possible Colon-targeted delivery. *Pharmaceutical Development and Technology* **26,** 362–372. ISSN: 1083-7450 1097-9867 (2021).

109. Bijari, N., Ghobadi, S. & Derakhshandeh, K. β-lactoglobulin-irinotecan inclusion complex as a new targeted nanocarrier for colorectal cancer cells. *Research in Pharmaceutical Sciences* **14.** ISSN: 1735-5362 (2019).

110. Abid, M. *et al.* Colon specific enzyme responsive oligoester crosslinked dextran nanoparticles for controlled release of 5-fluorouracil. *International Journal of Pharmaceutics* **586.** ISSN: 03785173 (2020).

111. Zeeshan, M., Ali, H., Khan, S., Khan, S. A. & Weigmann, B. Advances in orally-delivered pH-sensitive nanocarrier systems; an optimistic approach for the treatment of inflammatory bowel disease. *International Journal of Pharmaceutics* **558,** 201–214. ISSN: 03785173 (2019).

112. Ma, X. & Iii, W. Polymeric nanomedicines for poorly soluble drugs in oral delivery systems: an update. *Journal of Pharmaceutical Investigation* **48,** 61–75 (2018).

113. Mutalik, S. *et al.* Development and performance evaluation of novel nanoparticles of a grafted copolymer loaded with curcumin. *International Journal of Biological Macromolecules* **86,** 709–720. ISSN: 01418130 (2016).

114. Sahu, K. K. & Pandey, R. S. Development and characterization of HBsAg-loaded Eudragit nanoparticles for effective colonic immunization. *Pharmaceutical Development and Technology* **24,** 166–175. ISSN: 1083-7450 1097-9867 (2018).

115. Yoo, J.-W. *et al.* Colon-targeted delivery of budesonide using dual pH- and time-dependent polymeric nanoparticles for colitis therapy. *Drug Design, Development and Therapy.* ISSN: 1177-8881 (2015).

116. Lee, S. H. *et al.* Strategic Approaches for Colon Targeted Drug Delivery: An Overview of Recent Advancements. *Pharmaceutics* **12,** 68. ISSN: 1999-4923 (Jan. 2020).

117. Marques, M. R. C., Loebenberg, R. & Almukainzi, M. Simulated biological fluids with possible application in dissolution testing. *Dissolution Technol* **18,** 15–28 (2011).

118. Liu, F., Merchant, H. A., Kulkarni, R. P., Alkademi, M. & Basit, A. W. Evolution of a physiological pH6.8 bicarbonate buffer system: Application to the dissolution testing of enteric coated products. *European Journal of Pharmaceutics and Biopharmaceutics* **78,** 151–157. ISSN: 09396411 (2011).

119. Yang, L. Biorelevant dissolution testing of colon-specific delivery systems activated by colonic microflora. *Journal of Controlled Release* **125,** 77–86. ISSN: 01683659 (2008).

120. Wahlgren, M., Axenstrand, M., Håkansson, Å., Marefati, A. & Lomstein Pedersen, B. In Vitro Methods to Study Colon Release: State of the Art and An Outlook on New Strategies for Better In-Vitro Biorelevant Release Media. *Pharmaceutics* **11.** ISSN: 1999-4923 (2019).

121. Takagi, R. *et al.* A Single-Batch Fermentation System to Simulate Human Colonic Microbiota for High-Throughput Evaluation of Prebiotics. *PLoS One* **11.** ISSN: 1932-6203 (2016).

122. O'Donnell, M. M., Rea, M. C., Shanahan, F. & Ross, R. P. The Use of a Mini-Bioreactor Fermentation System as a Reproducible, High-Throughput ex vivo Batch Model of the Distal Colon. *Frontiers in Microbiology* **9.** ISSN: 1664-302X (2018).

123. Abrahamsson, B. *et al.* A Novel in Vitro and Numerical Analysis of Shear-Induced Drug Release from Extended-Release Tablets in the Fed Stomach. *Pharmaceutical Research* **22,** 1215–1226. ISSN: 0724-8741 1573-904X (2005).

124. Kostewicz, E. S. *et al.* Predicting the precipitation of poorly soluble weak bases upon entry in the small intestine. *Journal of Pharmacy and Pharmacology* **56,** 43–51. ISSN: 0022-3573 (2004).

125. Gu, C.-H., Rao, D., Gandhi, R. B., Hilden, J. & Raghavan, K. Using a novel multicompartment dissolution system to predict the effect of gastric pH on the oral absorption of weak bases with poor intrinsic solubility. *Journal of Pharmaceutical Sciences* **94,** 199–208. ISSN: 0022-3549 (2005).

126. Kourentas, A. *et al.* An in vitro biorelevant gastrointestinal transfer (BioGIT) system for forecasting concentrations in the fasted upper small intestine: design, implementation, and evaluation. *European Journal of Pharmaceutical Sciences* **82,** 106–114. ISSN: 0928-0987 (2016).

127. McNamara, D. P., Whitney, K. M. & Goss, S. L. Use of a physiologic bicarbonate buffer system for dissolution characterization of ionizable drugs. *Pharmaceutical Research* **20,** 1641–1646. ISSN: 1573-904X (2003).

128. Fadda, H. M., Merchant, H. A., Arafat, B. T. & Basit, A. W. Physiological bicarbonate buffers: stabilisation and use as dissolution media for modified release systems. *International Journal of Pharmaceutics* **382,** 56–60. ISSN: 0378-5173 (2009).

129. Merchant, H. A., Goyanes, A., Parashar, N. & Basit, A. W. Predicting the gastrointestinal behaviour of modified-release products: Utility of a novel dynamic dissolution test apparatus involving the use of bicarbonate buffers. *International Journal of Pharmaceutics* **475,** 585–591. ISSN: 0378-5173 (2014).

130. Garbacz, G., Kołodziej, B., Koziolek, M., Weitschies, W. & Klein, S. An Automated System for Monitoring and Regulating the pH of Bicarbonate Buffers. *AAPS PharmSciTech* **14,** 517–522. ISSN: 1530-9932 (2013).

131. Garbacz, G., Kołodziej, B., Koziolek, M., Weitschies, W. & Klein, S. A dynamic system for the simulation of fasting luminal pH-gradients using hydrogen carbonate buffers for dissolution testing of ionisable compounds. *European Journal of Pharmaceutical Sciences* **51,** 224–231. ISSN: 09280987 (2014).

132. Zakowiecki, D. *et al.* Preparation of delayed-release multiparticulate formulations of diclofenac sodium and evaluation of their dissolution characteristics using biorelevant dissolution methods. *Journal of Drug Delivery Science and Technology* **60.** ISSN: 17732247 (2020).

133. Karkossa, F. & Klein, S. Assessing the influence of media composition and ionic strength on drug release from commercial immediate-release and enteric-coated aspirin tablets. *Journal of Pharmacy and Pharmacology* **69,** 1327–1340. ISSN: 2042-7158 0022-3573 (2017).

134. Mercuri, A. *et al.* In vitro and in silico characterisation of Tacrolimus released under biorelevant conditions. *International Journal of Pharmaceutics* **515,** 271–280. ISSN: 03785173 (2016).

135. Franek, F., Jarlfors, A., Larsen, F., Holm, P. & Steffansen, B. In vitro solubility, dissolution and permeability studies combined with semi-mechanistic modeling to investigate the intestinal absorption of desvenlafaxine from an immediate- and extended release formulation. *European Journal of Pharmaceutical Sciences* **77,** 303–313. ISSN: 09280987 (2015).

136. Garbacz, G., Rappen, G.-M., Koziolek, M. & Weitschies, W. Dissolution of mesalazine modified release tablets under standard and bio-relevant test conditions. *Journal of Pharmacy and Pharmacology* **67,** 199–208. ISSN: 2042-7158 0022-3573 (2015).

137. Schellekens, R. C. A., Stuurman, F. E., van der Weert, F. H. J., Kosterink, J. G. W. & Frijlink, H. W. A novel dissolution method relevant to intestinal release behaviour and its application in the evaluation of modified release mesalazine products. *European Journal of Pharmaceutical Sciences* **30,** 15–20. ISSN: 09280987 (2007).

138. Karkossa, F. & Klein, S. Individualized in vitro and in silico methods for predicting in vivo performance of enteric-coated tablets containing a narrow therapeutic index drug. *European Journal of Pharmaceutics and Biopharmaceutics* **135,** 13–24. ISSN: 09396411 (2019).

139. Fine-Shamir, N. & Dahan, A. Methacrylate-Copolymer Eudragit EPO as a Solubility-Enabling Excipient for Anionic Drugs: Investigation of Drug Solubility, Intestinal Permeability, and Their Interplay. *Molecular Pharmaceutics* **16,** 2884–2891. ISSN: 1543-8384 1543-8392 (2019).

140. Georgaka, D., Butler, J., Kesisoglou, F., Reppas, C. & Vertzoni, M. Evaluation of Dissolution in the Lower Intestine and Its Impact on the Absorption Process of High Dose Low Solubility Drugs. *Molecular Pharmaceutics* **14,** 4181–4191. ISSN: 1543-8384 1543-8392 (2017).

141. Gulati, M. *et al.* Novel biorelevant dissolution medium as a prognostic tool for polysaccharide-based colon-targeted drug delivery system. *Journal of Advanced Pharmaceutical Technology & Research* **8.** ISSN: 2231-4040 (2017).

142. Andreas, C. J. *et al.* Mechanistic investigation of the negative food effect of modified release zolpidem. *European Journal of Pharmaceutical Sciences* **102,** 284–298. ISSN: 09280987 (2017).

143. Andreas, C. J. *et al.* Can dosage form-dependent food effects be predicted using biorelevant dissolution tests? Case example extended release nifedipine. *European Journal of Pharmaceutics and Biopharmaceutics* **105,** 193–202. ISSN: 09396411 (2016).

144. Andreas, C. J., Chen, Y.-C., Markopoulos, C., Reppas, C. & Dressman, J. In vitro biorelevant models for evaluating modified release mesalamine products to forecast the effect of formulation and meal intake on drug release. *European Journal of Pharmaceutics and Biopharmaceutics* **97,** 39–50. ISSN: 09396411 (2015).

145. Singh, S. K. *et al.* A novel dissolution method for evaluation of polysaccharide based colon specific delivery systems: A suitable alternative to animal sacrifice. *European Journal of Pharmaceutical Sciences* **73,** 72–80. ISSN: 09280987 (2015).

146. Gibson, G. R., Cummings, J. H. & Macfarlane, G. T. Use of a three-stage continuous culture system to study the effect of mucin on dissimilatory sulfate reduction and methanogenesis by mixed populations of human gut bacteria. *Applied and Environmental Microbiology* **54,** 2750–2755. ISSN: 0099-2240 1098-5336 (1988).

147. Venema, K. & van den Abbeele, P. Experimental models of the gut microbiome. *Best Practice & Research Clinical Gastroenterology* **27,** 115–126. ISSN: 15216918 (2013).

148. Martinez, M. N. *et al.* Workshop Report: USP Workshop on Exploring the Science of Drug Absorption. *Dissolution Technologies* **26,** 38–66. ISSN: 1521298X (2019).

149. Markopoulos, C., Andreas, C. J., Vertzoni, M., Dressman, J. & Reppas, C. In-vitro simulation of luminal conditions for evaluation of performance of oral drug products: Choosing the appropriate test media. *European Journal of Pharmaceutics and Biopharmaceutics* **93,** 173–182. ISSN: 09396411 (2015).

150. Macfarlane, G. T., Macfarlane, S. & Gibson, G. R. Validation of a Three-Stage Compound Continuous Culture System for Investigating the Effect of Retention Time on the Ecology and Metabolism of Bacteria in the Human Colon. *Microbial Ecology* **35,** 180–187. ISSN: 0095-3628 1432-184X (1998).

151. Possemiers, S., VerthÃ©, K., Uyttendaele, S. & Verstraete, W. PCR-DGGE-based quantification of stability of the microbial community in a simulator of the human intestinal microbial ecosystem. *FEMS Microbiology Ecology* **49,** 495–507. ISSN: 01686496 15746941 (2004).

152. Siew, L. F., Man, S.-M., Newton, J. M. & Basit, A. W. Amylose formulations for drug delivery to the colon: a comparison of two fermentation models to assess

colonic targeting performance in vitro. *International Journal of Pharmaceutics* **273,** 129–134. ISSN: 03785173 (2004).

153. Spratt, P., Nicolella, C. & Pyle, D. L. An Engineering Model of the Human Colon. *Food and Bioproducts Processing* **83,** 147–157. ISSN: 09603085 (2005).

154. Makivuokko, H., Nurmi, J., Nurminen, P., Stowell, J. & Rautonen, N. In Vitro Effects on Polydextrose by Colonic Bacteria and Caco-2 Cell Cyclooxygenase Gene Expression. *Nutrition and Cancer* **52,** 94–104. ISSN: 0163-5581 1532-7914 (2005).

155. Barry, J. L. *et al.* Estimation of the fermentability of dietary fibrein vitro: a European interlaboratory study. *British Journal of Nutrition* **74,** 303–322. ISSN: 0007-1145 1475-2662 (2007).

156. Blanquet-Diot, S. *et al.* Use of Artificial Digestive Systems to Investigate the Biopharmaceutical Factors Influencing the Survival of Probiotic Yeast During Gastrointestinal Transit in Humans. *Pharmaceutical Research* **29,** 1444–1453. ISSN: 0724-8741 1573-904X (2011).

157. Thévenot, J. *et al.* Enterohemorrhagic Escherichia coli O157:H7 Survival in anIn VitroModel of the Human Large Intestine and Interactions with Probiotic Yeasts and Resident Microbiota. *Applied and Environmental Microbiology* **79,** 1058–1064. ISSN: 0099-2240 1098-5336 (2013).

158. Thévenot, J. *et al.* Enterohemorrhagic Escherichia coli infection has donor-dependent effect on human gut microbiota and may be antagonized by probiotic yeast during interaction with Peyer's patches. *Applied Microbiology and Biotechnology* **99,** 9097–9110. ISSN: 0175-7598 1432-0614 (2015).

159. Sanz, Y. *et al.* Novel Polyfermentor Intestinal Model (PolyFermS) for Controlled Ecological Studies: Validation and Effect of pH. *PLoS One* **8.** ISSN: 1932-6203 (2013).

160. Venema, K. in *The Impact of Food Bioactives on Health* 293–304 (2015). ISBN: 978-3-319-15791-7 978-3-319-16104-4.

161. Barroso, E., Cueva, C., Peláez, C., Martínez-Cuesta, M. C. & Requena, T. Development of human colonic microbiota in the computer-controlled dynamic SIMulator of the GastroIntestinal tract SIMGI. *LWT - Food Science and Technology* **61,** 283–289. ISSN: 00236438 (2015).

162. Barroso, E., Cueva, C., Peláez, C., Martínez-Cuesta, M. C. & Requena, T. in *The Impact of Food Bioactives on Health* 319–327 (2015). ISBN: 978-3-319-15791-7 978-3-319-16104-4.

163. Giuliani, C. *et al.* Dietary supplement based on stilbenes: a focus on gut microbial metabolism by the in vitro simulator M-SHIME®. *Food & Function* **7,** 4564–4575. ISSN: 2042-6496 2042-650X (2016).

164. Wiese, M. *et al.* CoMiniGut—a small volumein vitrocolon model for the screening of gut microbial fermentation processes. *PeerJ* **6.** ISSN: 2167-8359 (2018).

165. Bondue, P. *et al.* A toddler SHIME® model to study microbiota of young children. *FEMS Microbiology Letters* **367.** ISSN: 1574-6968 (2020).

166. Macfarlane, G. T., Cummings, J. H., Macfarlane, S. & Gibson, G. R. Influence of retention time on degradation of pancreatic enzymes by human colonic bacteria grown in a 3-stage continuous culture system. *Journal of Applied Bacteriology* **67,** 521–527. ISSN: 00218847 (1989).

167. Van Nuenen, M. H. M. C., Diederick Meyer, P. & Venema, K. The Effect of Various Inulins andClostridium difficileon the Metabolic Activity of the Human Colonic Microbiotain vitro. *Microbial Ecology in Health and Disease* **15,** 137–144. ISSN: 1651-2235 (2009).

168. Marciani, L. *et al.* Stimulation of colonic motility by oral PEG electrolyte bowel preparation assessed by MRI: comparison of split vs single dose. *Neurogastroenterol Motil* **26,** 1426–1436. ISSN: 1365-2982 (Electronic) 1350-1925 (Linking). https://www.ncbi.nlm.nih.gov/pubmed/25060551 (2014).

169. Bayliss, W. M. & Starling, E. H. The movements and innervation of the small intestine. *The Journal of Physiology* **24,** 99–143. ISSN: 00223751 (1899).

170. Dinning, P. G. *et al.* Quantification of in vivo colonic motor patterns in healthy humans before and after a meal revealed by high-resolution fiber-optic manometry. *Neurogastroenterology & Motility* **26,** 1443–1457. ISSN: 13501925 (2014).

171. Chirra, H. D. *et al.* Planar Microdevices for Enhanced In Vivo Retention and Oral Bioavailability of Poorly Permeable Drugs. *Advanced Healthcare Materials* **3,** 1648–1654. ISSN: 21922640 (2014).

172. Barker, N., van de Wetering, M. & Clevers, H. The intestinal stem cell. *Genes & Development* **22,** 1856–1864. ISSN: 0890-9369 (2008).

173. Ainslie, K. M. *et al.* Microfabricated Devices for Enhanced Bioadhesive Drug Delivery: Attachment to and Small-Molecule Release Through a Cell Monolayer Under Flow. *Small* **5,** 2857–2863. ISSN: 16136810 16136829 (2009).

174. Tao, S. L. & Desai, T. A. Micromachined devices: The impact of controlled geometry from cell-targeting to bioavailability. *Journal of Controlled Release* **109,** 127–138. ISSN: 01683659 (2005).

175. Tao, S. L. & Desai, T. A. Gastrointestinal patch systems for oral drug delivery. *Drug Discovery Today* **10,** 909–915. ISSN: 13596446 (2005).

176. Tao, S. L., Lubeley, M. W. & Desai, T. A. Bioadhesive poly(methyl methacrylate) microdevices for controlled drug delivery. *Journal of Controlled Release* **88,** 215–228. ISSN: 01683659 (2003).

177. Ainslie, K. M., Kraning, C. M. & Desai, T. A. Microfabrication of an asymmetric, multi-layered microdevice for controlled release of orally delivered therapeutics. *Lab on a Chip* **8.** ISSN: 1473-0197 1473-0189 (2008).

178. Guan, J., He, H., Lee, L. J. & Hansford, D. J. Fabrication of Particulate Reservoir-Containing, Capsulelike, and Self-Folding Polymer Microstructures for Drug Delivery. *Small* **3,** 412–418. ISSN: 16136810 16136829 (2007).

179. Zhang, P. *et al.* Top-Down Fabrication of Polyelectrolyte-Thermoplastic Hybrid Microparticles for Unidirectional Drug Delivery to Single Cells. *Advanced Healthcare Materials* **2,** 540–545. ISSN: 21922640 (2013).

180. Fox, C. B. *et al.* Picoliter-volume inkjet printing into planar microdevice reservoirs for low-waste, high-capacity drug loading. *Bioengineering & Translational Medicine* **2,** 9–16. ISSN: 23806761 (2017).

181. Fox, C. B. *et al.* Fabrication of Sealed Nanostraw Microdevices for Oral Drug Delivery. *ACS Nano* **10,** 5873–5881. ISSN: 1936-0851 1936-086X (2016).

182. Ahmed, A., Bonner, C. & Desai, T. A. Bioadhesive microdevices with multiple reservoirs: a new platform for oral drug delivery. *Journal of Controlled Release* **81,** 291–306. ISSN: 01683659 (2002).

183. Wei, X. *et al.* Biomimetic Micromotor Enables Active Delivery of Antigens for Oral Vaccination. *Nano Letters* **19,** 1914–1921. ISSN: 1530-6984 1530-6992 (2019).

184. De Ávila, B. E.-F. *et al.* Micromotor-enabled active drug delivery for in vivo treatment of stomach infection. *Nature Communications* **8.** ISSN: 2041-1723 (2017).

185. Gao, W. *et al.* Artificial Micromotors in the Mouse's Stomach: A Step toward in Vivo Use of Synthetic Motors. *ACS Nano* **9,** 117–123. ISSN: 1936-0851 1936-086X (2015).

186. Sundararajan, S., Lammert, P. E., Zudans, A. W., Crespi, V. H. & Sen, A. Catalytic Motors for Transport of Colloidal Cargo. *Nano Letters* **8,** 1271–1276. ISSN: 1530-6984 1530-6992 (2008).

187. Wu, Z. *et al.* Self-Propelled Polymer-Based Multilayer Nanorockets for Transportation and Drug Release. *Angewandte Chemie International Edition* **52,** 7000–7003. ISSN: 14337851 (2013).

188. Gao, W. & Wang, J. Synthetic micro/nanomotors in drug delivery. *Nanoscale* **6,** 10486–10494. ISSN: 2040-3364 2040-3372 (2014).

189. Li, J. *et al.* Micromotors Spontaneously Neutralize Gastric Acid for pH-Responsive Payload Release. *Angewandte Chemie International Edition* **56,** 2156–2161. ISSN: 14337851 (2017).

190. Lock, J. Y., Carlson, T. L. & Carrier, R. L. Mucus models to evaluate the diffusion of drugs and particles. *Advanced Drug Delivery Reviews* **124,** 34–49. ISSN: 0169409X (2018).

191. Liu, L. *et al.* Mucus layer modeling of human colonoids during infection with enteroaggragative E. coli. *Scientific Reports* **10.** ISSN: 2045-2322 (2020).

192. Poletti, M., Arnauts, K., Ferrante, M. & Korcsmaros, T. Organoid-based Models to Study the Role of Host-microbiota Interactions in IBD. *Journal of Crohn's and Colitis* **15,** 1222–1235. ISSN: 1873-9946 (July 2021).

193. Schwank, G. *et al.* Functional Repair of CFTR by CRISPR/Cas9 in Intestinal Stem Cell Organoids of Cystic Fibrosis Patients. *Cell Stem Cell* **13,** 653–658. ISSN: 19345909 (2013).

194. Dekkers, J. F. *et al.* Characterizing responses to CFTR-modulating drugs using rectal organoids derived from subjects with cystic fibrosis. *Science Translational Medicine* **8,** 84–344. ISSN: 1946-6234 1946-6242 (2016).

195. Matano, M. *et al.* Modeling colorectal cancer using CRISPR-Cas9–mediated engineering of human intestinal organoids. *Nature Medicine* **21,** 256–262. ISSN: 1078-8956 1546-170X (2015).

196. Boilève, A. *et al.* Immunosurveillance against tetraploidization-induced colon tumorigenesis. *Cell Cycle* **12,** 473–479. ISSN: 1538-4101 1551-4005 (2014).

197. Engevik, M. A. *et al.* HumanClostridium difficileinfection: inhibition of NHE3 and microbiota profile. *American Journal of Physiology-Gastrointestinal and Liver Physiology* **308,** G497–G509. ISSN: 0193-1857 1522-1547 (2015).

198. Yin, Y. *et al.* Modeling rotavirus infection and antiviral therapy using primary intestinal organoids. *Antiviral Research* **123,** 120–131. ISSN: 01663542 (2015).

199. Yin, Y. *et al.* Mycophenolic acid potently inhibits rotavirus infection with a high barrier to resistance development. *Antiviral Research* **133,** 41–49. ISSN: 01663542 (2016).

200. Yin, Y. *et al.* PI3K-Akt-mTOR axis sustains rotavirus infection via the 4E-BP1 mediated autophagy pathway and represents an antiviral target. *Virulence* **9,** 83–98. ISSN: 2150-5594 2150-5608 (2017).

201. Fischer, N. *et al.* Histone deacetylase inhibition enhances antimicrobial peptide but not inflammatory cytokine expression upon bacterial challenge. *Proceedings of the National Academy of Sciences* **113,** E2993–E3001. ISSN: 0027-8424 1091-6490 (2016).

202. In, J. *et al.* Enterohemorrhagic Escherichia coli Reduces Mucus and Intermicrovillar Bridges in Human Stem Cell-Derived Colonoids. *Cellular and Molecular Gastroenterology and Hepatology* **2,** 48–62. ISSN: 2352345X (2016).

203. Zhou, J. *et al.* Infection of bat and human intestinal organoids by SARS-CoV-2. *Nature Medicine* **26,** 1077–1083. ISSN: 1078-8956 1546-170X (2020).

204. Bein, A. *et al.* Microfluidic Organ-on-a-Chip Models of Human Intestine. *Cellular and Molecular Gastroenterology and Hepatology* **5,** 659–668. ISSN: 2352345X (2018).

205. Donkers, J. M., Eslami Amirabadi, H. & van de Steeg, E. Intestine-on-a-chip: Next level in vitro research model of the human intestine. *Current Opinion in Toxicology* **25,** 6–14. ISSN: 24682020 (2021).

206. Kasendra, M. *et al.* Duodenum Intestine-Chip for preclinical drug assessment in a human relevant model. *eLife* **9.** ISSN: 2050-084X (2020).

207. Sontheimer-Phelps, A. *et al.* Human Colon-on-a-Chip Enables Continuous In Vitro Analysis of Colon Mucus Layer Accumulation and Physiology. *Cellular and Molecular Gastroenterology and Hepatology* **9,** 507–526. ISSN: 2352345X (2020).

208. Shin, W., Hinojosa, C. D., Ingber, D. E. & Kim, H. J. Human Intestinal Morphogenesis Controlled by Transepithelial Morphogen Gradient and Flow-Dependent Physical Cues in a Microengineered Gut-on-a-Chip. *iScience* **15,** 391–406. ISSN: 25890042 (2019).

209. Tovaglieri, A. *et al.* Species-specific enhancement of enterohemorrhagic E. coli pathogenesis mediated by microbiome metabolites. *Microbiome* **7.** ISSN: 2049-2618 (2019).

210. Apostolou, A. *et al.* A Micro-engineered Human Colon Intestine-Chip Platform to Study Leaky Barrier. *bioRxiv* (2020).

211. Shin, W. *et al.* Robust Formation of an Epithelial Layer of Human Intestinal Organoids in a Polydimethylsiloxane-Based Gut-on-a-Chip Microdevice. *Frontiers in Medical Technology* **2.** ISSN: 2673-3129 (2020).

212. Beaurivage, C. *et al.* Development of a human primary gut-on-a-chip to model inflammatory processes. *Scientific Reports* **10.** ISSN: 2045-2322 (2020).

213. Gazzaniga, F. S. *et al.* Harnessing Colon Chip Technology to Identify Commensal Bacteria That Promote Host Tolerance to Infection. *Frontiers in Cellular and Infection Microbiology* **11.** ISSN: 2235-2988 (2021).

214. Reddy, M. B., Clewell III, H. J., Lave, T. & E., M. in *New Insights into Toxicity and Drug Testing* (InTech, Jan. 2013).

215. Kambayashi, A. & Dressman, J. B. An in vitro–in silico–in vivo approach to predicting the oral pharmacokinetic profile of salts of weak acids: Case example dantrolene. *European Journal of Pharmaceutics and Biopharmaceutics* **84,** 200–207. ISSN: 09396411 (May 2013).

216. Scotcher, D., Jones, C., Rostami-Hodjegan, A. & Galetin, A. Novel minimal physiologically-based model for the prediction of passive tubular reabsorption and renal excretion clearance. *European Journal of Pharmaceutical Sciences* **94,** 59–71. ISSN: 09280987 (Oct. 2016).

217. Kuepfer, L. *et al.* Applied Concepts in PBPK Modeling: How to Build a PBPK/PD Model. *CPT: Pharmacometrics & Systems Pharmacology* **5,** 516–531. ISSN: 2163-8306 (Oct. 2016).

218. Patel, S. *et al.* Integration of Precipitation Kinetics From an In Vitro, Multicompartment Transfer System and Mechanistic Oral Absorption Modeling for Pharmacokinetic Prediction of Weakly Basic Drugs. *Journal of Pharmaceutical Sciences* **108,** 574–583. ISSN: 00223549 (Jan. 2019).

219. Chou, W.-C. *et al.* Development of a multi-route physiologically based pharmacokinetic (PBPK) model for nanomaterials: a comparison between a traditional versus a new route-specific approach using gold nanoparticles in rats. *Particle and Fibre Toxicology* **19,** 47. ISSN: 1743-8977 (Dec. 2022).

220. Jamei, M. *et al.* The Simcyp ® Population-based ADME Simulator. *Expert Opinion on Drug Metabolism & Toxicology* **5,** 211–223. ISSN: 1742-5255 (Feb. 2009).

221. Bermejo, M. *et al.* A Mechanistic Physiologically-Based Biopharmaceutics Modeling (PBBM) Approach to Assess the In Vivo Performance of an Orally Administered Drug Product: From IVIVC to IVIVP. *Pharmaceutics* **12,** 74. ISSN: 1999-4923 (Jan. 2020).

222. Heimbach, T. *et al.* Establishing the Bioequivalence Safe Space for Immediate-Release Oral Dosage Forms using Physiologically Based Biopharmaceutics Modeling (PBBM): Case Studies. *Journal of Pharmaceutical Sciences* **110,** 3896–3906. ISSN: 00223549 (Dec. 2021).

223. Patel, N., Pathak, S. M. & Turner, D. B. in *Oral Drug Delivery for Modified Release Formulations* 355–374 (Wiley, Apr. 2022).

224. Arafat, M., Sarfraz, M. & AbuRuz, S. Development and In Vitro Evaluation of Controlled Release Viagra® Containing Poloxamer-188 Using Gastroplus™ PBPK

Modeling Software for In Vivo Predictions and Pharmacokinetic Assessments. *Pharmaceuticals* **14,** 479. ISSN: 1424-8247 (May 2021).

225. Lin, H.-P., Sun, D., Zhang, X. & Wen, H. Physiologically Based Pharmacokinetic Modeling for Substitutability Analysis of Venlafaxine Hydrochloride Extended-Release Formulations Using Different Release Mechanisms: Osmotic Pump Versus Openable Matrix. *Journal of Pharmaceutical Sciences* **105,** 3088–3096. ISSN: 00223549 (Oct. 2016).

226. Shuklinova, O., Dorożyński, P., Kulinowski, P. & Polak, S. Quality Control Dissolution Data Is Biopredictive for a Modified Release Ropinirole Formulation: Virtual Experiment with the Use of Re-Developed and Verified PBPK Model. *Pharmaceutics* **14,** 1514. ISSN: 1999-4923 (July 2022).

227. Lloyd, R. S. *et al.* Negative Food Effect of Danirixin: Use of PBPK Modelling to Explore the Effect of Formulation and Meal Type on Clinical PK. *Pharmaceutical Research* **37,** 233. ISSN: 0724-8741 (Dec. 2020).

228. Grotberg, J. B. & Jensen, O. E. Biofluid Mechanics in Flexible Tubes. *Annual Review of Fluid Mechanics* **36,** 121–147. ISSN: 0066-4189 1545-4479 (2004).

229. Misra, J. C. & Pandey, S. K. in *Biomathematics* 167–193 (WORLD SCIENTIFIC, Sept. 2006).

230. Udaykumar, H. S., Krishman, S., Dillard, S., Marshall, J. S. & Schulze, K. Computation of peristaltic transport and mixing in the small intestine. *Journal of Biomechanics* **39,** S442–S443. ISSN: 00219290 (2006).

231. Pal, A. *et al.* Gastric flow and mixing studied using computer simulation. *Proceedings of the Royal Society of London. Series B: Biological Sciences* **271,** 2587–2594. ISSN: 0962-8452 1471-2954 (2004).

232. Ferrua, M. J. & Singh, R. P. Modeling the Fluid Dynamics in a Human Stomach to Gain Insight of Food Digestion. *Journal of Food Science* **75,** R151–R162. ISSN: 00221147 (2010).

233. Sinnott, M. D., Cleary, P. W., Arkwright, J. W. & Dinning, P. G. Investigating the relationships between peristaltic contraction and fluid transport in the human colon using Smoothed Particle Hydrodynamics. *Computers in Biology and Medicine* **42,** 492–503. ISSN: 00104825 (2012).

234. Alexiadis, A., Simmons, M. J. H., Stamatopoulos, K., Batchelor, H. K. & Moulitsas, I. The duality between particle methods and artificial neural networks. *Scientific Reports* **10.** ISSN: 2045-2322 (2020).

235. Sinnott, M. D., Cleary, P. W., Dinning, P. G., Arkwright, J. W. & Costa, M. Interpreting manometric signals for propulsion in the gut. *Computational Particle Mechanics* **2,** 273–282. ISSN: 2196-4378 2196-4386 (2015).

236. Alexiadis, A. *et al.* Using discrete multi-physics for detailed exploration of hydrodynamics in an in vitro colon system. *Comput Biol Med* **81,** 188–198. ISSN: 1879-0534 (Electronic) 0010-4825 (Linking). https://www.ncbi.nlm.nih.gov/pubmed/28088672 (2017).

237. Schütt, M., Stamatopoulos, K., Simmons, M. J. H., Batchelor, H. K. & Alexiadis, A. Modelling and simulation of the hydrodynamics and mixing profiles in the human proximal colon using Discrete Multiphysics. *Computers in Biology and Medicine* **121.** ISSN: 00104825 (2020).

238. Schütt, M., Stamatopoulos, K., Batchelor, H. K., Simmons, M. J. H. & Alexiadis, A. Modelling and Simulation of the Drug Release from a Solid Dosage Form in the Human Ascending Colon: The Influence of Different Motility Patterns and Fluid Viscosities. *Pharmaceutics* **13.** ISSN: 1999-4923 (2021).

239. Parker, D. J., Broadbent, C. J., Fowles, P., Hawkesworth, M. R. & McNeil, P. Positron emission particle tracking - a technique for studying flow within engineering equipment. *Nuclear Instruments and Methods in Physics Research Section A: Accelerators, Spectrometers, Detectors and Associated Equipment* **326,** 592–607. ISSN: 01689002 (1993).

240. Broadbent, C. J., Bridgwater, J., Parker, D. J., Keningley, S. T. & Knight, P. A phenomenological study of a batch mixer using a positron camera. *Powder Technology* **76,** 317–329. ISSN: 00325910 (1993).

241. Lundin, E. *et al.* Segmental colonic transit studies: comparison of a radiological and a scintigraphic method. *Colorectal Disease* **9,** 344–351. ISSN: 1462-8910 1463-1318 (2007).

242. Miller, L. E., Ibarra, A. & Ouwehand, A. C. Normative Values for Colonic Transit Time and Patient Assessment of Constipation in Adults With Functional Constipation: Systematic Review With Meta-Analysis. *Clinical Medicine Insights: Gastroenterology* **10.** ISSN: 1179-5522 1179-5522 (2017).

243. Maqbool, S., Parkman, H. P. & Friedenberg, F. K. Wireless Capsule Motility: Comparison of the SmartPill® GI Monitoring System with Scintigraphy for Measuring Whole Gut Transit. *Digestive Diseases and Sciences* **54,** 2167–2174. ISSN: 0163-2116 1573-2568 (2009).

244. Chen, J.-H. *et al.* Characterization of Simultaneous Pressure Waves as Biomarkers for Colonic Motility Assessed by High-Resolution Colonic Manometry. *Frontiers in Physiology* **9.** ISSN: 1664-042X (2018).

245. Li, Y.-W., Yu, Y.-J., Fei, F., Zheng, M.-Y. & Zhang, S.-W. High-resolution colonic manometry and its clinical application in patients with colonic dysmotility: A review. *World Journal of Clinical Cases* **7,** 2675–2686. ISSN: 2307-8960 (2019).

246. Milkova, N., Parsons, S. P., Ratcliffe, E., Huizinga, J. D. & Chen, J.-H. On the nature of high-amplitude propagating pressure waves in the human colon. *American Journal of Physiology-Gastrointestinal and Liver Physiology* **318,** G646–G660. ISSN: 0193-1857 1522-1547 (2020).

247. Dinning, P. G. *et al.* Colonic motor abnormalities in slow transit constipation defined by high resolution, fibre-optic manometry. *Neurogastroenterology & Motility* **27,** 379–388. ISSN: 13501925 (2015).

248. Van der Paardt, M. P. *et al.* Noninvasive automated motion assessment of intestinal motility by continuously tagged MR imaging. *Journal of Magnetic Resonance Imaging* **39,** 9–16. ISSN: 10531807 (2014).

249. Sprengers, A. M. J. *et al.* Use of continuously MR tagged imaging for automated motion assessment in the abdomen: A feasibility study. *Journal of Magnetic Resonance Imaging* **36,** 492–497. ISSN: 10531807 (2012).

250. Jonge, C. S., Sprengers, A. M. J., Rijn, K. L., Nederveen, A. J. & Stoker, J. Assessment of fasted and fed gastrointestinal contraction frequencies in healthy subjects using continuously tagged MRI. *Neurogastroenterology & Motility* **32.** ISSN: 1350-1925 1365-2982 (2019).

251. Wilkinson-Smith, V. *et al.* The MRI colonic function test: Reproducibility of the Macrogol stimulus challenge. *Neurogastroenterology & Motility* **32.** ISSN: 1350-1925 1365-2982 (2020).

252. Hopgood, M., Reynolds, G. & Barker, R. Using Computational Fluid Dynamics to Compare Shear Rate and Turbulence in the TIM-Automated Gastric Compartment With USP Apparatus II. *Journal of Pharmaceutical Sciences* **107,** 1911–1919. ISSN: 00223549 (2018).

253. Salehi, N. *et al.* Hierarchical Mass Transfer Analysis of Drug Particle Dissolution, Highlighting the Hydrodynamics, pH, Particle Size, and Buffer Effects for the Dissolution of Ionizable and Nonionizable Drugs in a Compendial Dissolution Vessel. *Molecular Pharmaceutics* **17,** 3870–3884. ISSN: 1543-8384 1543-8392 (2020).

254. M, A. S. & Harvey, P. D. *Engineering Properties of Steels* ISBN: 978-0-87170-144-2 (American Society for Metals (ASM) International, 1982).

255. Formlabs. Standard resin technical data sheet. https://archive-media.formlabs.com/upload/Clear-DataSheet.pdf (2017).

256. Formlabs. *Clear Resin* 2022. https://formlabs.com/store/clear-resin/.

257. Travieso-Rodriguez, J. A. *et al.* Mechanical Properties of 3D-Printing Polylactic Acid Parts subjected to Bending Stress and Fatigue Testing. *Materials* **12.** ISSN: 1996-1944 (2019).

258. MatWeb. *Overview of material properties for Nylon* 2022. https://www.matweb.com/search/DataSheet.aspx?MatGUID=8d78f3cfcb6f49d595896ce6ce6a2ef1&ckck=1.

259. Suteja, T. J. & Soesanti, A. Mechanical Properties of 3D Printed Polylactic Acid Product for Various Infill Design Parameters: A Review. *Journal of Physics: Conference Series* **1569.** ISSN: 1742-6588 1742-6596 (2020).

260. Alafaghani, A. & Qattawi, A. Investigating the effect of fused deposition modeling processing parameters using Taguchi design of experiment method. *Journal of Manufacturing Processes* **36,** 164–174. ISSN: 15266125 (2018).

261. Chacón, J. M., Caminero, M. A., García-Plaza, E. & Núñez, P. J. Additive manufacturing of PLA structures using fused deposition modelling: Effect of process parameters on mechanical properties and their optimal selection. *Materials & Design* **124,** 143–157. ISSN: 02641275 (2017).

262. IndustrialSpec. *EMX-18-1032M-BN, 1/8" Hose Barb x 10-32 Male UNF Swivel Elbow* 2019. https://www.industrialspec.com/shop/plastic-fittings/plastic-swivel-fittings/emx-series-elbow-male-thread-x-hose-barb.html.

263. S, R. *RS PRO, M3 Brass Threaded Insert diameter 4mm Depth 4.78mm* 2020. https://uk.rs-online.com/web/p/threaded-inserts/0278534?cm_mmc=UK-PLA-DS3A-_-google-_-CSS_UK_EN_Fasteners_%26_Fixings_Whoop-_-Threaded+Inserts_Whoop-_-278534&matchtype=&pla-299816839675&gclsrc=ds&gclsrc=ds.

264. Formlabs. *Elastic 50A Resin* 2022. https://formlabs.com/store/elastic-resin/.

265. Polycraft. *Techical Data Sheet: Polycraft T-15 Clear RTV Addition Cure Silicone Rubber* 2018. https://mbfgfiles.co.uk/datasheets/T-15_tech.pdf.

266. Formlabs. *Elastic 50 A Technical Data Sheet* 2020. https://formlabs-media.formlabs.com/datasheets/2001420-TDS-ENUS-0.pdf.

267. Bray, F. *et al.* Global cancer statistics 2018: GLOBOCAN estimates of incidence and mortality worldwide for 36 cancers in 185 countries. *CA: A Cancer Journal for Clinicians* **68,** 394–424. ISSN: 00079235 (2018).

268. Alatab, S. *et al.* The global, regional, and national burden of inflammatory bowel disease in 195 countries and territories, 1990–2017: a systematic analysis for the Global Burden of Disease Study 2017. *The Lancet Gastroenterology & Hepatology* **5,** 17–30. ISSN: 24681253 (2020).

269. Black, C. J. & Ford, A. C. Global burden of irritable bowel syndrome: trends, predictions and risk factors. *Nature Reviews Gastroenterology & Hepatology* **17,** 473–486. ISSN: 1759-5045 1759-5053 (2020).

270. Zaborenko, N. *et al.* First-Principles and Empirical Approaches to Predicting In Vitro Dissolution for Pharmaceutical Formulation and Process Development and for Product Release Testing. *The AAPS Journal* **21.** ISSN: 1550-7416 (2019).

271. Al-Tabakha, M. M. & Alomar, M. J. In Vitro Dissolution and in Silico Modeling Shortcuts in Bioequivalence Testing. *Pharmaceutics* **12.** ISSN: 1999-4923 (2020).

272. Axel, L., Ann Shimakawa, B. S. E. E. & MacFall, J. A time-of-flight method of measuring flow velocity by magnetic resonance imaging. *Magnetic Resonance Imaging* **4,** 199–205. ISSN: 0730725X (1986).

273. Moser, K. W. *et al.* Velocity measurements of flow through a step stenosis using Magnetic Resonance Imaging. *Experiments in Fluids* **29,** 438–447. ISSN: 0723-4864 1432-1114 (2000).

274. d'Avila, M. A. *et al.* Magnetic resonance imaging (MRI): a technique to study flow an microstructure of concentrated emulsions. *Brazilian Journal of Chemical Engineering* **22,** 49–60. ISSN: 0104-6632 (2005).

275. Grady, H. *et al.* Industry's View on Using Quality Control, Biorelevant, and Clinically Relevant Dissolution Tests for Pharmaceutical Development, Registration, and Commercialization. *Journal of Pharmaceutical Sciences* **107,** 34–41. ISSN: 00223549 (2018).

276. Major, G. *et al.* Demonstration of differences in colonic volumes, transit, chyme consistency, and response to psyllium between healthy and constipated subjects using magnetic resonance imaging. *Neurogastroenterology & Motility* **30.** ISSN: 13501925 (2018).

277. Stamatopoulos, K., Batchelor, H. K., Alberini, F., Ramsay, J. & Simmons, M. J. H. Understanding the impact of media viscosity on dissolution of a highly water soluble drug within a USP 2 mini vessel dissolution apparatus using an optical planar induced fluorescence (PLIF) method. *Int J Pharm* **495,** 362–373. ISSN: 1873-3476 (Electronic) 0378-5173 (Linking). https://www.ncbi.nlm.nih.gov/pubmed/26363111 (2015).

278. Vertzoni, M. *et al.* Impact of regional differences along the gastrointestinal tract of healthy adults on oral drug absorption: An UNGAP review. *European Journal of Pharmaceutical Sciences* **134,** 153–175. ISSN: 09280987 (2019).

279. Tanaka, Y., Goto, T., Kataoka, M., Sakuma, S. & Yamashita, S. Impact of Luminal Fluid Volume on the Drug Absorption After Oral Administration: Analysis Based on In Vivo Drug Concentration–Time Profile in the Gastrointestinal Tract. *Journal of Pharmaceutical Sciences* **104,** 3120–3127. ISSN: 00223549 (2015).

280. Nayak, K. S. *et al.* Cardiovascular magnetic resonance phase contrast imaging. *Journal of Cardiovascular Magnetic Resonance* **17.** ISSN: 1532-429X (2015).

281. Wymer, D. T., Patel, K. P., Burke, W. F. & Bhatia, V. K. Phase-Contrast MRI: Physics, Techniques, and Clinical Applications. *RadioGraphics* **40,** 122–140. ISSN: 0271-5333 1527-1323 (2020).

282. Ahmadi, S. & Mastikhin, I. Velocity Measurement of Fast Flows Inside Small Structures with Tagged MRI. *Applied Magnetic Resonance* **51,** 431–448. ISSN: 0937-9347 1613-7507 (2020).

283. O'Brien, K. R. *et al.* MRI phase contrast velocity and flow errors in turbulent stenotic jets. *Journal of Magnetic Resonance Imaging* **28,** 210–218. ISSN: 10531807 15222586 (2008).

284. Thorpe, M. P., Ehrenpreis, E. D., Putt, K. S. & Hannon, B. A dynamic model of colonic concentrations of delayed-release 5-aminosalicylic acid (Asacol). *Alimentary Pharmacology & Therapeutics* **29,** 1193–1201. ISSN: 02692813 13652036 (2009).

285. Dinning, P. G. *et al.* Pancolonic spatiotemporal mapping reveals regional deficiencies in, and disorganization of colonic propagating pressure waves in severe constipation. *Neurogastroenterology & Motility* **22,** e340–e349. ISSN: 13501925 (2010).

286. Bassotti, G. *et al.* Colonic mass movements in idiopathic chronic constipation. *Gut* **29,** 1173–1179. ISSN: 0017-5749 (1988).

287. Braun, R. J. & Parrott, E. L. Influence of Viscosity and Solubilization on Dissolution Rate. *Journal of Pharmaceutical Sciences* **61,** 175–178. ISSN: 00223549 (1972).

288. Vertzoni, M. *et al.* Characteristics of Contents of Lower intestine in the 65–74 Years of Age Range Could Impact the Performance of Safe and Efficacious Modified Release Products. *Journal of Pharmaceutical Sciences* **110,** 251–258. ISSN: 00223549 (2021).

289. Perman, W. H., Creswell, L. L., Wyers, S. G., Moulton, M. J. & Pasque, M. K. Hybrid dante and phase-contrast imaging technique for measurement of three- dimensional myocardial wall motion. *Journal of Magnetic Resonance Imaging* **5,** 101–106. ISSN: 10531807 15222586 (1995).

290. Kuijer, J. P. A., Marcus, T., Gtte, M. J. W., van Rossum, A. C. & Heethaar, R. M. Simultaneous MRI tagging and through-plane velocity quantification: A three-dimensional myocardial motion tracking algorithm. *Journal of Magnetic Resonance Imaging* **9,** 409–419. ISSN: 1053-1807 1522-2586 (1999).

291. Wang, B., Bredael, G. & Armenante, P. M. Computational hydrodynamic comparison of a mini vessel and a USP 2 dissolution testing system to predict the dynamic operating conditions for similarity of dissolution performance. *International Journal of Pharmaceutics* **539,** 112–130. ISSN: 03785173 (2018).

292. Yoshida, H., Kuwana, A., Shibata, H., Izutsu, K.-i. & Goda, Y. Particle Image Velocimetry Evaluation of Fluid Flow Profiles in USP 4 Flow-Through Dissolution Cells. *Pharmaceutical Research* **32,** 2950–2959. ISSN: 0724-8741 1573-904X (2015).

293. Shi, Y., Jiang, Y., Li, B. & Chen, J. Analysis of the Velocity Distribution in Partially-Filled Circular Pipe Employing the Principle of Maximum Entropy. *PLoS One* **11.** ISSN: 1932-6203 (2016).

294. Mark, E. B. *et al.* Ambulatory assessment of colonic motility using the electromagnetic capsule tracking system. *Neurogastroenterology & Motility* **31.** ISSN: 1350-1925 1365-2982 (2018).

295. Hiroz p, p., schlageter v, v., givel j c, j. c. & kucera p, p. Colonic movements in healthy subjects as monitored by a Magnet Tracking System. *Neurogastroenterology & Motility* **21,** 838–e57. ISSN: 13501925 13652982 (2009).

296. Sulaiman, S. & Marciani, L. MRI of the Colon in the Pharmaceutical Field: The Future before us. *Pharmaceutics* **11,** 146. ISSN: 1999-4923 (2019).

297. Watts, P. J. & Lllum, L. Colonic drug delivery. *Drug Development and Industrial Pharmacy* **23,** 893–913. ISSN: 0363-9045 (1997).

298. Sinnott, M. D., Cleary, P. W. & Harrison, S. M. Peristaltic transport of a particulate suspension in the small intestine. *Applied Mathematical Modelling* **44,** 143–159. ISSN: 0307904X (2017).

299. Alexiadis, A. The discrete multi-hybrid system for the simulation of solid-liquid flows. *PLoS One* **10,** e0124678. ISSN: 1932-6203 (2015).

300. Alexiadis, A. A new framework for modelling the dynamics and the breakage of capsules, vesicles and cells in fluid flow. *Procedia IUTAM* **16,** 80–88. ISSN: 2210-9838 (2015).

301. Ariane, M. *et al.* Discrete multi-physics: A mesh-free model of blood flow in flexible biological valve including solid aggregate formation. *PLoS One* **12,** e0174795. ISSN: 1932-6203 (2017).

302. Ariane, M., Kassinos, S., Velaga, S. & Alexiadis, A. Discrete multi-physics simulations of diffusive and convective mass transfer in boundary layers containing motile cilia in lungs. *Computers in Biology and Medicine* **95,** 34–42. ISSN: 0010-4825 (2018).

303. Ariane, M. *et al.* Modelling and simulation of flow and agglomeration in deep veins valves using discrete multi physics. *Computers in Biology and Medicine* **89,** 96–103. ISSN: 0010-4825 (2017).

304. Mohammed, A. M., Ariane, M. & Alexiadis, A. Using discrete multiphysics modelling to assess the effect of calcification on hemodynamic and mechanical deformation of aortic valve. *ChemEngineering* **4,** 48. ISSN: 2305-7084 (2020).

305. Rahmat, A., Barigou, M. & Alexiadis, A. Deformation and rupture of compound cells under shear: A discrete multiphysics study. *Physics of Fluids* **31,** 51903. ISSN: 1070-6631 (2019).

306. Rahmat, A. *et al.* Modeling the agglomeration of settling particles in a dewatering process. *Physics of Fluids* **32,** 123314. ISSN: 1070-6631 (2020).

307. Baksamawi, H. A., Ariane, M., Brill, A., Vigolo, D. & Alexiadis, A. Modelling Particle Agglomeration on through Elastic Valves under Flow. *ChemEngineering* **5,** 40. ISSN: 2305-7084 (2021).

308. Alexiadis, A., Ghraybeh, S. & Qiao, G. Natural convection and solidification of phase-change materials in circular pipes: A SPH approach. *Computational Materials Science* **150,** 475–483. ISSN: 0927-0256 (2018).

309. Ariane, M. *et al.* Using Discrete Multi-Physics for studying the dynamics of emboli in flexible venous valves. *Computers & Fluids* **166,** 57–63. ISSN: 0045-7930 (2018).

310. Rahmat, A., Barigou, M. & Alexiadis, A. Numerical simulation of dissolution of solid particles in fluid flow using the SPH method. *International Journal of Numerical Methods for Heat & Fluid Flow*. ISSN: 0961-5539 (2019).

311. Alexiadis, A. Deep Multiphysics and Particle–Neuron Duality: A Computational Framework Coupling (Discrete) Multiphysics and Deep Learning. *Applied Sciences* **9,** 5369. ISSN: 2076-3417 (2019).

312. Sanfilippo, D., Ghiassi, B., Alexiadis, A. & Hernandez, A. G. Combined peridynamics and discrete multiphysics to study the effects of air voids and freeze-thaw on the mechanical properties of asphalt. *Materials* **14,** 1579. ISSN: 1996-1944 (2021).

313. Liu, G.-R. & Liu, M. B. *Smoothed particle hydrodynamics: a meshfree particle method* ISBN: 9812564403 (World scientific, 2003).

314. Kot, M., Nagahashi, H. & Szymczak, P. Elastic moduli of simple mass spring models. *The visual computer* **31,** 1339–1350. ISSN: 1432-2315 (2015).

315. Lloyd, B., Székely, G. & Harders, M. Identification of spring parameters for deformable object simulation. *IEEE Transactions on Visualization and Computer Graphics* **13,** 1081–1094. ISSN: 1077-2626 (2007).

316. Pazdniakou, A. & Adler, P. M. Lattice spring models. *Transport in porous media* **93,** 243–262. ISSN: 1573-1634 (2012).

317. Alexiadis, A., Simmons, M. J. H., Stamatopoulos, K., Batchelor, H. K. & Moulitsas, I. The virtual physiological human gets nerves! How to account for the action of the nervous system in multiphysics simulations of human organs. *Journal of The Royal Society Interface* **18,** 20201024. ISSN: 1742-5662 (2021).

318. Sahputra, I. H., Alexiadis, A. & Adams, M. J. A Coarse Grained Model for Viscoelastic Solids in Discrete Multiphysics Simulations. *ChemEngineering* **4,** 30. ISSN: 2305-7084 (2020).

319. Lucy, L. B. A numerical approach to the testing of the fission hypothesis. *The astronomical journal* **82,** 1013–1024. ISSN: 0004-6256 (1977).

320. Monaghan, J. J. & Gingold, R. A. Shock simulation by the particle method SPH. *Journal of computational physics* **52,** 374–389. ISSN: 0021-9991 (1983).

321. Monaghan, J. J. Smoothed particle hydrodynamics. *Reports on progress in physics* **68,** 1703. ISSN: 0034-4885 (2005).

322. Birmingham, U. o. *University of Birmingham's BlueBEAR HPC Service* http://www.birmingham.ac.uk/bear.

323. Ganzenmüller, G. C., Steinhauser, M. O. & Van Liedekerke, P. *The Implementation of Smoothed Particle Hydrodynamics in LAMMPS* 2019. Lammps.sandia.gov/doc/PDF/SPH_LAMMPS_userguide.pdf.

324. Plimpton, S. Fast parallel algorithms for short-range molecular dynamics. *Journal of computational physics* **117,** 1–19. ISSN: 0021-9991 (1995).

325. Stukowski, A. Visualization and analysis of atomistic simulation data with OVITO–the Open Visualization Tool. *Modelling and simulation in materials science and engineering* **18,** 15012. ISSN: 0965-0393 (2009).

326. MatLab. 9.9. 0.1495850 (R2020b). *The MathWorks Inc.: Natick, MA, USA* (2020).

327. Stathopoulos e, e., schlageter v, v., meyrat b, b., ribaupierre y, y. & kucera p, p. Magnetic pill tracking: a novel non-invasive tool for investigation of human digestive motility. *Neurogastroenterology and Motility* **17,** 148–154. ISSN: 1350-1925 1365-2982 (2005).

328. Liem, O. *et al.* Solid-state vs water-perfused catheters to measure colonic high-amplitude propagating contractions. *Neurogastroenterology & Motility* **24,** 345–e167. ISSN: 13501925 (2012).

329. Bassotti, G. & Gaburri, M. Manometric investigation of high-amplitude propagated contractile activity of the human colon. *American Journal of Physiology-Gastrointestinal and Liver Physiology* **255,** G660–G664. ISSN: 0193-1857 1522-1547 (1988).

330. Bai, G. *et al.* Hydrodynamic Investigation of USP Dissolution Test Apparatus II. *Journal of Pharmaceutical Sciences* **96,** 2327–2349. ISSN: 00223549 (2007).

331. Vrbanac, H. & Krese, A. The influence of different mechanical stress on the release properties of HPMC matrix tablets in sucrose-NaCl media. *Journal of Drug Delivery Science and Technology* **54.** ISSN: 17732247 (2019).

332. Dinning, P. G. *et al.* Abnormal predefecatory colonic motor patterns define constipation in obstructed defecation. *Gastroenterology* **127,** 49–56. ISSN: 00165085 (2004).

333. Narducci, F., Bassotti, G., Gaburri, M. & Morelli, A. Twenty four hour manometric recording of colonic motor activity in healthy man. *Gut* **28,** 17–25. ISSN: 0017-5749 (1987).

334. Rao, S. S. C., Sadeghi, P., Beaty, J., Kavlock, R. & Ackerson, K. Ambulatory 24-h colonic manometry in healthy humans. *American Journal of Physiology-Gastrointestinal and Liver Physiology* **280,** G629–G639. ISSN: 0193-1857 1522-1547 (2001).

335. Hoad, C. L. *et al.* Colon wall motility: comparison of novel quantitative semi-automatic measurements using cine MRI. *Neurogastroenterology & Motility* **28,** 327–335. ISSN: 13501925 (2016).

336. Asman, G. & Akçay, E. Effect of Membrane Preparation Methods on the Release of Theophylline through CA Membranes atIn-VitroConditions. *Journal of Macromolecular Science, Part A* **51,** 326–338. ISSN: 1060-1325 1520-5738 (2014).

337. Arkwright, J. W. *et al.* The effect of luminal content and rate of occlusion on the interpretation of colonic manometry. *Neurogastroenterology & Motility* **25,** e52–e59. ISSN: 13501925 (2013).

338. United States Pharmacopeial Convention, I. in. Chap. <711> Dissolution (United States Pharmacopeia. The National Formulary., 2011).

339. Diaz, D. A. *et al.* Dissolution Similarity Requirements: How Similar or Dissimilar Are the Global Regulatory Expectations? *The AAPS Journal* **18,** 15–22. ISSN: 1550-7416 (2015).

340. Shah, V. P., Tsong, Y., Sathe, P. & Liu, J.-P. In Vitro Dissolution Profile Comparison—Statistics and Analysis of the Similarity Factor, f2. *Pharmaceutical Research* **15,** 889–896. ISSN: 07248741 (1998).

341. Xie, F., Ji, S. & Cheng, Z. In vitro dissolution similarity factor (f2) and in vivo bioequivalence criteria, how and when do they match? Using a BCS class II drug as a simulation example. *European Journal of Pharmaceutical Sciences* **66,** 163–172. ISSN: 09280987 (2015).

342. Garbacz, G., Klein, S. & Weitschies, W. A biorelevant dissolution stress test device – background and experiences. *Expert Opinion on Drug Delivery* **7,** 1251–1261. ISSN: 1742-5247 1744-7593 (2010).

343. Abuhelwa, A. Y., Foster, D. J. R. & Upton, R. N. A Quantitative Review and Metamodels of the Variability and Factors Affecting Oral Drug Absorption—Part II:

Gastrointestinal Transit Time. *The AAPS Journal* **18,** 1322–1333. ISSN: 1550-7416 (Sept. 2016).

344. Tannergren, C., Bergendal, A., Lennernäs, H. & Abrahamsson, B. Toward an Increased Understanding of the Barriers to Colonic Drug Absorption in Humans: Implications for Early Controlled Release Candidate Assessment. *Molecular Pharmaceutics* **6,** 60–73. ISSN: 1543-8384 (Feb. 2009).

345. Thombre, A. G. Assessment of the feasibility of oral controlled release in an exploratory development setting. *Drug Discovery Today* **10,** 1159–1166. ISSN: 13596446 (Sept. 2005).

346. Xu, C. *et al.* The colonic motility and classification of patients with slow transit constipation by high-resolution colonic manometry. *Clinics and Research in Hepatology and Gastroenterology* **46,** 101998. ISSN: 22107401 (Nov. 2022).

347. Zhao, C., Cai, L., Chen, H., Tan, H. & Yan, D. Oral biomaterials for intestinal regulation. *Engineered Regeneration* **2,** 116–132. ISSN: 26661381 (2021).

348. Zhang, X. & Lionberger, R. A. Modeling and Simulation of Biopharmaceutical Performance. *Clinical Pharmacology & Therapeutics* **95,** 480–482. ISSN: 0009-9236 (May 2014).

349. Clear, N. J. *et al.* Evaluation of the Intelisite capsule to deliver theophylline and frusemide tablets to the small intestine and colon. *European Journal of Pharmaceutical Sciences* **13,** 375–384. ISSN: 09280987 (July 2001).

350. Staib, A. H., Loew, D., Harder, S., Graul, E. H. & Pfab, R. Measurement of theophylline absorption from different regions of the gastro-intestinal tract using a remote controlled durg delivery device. *European Journal of Clinical Pharmacology* **30,** 691–697. ISSN: 0031-6970 (1986).

351. Habib, M. P., Schifman, R. B., Shon, B. Y., Fiastro, J. F. & Campbell, S. C. Evaluation of Whole Blood Theophylline Enzyme Immunochromatography Assay. *Chest* **92,** 129–131. ISSN: 00123692 (July 1987).

352. Lombardo, F., Obach, R. S., Shalaeva, M. Y. & Gao, F. Prediction of Human Volume of Distribution Values for Neutral and Basic Drugs. 2. Extended Data Set and Leave-Class-Out Statistics. *Journal of Medicinal Chemistry* **47,** 1242–1250. ISSN: 0022-2623 (Feb. 2004).

353. Abduljalil, K., Gardner, I. & Jamei, M. Application of a Physiologically Based Pharmacokinetic Approach to Predict Theophylline Pharmacokinetics Using Virtual Non-Pregnant, Pregnant, Fetal, Breast-Feeding, and Neonatal Populations. *Frontiers in Pediatrics* **10.** ISSN: 2296-2360 (May 2022).

354. Olivares-Morales, A., Ghosh, A., Aarons, L. & Rostami-Hodjegan, A. Development of a Novel Simplified PBPK Absorption Model to Explain the Higher Relative Bioavailability of the OROS® Formulation of Oxybutynin. *The AAPS Journal* **18,** 1532–1549. ISSN: 1550-7416 (Nov. 2016).

355. Gisclon, L. G. *et al.* Absence of a Pharmacokinetic Interaction Between Intravenous Theophylline and Orally Administered Levofloxacin. *The Journal of Clinical Pharmacology* **37,** 744–750. ISSN: 00912700 (Aug. 1997).

356. Hendeles, L., Weinberger, M. & Bighley, L. Absolute bioavailability of oral theophylline. *American journal of hospital pharmacy* **34,** 525–7. ISSN: 0002-9289 (May 1977).

357. Bruguerolle, B., Toumi, M., Faraj, E., Vervloet, D. & Razzouka, H. Influence of the menstrual cycle on theophylline pharmacokinetics in asthmatics. *European Journal of Clinical Pharmacology* **39,** 59–61. ISSN: 0031-6970 (Oct. 1990).

358. Samigun, Mulyono & Santoso, B. Lowering of theophylline clearance by isoniazid in slow and rapid acetylators [see comments]. *British Journal of Clinical Pharmacology* **29,** 570–573. ISSN: 03065251 (May 1990).

359. Batty, K., Davis, T., Ilett, K., Dusci, L. & Langton, S. The effect of ciprofloxacin on theophylline pharmacokinetics in healthy subjects. *British Journal of Clinical Pharmacology* **39,** 305–311. ISSN: 03065251 (Mar. 1995).

360. Sirmans, S. M., Pieper, J. A., Lalonde, R. L., Smith, D. G. & Self, T. H. Effect of calcium channel blockers on theophylline disposition. *Clinical Pharmacology and Therapeutics* **44,** 29–34. ISSN: 0009-9236 (July 1988).

361. Gillum, J. G., Sesler, J. M., Bruzzese, V. L., Israel, D. S. & Polk, R. E. Induction of theophylline clearance by rifampin and rifabutin in healthy male volunteers. *Antimicrobial Agents and Chemotherapy* **40,** 1866–1869. ISSN: 0066-4804 (Aug. 1996).

362. Rovei, V., Chanoine, F. & Benedetti, S. M. Pharmacokinetics of theophylline: a dose-range study. *British Journal of Clinical Pharmacology* **14,** 769–778. ISSN: 03065251 (Dec. 1982).

363. Jones, H. M., Gardner, I. B. & Watson, K. J. Modelling and PBPK Simulation in Drug Discovery. *The AAPS Journal* **11,** 155–166. ISSN: 1550-7416 (Mar. 2009).

364. Zhang, X., Lionberger, R. A., Davit, B. M. & Yu, L. X. Utility of Physiologically Based Absorption Modeling in Implementing Quality by Design in Drug Development. *The AAPS Journal* **13,** 59–71. ISSN: 1550-7416 (Mar. 2011).

365. Leslie, S., Malkowska, S., Marchant, J. & Neale, P. *Spheroids* 1987.

366. Khosla, R. & Davis, S. The effect of tablet size on the gastric emptying of non-disintegrating tablets. *International Journal of Pharmaceutics* **62,** R9–R11. ISSN: 03785173 (July 1990).

367. Haughton, V. M., Korosec, F. R., Medow, J. E., Dolar, M. T. & Iskandar, B. J. Peak systolic and diastolic CSF velocity in the foramen magnum in adult patients with Chiari I malformations and in normal control participants. *AJNR Am J Neuroradiol* **24,** 169–176. ISSN: 0195-6108 (Print) 0195-6108 (Linking). https://www.ncbi.nlm.nih.gov/pubmed/12591629 (2003).

368. Armonda, R. A., Citrin, C. M., Foley, K. T. & Ellenbogen, R. G. Quantitative Cine-mode Magnetic Resonance Imaging of Chiari I Malformations. *Neurosurgery* **35,** 214–224. ISSN: 1524-4040 0148-396X (1994).

369. Levy, L. M. & Di Chiro, G. MR phase imaging and cerebrospinal fluid flow in the head and spine. *Neuroradiology* **32,** 399–406. ISSN: 0028-3940 1432-1920 (1990).

370. Enzmann, D. R. & Pelc, N. J. Cerebrospinal fluid flow measured by phase-contrast cine MR. *AJNR Am J Neuroradiol* **14,** 1301–7. ISSN: 0195-6108 (Print) 0195-6108 (Linking). https://www.ncbi.nlm.nih.gov/pubmed/8279323 (1993).

371. Enzmann, D. R. & Pelc, N. J. Normal flow patterns of intracranial and spinal cerebrospinal fluid defined with phase-contrast cine MR imaging. *Radiology* **178,** 467–474. ISSN: 0033-8419 1527-1315 (1991).

372. Macgowan, C. K., Henkelman, R. M. & Wood, M. L. Pulse-wave velocity measured in one heartbeat using MR tagging. *Magnetic Resonance in Medicine* **48,** 115–121. ISSN: 0740-3194 1522-2594 (2002).

373. Moser, K. W., Georgiadis, J. G. & Buckius, R. O. On the Use of Optical Flow Methods with Spin-Tagging Magnetic Resonance Imaging. *Annals of Biomedical Engineering* **29,** 9–17. ISSN: 0090-6964 (2001).

374. Kramer, C. M. *et al.* Standardized cardiovascular magnetic resonance imaging (CMR) protocols: 2020 update. *Journal of Cardiovascular Magnetic Resonance* **22.** ISSN: 1532-429X (2020).

375. Pelc, N. J., Herfkens, R. J., Shimakawa, A. & Enzmann, D. R. Phase contrast cine magnetic resonance imaging. *Magn Reson Q* **7,** 229–254. ISSN: 0899-9422 (Print) 0899-9422 (Linking). https://www.ncbi.nlm.nih.gov/pubmed/1790111 (1991).

376. Ståhlberg, F., Søndergaard, L., Thomsen, C. & Henriksen, O. Quantification of complex flow using MR phase imaging—A study of parameters influencing the phase/velocity relation. *Magnetic Resonance Imaging* **10,** 13–23. ISSN: 0730725X (1992).

377. Eichenberger, A. C., Jenni, R. & von Schulthess, G. K. Aortic valve pressure gradients in patients with aortic valve stenosis: quantification with velocity-encoded cine

MR imaging. *American Journal of Roentgenology* **160,** 971–977. ISSN: 0361-803X 1546-3141 (1993).

378. Pelc, N. J. *et al.* Tracking of cyclic motion with phase-contrast cine MR velocity data. *Journal of Magnetic Resonance Imaging* **5,** 339–345. ISSN: 10531807 15222586 (1995).

Appendix One: Luminal fluid motion inside an in vitro dissolution model of the human ascending colon assessed using magnetic resonance imaging

A1: A scrutininsation of tagging versus phase contrast cine-MRI velocity measurements

MR tagging has been used to measure velocity in fluid flows, primarily in blood vessels [272] and more recently in engineering systems [273, 274]. In both applications however, flows have typically been much faster than those previously measured inside the DCM (which were of the order of 2 - 4 $\mathrm{cm\,s^{-1}}$ [10]) and mostly occurred within far smaller geometries, such as veins or nozzles, and usually with the application of only a single tag. Phase contrast (PC) cine-MRI, described in detail in [280], is also used to measure blood flow [281]. However, PC cine-MRI has also been applied to measure lower velocity cerebrospinal fluid (CSF) flows which are commonly of the order 0.5 – 5 $\mathrm{cm\,s^{-1}}$ [367–371] and therefore much more comparable to flows inside the DCM. Moser *et al.* [273] compared both techniques to study flow inside a pipe with a step stenosis. It was found that PC cine-MRI gave more accurate results than tagging techniques for flows of $< 100\ \mathrm{cm\,s^{-1}}$.

Contrarily, d'Avila found that tagging techniques made accurate measurements for flows as low as 0.1 cm s^{-1} inside a concentric cylinder system [274].

The precision of the measurements must be scrutinised by delving into the characteristics of the tagged technique, since measurements inside the DCM were consistently higher than those found using PC cine-MRI. Tagged methods have been reported to measure velocities accurately in phantoms [273, 274, 282, 372], including low flows [274], pulsatile flow [372], and in vivo [372] Contrarily, when compared with PC cine-MRI, Moser *et al.* [273] found that only 50 and 79 % of tagged velocity measurements agreed, to within 10 % of CFD velocity measurements for Reynolds numbers of 100 and 258, respectively, compared to 90 and 94 % for PC cine-MRI. Flows studied were between 0 and 10 cm s^{-1}, similar to flows inside of the DCM. To minimise errors in future tagged experiments, small evolution times can be chosen since the estimated velocity of a tag is given by $u_x = \frac{\Delta x}{\Delta t}$; however, this causes the error in measuring displacement to become more significant. Additionally, a decrease in the evolution time at a constant voxel size has been shown to improve accuracy of tagged velocity measurements from 0.30 m s^{-1} to 0.13 m s^{-1} [282]. PC cine-MRI has been reported to be more accurate than tagged TOF for steady, laminar Poiseuille flow [373]. Moreover, Moser *et al.* [273] similarly used both techniques to measure velocities of a similar magnitude ($0 - 10$) in a pipe with a step stenosis. For slower velocities, PC cine-MRI gave more accurate results compared to numerical CFD solutions of velocity. Therefore, it may be hypothesised that the tagged TOF methodology has overshot the velocity measurements inside the DCM and therefore, potentially inside the human AC too. Further, problems arose from the blurring of tag lines. In addition to complex flows, blurring of tags lines can happen at elevated flows due to an influx of spins from outside the radiofrequency (RF) coil entering the FOV during the tag evolution time [273].

It is unsurprising that PC cine-MRI may yield more accurate velocities than tagging, considering the tagged method utilises a point-based data reduction method used to extract velocity, which is essentially a hand-measured velocity extraction technique. In contrast, PC cine-MRI does not require such an intermediate step; it directly provides a velocity map of the lumen wherein each voxel value represents the weighted average velocity measured in that voxel.

However, the same study by Moser *et al.* [273] found that the largest discrepancy between PC cine-MRI and CFD measured velocities occurred just downstream of the sudden contraction of the stenosis. Here, PC cine-MRI measured velocities were lower than the numerical predictions towards the centre of the pipe. This suggests that the similar contractile behaviour inside the DCM may have led to underestimations on the part of PC cine-MRI, rather than overestimations from tagging. Similarly, Ahmadi & Mastikhin [282] found that phase encoding (MS SPRITE) velocity measurements underestimated velocity, whilst tagged velocity measurements were more accurate. Underestimated velocity measurements are consistently reported in the literature when the TE has been high. For example, O'Brien *et al.* [283] found significant errors in velocity measurements in in vitro stenotic flow, with large underestimates of velocity that reduced with a shorter TE: average error: $\lambda 166\%/\lambda 67\%/\lambda 25\%/\lambda 13\%/\lambda 8.8\%$ for TEs of $4.8/4.0/3.3/2.2/2.0$ ms. This study used a comparatively high TE of 7.6 ms which could explain the large discrepancies between the tagged and PC velocities during contractions of the DCM walls, with PC measurements consistently lower than those of tagging. However, it is appreciated that the studies are not entirely comparable since O'Brien *et al.* [283] studied flows of up to 900 $\mathrm{cm\,s^{-1}}$.

Furthermore, the need to develop methods of extracting velocity fields from spin-tagging images, due to the drawbacks of PC cine-MRI, has been emphasised in the literature [373]. PC cine-MRI assumes that velocity does not vary significantly across each voxel. In the case of complex 3D flows or regions of high shear, this assumption is violated.

Due to the level of complex flows observed in the stimulated AC in vivo, PC cine-MRI is unlikely to make reliable measurements. Furthermore, although PC cine-MRI can measure slow and fast flows, its dynamic range is limited by the signal-to-noise ratio, because the flow-encoding gradient must be limited to avoid phase wraparound. PC cine-MRI is also susceptible to error from phase accumulation caused by fluid acceleration, velocity averaging over the slice thickness, spin flow-through and magnetic susceptibility differences between the media and the walls [273]. Considering in vivo applications, PC cine-MRI is sensitive to bulk motion, which can lead to difficulties associated with respiratory motion [35]. MR tagging is also sensitive to bulk motion but is advantageous as tag lines can easily be tracked outside of the colon to help differentiate bulk from local motion. Secondly, tagging also provides a greater spatial coverage of the colon compared to PC cine-MRI, although there are limitations on the direction of flow that can be quantified (perpendicular to the tag line placement only). Lastly, PC cine-MRI loses sensitivity if the T2 of the sample is short, as the signal will decay during the phase encoding period, whilst tagging loses sensitivity if the T1 of the sample is too short, as the tags will recover (and hence disappear) in the delay period. These properties are likely to favour the use of tagging over PC cine-MRI based on the MR properties of normal human colonic contents.

A critical advantage of the tagging technique in this study was the temporal resolution of 0.6 s compared to the poorer resolution of 2 s for PC cine-MRI. This meant additional measurements from tagging, between the PC cine-MRI measurements, could be detected. This revealed peak velocities during local wall motility, where flow was rapidly evolving and fluctuating. Improved temporal resolution is achievable with PC cine-MRI, at the cost of decreased sensitivity to flows inside the DCM and lower spatial resolution, which is important to precisely track wall motion and synchronise this with the incurred flows. Typically, the temporal resolution for PC blood velocity measurements is $\leq$ 50ms [374]. PC cine-MRI can often be limited by temporal resolution when studying slow flows because the slower the velocity encoding, the stronger the magnitude of bipolar gradients

that must be applied for a longer period of time, thus increasing TR. On the contrary, TR cannot be indefinitely increased, as a relatively short TR is required to achieve maximal temporal resolution [375].

A2: Exclusion of phase contrast cine-MRI datapoints

The image taken immediately prior to maximum contraction was discarded in all PC cine-MRI scans, due to intravoxel dephasing, resulting in signal loss and therefore velocities were unable to be measured with any degree of certainty. This could be due to higher order motion, i.e., acceleration, [376] or turbulence [377, 378]. Although the flow regime inside the DCM is not considered to be turbulent, complex hydrodynamics are expected to occur due to the pulsatile, unsteady nature of peristalsis, such as the 'pouring mode' described by Alexiadis *et al.* [236], [376] demonstrated that intravoxel dephasing can be combatted by shortening the TE. This phenomenon was absent in the tagged methodology which captured viable data at each time point.

Appendix Two: The effect of biorelevant hydrodynamic conditions on drug dissolution from extended-release tablets in the dynamic colon model

B1: Motility index

Using the original method developed by Marciani *et al.* [168] (Equation (6)) to quantify the mimicked baseline pattern as an example; there is one single contraction in each of the first 20 s windows, 2 segments contracting as part of an antegrade wave in the third interval and again in the 4th, followed by another isolated contraction in each of the 5th and 6th intervals. This yields a motility index of 180 $[segments \times s]$. In the CPPW, the only activity is from all segments in the first window, yielding an MI of $[200 segments \times s]$.

Baseline

$$MI = (1 \times 20) + (1 \times 20) + (2 \times 20) + (2 \times 20) + (1 \times 20) + (1 \times 20) \quad (1)$$

$$MI = 180[segments \times s] \quad (2)$$

CPPWs

$$MI = (10 \times 20) + (0 \times 20) + (0 \times 20) + (0 \times 20) + (0 \times 20) + (0 \times 20) \quad (3)$$

$$MI = 200[segments \times s] \quad (4)$$

Stimulated (PEG)

$$MI = (5 \times 20) + (4 \times 20) + (5 \times 20) + (1 \times 20) + (3 \times 20) + (4 \times 20) \quad (5)$$

$$MI = 440[segments \times s] \quad (6)$$

Stimulated (Maltose)

$$MI = (5 \times 20) + (2 \times 20) + (4 \times 20) + (1 \times 20) + (3 \times 20) + (4 \times 20) \quad (7)$$

$$MI = 440[segments \times s] \quad (8)$$

B2: Specific motility index

Schütt *et al.* [238] developed several models of the proximal colon that varied in size and number of segments. To enable comparison of MI between these models, the index was normalised by the number of segments in the model, arriving at the specific MI (Equation (A1)). In vivo, this may hold value for comparing motility between populations, such as paediatric versus adult.

$$SMI = \frac{\sum_{k=1}^{K}(t_i v \cdot N_{seg})_k}{N_{seg,total}} \quad (9)$$

The present study applied different motility patterns inside the DCM, wherein the geometry was constant. Characterisation of motility using the specific MI was therefore not appropriate.

B3: DCM Motility index i, $MI_{DCM,i}$

The number of segments, N_{seg}, used by Marciani *et al.* [168] was also derived from analysis of MRI data and depended on visible motility and interpatient variability. For example, the ascending colon was considered to be one segment. Using in vitro and in silico models, the number of segments is well-defined in the geometry of the system and does not rely on imaging capabilities and unpredictable in vivo motility to distinguish between segments. Since parameters that drive motion of the luminal contents, such as occlusion rate and duration of a contraction, are predefined in vitro, as opposed to in vivo situation (which is limited by accessibility of the colon and the current limitations of in vivo imaging techniques), a more precise version of the motility index, MI_{DCM}, can be introduced to enable quick and easy comparison of motility patterns. This is a necessary development due to downfalls of the existing methodology. Firstly, discrepancies could be introduced to the calculation when a single contractile episode spans more than one time interval. This can be overcome by replacing t_{iv} with the known duration of a contractile episode, t_c, as in Equation (A2), calculating $MI_{DCM,i}$ (an iteration of the MI_{DCM}). In this case, K becomes the total number of motility episodes in the 120 s window.

$$MI_{DCM,i} = \sum_{k=1}^{K}(t_c \cdot N_{seg})_k \quad (10)$$

However, this highlights the issue of using a temporal expression, since an unfairly

heavy weighting is awarded to slow contractions that are less likely to generate higher luminal pressures, flows and intense mixing. For example, the $MI_{DCM,i}$ calculated for the PEG and maltose stimulated motility using this methodology was 81.17 and 26.42 compared to the baseline MI of 80.52 which is clearly misleading:

Baseline

$$MI_{DCM,i} = (2.94 \times 1) + (2.94 \times 1) + (22.92 \times 3) + (2.94 \times 1) \quad (11)$$

$$MI_{DCM,i} = 80.52 \quad (12)$$

CPPWs

$$MI_{DCM,i} = (10 \times 13.88) \quad (13)$$

$$MI_{DCM,i} = 138.8 \quad (14)$$

Stimulated (PEG)

$$MI_{DCM,i} = (4\times2.64)+(1\times0.53)+(4\times5.14)+(1\times0.53)+(3\times5.05)+(1\times0.53)+(3\times5.26) \quad (15)$$

$$MI_{DCM,i} = 81.17 \quad (16)$$

Stimulated (Maltose)

$$MI_{DCM,i} = (4\times1.84)+(2\times1.58)+(3\times1.52)+(3\times1.58)+(3\times1.52)+(4\times0.51) \quad (17)$$

$$MI_{DCM,i} = 26.42 \quad (18)$$

This highlights the downfall of this calculation; that the duration of the motility increases inversely with occlusion velocity, therefore a falsely high weighting is awarded to slower waves.

B4: DCM Motility index, MI_{DCM}

Stamatopoulos *et al.* [9] and Arkwright *et al.* [337] demonstrated occlusion velocity to be key in generating pressure during non-occluding events (more important than occlusion degree). Therefore, the index was further developed by replacing the duration of a contraction t_c with occlusion velocity, v. A critical benefit of the existing Marciani *et al.* [168] methodology was that the summative nature of the calculation inherently increases MI with the frequency of contractile activity, which Schütt *et al.* [238] reported to be an effective predictor of dissolution ability. To further increase discriminatory power of the MI_{DCM} between motility patterns that may have different repetition frequencies, MI_{DCM} was normalised by the frequency, 120 s for all patterns in this study. Therefore, the resulting MI (Equation (A3). Equation (7) in main text) is sensitive to occlusion velocity, frequency of occluding events and the number of segments involved in a contractile episode. Finally, to non-dimensionalise the index, the number of segments was divided by the length of a segment, L.

$$MI_{DCM} = \frac{1}{\omega \times L} \sum_{k=1}^{K} (v \cdot N_{seg})_k \tag{19}$$

Baseline

$$MI_{DCM} = \frac{1}{120 \times 28}[(1 \times 1.64) + (1 \times 1.64) + (3 \times 1.55) + (1 \times 1.64) + (1 \times 1.64)] \tag{20}$$

$$MI_{DCM} = 0.0033 \tag{21}$$

CPPWs

$$MI_{DCM} = \frac{1}{120 \times 28}[(1 \times 5.4) + (9 \times 5.4)] \tag{22}$$

$$MI_{DCM} = 0.016 \tag{23}$$

Stimulated (PEG)

$$MI_{DCM} = \frac{1}{120 \times 28}[(4\times12.98)+(1\times12.98)+(4\times12.98)+(1\times12.98)+(4\times12.98)+(1\times12.98)+(3\times12.98) \tag{24}$$

$$MI_{DCM} = 0.085 \tag{25}$$

Stimulated (Maltose)

$$MI_{DCM} = \frac{1}{120 \times 28}[(4\times12.98)+(1\times12.98)+(2\times12.98)+(1\times12.98)+(3\times12.98)+(1\times12.98)+(3\times12.98) \tag{26}$$

$$MI_{DCM} = 0.074 \tag{27}$$

The MI_{DCM} discriminated more between the baseline and CPPW patterns which is important given the differences in occlusion rate, which was dampened using the MI from the existing methodology. Since the motility index increased with occlusion velocity, frequency of pressure-generating events and number of segments involved, this index was considered to be sufficient for this study. In this iteration of motility index, equal weighting is given to single, isolated contractions, as to a contraction that is part of a propagating wave. However, it is likely that the additional relaxation step prior to contraction and the

progressive contractions lends a heightened hydrodynamics effect and should be weighted more heavily. However, until this data is available, adjustment may be somewhat arbitrary, so this was considered to be beyond the scope of this work. This provides an insight into a possible representation of in vivo MI in the future as imaging capabilities develop.

Appendix Three: Application of the DCM as a biopredictive tool for controlled release theophylline formulations through integration into physiologically-based biopharmaceutics modelling (PBBM)

C1: Colonic water absorption

Figure C.1 presents a tree diagram collating all published data (known to the author at the time of writing) measuring water absorption from the human colon. Whilst there is limited data available, these data exhibit a very large range. This appears to be largely attributable to the test method, since studies quoting data upwards of 50 mL h^{-1} involved perfusion to push the absorptive capacity of the colon and measure maximum capacity. The coloured lines show the absorption rates mimicked in this study using the DCM. Samples 1 mL in size were used initially for comparison with pharmacopeial methods, then increased to 2, 5 and 10 mL, for which absorption rates overlapped with the 3 datapoints for the

non-perfused colon. Additionally, the DCM mimics just the ascending colon rather than the entire colon, so absorption measurements are likely to be much lower than the values measured across the entire colon in vivo.

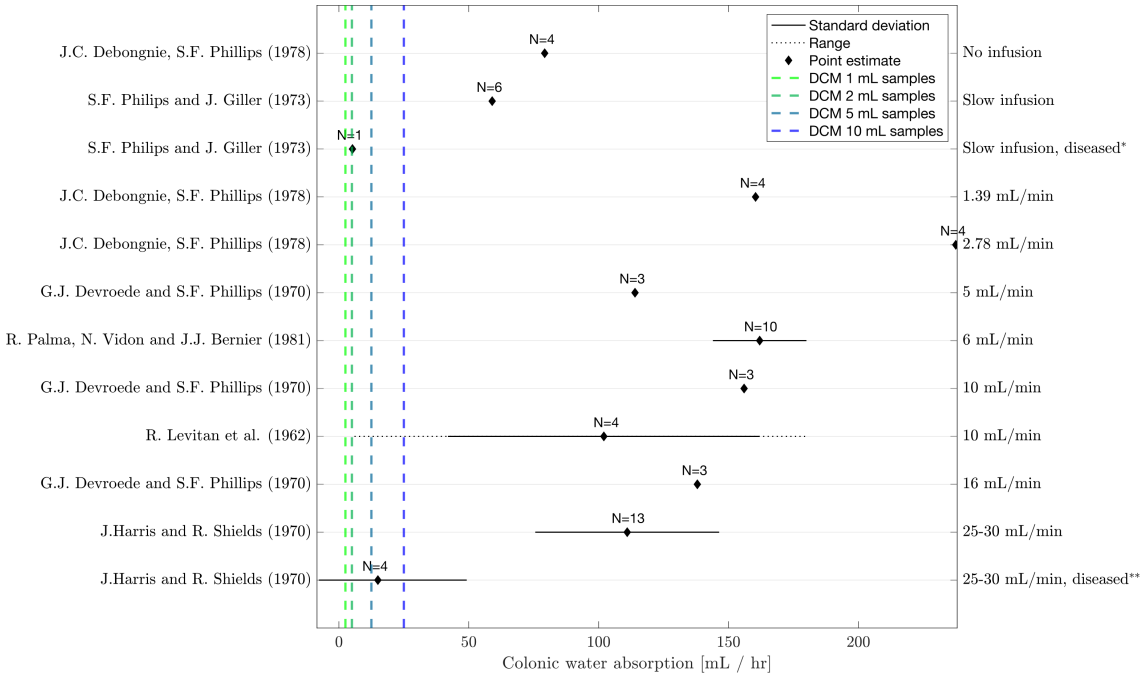

Figure C1.1: Absorption of water in the colon